University of Strathclyde

Electrical and Electronic Engineering Department

Glasgow, UK

Wind farm high frequency electrical resonances: impedance-based stability analysis and mitigation techniques

by

Gabriele Amico

A thesis submitted in fulfilment of the requirements for the degree of Doctor of Philosophy

2019

To my family

Declaration

This thesis is the result of the author's original research. It has been composed by the author and has not been previously submitted for examination which has led to the award of a degree.

The copyright of this thesis belongs to the author under the terms of the United Kingdom Copyright Acts as qualified by University of Strathclyde Regulation 3.50. Due acknowledgement must always be made of the use of any material contained in, or derived from, this thesis.

Signed:

Date:

Acknowledgements

A special thank is to my academic supervisors, Dr. Agustí Egea-Àlvarez and Prof. Lie Xu, and to my industrial supervisor, Dr. Paul Brogan, for their precious technical advice.

I am greatly thankful to Dr. Shuo Zhang for his invaluable guidance with the maths used in this work.

Particular gratitude is for Prof. William Leithead, Dr. Alasdair McDonald and Prof. Olimpo Anaya-Lara, who have offered me the opportunity to pursue this PhD project.

I thankfully acknowledge the funding received towards my PhD from the EP/L016680/1 EPSRC Centre for Doctoral Training in Wind and Marine Energy Systems and from Siemens Gamesa Renewable Energy.

Finally, I would like to express my most gratitude to my friends, and in particular to Ife, for their support during my PhD journey.

Abstract

The installation of larger wind farms has introduced new grid integration challenges. Among these, high frequency electrical resonances caused by the cables and lines connecting the wind farm to the grid have been described in literature. These resonances may cause instability as they typically occur at frequencies close to the current controller bandwidth of the wind turbine inverter. Different mitigation techniques have been proposed in the literature to counteract these resonances. However, these techniques lack of generality as they rely on parameter tuning, which varies on a case-by-case scenario. In order to analyse the problem, an impedance-based stability approach has been applied. A systematic technique to derived the sequence-frame converter admittance has been defined, and a stability study methodology including the coupling between the positive and negative sequence converter admittances has been formulated. Compared to the existing impedance-based stability criterion, where such coupling is ignored, the proposed technique is more accurate in the system stability assessment. The study has shown that the delay introduced by the controller implementation is the main cause of the investigated wind farm stability issues. An innovative hardware implementation of the controller is proposed to compensate for this delay, without altering the converter switching frequency but making a more efficient use of the available hardware processing power. Hence, a more general and portable solution to the problem is proposed, which does not require parameter tuning. An experimental validation of the applied stability analysis methodology and of the proposed mitigation techniques has been carried out, making use of a purposed built prototype of a converter-grid system.

Contents

List of Figures

List of Tables

Chapter 1

Introduction

Wind energy is currently seen as one of the most cost-effective renewable resources [1]. As a result of this, installation of wind power plants has significantly increased over the last decades [2].

As modern wind turbines are based on power electronics equipment, a reduction on standard synchronous machine generation has been observed [3], resulting in a more complex power network operation. Some of the challenges include voltage regulation, power quality and grid stability [4], [5], [6].

New stability issues attributed to the use of power converters have been reported, such as resonances due to cables [7], [8], sub-synchronous resonances within DFIG-based wind farms [9] [10], or the connection of power converters to weak grids [11], [12]. Compared to rotating electrical generators the control bandwidth of power converters is typically much higher, with a consequent increased risk of instability [13].

This work focuses on a specific stability issue observed in wind farms, which is caused by the electrical resonances generated by the cables and lines installed to connect a wind park to the grid [8]. These resonances typically occur in a range of frequency from a few hundred Hz to 1 kHz [14], [8], [15] and, for this reason, will be referred to as wind farm high frequency electrical resonances, or simply wind farm resonances. As it will be discussed in the following Section, the parasitic capacitance of such cables and lines plays an crucial role to the generation of such stability issues.

1.1 Wind farm resonances

The resonances considered in this work originate, as mentioned, in the interconnection between a wind farm and the grid [14]. A network of Medium Voltage (MV) cables is typically employed to constitute the collector system of the wind farm, interconnecting the turbines and gathering the power produced by each individual unit. An export system is then used to deliver this power to the grid. In offshore sites this typically is either a High Voltage (HV) AC submarine cable [16], [17], or HVDC technology when the offshore park is installed at larger distances from the shore [18], [19], [20]. When it comes to the onshore case, the search for sites with a higher wind resource typically leads to intallation of wind parks in remote locations, far from the trasmission network, with the need of a long HV AC overhead line or underground cable to export the generated power to the grid [21], [22].

While collector cables typically are tens of kilometers long [23], the export cables/lines may even reach the length of a hundred kilometres [14]. The parasitic capacitive elements of such extended cabling system become significant and can not be overlooked in the design of the interconnenction between the grid and the wind farm. Despite the fact that the turbine controller is specifically designed to effectively achieve disturbance rejection, its robustness (quantified by stability margins such as gain margin, phase margin, vector gain margin [24], [25]) is seen to be strongly imperilled by the inductance and parasitic capacitance of the cables and lines.

Firstly, as discussed in [26], the interaction between the high shunt capacitance of the cables (particularly the large submarine cables) and the inductive element of some of the installed equipment (particularly the transformers) generates parallel and series resonances. These typically occur at frequencies close to the upper limit of the turbine inverter current controller bandwidth [14], [15]. These so-called wind farm electrical resonances are likely to interact with the dynamics of the wind turbine power converter controller, hence increasing the probablility of triggering unstable behaviours if these resonances are excited. Even though these phenomena have been observed both in onshore and in offshore sites [14], the resonances of offshore scenarios have been mainly studied in the literature, as the bigger and bigger size of offshore parks, combined with their increasingly complex structure, exacerbate these stability issues [27], [28]. This is mostly due to the longer cables needed to interconnect the higher number of turbines of these larger plants [29], which makes the cable parasitic capacitance increasingly significant. Moreover, the use of a long HV AC export cable and the problable low short circuit ratio values at the point of common coupling, are likely to further threaten the stability of the system, by introducing resonances within the bandwidth of the turbine current controller [30].

Secondly, as the parasitic capacitive and inductive elements of the cables and lines require additional reactive power to assure that the interconnection operates in compliance with grid codes [31], [32], further equipment such as capacitors and inductors are usually installed to make up for this extra reactive power requirement [33]. These devices introduce further undesired resonances making the stable operation of the system even more difficult to preserve [33].

In order to avoid uncontrolled voltages and currents when unstable dynamics build up, generation units are usually disconnected from the grid [8]. To resolve the issue, different mitigation techniques have been proposed, which typically consist in the use of filters specifically tuned to damp these resonances [34], [35]. Each wind farm has its own resonance frequencies, which depend on factors such as the grid characteristics, the wind farm configuration and operating point, etc. For example, variations in the number of operating turbines have been seen to substantially change the frequencies and the gains of the resonances [8], [14]. This aspect becomes more important in the larger offshore wind farms, as the number of generating turbines can vary from a few units to several hundreds. The variety of the possible scenarios makes it difficult to indentify a unique, universal solution to the problem. In order to investigate the potential resonances of each wind farm, expensive field measurements need to be carried out, together with complex model based studies of the system [27], eventually producing solutions specifically tailored on a case-by-case basis, which de facto limits their portability. Hence, this research work is inspired by such need of a more general solution to the problem, which can effectively be applied in disparate scenarios, regardless of the wind farm design.

An overview of the currently proposed techniques is presented as follows.

1.2 Mitigation techniques: state-of-the-art

The study of wind farm resonances constitutes a broad area of research and, as a consequence of the increased size of wind parks, the problem is rising in relevance. Different solutions have been suggested in the literature, which typically consist in the installation of additional equipment in the wind farm, or in the implementation of active filters in the turbine control scheme [34].

A study of wind farm resonances for both onshore and offshore wind parks is presented in [36]. In the work, analytical expressions of the resonance frequencies are provided, which allow to point out how cable resonances are related to wind farm parameters such as transformer, capacitor banks and cable impedances. Thereafter, the uses of both passive notch filters and high-pass filters, installed at specific wind farm buses, are compared. The study concludes that the latter filter type is more effective at damping resonances above its tuned frequency, while the notch filter, despite being effective at its resonance frequency, has the drawback of introducing potential further resonances in the system. Similar conclusions on the use of passive filters are drawn in [37].

Wind farms resonances are also studied in [38], where it is highlighted how the use of capacitor banks can detrimentally shift the resonance frequencies in the range of the 5^{th} and 7^{th} harmonics, causing their amplification. Thereby, the installation of an inductor in series to the capacitor banks is proposed to shift the resonance frequencies to less critical (higher) values. Last but not least, the study emphasises that, as the resonances vary with the operating point of the wind farm, inductors of different sizes should be used for a more effective damping action, hence pointing out how simple fixed passive filters are prone to variations in the resonance frequencies.

In [23] and [39], a comprehensive analytical study of wind farm resonances is presented making use of both the Harmonic Resonance Mode Analysis (HRMA) method and the frequency scan technique. Considering the case study of a 400MW offshore wind farm, the length of the MV collector submarine cable is varied in the work to emphasize its central role to determine the values of the resonance frequencies, showing how, expectedly, longer lengths reduce the frequencies of the resonances. Thereby, the effect of installing either passive or hybrid ad hoc tuned filters at critical buses of the collector system is compared. The study concludes that the hybrid ones, despite the fact of being the more expensive and complex alternative, provide a better performance, damping the desired resonances without, unlike the passive filters, introducing new resonances at other frequencies.

In [40], [14] the study of wind farm resonances is carried out considering both onshore and offshore real plants. Field measurement data are used to support the analysis and a frequency domain model of the turbine controller is built to assess the stability of the system. The work confirms that instability is more likely to occur in the case of large offshore wind farms, where the higher shunt capacitance of the cables can generate resonances at frequencies as low as 200 Hz, thereby making the controller design of offshore wind turbines more challenging. Furthermore, the study proves the strong dependancy of the resonance frequencies on the number of turbines in operation, as similarly found in [8], [23]. The use of resonant selective control loops, tuned to eliminate specific frequencies and integrated in the inverter current controller of the turbine, is then proposed to damp the cable resonances. However, albeit these studies prove the effectiveness of such methods, they also point out how a careful design of these filters is needed to avoid side effect stability issues.

In [29] resonances in offshore wind farms are investigated and attributed to the long HV AC export cable connecting the wind park to the onshore grid, and in particular to its big shunt capacitance. A notch based active damping control strategy is then successfully used to resolve the stability issue. This is cascaded to the Proportional Resonance (PR) current controller [41], which is implemented in the $\alpha\beta$-frame, and tuned to specifically neutralise the high frequency LC cable resonance. However, as pointed out in [40], the tuning of this active filter is critical not to introduce further stability problems.

A comprehensive panorama of mitigation techniques for the neutralisation of wind farm resonances is presented in [34]. These are divided into two categories depending on whether resonance damping is carried out by the turbine inverter current controller or by an external device. In the former case, a revision of the control strategy is required. This may for example consist in the inclusion of a derivative term in the Voltage Feed-Forward (VFF) term of the controller [42], [43], or in the implementation of virtual resistors by adding extra current feedback paths [44]. These approaches are based on the passivity-based method [45], which aims to make the inverter output admittance passive to assure the system closed loop stability (under the assumption that the grid impedance is also passive). Despite the fact that these proposed methods have been proven to be successful, their applicability in a real scenario is limited by the need to have an accurate knowledge of the plant parameters, necessary to tune the controller effectively. The use of a notch filter to attenuate selected resonant frequencies is proposed in [46]. In the study, the filter is cascaded to the PI current controller and tuned based on an estimation of the system resonance frequency obtained with the Goertzel algorithm [47]. However, this on-site tuning method, despite the fact that it is robust to minor variations in the resonance frequency (for example due to aging), is not adequate to cope with the larger frequency changes of the wind farm resonances. The use of a low quality factor notch filter is proposed in [8] and included in the current and voltage feedback of the controller. In this study, instability caused by cable resonances in an offshore wind park is studied, in particular highlighting how relevant the number of operating turbines is to determine the resonance frequency of the system. Thereby, a wider band notch filter is used to make up for these broad changes in the resonance frequencies, with the consequence of reduced stability margins, caused by the poorer phase performance of such filter.

An alternative approach is the use of Selective Harmonic Elimination (SHE) PWM algorithms in the control of the wind turbine inverter [48], [49], as a method to avoid excitation of the wind farm resonances. However, the complexity of their implementation, which may require, for example, the use of time-dependant carriers, not to mention the dependency of these PWM patterns on the measured voltage phase angle, curbs their application in real scenarios.

When it comes to active devices, STATCOMs are among the most used components in wind farms. While traditionally used for the provision of reactive power [34], their use as active dampers has been proposed more recently. For example, in [50], a shunt active filter is designed to behave like a damping resistor at the resonance frequency. The main limit of these devices is that they are suitable only for the elimination of lower frequency resonances, because of the practical contraints on their current controller bandwidth [34]. A proposed possible solution is the use of hybrid active filters [51], [52]. In this case one or more Voltage Source Converters (VSC) is combined to a passive filter, allowing for lower ratings for the VSC and, therefore, a higher current controller bandwidth. A more flexible active filter is then proposed in [53], where power converters are used to imitate the behaviour of a damping resistor, whose tuned frequency is extracted on-line from the spectral analysis of the measured bus voltage. While allowing for the possibility of automatic filter tuning, on the downside, this solution does not allow for the rejection of multiple resonances simultaneously.

1.3 Motivation and aims of the work

The main limitation of the solutions discussed in Section 1.2 is seen to be lack of generality. The common denominator of these methods is the use of filters able to damp specific resonance frequencies. However, as the resonances of each wind park depend on many parameters such as the cable parameters and length, wind farm layout, use of capacitor banks, grid specifications, these filters need to be tuned on a case-by-case basis. Moreover, the resonance frequencies strongly depend on the operating conditions of the wind farm and, in particular, on the number of active turbines [8], making the scenarios even more changeable.

The design of these filters requires an accurate study of the resonances for each wind farm installation, which can be both time consuming and costly. A more flexible solution, able to cope with potential broad changes in the resonance frequencies, and that is easy to implement, would be desirable for wind turbine manufacturers. This would allow them to confidently install their wind turbines in disparate wind farm scenarios, eliminating the necessity to customise their design for each single case. In more general terms, the challenge lies in the intrinsic dependence of the grid-connected turbine stability performance on the grid impedance, which varies from site to site.

A first aim of the work is therefore the implementation of a turbine controller scheme able to enhance its stability robustness against the occurrence of these wind farm electrical resonances. A controller whose design and parameter tuning does not rely on an a priori knowledge of the wind farm specifics.

In a context where a large variety of designs are possible for the interconnection between a wind farm and the grid, the modelling of the wind farm system and the assessment of its stability performance also become more complex tasks. The use of an analytical method which does not require a detailed knowledge of the system paramters would be desirable and has been proposed in [54], where the impedance-based stability criterion is discussed and applied to the study of a converter-grid system. This requires the definition of a small-signal model of the system in the sequence-frame, formulated in terms of the small-signal converter admittance and of the Thévenin equivalent small-signal grid impedance.

A second aim of the work is to enhance the potential of the method presented in [54]. While in the existing literature formulas to calculate the converter admittance are provided only for a limited number of converter control schemes [55], a systematic methodology has been defined in this work to calculate the small-signal converter admittance for any generic converter control scheme. Moreover, while in the method proposed in [54] the cross-coupling terms between the positive and the negative sequence terms of the converter small-signal admittance are neglected, a technique has been formulated to include them in the analysis, allowing a more accurate stability assessment of the system. The methodology has been applied to study the wind farm electrical resonances, both to investigate the related critical aspects of the controller design, and to evaluate the effectiveness of the proposed mitigation techniques on the stability performance of the wind farm.

1.4 Methodology

In order to study the wind farm resonances, the case study of a real grid-connected wind farm system where such a problem was observed, has been considered. Firstly, a model of the interconnection between a single wind turbine and the grid has been built. Thereafter, along the line of similar works published in the literature ([56], [33], [8]) an aggregation technique has been applied to model the wind farm-grid interconnection.

In the defined model of the system, as the wind farm resonances are likely to generate unstable dynamics by interacting with the current controller of the turbine's inverter [15], [57], [23], the focus of the study has been on this section of the inverter controller. In particular, a standard configuration of such a controller has been considered, implementing the so-called dual vector current control algorithm in the *dq*-frame [8], [58].

Having defined a model of the wind farm-grid interface, the second step of the study has been the analysis of its stability performance. In order to carry out such stability study, a small-signal Linear Time-Invariant (LTI) model of the system has been built, which has enabled to describe the linearised dynamics of the system around its steady-state operating point. Such small-signal model, which is derived in the frequency-domain and is implemented in the positive *dq*-frame, has been used to study the system stability applying classical feedback control theory [11], [25], [59]. It is worth mentioning that, in such a model, the negative sequence current controller, which is implemented in the negative *dq*-frame, is referred to the positive *dq*-frame. For this purpose, a mathematical translation has been introduced to map the transfer function models used to describe the controller operation, from the negative to the positive *dq*-frame. Along this line, an equivalent mapping technique has been derived to translate transfer function models from the *abc*- to the *dq*-frame.

Such a small-signal model constitutes a Multiple-Input-Multiple-Output (MIMO) LTI system, hence requiring the application of MIMO control theory tools [24]. Carrying out this task in the *dq*-frame is effortful for at least two reasons. Firstly, because of existing couplings between variables in the *d*- and in the *q*-axis [58], [60]. Secondly, because it requires a *dq*-frame representation of the grid impedance, which can be a time-consuming task especially when this has a complex structure (as in the case when it also includes the cabling system connecting a wind farm to the grid). Based on the impedance-based stability criterion [55], [54], [61], [62], [13], a representation of the sys-

tem in the sequence-frame as an electrical circuit composed of a source (the inverter) and a load (the grid), each respectively modelled by their Norton/Thévenin equivalent, has been used. The main advantage of this approach is the substantial diagonalisation of the MIMO control system, which allows to treat the system as a combination of two independent Single-Input-Single-Output (SISO) systems [54]. This facilitates both the study of the system absolute stability, and of its relative stability [63], allowing to use familiar tools like the gain and phase margin [25]. Moreover, by representing the inverter-grid interface as two separate entities, the converter and the grid small-signal impedances, for a given inverter controller design, the associated small-signal converter impedance/admittance is unique and only depends on the converter operating point. Thereby, the stability of the system for different grid impedances can be verified in a straightforward way, simply updating the sequence-frame small-signal grid impedance (which corresponds to the *abc*-frame impedance for a passive and balanced grid [64]). Only changes in the inverter controller architecture or in its parameters would require an updated calculation of the small-signal converter impedance/admittance.
Given that the small-signal model of the system has been implemented in the *dq*-frame, a tool is needed to map it on the sequence-frame. More specifically, this is necessary to derive the sequence-frame expression of the small-signal converter admittance. Different approaches have been proposed in the literature [13], [65], [66], [67], which calculate the small-signal converter impedance from a small-signal model of the system either in the *dq*-frame, or in the *abc*-frame, or in the $\alpha\beta$-frame. An alternative technique has been implemented in this work, where the small-signal converter admittance is first calculated in the *dq*-frame and then mapped onto the sequence-frame, making use of a set of equations. The resulting sequence-frame small-signal converter admittance is then combined with the small-signal grid impedance to carry out the stability study by application of the Generalised Nyquist Criterion (GNC) [68], [69]. A significant advantage of the proposed method is that it can be used for any converter control scheme, once its small-signal equivalent model is formulated in the *dq*-frame. Moreover, the method allows a calculation of the cross-coupling terms between the positive and the negative sequence components of the small-signal converter admittance. This has allowed

their inclusion in the stability study, unlike in the application of the impedance-based stability criterion, where they are neglected [54]. A more in depth analysis of such coupling has been carried out, investigating how this is affected by the converter control scheme and how it impacts the stability analysis. The definition of a perturbation norm stability margin that takes such coupling into account is also given, exploiting the typically verified diagonal dominance property of the converter-grid interface small-signal impedance-based model in the sequence-frame.

As mentioned, the developed methodology has been used to study the stability performance of a wind farm system where such type of investigated resonances was observed. This has allowed to highlight the significant role of the controller delay in building up these unstable dynamics. Moreover, the stability analysis has revealed that a grid connected wind farm can indeed suffer from two types of resonances. One is a low frequency resonance, associated to a weak grid effect. The other is the high frequency resonance so far discussed, which is due to the high shunt capacitance of such cables/lines. Despite the fact that the focus of this work has been on the study of the latter type of resonances, i.e. the high frequency ones, the beneficial effect of one of the proposed techniques, the Fast Voltage Feed-Forward (FVFF) strategy, on the low frequency resonance problem will also be highlighted.

Two complementary mitigations techniques have been designed. Based on the observation that the controller delay is seen to be critical to the high frequency wind farm resonance issues, they aim to compensate for such delay, without changing the switching frequency of the inverter, but making a more efficient use of the controller hardware. The first strategy, the FVFF one, uses the latest available plant voltage sample to maximise the damping properties of the converter controller. The second strategy, named Reduced Current Delay (RCD), eliminates the sampling delay affecting the current control loop, making use of the latest available plant signals to adjust the PWM pattern currently applied to modulate the inverter voltage. The stabilising effects of these methods has been verified both analytically, based on the small-signal model of the system, and experimentally, making use of a built grid-connected converter prototype, where a cable resonance similar to those observed in wind farms has been reproduced [14], [8]. It will be shown how the optimal performance of the controller is obtained when the FVFF and the RCD strategies operate together, which therefore constitutes the eventual controller design proposed in this work.

1.5 Structure of the thesis

The work is composed of five more Chapters and six Appendices, whose content is outlined as follows.

In Chapter 2, the model of the studied wind farm system is presented. As its elementary block is the interface between the turbine's inverter and the grid, the components of such interface are described in more detail, with a particular focus on the converter controller. Thereby, the aggregated model of the studied wind farm system is illustrated, highlighting how this has allowed a reproduction of the studied high frequency resonances. Subsequently, the built scaled-down laboratory prototype of an inverter-grid interface, which has been used throughout the work to validate the analytical results experimentally, is described, specifying its different set-ups that have been considered.

In Chapter 3, the derivation of the small-signal model of the studied inverter-grid system is provided. As mentioned, this is represented in the frequency domain and implemented in the dq-frame. In particular, the focus of the derivation has been on the methodologies that have been used to include both the PLL dynamics and the negative sequence current controller in the model. Thereafter, a validation of this analytical model both against an equivalent Simulink based time-domain model of the considered interface, and against the built laboratory prototype, is provided. This small-signal model has been used in the stability studies carried out throughout the work, and in particular in the analysis of the wind farm stability performance.

In Chapter 4, the methodology used to study the stability of the system is presented. The notion of small-signal converter admittance is introduced, and the equations used to calculate its analytical expression in the sequence-frame are provided and validated experimentally. A more in depth analysis of the existing coupling between the positive and the negative sequence terms of the small-signal converter admittance is presented, showing how their magnitude is significantly affected by the used control scheme.

Thereafter, the criterion to assess the absolute stability of the system is described and applied to study the considered wind farm system. Then, how the stability study is affected by the mentioned coupling terms is investigated and a criterion to decide whether such coupling should be included or not in the study is provided. This is based on the diagonal dominance property of the converter-grid system in the sequence-frame. Finally, such a property of diagonal dominance is exploited to introduce a perturbation norm stability margin which takes the aforementioned coupling terms into account.

In Chapter 5, the proposed techniques to mitigate the wind farm resonances are described, namely the FVFF and the RCD strategies. Their hardware implementation is outlined, and their effectiveness to counteract such resonance issues is shown, both analytically and experimentally. Finally, based on these strategies, an optimal controller design is suggested and its stability performance is quantified.

Final conclusions and future work are presented in Chapter 6.

Six complementary Appendices have been included. In Appendix A, a description of the used Space Vector Modulation (SVM) technique is presented. In Appendix B, the definitions of the positive and negative *dq*-frames are provided. In Appendix C, the analytical derivations of the most relevant equations used throughout the work are provided, in particular for the expressions relating a generic *dq*-frame admittance to its equivalent sequence-frame formulation. In Appendix D, a description of the hardware used to build the converter laboratory prototype is provided. In Appendix E, the carried out digital implementation of the controller algorithm is presented. Finally, in Appendix F, the publications and inventions generated by this work are listed.

Chapter 2

Wind farm-grid modelling and prototyping

This Chapter describes the model of a wind farm-grid system where the problem of wind farm resonances has been observed. Such a model makes use of an aggregated wind turbine model and a grid model, defined based on similar studies published in the literature [56], [33], [8]. The individual turbines of the wind farm are replaced by an equivalent scaled-up turbine, and the network of cables and lines connecting the wind farm to the grid is modelled by a lumped RLC equivalent circuit.

A simplified model of a single grid-connected wind turbine is also introduced, which has been used to carry out some of the analytical studies presented in the next Chapters.

As the wind farm resonances typically occur at frequencies much higher than those of the mechanical and aerodynamic modes of the turbine [8], [15], [22], these have not been included in the used turbine model. The focus has been limited to the turbine inverter, as it is its interaction with the wind farm resonances which has been seen to be responsible for the investigated stability issues [14], [30]. The design of the inverter controller will be presented in detail, as it has a central role in the inverter operation, and it is where the proposed mitigation techniques will be acting on.

A description of a built prototype of the inverter-grid interconnection is also provided. It reproduces the cable due instability dynamics of real wind farms on a laboratory scale. It will be used to verify the effectiveness of the mitigation techniques presented in Chapter 5, as well as to validate the theoretical analyses presented in Chapters 3 and 4.

The Chapter is organised as follows. In Section 2.1 the models used throughout the work are described. In particular, these include the turbine and the grid models, the model of a turbine-grid interconnection and that of the wind farm-grid system where the resonance issues have been observed. In Section 2.2, the design of the turbine inverter controller is presented, and how this is adjusted for the scaled-up turbine of the wind farm aggregated model is illustrated. Finally, in Section 2.3, the built laboratory prototype of the inverter-grid system is presented, describing the different set-ups that have been considered in the carried out tests.

2.1 Modelling

The models that have been used in this work are presented as follows. In Section 2.1.1, the model of the turbine is presented. In Section 2.1.2, the simplified Thévenin equivalent grid model considered in the work is described. Thereafter, in Section 2.1.3, the model of a turbine-grid interconnection is outlined. Such a model will be used in some of the theoretical analyses presented in Chapters 3 and 4. Finally, in Section 2.1.4, the aggregated model of a wind farm-grid system where the wind farm resonance issue has been observed is presented. This model will be used in Chapter 4 to analyse the stability problems associated to such resonances, and in Chapter 5 to verify the effectiveness of the proposed mitigation techniques on the wind farm system stability behaviour.

2.1.1 Turbine model

A variable speed Full Scale Converter (FSC) turbine has been considered [22], whose scheme is shown in Figure 2.1. The drivetrain consists of a Permanent Magnet (PM) synchronous generator connected to a back-to-back power converter [21]. The generator controls the speed of the wind turbine rotor to maximise its aerodynamic efficiency. As the machine currents and voltages have variable frequency and amplitude [70] a full power converter is required to connect the generator to the grid.

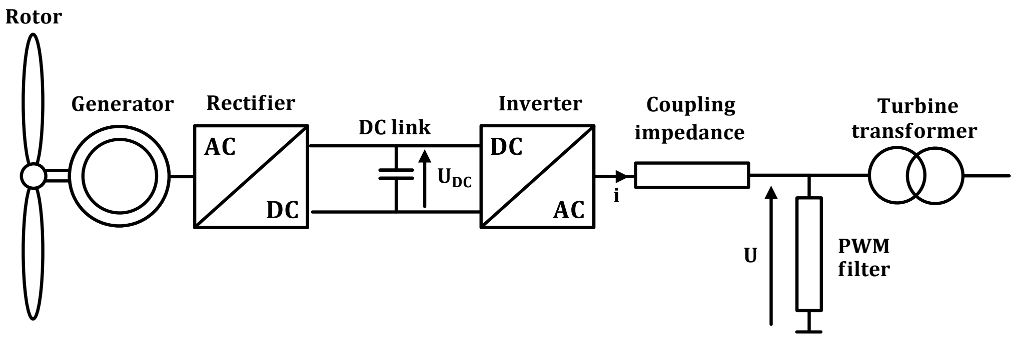

Figure 2.1: Standard grid-connection scheme of a FSC wind turbine.

The inverter is connected to the Low Voltage (LV) bus by means of a coupling inductor and of a shunt filter, which is used to attenuate the Pulse Width Modulation (PWM) harmonics generated by the inverter. A transformer is then utilised to increase the voltage up to the Medium Voltage (MV) bus. A three wire star connected system has been assumed. The U voltage and the i current are measured by the inverter controller to control the inverter operation, as it will be discussed in Section 2.2.1.
As the electrical resonances object of this work typically occur in the [200 Hz, 1000 Hz] range [39], the lower frequency dynamics caused by the mechanical and aerodynamic modes of the wind turbine [22], as well as the dynamics of the DC link voltage, whose bandwidth is much lower than 200 Hz [58], have been neglected in the study. The focus has been on the turbine inverter, ignoring any variations in the DC link electrical signals. Hence, in the considered model of the turbine the DC link capacitor has been replaced by an ideal DC voltage generator.
The used inverter model will be discussed in the following Section. Thereafter, in Section 2.1.1.2 the resulting equivalent electrical circuit used to model the turbine is presented.

2.1.1.1 Inverter model

Reflecting the trend in the industry [58], a three phase two level Voltage Source Converter (VSC) using IGBT switches has been considered. Its equivalent electrical diagram is shown in Figure 2.2.

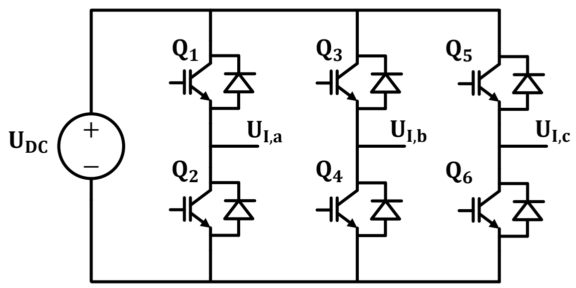

Figure 2.2: Standard three phase two level VSC with IGBT switching devices.

An average model of the inverter has been considered [58]. This consists of three controlled voltage sources, one for each phase. Based on (A.2), the inverter output voltage, $U_{I,abc}(t)$, is calculated as:

$$U_{I,abc}(t) = \frac{U_{DC}}{2} m_{abc}(t) \tag{2.1}$$

where $m_{abc}(t)$ are the three phase modulation functions used by the PWM technique to control the turn-on and turn-off times of the inverter switches [71], [72]. These are calculated by the inverter controller, as it will be discussed in Section 2.2.1.

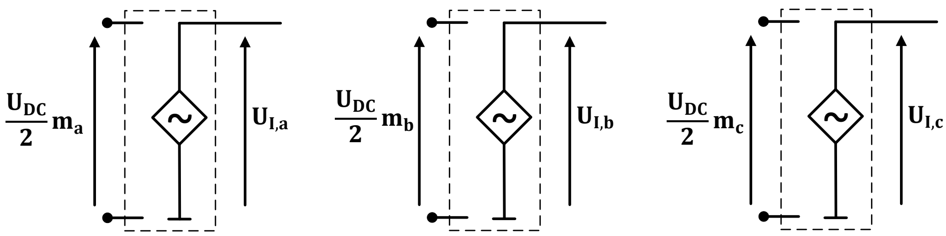

Figure 2.3: Equivalent circuit of the used average model of the VSC.

Equation (2.1) results from the assumption that linear modulation is used [71], which requires to limit the range of variation of $m_{abc}(t)$, typically to the $[-1, 1]$ interval. Thanks to the Space Vector Modulation (SVM) technique, which has been used in this work, this range can be extended by approximately 15 % [73]. More details on the inverter operation and on the SVM method can be found in Appendix A.

The equivalent circuit associated to the used average model of the inverter is composed of three controlled voltage sources, as shown in Figure 2.3.

2.1.1.2 Turbine equivalent circuit

The equivalent one-line electrical diagram of the considered turbine model is shown in Figure 2.4, where all the impedances are referred to LV. The coupling inductor and the transformer are modelled by equivalent RL impedances. The considered PWM filter is composed by a parallel connection of an RC branch and two LC branches respectively resonating at f_s and $2f_s$, where f_s is the switching frequency of the inverter.

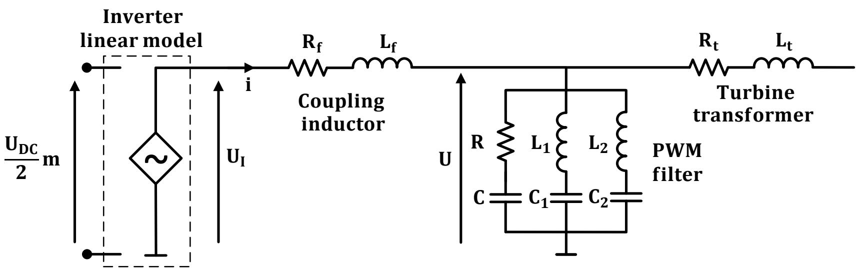

Figure 2.4: Equivalent one-line circuit of the modelled turbine.

2.1.2 Grid model

An RL Thévenin equivalent grid model has been assumed throughout the work. Its equivalent circuit is represented in Figure 2.5. In the study, the grid voltage $U_g(t)$ has been assumed harmonics free and its frequency f_0 has been assumed constant and equal to 50 Hz. Thereby, the analytical expression of $U_g(t)$ is:

$$\begin{aligned} U_{g,a}(t) &= \hat{U}_g cos(\omega_0 t) \\ U_{g,b}(t) &= \hat{U}_g cos(\omega_0 t - \frac{2}{3}\pi) \\ U_{g,c}(t) &= \hat{U}_g cos(\omega_0 t - \frac{4}{3}\pi) \end{aligned} \tag{2.2}$$

where $\hat{U}_g$ is the maximum amplitude of the phase voltage and $\omega_0 = 2\pi f_0$.

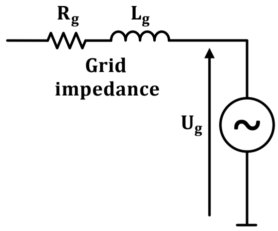

Figure 2.5: Equivalent one-line diagram of modelled grid.

2.1.3 Turbine-grid model

A model of a single grid-connected wind turbine has been derived. This model is used to validate the small-signal modelling theory presented in Chapter 3 (see Section 3.2.1) as well as to validate the equations introduced in Chapter 4 to calculate the small-signal converter admittance in the sequence-frame (see Section 4.1.3.1).
The considered interconnection is that between the turbine modelled in Section 2.1.1 and the RL grid modelled in Section 2.1.2. The resulting one-line diagram of such interconnection is shown in Figure 2.6.

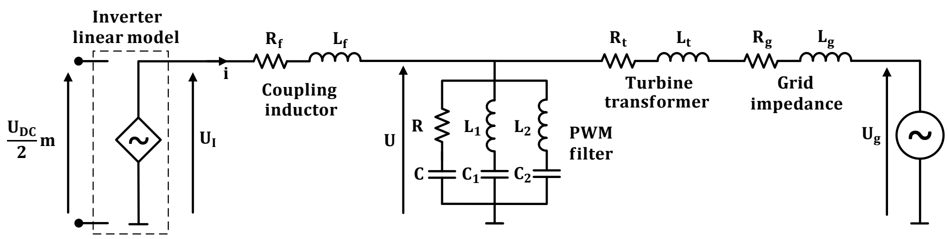

Figure 2.6: Equivalent one-line diagram of the modelled inverter-grid interconnection.

The electrical parameters used for this model are listed in Table 2.1[1]. Sizing of the coupling inductor and of the PWM filter has been carried out in line with [74].

[1] The electrical parameters of the coupling inductor and of the PWM filter are omitted as they constitute confidential information.

Table 2.1: Electrical parameters of the modelled turbine-grid interconnection. Impedance per unit values are also specified.

Parameter	**Value**
Grid line voltage $U_{g,LL}$	690 V_{rms}
Grid frequency f_0	50 Hz
DC link voltage U_{DC}	1100 V
Turbine rated power P_{rat}	3 MW
SCR	5
X/R ratio	10
Grid inductance L_g	100.53 μH (0.2 pu)
Grid resistance R_g	3.2 mΩ (0.02 pu)
Transformer inductance L_t	40.41 μH (0.08 pu)
Transformer resistance R_t	1.3 mΩ (0.008 pu)

2.1.4 Wind farm-grid model

The final model that is introduced is that of the studied wind farm-grid system. The case of an offshore wind park where the wind farm resonance issue was observed has been considered. A schematic layout of this system is shown in Fig. 2.7.

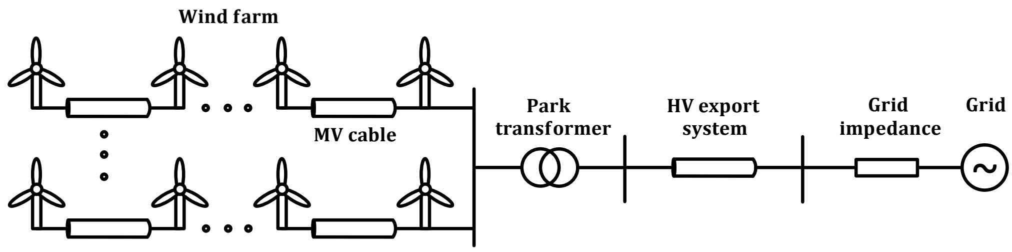

Figure 2.7: Schematic layout of the interconnection between the wind park and the grid in the considered case study.

A Medium Voltage (MV) network of 33 kV cables interconnecting the wind turbines to the Park transformer constitutes the collector system, while a combination of 132 kV High Voltage (HV) overhead lines and cables constitutes the export system, delivering the generated power to the grid [75]. A total of N = 54 turbines are installed, each with a rated power of 3.6 MW.

The system shown in Figure 2.7 has been represented in terms of a lumped equivalent circuit, applying an analogous aggregation technique used in similar works published in the literature (see for example [56], [33], [8]). The turbine model introduced in Section 2.1.1 has been used. Starting from its one line diagram, shown in Figure 2.4, an equivalent N-scaled turbine is formulated. In this aggregation process it has been assumed that the operating turbines all inject the same current i into the grid, making the current of the N-scaled turbine equal to Ni. By indicating with $Z_f(s)$, $Z_t(s)$ and $Z_{PWM}(s)$ the equivalent impedances of the coupling reactor, the wind turbine transformer and the PWM filter respectively, the corresponding impedances of the aggregated turbine model, $Z_{f_N}(s)$, $Z_{t_N}(s)$ and $Z_{PWM_N}(s)$, are [76]:

$$Z_{f_N}(s) = \frac{Z_f(s)}{N}; Z_{t_N}(s) = \frac{Z_t(s)}{N}; Z_{PWM_N}(s) = \frac{Z_{PWM}(s)}{N}. \tag{2.3}$$

Both the MV collector system and the HV export system in Figure 2.7 have been replaced by equivalent RLC lumped models, applying the methodology illustrated in [76], while the RL Thévenin equivalent model introduced in Section 2.1.2 has been used for the grid (see Figure 2.8).

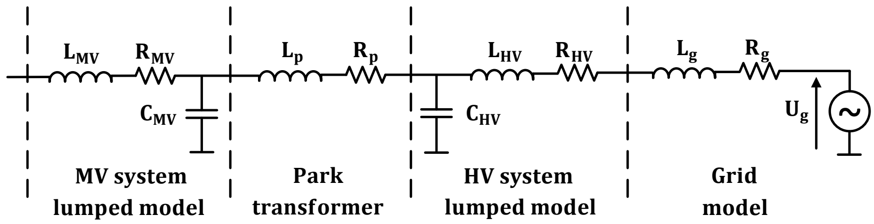

Figure 2.8: Equivalent circuit composed by the lumped model of the MV and HV cabling systems, the Park transformer impedance and the grid RL representation.

The resulting Thévenin equivalent representation of the circuit in Figure 2.8, characterized by $Z_{SYS}(s)$ and U_{SYS}, forms the final one-line diagram of the system, shown in Figure 2.9. All the impedances are referred to the LV voltage bus. The electrical parameters used to calculate $Z_{SYS}(s)$ are listed in Table 2.2 while the other system parameters are detailed in Table 2.3[2].

[2]The electrical parameters of the turbine inductor and PWM filter are omitted as they constitute confidential information.

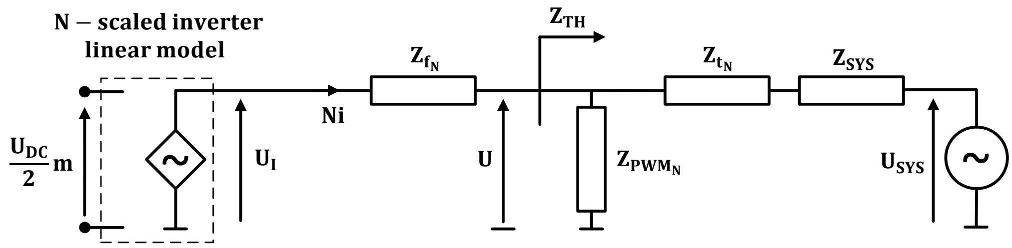

Figure 2.9: Equivalent one-line diagram of the interconnection between the wind farm and the grid.

Table 2.2: Plant parameters for the studied grid-connected wind farm. Impedance per unit values are also specified.

Component	Symbol	Value	Note
Turbine Transformer	L_t	22.7 μH (0.054 pu)	@690 V_{rms}, @3.6 MVA
$690V/33kV$	R_t	0.99 mΩ (0.0075 pu)	
MV cable capacitance	C_{MV}	2.1 μF (67.6 pu)	@132 kV_{rms}, @777 MVA
MV cable inductance	L_{MV}	8 mH (0.11 pu)	
MV cable resistance	R_{MV}	1.6 Ω (0.07 pu)	
Park Transformer inductance	L_p	52.3 mH (0.73 pu)	@132 kV_{rms}, @777 MVA
Park Transformer resistance	R_p	0.39 Ω (0.017 pu)	
HV cable capacitance	C_{HV}	1.5 μF (94.6 pu)	@132 kV_{rms}, @777 MVA
HV cable inductance	L_{HV}	40.9 mH (0.57 pu)	
HV cable resistance	R_{HV}	5.8 Ω (0.26 pu)	
Grid short circuit power	S	777 MVA	@132 kV_{rms}, @777 MVA
Grid inductance	L_g	71.4 mH (1 pu)	
Grid resistance	R_g	3.03 Ω (0.14 pu)	

Table 2.3: System parameters of the studied grid-connected wind farm.

System parameters	Value
DC link voltage U_{DC}	1100 V
Turbine LV bus voltage $U_{g,LL}$	690 V_{rms}
Grid frequency f_0	50 Hz
Turbine rated power P_{rat}	3.6 MW

Figure 2.10 shows the Bode plot of the *abc*-frame phase admittance $Y_{TH}(s) = Z_{TH}^{-1}(s)$, highlighted in Figure 2.21, as a function of the number N of operating turbines, with $1 \leq N \leq 54$.

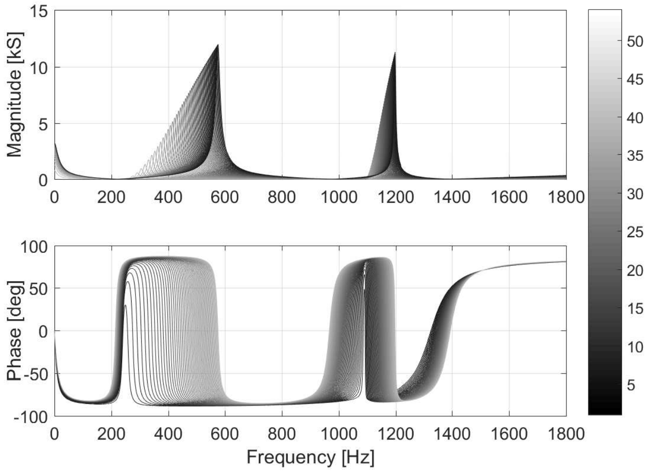

Figure 2.10: System admittance $Y_{TH}(s)$ for different values of the number of operating turbines N.

It can be noticed that two groups of spectral peaks are present, one in the [300 Hz, 600 Hz] range, the other in the [1100 Hz, 1200 Hz] range. These resonances are attributed to the non-negligible capacitance of the cables and lines of both the collector and export systems [40], and are charachterized by a frequency and a magnitude both varying with N [8], [77]. As it will be discussed in Chapter 4, these resonances are responsible for the studied wind farm instability issues.

2.2 Inverter controller design

The inverter controller is designed to regulate the active and reactive power delivered to the grid. Based on the voltage U and the current i signals measured at the LV bus (see Figure 2.1), it calculates the PWM signals modulating the inverter AC voltage.

The design of the inverter controller is presented in Section 2.2.1. Thereafter, in Section 2.2.2, the corresponding inverter controller of the scaled turbine used to model wind farm-grid system is presented. This requires to adjust the controller parameters, applying scaling rules equivalent to those introduced in Section 2.1.4.

2.2.1 Inverter controller

The inverter controller is typically composed of an inner current controller, and of a slower outer loop, consisting of an active power controller, and of a voltage regulator.

The former controls the amount of active power injected by the inverter into the grid, the latter makes sure that the voltage at the LV bus is at its nominal value, by exchanging reactive power with the grid [58]. A PLL loop is included in the controller scheme and is used to estimate the grid angle, thus allowing the synchronization between the inverter operation and the grid [78].

Different frames are typically employed to implement the inverter controller, such as the *abc*-frame [79], or the $\alpha\beta$-frame [13] or the dq-frame [55], [11]. The last of these has been chosen in this work. The analytical definition of the dq-frame can be found in Appendix B.

One of the main advantages of operating the controller in the dq-frame is the possibility of exploiting the capability of PI regulators to track constant reference signals with no steady-state error [80]. This combines with the simplicity to tune these regulators, making such solution the preferred alternative in industrial applications [58]. Designing the controller in the dq-frame requires to implement the so-called vector control algorithm [8], where separate loops are used to control the d- and q-components of the measured current signal i. In the implemented controller design, both the positive and the negative sequence components of i are controlled.

Another significant advantage of implementing the controller in the dq-frame is the possibility of decoupling the control of the active and reactive power, $P(t)$ and $Q(t)$ respectively, generated by the controller [58]. These can be expressed in terms of the dq-frame components of $U(t)$ and $i(t)$, respectively $U_{dq}(t)$ and $i_{dq}(t)$:

$$\begin{aligned}
P(t) &= \frac{3}{2}[U_d(t)i_d(t) + U_q(t)i_q(t)] \\
Q(t) &= \frac{3}{2}[U_q(t)i_d(t) - U_d(t)i_q(t)]
\end{aligned} \tag{2.4}$$

Equations (2.4) are simplified by choosing a dq-frame where either the d- or the q-axis is aligned to the $U_a(t)$ phasor. The latter alignment has been chosen in this work [81]. Thanks to this alignment, which is assured by the PLL loop operation, at steady state:

$$\begin{aligned} U_{d,0} &= 0 \\ U_{q,0} &= \hat{U} \end{aligned} \tag{2.5}$$

where $\hat{U}$ it the magnitude of the $U_a(t)$ phasor. This allows to rewrite (2.4), at steady state, as:

$$\begin{aligned} P_0 &= \frac{3}{2} U_{q,0} i_{q,0} \\ Q_0 &= \frac{3}{2} U_{q,0} i_{d,0} \end{aligned} \tag{2.6}$$

Equations (2.6) indicate that the active power is controlled exclusively by $i_q(t)$, whilst the reactive power is regulated only by $i_d(t)$.

The controller design is also affected by its hardware implementation. Tipically, the controller algorithm is executed by the control board at discrete times, corresponding to the instants when the voltage and the current signals are sampled. The discrete sampling of such signals is executed regularly every T_{sample}. In particular, by indicating with f_s the converter switching frequency, $T_{sample} = \frac{1}{2f_s}$ if asymmetrical regular sampling is used, or $T_{sample} = \frac{1}{f_s}$ if symmetrical regular sampling is applied [73] (see Appendix A for a more detailed description of these sampling methods). Thanks to these sampling techniques, it is possible to substantially eliminate the PWM harmonics from the sampled current signal i [82]. However, because of the existing phase shift between the U voltage and the i current, caused by the reactive components of the electrical system impedances, these PWM harmonics are not eliminated from the sampled U voltage, and generate aliasing [83]. Therefore, while there is no need of an anti-aliasing filter for the sampled i current, this is instead necessary for the sampled U voltage. Therefore, as this filter has been implemented via software, it needs to be included in the controller scheme.

It is highlighted that the discrete sampling of the voltage and current signals, as well as the PWM technique used to modulate the inverter voltage, generate a delay in the controller action [82]. Such delay has been included in the analytical models defined in the carried out study and, as it will be discussed, plays a central role in the wind farm resonance issue.

The design of the inverter controller is presented as follows. In Section 2.2.1.1, the structure of the inner controller is illustrated. Thereafter, in Section 2.2.1.2 and 2.2.1.3, the PLL loop and the outer loops are respectively presented. The implementation of the voltage anti-aliasing filter is outlined in Section 2.2.1.4. while the method used to model the controller delay is presented in Section 2.2.1.5. Finally, in Section 2.2.1.6, the complete inverter controller scheme is summarised.

2.2.1.1 Inner controller

This controller consists of two separate control loops, the positive sequence and the negative sequence current controllers, which respectively regulate the positive and negative sequence components of the inverter current.

2.2.1.1.1 Positive sequence current loop

Taking into consideration the electrical diagram in Figure 2.4, the structure of this controller is defined upon equation (2.7). This describes the relation between the space vectors of the inverter current, the inverter voltage, and the measured voltage, $\vec{i}(t)$, $\vec{U}_I(t)$ and $\vec{U}(t)$ respectively:

$$\vec{U}_I(t) - \vec{U}(t) = L_f \frac{d\vec{i}(t)}{dt} + R_f \vec{i}(t) \tag{2.7}$$

The definition of space-vector can be found in Appendix B.1. By applying the Park transformation (B.16), it is possible to map these signals into the positive dq-frame. In particular, based on (B.9), (B.13), (2.7) can be reformulated in the positive dq-frame as:

$$\begin{aligned} U_{I,d}^{+}(t) - U_d^{+}(t) &= L_f \frac{di_d^{+}(t)}{dt} + R_f i_d^{+}(t) - L_f \omega_0 i_q^{+}(t) \\ U_{I,q}^{+}(t) - U_q^{+}(t) &= L_f \frac{di_q^{+}(t)}{dt} + R_f i_q^{+}(t) + L_f \omega_0 i_d^{+}(t) \end{aligned} \tag{2.8}$$

where ω_0 is the frequency of the three phase electrical signals, assumed equal to 100π rads^{-1}.

Based on (2.1), it is possible to express $U^+_{I,d}(t)$ and $U^+_{I,q}(t)$ in terms of the inverter modulation functions:

$$\begin{aligned} U^+_{I,d}(t) &= m^+_d(t)\frac{U_{DC}}{2} \\ U^+_{I,q}(t) &= m^+_q(t)\frac{U_{DC}}{2} \end{aligned} \tag{2.9}$$

where $m^+_d(t)$, $m^+_q(t)$ respectively are the d- and q-components of $m_{abc}(t)$ in the positive dq-frame. These essentially represent the outputs of the positive sequence controller loop. In the following description, $U^+_{S_d}(t)$ and $U^+_{S_q}(t)$ indicate the d- and q-components of the voltage signal $U_S(t)$. As it will be discussed in Section 2.2.1.4, $U_S(t)$ is the version of the measured voltage $U(t)$, after the application of the anti-aliasing filter. Based on (2.8), $m^+_d(t)$ and $m^+_q(t)$ are calculated as:

$$\begin{aligned} m^+_d(t) &= \frac{2}{U_{DC}}[u^+_d(t) - L_f\omega i^+_q(t) + U^+_{S_d}(t)] \\ m^+_q(t) &= \frac{2}{U_{DC}}[u^+_q(t) + L_f\omega i^+_d(t) + U^+_{S_q}(t)] \end{aligned} \tag{2.10}$$

with:

$$\begin{aligned} u^+_d(t) &= L_f\frac{di^+_d(t)}{dt} + R_f i^+_d(t) \\ u^+_q(t) &= L_f\frac{i^+_q(t)}{dt} + R_f i^+_q(t) \end{aligned} \tag{2.11}$$

Equations (2.10) shows how the $m^+_{dq}(t)$ include the $\pm L_f\omega_0 i^+_{dq}(t)$ coupling terms resulting from the representation of (2.7) in the dq-frame [58].
It is highlighted that (2.11) are the equations of the voltage drop across the coupling inductor in Figure 2.1, modelled by the series connection of L_f and R_f in Figure 2.4. In order to compensate for this voltage drop, based on the Internal Model Control (IMC) technique [84], [58], a PI regulator is employed to calculate $u^+_{dq}(t)$.
Two feedback loops are defined, one operating in the positive d-axis, the other operating

in the positive q-axis. While the former calculates $m_d^+(t)$, the latter calculates $m_q^+(t)$, based on (2.10). Each of these loops employs a PI regulator which computes either $u_d^+(t)$ or $u_q^+(t)$, for the d- and q- axis control loops respectively. Both of these regulators operate on the error between the reference signal to be tracked ($i_{d,ref}^+$ or $i_{q,ref}^+$) and the feedback current signals ($i_d^+(t)$ or $i_q^+(t)$).

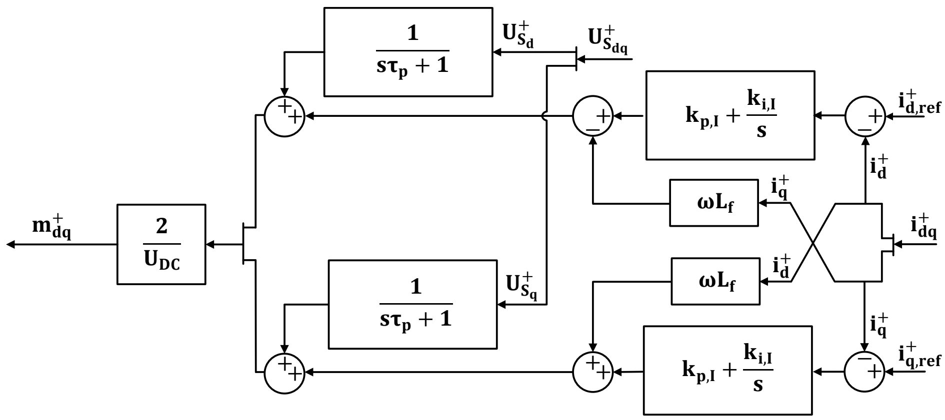

Figure 2.11: Structure of the positive sequence controller.

Figure 2.11 shows the resulting structure of the positive sequence current controller where transfer function models, defined in the s-domain [85], have been used to describe the used control elements. It is highlighted the presence of a low pass filter [86] in the Voltage Feed-Forward (VFF) term of the controller. Its use represents common practice [58], [8], and aims to the attenuation of the higher frequency harmonics of the measured voltage signal. In the scheme, ω is the estimated value of ω_0, provided by the PLL loop (see Section 2.2.1.2).

The employed current PI regulator relies on two tuning parameters, the proportional gain $k_{p,I}$ and the integral gain $k_{i,I}$ [80]. Different PI tuning techniques can be found in the literature, such as the previously mentioned IMC or the Modulus Optimum methods [84], [87]. These methods provide a straightforward methodology to define the values of $k_{p,I}$ and $k_{i,I}$, based on the plant electrical parameters (L_f and R_f) and on the desired controller bandwidth [58]. This has been set to 700 rads^{-1}.

2.2.1.1.2 Negative sequence current loop

The other element of the inner controller is the negative sequence current controller. This controller operates on the negative sequence component of the measured signals, defined according to the theory presented in Appendix B.4. The implementation of this loop requires to define a negative dq-frame, which is rotating at the same speed of the positive dq-frame, but in the opposite direction, as illustrated in Figure B.3.
The $U_S(t)$ and $i(t)$ AC signals are mapped both on the positive dq-frame, applying the Park transformation $T(\theta(t))$ in (B.16), and on the negative dq-frame, applying $T(-\theta(t))$ [58]. $T(\theta(t))$ generates the $\hat{U}^+_{S_{dq}}(t)$ and $\hat{i}^+_{dq}(t)$ components of $U_S(t)$ and $i(t)$, respectively. These signals have been indicated as $U^+_{S_{dq}}(t)$ and $i^+_{dq}(t)$ in Section 2.2.1.1.1. $T(-\theta(t))$ produces the $\hat{U}^-_{S_{dq}}(t)$ and $\hat{i}^-_{dq}(t)$ components of $U_S(t)$ and $i(t)$, respectively. As shown in equation (B.21), these positive and negative sequence dq-components present sinusoidal coupling terms at $2\omega_0$:

$$\begin{aligned}
\begin{bmatrix} \hat{U}^+_{S_d}(t) \\ \hat{U}^+_{S_q}(t) \end{bmatrix} &= \begin{bmatrix} U^+_{S_d} \\ U^+_{S_q} \end{bmatrix} + \begin{bmatrix} cos(2\omega_0 t) & sin(2\omega_0 t) \\ -sin(2\omega_0 t) & cos(2\omega_0 t) \end{bmatrix} \begin{bmatrix} U^-_{S_d}(t) \\ U^-_{S_q}(t) \end{bmatrix} \\
\begin{bmatrix} \hat{U}^-_{S_d}(t) \\ \hat{U}^-_{S_q}(t) \end{bmatrix} &= \begin{bmatrix} U^-_{S_d} \\ U^-_{S_q} \end{bmatrix} + \begin{bmatrix} cos(2\omega_0 t) & -sin(2\omega_0 t) \\ sin(2\omega_0 t) & cos(2\omega_0 t) \end{bmatrix} \begin{bmatrix} U^+_{S_d} \\ U^+_{S_q} \end{bmatrix}
\end{aligned} \tag{2.12}$$

$$\begin{aligned}
\begin{bmatrix} \hat{i}^+_d(t) \\ \hat{i}^+_q(t) \end{bmatrix} &= \begin{bmatrix} i^+_d \\ i^+_q \end{bmatrix} + \begin{bmatrix} cos(2\omega_0 t) & sin(2\omega_0 t) \\ -sin(2\omega_0 t) & cos(2\omega_0 t) \end{bmatrix} \begin{bmatrix} i^-_d \\ i^-_q \end{bmatrix} \\
\begin{bmatrix} \hat{i}^-_d(t) \\ \hat{i}^-_q(t) \end{bmatrix} &= \begin{bmatrix} i^-_d \\ i^-_q \end{bmatrix} + \begin{bmatrix} cos(2\omega_0 t) & -sin(2\omega_0 t) \\ sin(2\omega_0 t) & cos(2\omega_0 t) \end{bmatrix} \begin{bmatrix} i^+_d \\ i^+_q \end{bmatrix}
\end{aligned} \tag{2.13}$$

At steady state, $U^+_{S_d}$, $U^+_{S_q}$, i^+_d, i^+_q, $U^-_{S_d}$, $U^-_{S_q}$, i^-_d, i^-_q are constant quantities. In order to attenuate this coupling effect, among the different methods proposed in the literature (see for example [58]), the use of an notch filter, tuned at $2\omega_0$, has been chosen [8].

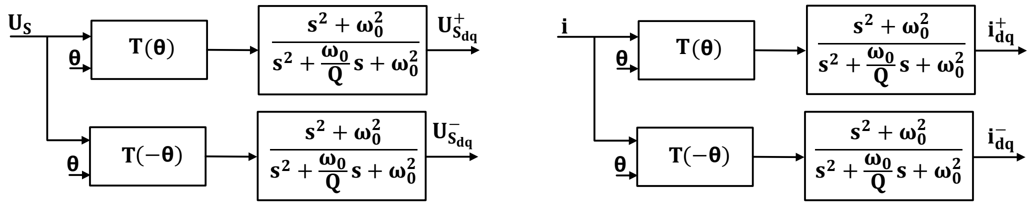

Figure 2.12: Block diagram for the calculation of the positive and negative sequence components of the measured AC signals.

The complete block diagram designed to extract the positive and negative sequence components of the AC plant signals is shown in Figure 2.12. The design of this notch filter is described in more detail in Section E.2.2. There, in particular, its digital implementation as an adaptive filter is presented. In such a design, the filter tuned frequency tracks the grid frequency estimation provided by the PLL loop.

The structure of the negative sequence controller is equal to that of the positive sequence controller, hence consisting of two loops controlling $i_d^-(t)$ and $i_q^-(t)$, as shown in Figure 2.13. The output of this controller are the negative sequence modulation functions $m_d^-(t)$ and $m_q^-(t)$. These are projected onto the positive dq-frame and combined with $m_d^+(t)$ and $m_q^+(t)$ to determine the final inverter modulation functions $m_d(t)$ and $m_q(t)$. In particular, based on (B.21):

$$\begin{bmatrix} m_d(t) \\ m_q(t) \end{bmatrix} = \begin{bmatrix} m_d^+(t) \\ m_q^+(t) \end{bmatrix} + \begin{bmatrix} cos(2\omega t) & sin(2\omega t) \\ -sin(2\omega t & cos(2\omega t) \end{bmatrix} \begin{bmatrix} m_d^-(t) \\ m_q^-(t) \end{bmatrix} \tag{2.14}$$

where $\omega t = \phi(t)$ is provided by the PLL loop. It is worth underlining that regardless of the presence of the negative sequence controller, the controller is synchronized to the positive sequence component of the measured $U(t)$ voltage.

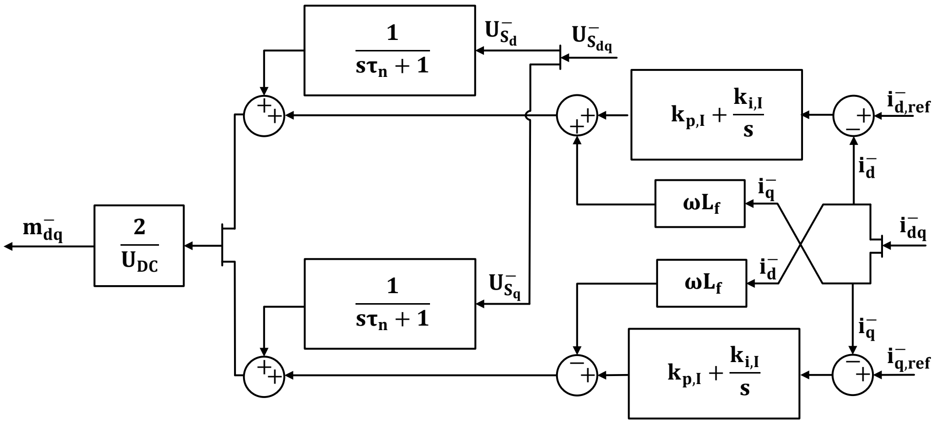

Figure 2.13: Structure of the negative sequence controller.

2.2.1.2 PLL loop

The PLL loop is used to provide the inverter controller with an estimation of the grid angle and frequency [78], thus allowing to synchronise its operation with the grid. In particular, the estimated grid angle $\theta(t)$ is used by the controller to map the AC signals from the *abc*- to the *dq*-frame and vice-versa, making use of the Park transformation and of its inverse, respectively.

As mentioned, the designed PLL loop aims to align the q-axis of the converter dq-frame to the positive sequence phasor of the $U_{S,a}(t)$ voltage, allowing decoupling of active and reactive power control (see (2.6)). For this purpose, the PLL is implemented as the feedback loop shown in Figure 2.14, tracking a zero set-point for $U^+_{S,d}(t)$.

Thanks to the use of a PI controller, at steady state, a zero tracking error is achieved, making $\phi(t)$ equal to the phase of the positive sequence component of $U_{S,a}(t)$ and $\omega(t) = \omega_0$. Tuning of the PLL loop relies on the proportional and integral gain of its PI regulator, respectively indicated as $k_{p,PLL}$ and $k_{i,PLL}$, and has been based on [78].

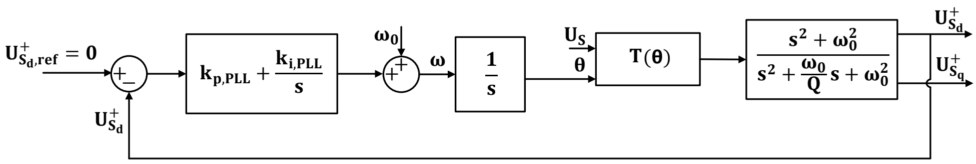

Figure 2.14: Block diagram of the PLL loop.

2.2.1.3 Outer controller

The outer controller consists of two loops, the active power regulator, and the voltage regulator. The former controls the active power generated by the inverter, the latter aims to keep the measured U voltage at its nominal value, by regulating the amount of reactive power the inverter exchanges with the grid. It is worth mentioning that, as the frequency range of the wind farm resonances is significantly higher than the -3 dB bandwidth of the controller outer loops [58], their dynamics have been neglected in the study of these resonances. However, they have been included in some of the analyses presented in Chapter 4, where the stability methodology applied in the work is discussed (see in particular Section 4.1.3.2 and Section 4.4).

2.2.1.3.1 Active power loop

The active power loop controls the set-point of the q^+ current loop, $i^+_{q,ref}$. It operates on the signal error between the active power set-point, P_{ref}, and the calculated power $P(t)$, obtained considering the positive sequence components of the measured voltage and current signals [58]:

$$P(t) = \frac{3}{2}[U^+_{S_d}(t)i^+_{S_d}(t) + U^+_{S_q}(t)i^+_{S_q}(t)] \tag{2.15}$$

A PI regulator is employed to assure a zero tracking error under steady state conditions. The equivalent block diagram of the loop is shown in Figure 2.15, where $k_{p,P}$ and $k_{i,P}$ are the tuning parameters of the loop.

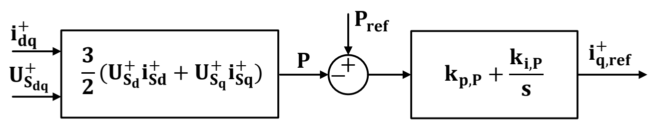

Figure 2.15: Block diagram of the active power loop.

2.2.1.3.2 Voltage loop

The voltage loop controls the set-point of the d^+ current loop, $i^+_{d,ref}$. It operates on the error between the voltage nominal magnitude, $\hat{U}_{ref}$, and the corresponding calculated value $\hat{U}_S(t)$, obtained considering the positive sequence components of the measured voltage [58]:

$$\hat{U}_S(t) = \sqrt{[U^+_{S_d}(t)]^2 + [U^+_{S_q}(t)]^2} \tag{2.16}$$

A PI regulator is utilised to assure a zero tracking error under steady state conditions. The equivalent block diagram of the loop is shown in Figure 2.16, where $k_{p,V}$ and $k_{i,V}$ are the tuning parameters of the loop.

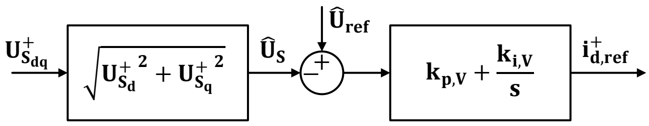

Figure 2.16: Block diagram of the voltage loop.

2.2.1.4 Voltage anti-aliasing filter

A straightforward implementation of the anti-aliasing filter is a Moving Average (MA) filter [88], where the filter output is the average of the last M values of the sampled signal [89]. By appropriately choosing the value of M, it is possible to attenuate the PWM harmonics of the sampled signal occurring at side-bands of multiples of the converter switching frequency [71]. Mainly because of the simplicity of its software implementation, this represents a preferred solution in electronic indutrial applications. The input-output relationship of such a filter is defined in the discrete time domain as [89]:

$$y[k] = \frac{1}{M} \sum_{j=0}^{M-1} x[k-j] \tag{2.17}$$

The equivalent transfer function of the MA filter in the Laplace domain [85],

$G_{MA}(s)$, is:

$$G_{MA}(s) = \frac{1}{M}\frac{1 - e^{-sT_{OS}M}}{1 - e^{-sT_{OS}}} \tag{2.18}$$

where T_{OS} is the voltage oversampling period. Oversampling of the U voltage will be discussed in Chapter 5 and is central to the implementation of one of the presented wind farm resonance mitigation techniques, the Fast Voltage Feed Forward (FVFF) strategy.

A different filter design has been formulated in this work, as it provides more tuning flexibility. The filter consists of a cascaded connection of four notch filters and of a first order low pass filter. Its equivalent block diagram is shown in Figure 2.17. The tuning parameters are listed in Table 2.4, for both the asymmetrical and symmetrical sampling techniques considered in this work.

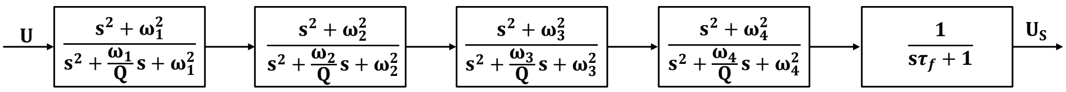

Figure 2.17: Equivalent block diagram of the designed anti-aliasing filter.

Table 2.4: Anti-aliasing filter tuning parameters.

Parameter	**Asymmetrical sampling**	**Symmetrical sampling**
Notch filter tuned frequency ω_1	$2\pi 4800$ rads^{-1}	$2\pi 2500$ rads^{-1}
Notch filter tuned frequency ω_2	$2\pi 5200$ rads^{-1}	$2\pi 5000$ rads^{-1}
Notch filter tuned frequency ω_3	$2\pi 9800$ rads^{-1}	$2\pi 7500$ rads^{-1}
Notch filter tuned frequency ω_4	$2\pi 10200$ rads^{-1}	$2\pi 1000$ rads^{-1}
Notch filter quality factor Q	2	2
Time constant τ_f	60 μs	100 μs
Filter sampling period T_{OS}	10 μs	10 μs
MA filter window M	20	40

Figure 2.18 compares the Bode plots of the MA filter with that of the used filter, for the case when asymmetrical sampling is used.

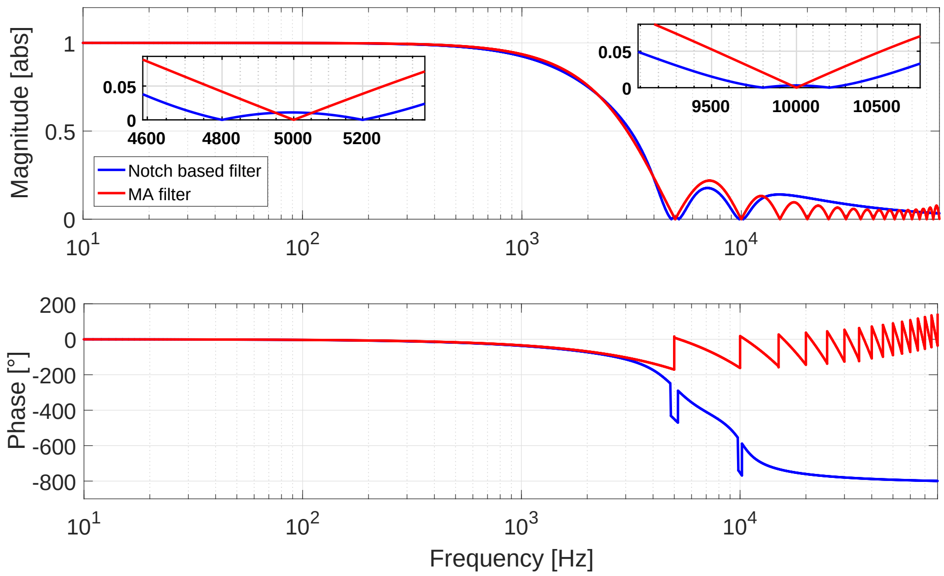

Figure 2.18: Bode plot of the anti-aliasing filter when asymmetrical regular sampling is used. Comparison between the MA filter solution and the notch based alternative.

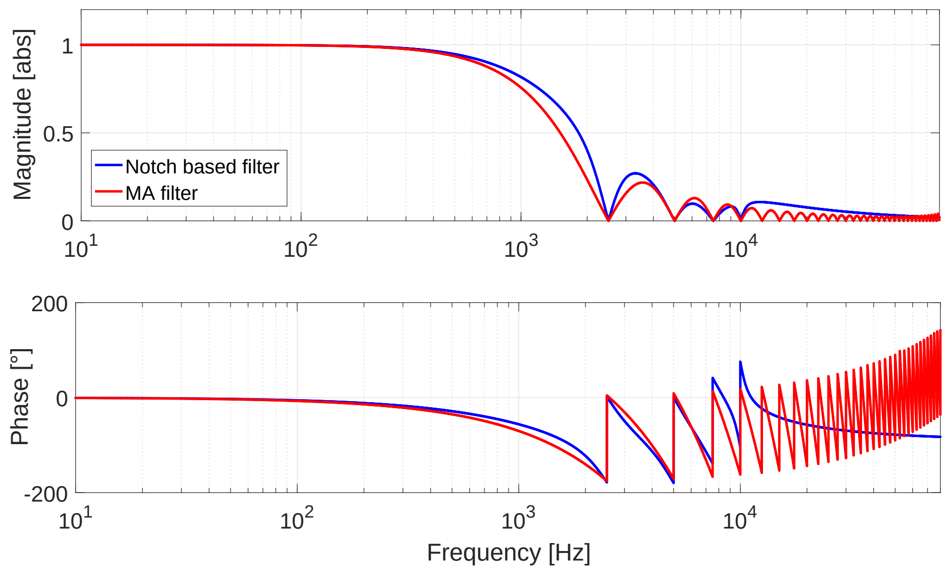

Figure 2.19: Bode plot of the anti-aliasing filter when symmetrical regular sampling is used. Comparison between the MA filter solution and the notch based alternative.

While in the lower frequency range the two filters have a pretty similar performance, the notch based filter allows an increased attenuation of the side-band harmonics at 5 kHz and at 10 kHz [90]. This is thanks to the possibility of tuning the notch frequencies of the filter independently, unlike the MA filter where the tuning parameter M defines all of them uniquely. This comes at the cost of necessitating more hardware processing power compared to the MA filter solution, as well as of a reduced attenuation of the higher frequency PWM harmonics. The design of the filter therefore results from a trade-off between these aspects.

Figure 2.19 compares the Bode plots of the MA filter and the notch based alternative for the symmetrical sampling case. They confirm the equivalent performances of the two designs, particularly in the lower frequency range. It is worth mentioning that, in this case, the use of a lower sampling frequency requires to reduce the bandwidth of the filter to avoid aliasing of the PWM harmonics at side-bands of 2.5 kHz [83].

The digital implementation of the anti-aliasing filter is described in Appendix E.1, where the results of the experimental tests carried out to verify its effectiveness are also reported.

2.2.1.5 Controller delay

The model used to include the controller delay in the analyses carried in the work is presented as follows.

Such delay is due both to the discrete sampling of the voltage and current signals and to the converter modulation [82]. The discrete sampling delay is equal to T_{sample}, and represents the delay between the instant when the plant signals are sampled and the time when the corresponding PWM pattern calculated by the controller is delivered (these times are indicated as t_k and t_{k+1} in the timing diagram in Figure 5.5). The converter modulation delay is associated to the PWM modulator and is equivalent to the delay effect of a Sample & Hold device, equal to $\frac{T_{sample}}{2}$ [91]. The total controller delay T_d therefore is [82], [92]:

$$T_d = \frac{3}{2} T_{sample} \tag{2.19}$$

which has been modelled with the transfer function $G_D(s)$, defined as:

$$G_D(s) = e^{-sT_d} \tag{2.20}$$

As the sampling period T_{sample} is inversely proportional to the converter switching frequency f_s, in order to reduce the controller delay, an increase of f_s would be necessary. However, this would reduce the efficiency of the inverter, magnifying its conduction and switching losses [71]. As it will be discussed, this aspect represents a bottleneck to the solution of the stability issues caused by the wind farm resonances.

2.2.1.6 Complete structure of the controller

Figure 2.20 shows the overall structure of the designed inverter controller. Such control scheme will be used throughout the work[3].

The outer loops have not been included in the shown control scheme as these loops have been utilised only in some specific analyses (see Section 4.1.3.2 and Section 4.4).

2.2.2 Inverter controller scaling

The controller of the lumped turbine model used in the wind farm-grid system described in Section 2.1.4 has the same structure of the control scheme shown in Figure 2.20.

The controller parameters are scaled by N (i.e. the number of operating turbines), according to the scaling rules applied to define the lumped turbine model [8]. The N-scaled controller scheme is shown in Figure 2.21[3].

It is worth mentioning that in the baseline operation of the turbines' inverters employed in the studied wind farm system, a symmetrical regular sampling technique is used.

[3]The controller parameters are omitted as they constitute confidential information.

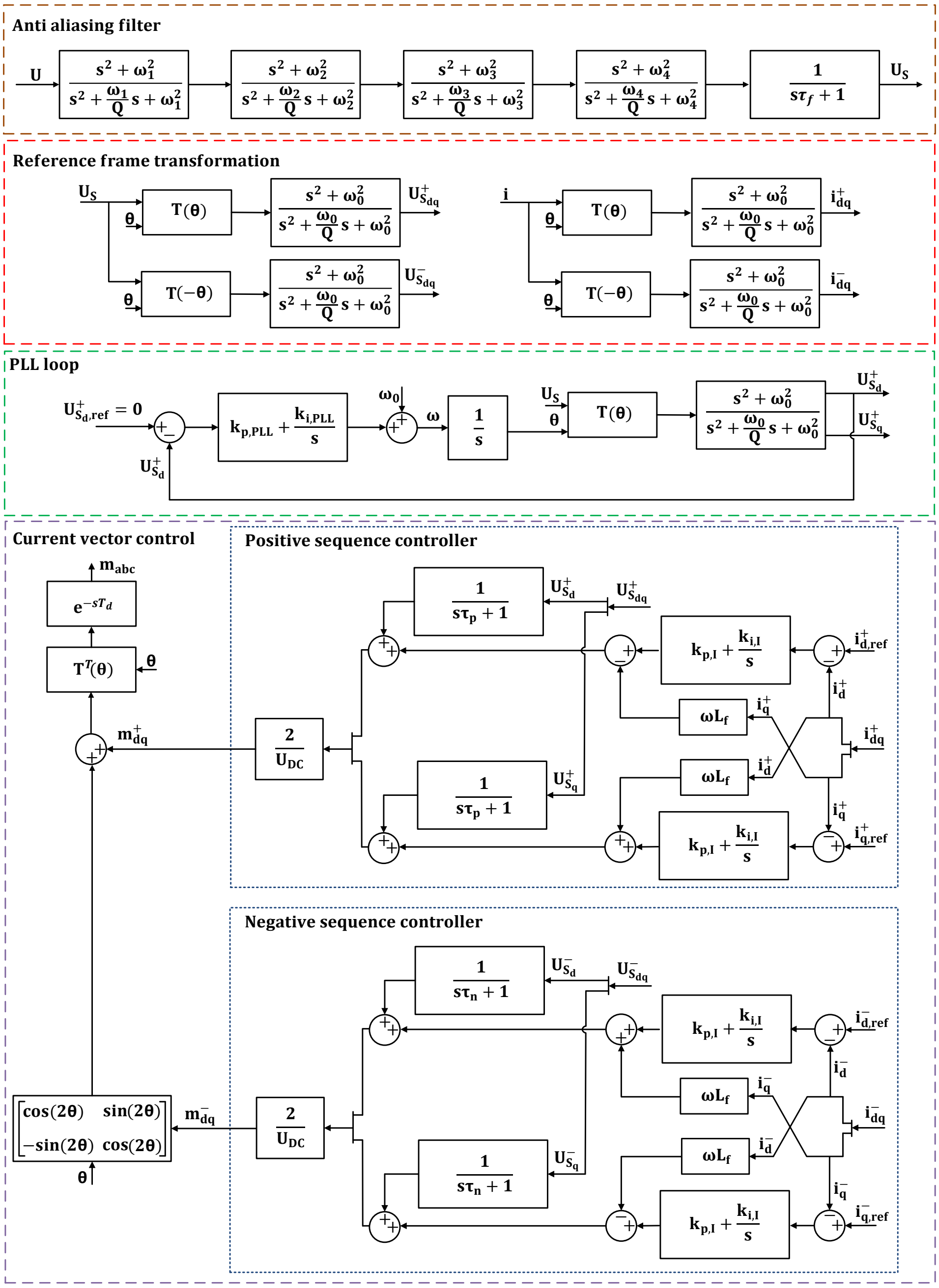

Figure 2.20: Complete inverter controller scheme used in the carried out study.

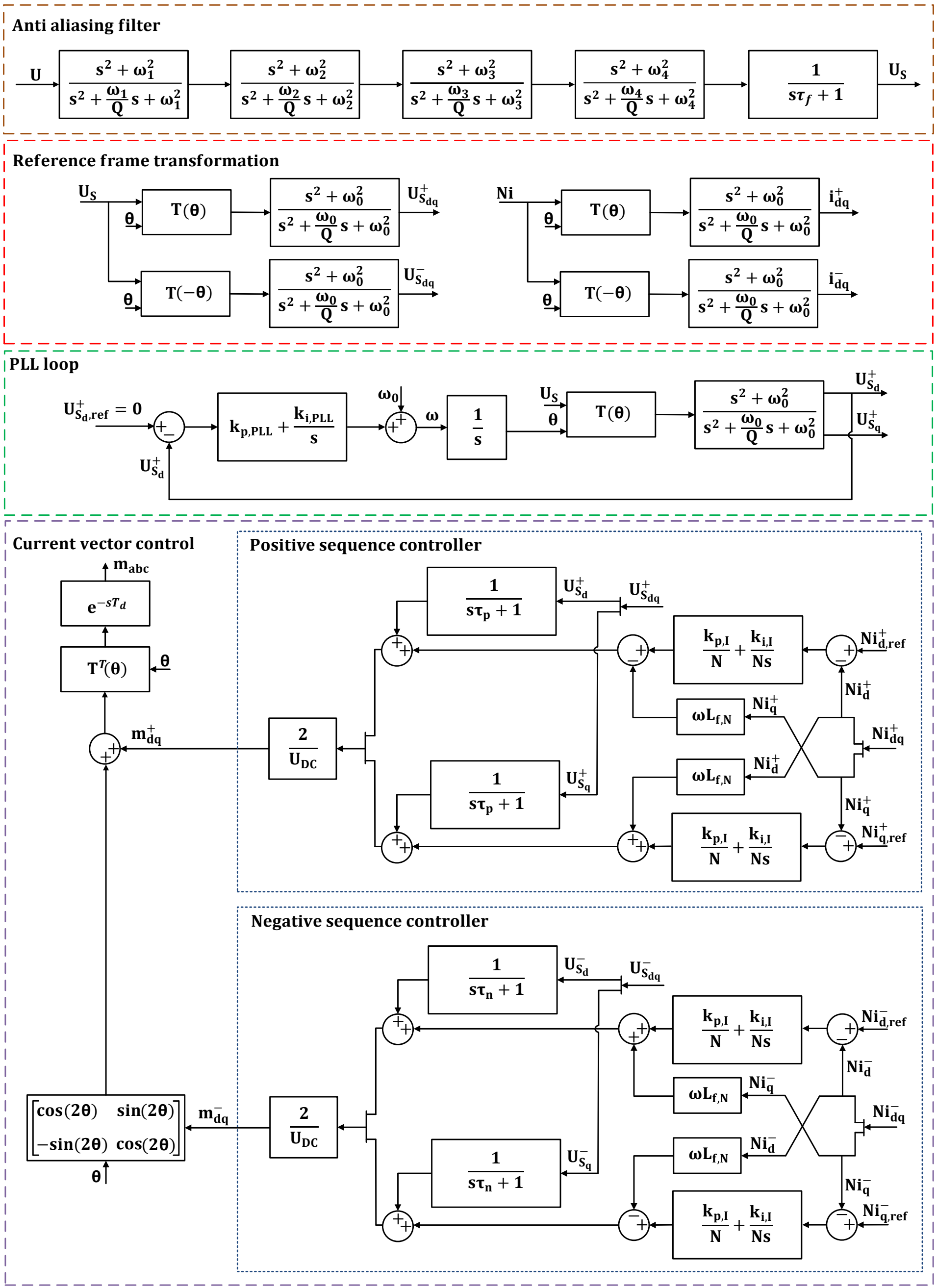

Figure 2.21: Complete model of the grid-connected aggregated wind farm system.

2.3 Scaled-down inverter-grid laboratory prototype

A laboratory prototype of the inverter-grid interconnection has been built in the laboratory. The purpose of this prototype is to verify the results of the study carried out on the wind farm resonances, and in particular to verify the effectiveness of the proposed mitigation techniques. Also, it has been used to validate the stability methodology used in the work, and for this purpose specific configurations of the test-rig have been utilised. The same controller scheme discussed in Section 2.2 has been employed, with the tuning parameters opportunely scaled-down to maintain the same current controller bandwidth (equal to 700 rads^{-1}, as mentioned in Section 2.2.1.1.1). In Section 2.3.1 the components of the test-rig are outlined, while in Section 2.3.2, the different test-rig configurations used in the experimental tests carried out throughout the work are described.

2.3.1 Hardware setup

A schematic representation of the prototype hardware is shown in Figure 2.22.

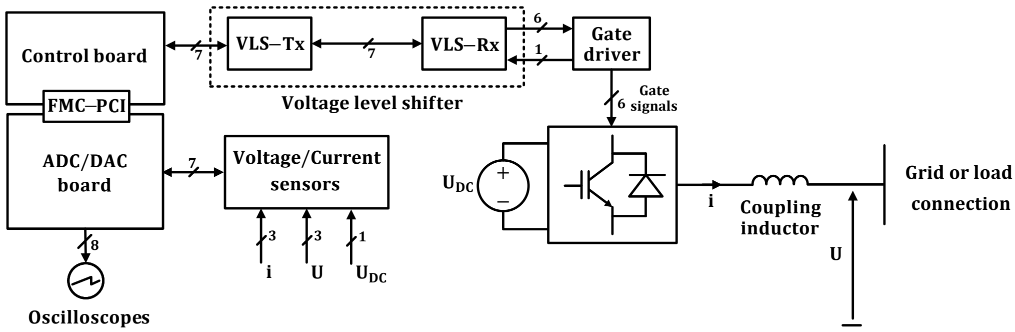

Figure 2.22: Schematic structure of the experimental laboratory setup.

This mainly includes a control board, a set of sensors to read the plant signals, an ADC/DAC board used both to interface the sensors to the control board and to display debugging signals on the oscilloscopes, the converter, the gate drivers and a set of interface boards. The converter is connected to the mains electricity supply through an autotransformer which has allowed to step-down the grid AC voltage. A detailed description of each of these components can be found in Appendix D. Table 2.5 lists the system parameters of the built prototype. Unless otherwise specified, asymmetrical regular sampling has been used.

Table 2.5: System parameters of the built inverter-grid interconnection prototype. Per unit impedance values are also specified.

System parameters	**Value**
DC link voltage U_{DC}	300 V
Inverter rated power P_{rat}	2 kW
Coupling inductance L_f	2.5 mH (0.086 pu)
X/R ratio	10
Converter switching frequency f_s	2.5 kHz

2.3.2 Experimental configurations

The different set-ups that have been used for the laboratory prototype are described as follows. In each of these configurations the electrical interface of the inverter is varied, and the controller scheme is modified, by changing its tuning parameters and/or including/excluding some of its regulators (such as the power loop, the voltage loop, the PLL loop, etc.). The purpose of using different configurations has been to reproduce specific scenarios capable to highlight the aspects of the system stability performance being investigated. The configuration outlined in Section 2.3.2.1 is the one that reproduces a cable due resonance in the same range of frequencies where the studied wind farm resonances typically occur [14], [8]. This has been used to validate the analysis carried on the wind farm resonances, as well as to provide an experimental verification of the stabilising effect of the proposed mitigation techniques. In Section 2.3.2.2, the configuration where the inverter is connected to a resistive load is described. Such a set-up has been used to validate the equations presented in Chapter 4 to map a small-signal admittance from the *dq*-frame to the sequence-frame, as well as to verify the Mirror Frequency Decoupled (MFD) property of the inverter-grid system [60]. Finally, in Section 2.3.2.3, the more generic configuration of an inverter connected to an inductive grid is presented. Such a scheme has been used to validate the derived small-signal model of the inverter-grid system, described in Chapter 3, to verify some aspects of the stability study discussed in Chapter 4, and to prove the effectiveness of one of the proposed strategies, the FVFF technique, to counteract weak grid issues.

2.3.2.1 Wind farm resonance reproduction

In this set-up, shown in Figure 2.23, the studied cable due resonance issue is reproduced. The corresponding one-line diagram of the system is illustrated in Figure 2.24.

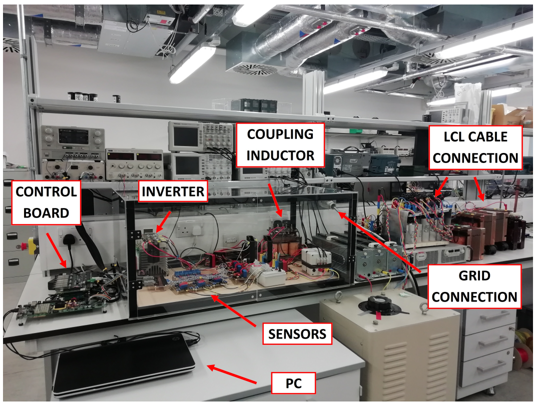

Figure 2.23: Picture of the laboratory grid-connected inverter prototype used to reproduce the cable due resonance issue.

In the baseline operation of the controller, the control scheme shown in Figure 2.20 is used, with the system parameters detailed in Table 2.6[4]. In particular, as it will be discussed in Chapters 4 and 5, the test-rig has been tested using both a symmetrical and an asymmetrical regular sampling technique, with the tuning parameters of the anti-aliasing filter defined as specified in Table 2.4.

Table 2.6: System parameters for the test-rig configuration used to reproduce the cable due resonance issue. Impedance per unit values are also specified.

System parameters	Value
AC grid line voltage $U_{g,LL}$	135 V_{rms}
Grid nominal frequency	50 Hz
Inductance L_a	1.5 mH (0.052 pu)
Inductance L_b	2 mH (0.069 pu)
Capacitance C	30 μF (11.64 pu)

In the set-up, the values of the electrical parameters L_a, L_b and C have been carefully chosen to generate an electrical resonance in the same range of frequencies where the wind farm cable due resonances typically occur [14], [8]. The resulting

[4]The controller parameters are omitted as they constitute confidential information.

frequency of such resonance is 750 Hz, as shown in Figure 2.25, where the magnitude plot of the equivalent impedance seen by the grid-side terminal of the coupling inductor L_f is reported.

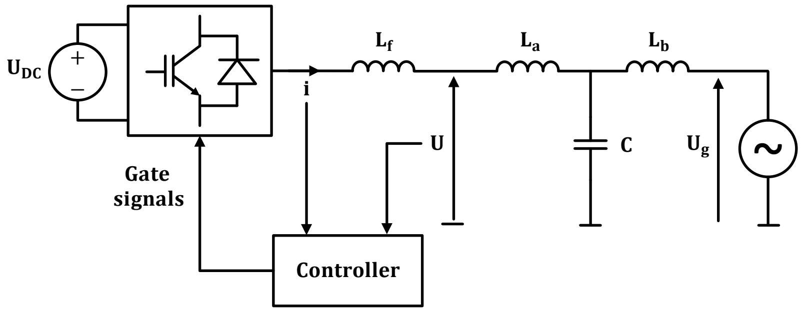

Figure 2.24: One-line diagram of the grid-connected converter prototype used to reproduce the cable due resonance issue.

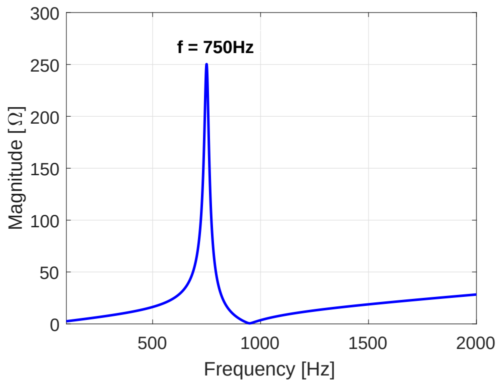

Figure 2.25: Magnitude of the equivalent impedance seen by the L_f coupling inductor grid-side terminal (see Figure 2.24).

2.3.2.2 Connection to a resistive load

In this set-up, whose one-line diagram is shown in Figure 2.26, the inverter is connected to a resistive load. This configuration has been used in the tests described in Section 4.1.3.2 to validate the analytical calculation of the small-signal admittance in the sequence-frame, as well as to verify the MFD property of the system [60]. As it will be discussed in more detail in Section 4.1.3.2, in these tests the configuration of the controller scheme has been varied, including/excluding some of the regulators, such as the active power loop and the negative sequence current controller. Moreover, in all of these controller configurations the PLL loop has not been employed. The used system and controller parameters are listed in Table 2.7.

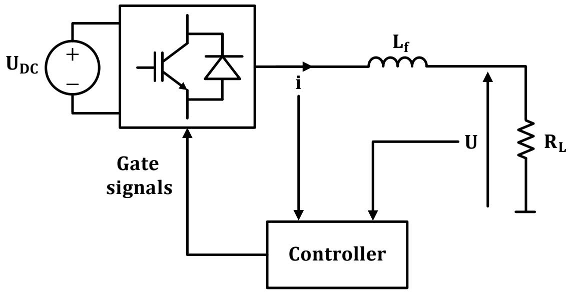

Figure 2.26: Equivalent one-line circuit used in the tests described in Section 4.1.3.2.

Table 2.7: System parameters for the prototype set-up used in the tests described in Section 4.1.3.2.

System parameters	**Value**
Load resistance R_L	33 Ω (3.6 pu)
Controller parameters	**Value**
Current loop PI proportional gain $k_{I,p}$	1.625 VA^{-1}
Current loop PI integral gain $k_{I,i}$	1056.3 VA^{-1}s^{-1}
Power loop PI proportional gain $k_{P,p}$	0.0325 AW^{-1}
Power loop PI integral gain $k_{P,i}$	10.563 AW^{-1}s^{-1}
Time constant τ_p	0.4 s
Time constant τ_n	0.04 s
Notch filter frequency ω_N	2π100 rads^{-1}
Notch filter quality factor Q	2

2.3.2.3 Connection to an inductive grid

This set-up reproduces a scaled-down prototype of a grid-connected VSC system. An RC filter has been used for the attenuation of the PWM harmonics, while an inductance L_g of different sizes has been used to vary the grid Short Circuit Ratio (SCR). The equivalent one-line diagram of such system is shown in Figure 2.27.

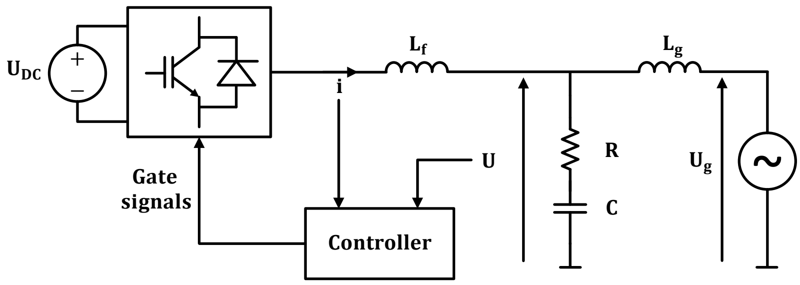

Figure 2.27: Equivalent one-line circuit of the laboratory prototype inverter-grid interface connected to an inductive grid.

This configuration has been used to validate the dq-frame small-signal model of the inverter-grid interface described in Chapter 3. In more detail, this set-up has been used to validate the frequency responses of the current control loops calculated from the inverter-grid small-signal model outlined in Chapter 3 (see Section 3.2). For these tests, the system parameters detailed in Table 2.8[5] have been used, while the control scheme in Figure 2.20 has been considered.

Table 2.8: System parameters used to validate the frequency response of the current-loops. Impedance per unit values are also specified.

System parameters	**Value**
AC grid line voltage $U_{g,LL}$	135 V_{rms}
Grid nominal frequency	50 Hz
Inductance L_g	0 mH (stiff grid)
PWM filter resistance R	33 Ω (3.6 pu)
PWM filter capacitance C	25 μF (14 pu)

Thereafter, the set-up has been used to validate the frequency responses of the outer loops, i.e. the active power and voltage regulators described in Section 2.2.1.3. In these tests, the system and controller parameters detailed in Table 2.9 have been used. These paramenters have also been used in the case study illustrated in Section 4.3, where the property of diagonal dominance [93] of the inverter-grid system in the sequence-frame is investigated.

Subsequently, a different set of system and controller parameters, detailed in Table 2.10, has been considered when using this set-up to validate the study presented in

[5]The controller parameters are omitted as they constitute confidential information.

Section 4.4, where a stability margin is introduced to assess the relative stability of the inverter-grid system. In this scenario, the outer loops have been excluded by the control scheme, so is the negative sequence current controller.

Table 2.9: System and controller parameters in the case study presented in Section 4.3. Impedance per unit values are also specified.

System parameters	**Value**
AC grid line voltage $U_{g,LL}$	135 V_{rms}
Grid nominal frequency	50 Hz
Inductance L_g (SCR = 1.9/5.2)	15/5 mH (0.52/0.17 pu)
PWM filter resistance R	33 Ω (3.6 pu)
PWM filter capacitance C	25 μF (14 pu)
Controller parameters	**Value**
Current loop PI proportional gain $k_{I,p}$	5 VA^{-1}
Current loop PI integral gain $k_{I,i}$	200 $VA^{-1}s^{-1}$
Power loop PI proportional gain $k_{P,p}$	0.0001 AW^{-1}
Power loop PI integral gain $k_{P,i}$	0.025 $AW^{-1}s^{-1}$
Voltage loop PI proportional gain $k_{V,p}$	0.0001 AV^{-1}
Voltage loop PI integral gain $k_{V,i}$	20 $AV^{-1}s^{-1}$
PLL loop PI proportional gain $k_{PLL,p}$, (SCR = 1.9/5.2)	0.01/2.74 $radV^{-1}s^{-1}$
PLL loop PI integral gain $k_{PLL,i}$, (SCR = 1.9/5.2)	0.9/246.7 $radV^{-1}s^{-2}$
Time constants τ_p, τ_n	0.1 s
Notch filter frequency ω_N	2π100 $rads^{-1}$
Notch filter quality factor Q	2

Table 2.10: System and controller parameters used in the case study presented in Section 4.4. Impedance per unit values are also specified.

System parameters	**Value**
AC grid line voltage $U_{g,LL}$	135 V_{rms}
Grid nominal frequency	50 Hz
Inductance L_g	15 mH (0.52 pu)
PWM filter resistance R	33 Ω (3.6 pu)
PWM filter capacitance C	25 μF (14 pu)
Controller parameters	**Value**
Current loop PI proportional gain $k_{I,p}$	1.625 VA^{-1}
Current loop PI integral gain $k_{I,i}$	1056.3 $VA^{-1}s^{-1}$
PLL loop PI proportional gain $k_{PLL,p}$	0.13 $radV^{-1}s^{-1}$
PLL loop PI integral gain $k_{PLL,i}$	11.6 $radV^{-1}s^{-2}$
Time constant τ_p	0.1 s

The set-up has been then used to prove how the FVFF strategy proposed in Chapter 5 to mitigate the high frequency wind farm resonances, is also effective to counteract weak grid issues [11]. In this case, the system parameters listed in Table 2.11[6].

[6]The controller parameters are omitted as they constitute confidential information.

Finally, this configuration has been used to verify the functionality of the proposed RCD technique, making use of the system parameters listed in Table 2.12[6].

Table 2.11: System parameters used to verify the beneficial effect of the FVFF strategy on weak grid issues.

System parameters	**Value**
AC grid line voltage $U_{g,LL}$	135 V_{rms}
Grid nominal frequency	50 Hz
Inductance L_g	varied
PWM filter resistance R	33 Ω (3.6 pu)
PWM filter capacitance C	25 μF (14 pu)

Table 2.12: System parameters used to verify the functionality of the RCD strategy. Impedance per unit values are also specified.

System parameters	**Value**
AC grid line voltage $U_{g,LL}$	135 V_{rms}
Grid nominal frequency	50 Hz
Inductance L_g	5.5 mH (0.19 pu)
PWM filter resistance R	33 Ω (3.6 pu)
PWM filter capacitance C	25 μF (14 pu)

2.4 Chapter Summary

An analytical model of the studied wind farm-grid system where the wind farm resonance problem has been observed has been defined. For this purpose, a turbine-grid model has been formulated and an aggregation technique has been applied to derive the corresponding wind farm-grid model. The design of the employed turbine's inverter controller has been discussed, focusing on the implementation of its current controller. A description of the built scaled-down laboratory prototype of the studied inverter-grid system has been presented, outlining the different set-ups that have been used throughout the work.

Chapter 3

Small-signal modelling

In this Chapter, the models used to study the system stability and performance are presented.

The standard approach taken in stability studies is based on the representation of the system dynamics in the frequency domain [11], [58] and on the application of classic control theory [25]. This approach relies on the assumption that the system is Linear Time-Invariant (LTI) [94]. Therefore, the preliminary step of studying the stability of a non-linear system is to build its small-signal model, which, for small variations of the signals close to the system operating point, is capable of reproducing the system behaviour confidently. For this purpose, for any of the Time-Domain (TD) models described in Chapter 2 a corresponding small-signal model is derived in the Frequency-Domain (FD).

These small-signal models have been implemented in the positive *dq*-frame. As most of the components of the inverter controller are implemented in such *dq*-frame, the derivation of their equivalent FD model is straightforward. The exceptions are represented by the negative sequence current controller, the voltage anti-aliasing filter, the controller delay model and the electrical system model. While the first one operates in the negative *dq*-frame, the other three are in the *abc*-frame. Hence, frame transformations have been applied to refer the dynamics of these elements to the positive *dq*-frame. In particular, by mapping the dynamics of the negative sequence current controller onto the positive *dq*-frame, it has been possible to include the coupling between the positive and the negative sequence current loops in a single controller FD model. This approach differs from the standard techniques presented in the literature, which, by modelling these current controllers separately, are unable to take such coupling into account [58], [54].

The method used to include the PLL dynamics in the controller FD model will be discussed in detail, both deriving the equivalent small-signal model of the PLL loop, and describing how such dynamics affect the grid synchronisation of the converter.

In Section 3.1, for the purpose of illustrating the application of the used theory, the derivation of the small-signal model of the turbine-grid system described in Section 2.1.3 is discussed. In Section 3.2, the validation of the applied theory is presented. The FD model of the mentioned turbine-grid system is validated against its equivalent TD model while the FD model of the laboratory prototype described in Section 2.3.2.3 is validated both against its equivalent TD model and against experimental data.

As it will be discussed in Chapter 4, the theory used to derive these small-signal models is used to formulate the FD model of the studied wind farm-grid system. Such small-signal model will be used to assess the stability performance of the wind farm-grid system, applying the impedance-based approach presented in that Chapter.

3.1 Small-signal model of the turbine-grid system

The derivation of the small-signal model of the turbine-grid system described in Section 2.1.3, including its controller, is described as follows.

This small-signal model has been implemented in the positive *dq*-frame, which represents common practice in the literature [58], [95], [11]. The positive-sequence current controller, the PLL loop and the outer loops are already implemented in this frame. But, the electrical system, the voltage anti-aliasing filter and the controller delay are formulated in the *abc*-frame and the negative sequence current controller is implemented in the negative *dq*-frame. Hence, these elements that are not defined in the positive *dq*-frame need to be projected onto such frame.

In the following description, the positive *dq*-frame will be referred to as grid positive *dq*-frame, or simply grid *dq*-frame, as it rotates (anti-clockwise) at the grid frequency

ω_0, assumed to be constant throughout the presented analysis. The converter controller operates in a different dq-frame, the converter dq-frame, which the PLL tries to align to the grid dq-frame. Under steady-state conditions this alignment is perfect, thanks to the presence of the PI regulator in the PLL loop (see Figure 2.14), which assures a zero steady-state error in the detection of the phase angle of the positive sequence component of the measured U_a voltage. However, during transients, the PLL dynamics generate a misalignment between the converter and the grid dq-frames. As the orientation of the converter dq-frame is carried out by the PLL through the Park transform (B.16), which is a non-linear operator, the frame-alignment between the grid and the converter dq-frames also undergoes non-linear dynamics. As a result of this, such dynamics need linearising in the derivation of the controller small-signal model.

The derivation of the small-signal model of the components of the inverter controller is presented in Section 3.1.1. Thereafter, the small-signal model of the turbine-grid electrical system is described in Section 3.1.2. Finally, the complete FD model of the considered turbine-grid system is summarised in Section 3.1.3.

3.1.1 Inverter controller

The linearised models of the inverter controller elements will be presented as follows. The small-signal model of the PLL loop is derived in Section 3.1.1.1, while the linearisation of the frame-alignment between the grid and the converter dq-frames is discussed in Section 3.1.1.2. Thereafter, the small-signal models of the inner current loops are discussed in Section 3.1.1.3, in particular illustrating how the dynamics of the negative sequence controller have been mapped onto the positive dq-frame. In Section 3.1.1.4, the dq-frame small-signal model of the abc-frame voltage anti-aliasing filter is derived. In Section 3.1.1.5, the dq-frame small-signal model of the controller delay, which has been modelled in the abc-frame, is presented. Finally, in Section 3.1.1.6, the small-signal models of the outer loops, namely the active power controller and the voltage regulator, are presented.

3.1.1.1 PLL loop

As discussed in Section 2.2.1.2, the purpose of the PLL loop is the definition of the converter dq-frame orientation, allowing to synchronize the controller to $U_S^+(t)$, which is the positive sequence component of the measured voltage $U(t)$, after that this has been filtered by the anti-aliasing filter (see Figure 2.20).

Based on (B.14), by indicating with $\vec{U}_S^+(t)$ the space-vector of the positive sequence component of the measured voltage, defined in the grid dq-frame, and with $\vec{U}_{S,c}^+(t)$ its version defined in the converter dq-frame, the following equations can be formulated:

$$\begin{aligned}\vec{U}_{S,c}^+(t) &= [U_{S_d,c}^+(t) + jU_{S_q,c}^+(t)]e^{j(\theta(t)-\frac{\pi}{2})}\\ \vec{U}_S^+(t) &= [U_{S_d}^+(t) + jU_{S_q}^+(t)]e^{j(\omega_0 t-\frac{\pi}{2})}\end{aligned} \tag{3.1}$$

where $\theta(t) = \omega_0 t + \delta\theta(t)$ is the PLL angle. It is pointed out that, at steady-state, $\delta\theta(t) = 0$, $\omega = \omega_0$, $U_{S_d}^+(t) = 0$ and $U_{S_q}^+(t) = U_{S,0}^+ = |\vec{U}_{S,0}^+(t)|$, where $\vec{U}_{S,0}^+(t) = \vec{U}_S^+(t)$ at steady-state. Thanks to the PLL action, under such stationary conditions, $\vec{U}_{S,c}^+(t)$ is aligned to the grid q-axis and, therefore, is calculated as:

$$\vec{U}_{S,c}^+(t) = \vec{U}_{S,0}^+(t) = U_{S,0}^+ e^{j\omega_0 t} \tag{3.2}$$

From (3.1), (B.3), $\vec{U}_{S,c}^+(t)$ and $\vec{U}_S^+(t)$ can be related to each other as [96], [97]:

$$\vec{U}_{S,c}^+(t) = \vec{U}_S^+(t)e^{-j\delta\theta(t)} = \overline{U}_S^+(t)e^{j\omega_0 t}e^{-j\delta\theta(t)} \tag{3.3}$$

where, based on (B.12), (B.14):

$$\overline{U}_S^+(t) = [U_{S_d}^+(t) + jU_{S_q}^+(t)]e^{-j\frac{\pi}{2}} \tag{3.4}$$

During transient conditions, $\overline{U}_S^+(t)$ can be expressed as:

$$\overline{U}_S^+(t) = \overline{U}_{S,0}^+ + \delta\overline{U}_S^+(t) \tag{3.5}$$

where $\delta\overline{U}^+_S(t)$ is the small-signal perturbation added to the steady-state value $\overline{U}^+_{S,0} = U^+_{S,0}$. For small values of $\delta\theta(t)$, (3.3) can be linearised as:

$$\begin{aligned}\vec{U}^+_{S,c}(t) &\approx [1 - j\delta\theta(t)][\overline{U}^+_{S,0} + \delta\overline{U}^+_S(t)]e^{j\omega_0 t} \\ &\approx [\overline{U}^+_{S,0} - j\delta\theta(t)\overline{U}^+_{S,0} + \delta\overline{U}^+_S(t]e^{j\omega_0 t}\end{aligned} \tag{3.6}$$

where the $\delta\theta(t)\delta\overline{U}^+_S(t)$ term has been neglected. As $\overline{U}^+_{S,c}(t) = [U^+_{S_d,c}(t) + jU^+_{S_q,c}(t)]e^{-j\frac{\pi}{2}}$, from (3.6):

$$\begin{aligned}U^+_{S_d,c}(t) &= -\Im\{\overline{U}_{S,c}(t)\} = -\Im\{\overline{U}^+_{S,0} - j\delta\theta(t)\overline{U}^+_{S,0} + \delta\overline{U}^+_S(t)\} \\ &= \delta\theta(t)U^+_{S,0} + \delta U^+_{S_d}(t)\end{aligned} \tag{3.7}$$

Based on the PLL block diagram in Figure 2.20:

$$\delta\theta(s) = -\frac{k_{p,PLL} + \frac{k_{I,PLL}}{s}}{s}U^+_{S_d,c}(s) = -\frac{G_{PI,PLL}}{s}U^+_{S_d,c}(s) \tag{3.8}$$

where $\delta\theta(s) = \mathcal{L}\{\delta\theta(t)\}$ and $U^+_{S_d,c}(s) = \mathcal{L}\{U^+_{S_d,c}(t)\}$. $\mathcal{L}$ is the Laplace operator [85]. Based on (3.7), (3.9), the following relation can be found between $\delta U^+_{S_d}(s)$ and $\delta\theta(s)$:

$$\delta\theta(s) = -\frac{\frac{G_{PI,PLL}}{s}}{1 + \frac{G_{PI,PLL}}{s}U^+_{S,0}}\delta U^+_{S_d}(s) = G_{PLL}(s)\delta U^+_{S_d}(s) \tag{3.9}$$

Figure 3.1 illustrates the equivalent feedback loop of the small-signal model of the PLL [97].

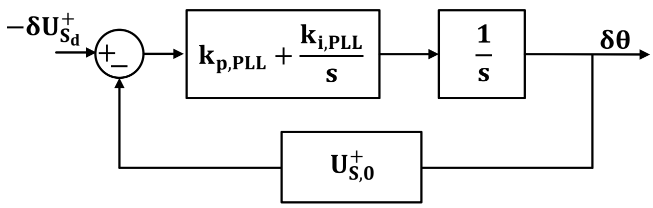

Figure 3.1: Block diagram equivalent to the small-signal model of the PLL.

3.1.1.2 Frame alignment

The methodology used to include the PLL loop dynamics in the derived small-signal models is discussed as follows.

As mentioned, the PLL dynamics generate a misalignment between the grid and the converter dq-frames. Such misalignment, which is quantified by the $\delta\theta(t)$ angle calculated based on (3.9), occurs both for the positive and for the negative dq-frames, as illustrated in Figure 3.2. The technique of including such effect in the small-signal model of the system is called frame-alignment [98] and will be illustrated first for the positive sequence components of the plant signals and then for their negative sequence components.

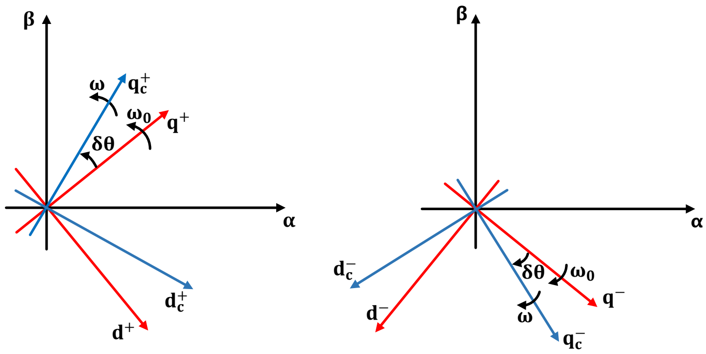

Figure 3.2: Misalignment between the grid and converter dq-frames under unsteady conditions.

Based on (3.3), and applying the same notation used in (2.12) and (2.13), the positive sequence space vectors $\vec{\hat{U}}_S^+(t)$ and $\vec{\hat{i}}^+(t)$, defined in the grid positive dq-frame, can be related to the corresponding $\vec{\hat{U}}_{S,c}^+(t)$ and $\vec{\hat{i}}_c^+(t)$ vectors, calculated in the converter positive dq-frame, as:

$$
\begin{aligned}
\vec{\hat{U}}_{S,c}^+(t) &= [\hat{U}_{S_d,c}^+(t) + j\hat{U}_{S_q,c}^+(t)]e^{j(\theta(t)-\frac{\pi}{2})} = \vec{\hat{U}}_S^+(t)e^{-j\delta\theta(t)} \\
&= [\hat{U}_{S_d}^+(t) + jU_{S_q}^+(t)]e^{j(\omega_0 t-\frac{\pi}{2})}e^{-j\delta\theta(t)} \\
\vec{\hat{i}}_c^+(t) &= [\hat{i}_{d,c}^+(t) + j\hat{i}_{q,c}^+(t)]e^{j(\omega_0 t-\frac{\pi}{2})} = \vec{\hat{i}}^+(t)e^{-j\delta\theta(t)} \\
&= [\hat{i}_d^+(t) + j\hat{i}_q^+(t)]e^{j(\omega_0 t-\frac{\pi}{2})}e^{-j\delta\theta(t)}
\end{aligned}
\tag{3.10}
$$

Equations (3.10) can be reformulated in terms of the converter dq-frame components $\hat{U}^{+}_{S_{dq},c}(t)$, $i^{+}_{dq,c}(t)$ and the grid dq-frame components $\hat{U}^{+}_{S_{dq}}(t)$, $i^{+}_{dq}(t)$, as:

$$\begin{aligned}
\begin{bmatrix} \hat{U}^{+}_{S_d,c}(t) \\ \hat{U}^{+}_{S_q,c}(t) \end{bmatrix} &= \begin{bmatrix} cos(\delta\theta(t)) & sin(\delta\theta(t)) \\ -sin(\delta\theta(t)) & cos(\delta\theta(t)) \end{bmatrix} \begin{bmatrix} \hat{U}^{+}_{S_d}(t) \\ \hat{U}^{+}_{S_q}(t) \end{bmatrix} \\
\begin{bmatrix} \hat{i}^{+}_{d,c}(t) \\ \hat{i}^{+}_{q,c}(t) \end{bmatrix} &= \begin{bmatrix} cos(\delta\theta(t)) & sin(\delta\theta(t)) \\ -sin(\delta\theta(t)) & cos(\delta\theta(t)) \end{bmatrix} \begin{bmatrix} \hat{i}^{+}_{d}(t) \\ \hat{i}^{+}_{q}(t) \end{bmatrix}
\end{aligned} \tag{3.11}$$

Under steady-state conditions $\delta\theta(t) = 0$, therefore:

$$\begin{aligned}
\vec{\hat{U}}^{+}_{S,c}(t) = \vec{\hat{U}}^{+}_{S}(t) = \vec{\hat{U}}^{+}_{S,0}(t) &= (\hat{U}^{+}_{S_d,0} + j\hat{U}^{+}_{S_q,0})e^{j(\omega_0 t - \frac{\pi}{2})} \\
\vec{\hat{i}}^{+}_{c}(t) = \vec{\hat{i}}^{+}(t) = \vec{\hat{i}}^{+}_{0}(t) &= (\hat{i}^{+}_{d,0} + j\hat{i}^{+}_{q,0})e^{j(\omega_0 t - \frac{\pi}{2})}
\end{aligned} \tag{3.12}$$

where $\hat{U}^{+}_{S_d,0}$, $\hat{U}^{+}_{S_q,0}$, $\hat{i}^{+}_{d,0}$, $\hat{i}^{+}_{q,0}$ represent the positive sequence steady-state dq-components of the measured voltage and current signals respectively, taken at the system operating point. During transient conditions the following equations can be formulated:

$$\begin{aligned}
\hat{U}^{+}_{S_{dq}}(t) &= \hat{U}^{+}_{S_{dq},0} + \delta\hat{U}^{+}_{S_{dq}}(t) \\
\hat{i}^{+}_{dq}(t) &= \hat{i}^{+}_{dq,0} + \delta\hat{i}^{+}_{dq}(t) \\
\hat{U}^{+}_{S_{dq},c}(t) &= \hat{U}^{+}_{S_{dq},0} + \delta\hat{U}^{+}_{S_{dq},c}(t) \\
\hat{i}^{+}_{dq,c}(t) &= \hat{i}^{+}_{dq,0} + \delta\hat{i}^{+}_{dq,c}(t)
\end{aligned} \tag{3.13}$$

where $\delta\hat{U}^{+}_{S_{dq}}(t)$, $\delta\hat{i}^{+}_{dq}(t)$, $\delta\hat{U}^{+}_{S_{dq},c}(t)$, $\delta\hat{i}^{+}_{dq,c}(t)$ are the small-signal perturbations around the steady-state values $U^{+}_{S_{dq},0}$, $i^{+}_{dq,0}$. From (3.12), (3.13), the small-signal linearised version of (3.11) is:

$$\begin{bmatrix} \delta\hat{U}^{+}_{S_d,c}(t) \\ \delta\hat{U}^{+}_{S_q,c}(t) \end{bmatrix} = \begin{bmatrix} 1 & 0 & U^{+}_{S_q,0} \\ 0 & 1 & -U^{+}_{S_d,0} \end{bmatrix} \begin{bmatrix} \delta\hat{U}^{+}_{S_d}(t) \\ \delta\hat{U}^{+}_{S_q}(t) \\ \delta\theta(t) \end{bmatrix}, \begin{bmatrix} \delta\hat{i}^{+}_{d,c}(t) \\ \delta\hat{i}^{+}_{q,c}(t) \end{bmatrix} = \begin{bmatrix} 1 & 0 & i^{+}_{q,0} \\ 0 & 1 & -i^{+}_{d,0} \end{bmatrix} \begin{bmatrix} \delta\hat{i}^{+}_{d}(t) \\ \delta\hat{i}^{+}_{q}(t) \\ \delta\theta(t) \end{bmatrix} \tag{3.14}$$

An equivalent procedure is applied for the frame alignment of the negative sequence space vectors of the plant signals, namely $\vec{\hat{U}}_S^-(t)$ and $\vec{\hat{i}}^-(t)$. As illustrated in Figure 3.2, the misalignment between the converter and the grid negative dq-frame is equal to $-\delta\theta(t)$. Similarly to (3.10), $\vec{\hat{U}}_S^-(t)$ and $\vec{\hat{i}}^-(t)$, which are defined in the grid negative dq-frame, can be related to the corresponding $\vec{\hat{U}}_{S,c}^-(t)$ and $\vec{\hat{i}}_c^-(t)$ vectors, defined in the converter negative dq-frame, as:

$$\begin{aligned}
\vec{\hat{U}}_{S,c}^-(t) &= [\hat{U}_{S_d,c}^-(t) + j\hat{U}_{S_q,c}^-(t)]e^{-j(\theta(t)+\frac{\pi}{2})} = \vec{\hat{U}}_S^-(t)e^{j\delta\theta(t)} \\
&= [\hat{U}_{S_d}^-(t) + j\hat{U}_{S_q}^-(t)]e^{-j(\omega_0 t+\frac{\pi}{2})}e^{j\delta\theta(t)} \\
\vec{\hat{i}}_c^-(t) &= [\hat{i}_{d,c}^-(t) + j\hat{i}_{q,c}^-(t)]e^{-j(\theta(t)+\frac{\pi}{2})} = \vec{\hat{i}}^-(t)e^{j\delta\theta(t)} \\
&= [\hat{i}_d^-(t) + j\hat{i}_q^-(t)]e^{-j(\omega_0 t+\frac{\pi}{2})}e^{j\delta\theta(t)}
\end{aligned} \tag{3.15}$$

As previously done with (3.11), equations (3.15) can be reformulated in terms of the converter negative dq-frame components $\hat{U}_{S_{dq},c}^-(t)$, $\hat{i}_{dq,c}^-(t)$ and of the grid negative dq-frame components $\hat{U}_{S_{dq}}^-(t)$, $\hat{i}_{dq}^-(t)$, as:

$$\begin{aligned}
\begin{bmatrix} \hat{U}_{S_d,c}^-(t) \\ \hat{U}_{S_q,c}^-(t) \end{bmatrix} &= \begin{bmatrix} cos(\delta\theta(t)) & -sin(\delta\theta(t)) \\ sin(\delta\theta(t)) & cos(\delta\theta(t)) \end{bmatrix} \begin{bmatrix} \hat{U}_{S_d}^-(t) \\ \hat{U}_{S_q}^-(t) \end{bmatrix} \\
\begin{bmatrix} \hat{i}_{d,c}^-(t) \\ \hat{i}_{q,c}^-(t) \end{bmatrix} &= \begin{bmatrix} cos(\delta\theta(t)) & -sin(\delta\theta(t)) \\ sin(\delta\theta(t)) & cos(\delta\theta(t)) \end{bmatrix} \begin{bmatrix} \hat{i}_d^-(t) \\ \hat{i}_q^-(t) \end{bmatrix}
\end{aligned} \tag{3.16}$$

Under steady-state conditions, $\delta\theta(t) = 0$, therefore:

$$\begin{aligned}
\vec{\hat{U}}_{S,c}^-(t) &= \vec{\hat{U}}_S^-(t) = \vec{\hat{U}}_{S,0}^-(t) = (\hat{U}_{S_d,0}^- + j\hat{U}_{S_q,0}^-)e^{-j(\omega_0 t+\frac{\pi}{2})} \\
\vec{\hat{i}}_c^-(t) &= \vec{\hat{i}}^-(t) = \vec{\hat{i}}_0^-(t) = (\hat{i}_{d,0}^- + j\hat{i}_{q,0}^-)e^{-j(\omega_0 t+\frac{\pi}{2})}
\end{aligned} \tag{3.17}$$

where $\hat{U}_{S_d,0}^-$, $\hat{U}_{S_q,0}^-$, $\hat{i}_{d,0}^-$, $\hat{i}_{q,0}^-$ are the negative sequence steady-state dq-components of the measured voltage and current signals, taken at the system operating point. During transient conditions, the following equations are formulated:

$$\begin{aligned}
\hat{U}^{-}_{S_{dq}}(t) &= \hat{U}^{-}_{S_{dq},0} + \delta U^{-}_{S_{dq}}(t) \\
\hat{i}^{-}_{dq}(t) &= \hat{i}^{-}_{d,0} + \delta\hat{i}^{-}_{dq}(t) \\
\hat{U}^{-}_{S_{dq},c}(t) &= \hat{U}^{-}_{S_{dq},0} + \delta\hat{U}^{-}_{S_{dq},c}(t) \\
\hat{i}^{-}_{dq,c}(t) &= \hat{i}^{-}_{d,0} + \delta\hat{i}^{-}_{dq,c}(t)
\end{aligned} \tag{3.18}$$

where $\delta\hat{U}^{-}_{S_{dq}}(t)$, $\delta\hat{i}^{-}_{dq}(t)$, $\delta\hat{U}^{-}_{S_{dq},c}(t)$, $\delta\hat{i}^{-}_{dq,c}(t)$ are the small-signal perturbations around the steady-state values $\hat{U}^{-}_{S_{dq},0}$, $\hat{i}^{-}_{dq,0}$, respectively. From (3.17), (3.18), the small-signal linearised version of (3.16) is:

$$\begin{bmatrix} \delta\hat{U}^{-}_{S_d,c}(t) \\ \delta\hat{U}^{-}_{S_q,c}(t) \end{bmatrix} = \begin{bmatrix} 1 & 0 & -U^{-}_{S_q,0} \\ 0 & 1 & U^{-}_{S_d,0} \end{bmatrix} \begin{bmatrix} \delta\hat{U}^{-}_{S_d}(t) \\ \delta\hat{U}^{-}_{S_q}(t) \\ \delta\theta(t) \end{bmatrix}, \begin{bmatrix} \delta\hat{i}^{-}_{d,c}(t) \\ \delta\hat{i}^{-}_{q,c}(t) \end{bmatrix} = \begin{bmatrix} 1 & 0 & -\hat{i}^{-}_{q,0} \\ 0 & 1 & \hat{i}^{-}_{d,0} \end{bmatrix} \begin{bmatrix} \delta\hat{i}^{-}_{d}(t) \\ \delta\hat{i}^{-}_{q}(t) \\ \delta\theta(t) \end{bmatrix} \tag{3.19}$$

As the small-signal model of the electrical system is implemented in the grid positive dq-frame, in order to refer the measured plant signals to the negative grid dq-frame, based on (B.21), these need multiplying by $e^{j2\omega_0 t}$, which represents a rotation operator in the $\alpha\beta$-frame. In particular:

$$\begin{aligned}
\hat{U}^{-}_{S_{dq}}(t) &= \hat{U}^{+}_{S_{dq}}(t)e^{j2\omega_0 t} \\
\hat{i}^{-}_{dq}(t) &= \hat{i}^{+}_{dq}(t)e^{j2\omega_0 t}
\end{aligned} \tag{3.20}$$

As discussed in Section 2.2.1.1.2, the positive and negative sequence components $U^{+}_{S_{dq}}(t)$, $i^{+}_{dq}(t)$, $U^{-}_{S_{dq}}(t)$, $i^{-}_{dq}(t)$ in (2.12) and (2.13) are extracted from $\hat{U}^{+}_{S_{dq}}(t)$, $\hat{i}^{+}_{dq}(t)$, $\hat{U}^{-}_{S_{dq}}(t)$, $\hat{i}^{-}_{dq}(t)$ by applying a notch filter tuned at $2\omega_0$ (see Figures 2.12).

A further frame alignment which needs doing is that associated to the outputs of the positive and the negative sequence current controllers $U^{+}_{I_{dq},c}(t)$ and $U^{-}_{I_{dq},c}(t)$. Based on (3.10), (3.15), these signals can be related to the corresponding $U^{+}_{I_{dq}}(t)$ and $U^{-}_{I_{dq}}(t)$

signals, defined in the grid dq-frame, as:

$$\begin{aligned} U^+_{I_{dq}}(t) &= U^+_{I_{dq},c}(t)e^{j\delta\theta(t)} \\ U^-_{I_{dq}}(t) &= U^-_{I_{dq},c}(t)e^{-j\delta\theta(t)} \end{aligned} \tag{3.21}$$

From (3.21), (B.21), by indicating with $\hat{U}^+_{I_{dq}}$ the overall output of the current controller, expressed in the grid positive dq-frame, this is calculated as:

$$\begin{aligned} \hat{U}^+_{I_{dq}}(t) &= U^+_{I_{dq}}(t) + U^-_{I_{dq}}(t)e^{-j2\omega_0 t} \\ &= U^+_{I_{dq},c}(t)e^{j\delta\theta(t)} + U^-_{I_{dq},c}(t)e^{-j\delta\theta(t)}e^{-j2\omega_0 t} \end{aligned} \tag{3.22}$$

Under steady-state conditions $\theta(t) = \omega_0 t$, therefore:

$$\hat{U}^+_{I_{dq}}(t) = \hat{U}^+_{I_{dq},0}(t) = U^+_{I_{dq},0} + U^-_{I_{dq},0}e^{-j2\omega_0 t} \tag{3.23}$$

where $U^+_{I_{dq},0}$ and $U^-_{I_{dq},0}$ respectively are the stationary outputs of the positive and the negative sequence controllers. Under unsteady conditions, the following expressions can be formulated:

$$\begin{aligned} U^+_{I_{dq},c}(t) &= U^+_{I_{dq},0} + \delta U^+_{I_{dq},c}(t) \\ U^-_{I_{dq},c}(t) &= U^-_{I_{dq},0} + \delta U^-_{I_{dq},c}(t) \\ \hat{U}^+_{I_{dq},c}(t) &= \hat{U}^+_{I_{dq},0}(t) + \delta\hat{U}^+_{I_{dq},c}(t) \end{aligned} \tag{3.24}$$

where $\delta U^+_{I_{dq},c}(t)$, $\delta U^-_{I_{dq},c}(t)$ and $\delta\hat{U}^+_{I_{dq},c}(t)$ are the small-signal perturbations around the steady-state values $U^+_{I_{dq},0}$, $U^-_{I_{dq},0}$ and $\hat{U}^+_{I_{dq},0}(t)$, respectively. From (3.22), (3.23), (3.24), (B.21), by linearising the $e^{j\delta\theta(t)}$ and $e^{-j\delta\theta(t)}$ terms in (3.22), it derives that:

$$\begin{aligned}\begin{bmatrix}\delta\hat{U}^{+}_{I_d}(t)\\ \delta\hat{U}^{+}_{I_q}(t)\end{bmatrix} &= \begin{bmatrix}1 & 0 & -U^{+}_{I_q,0}\\ 0 & 1 & U^{+}_{I_d,0}\end{bmatrix}\begin{bmatrix}\delta U^{+}_{I_d,c}(t)\\ \delta U^{+}_{I_q,c}(t)\\ \delta\theta(t)\end{bmatrix}\\ &+ \begin{bmatrix}cos(2\omega_0 t) & sin(2\omega_0 t)\\ -sin(2\omega_0 t) & cos(2\omega_0 t)\end{bmatrix}\begin{bmatrix}1 & 0 & U^{-}_{I_q,0}\\ 0 & 1 & -U^{-}_{I_d,0}\end{bmatrix}\begin{bmatrix}\delta U^{-}_{I_d,c}(t)\\ \delta U^{-}_{I_q,c}(t)\\ \delta\theta(t)\end{bmatrix}\end{aligned} \tag{3.25}$$

The result (3.25) highlights that in order to map the output of the negative sequence controller $\delta U^{-}_{I_{dq},c}(t)$ onto the grid positive dq-frame, both a $e^{-j2\omega_0 t}$ rotation and a frame alignment need to be applied. Just a frame alignment is instead needed to map the positive sequence controller output $\delta U^{+}_{I_{dq},c}(t)$ onto the grid positive dq-frame.

Figure 3.3 illustrates how the described frame alignment terms are included in the small-signal model of the system. In particular, $G_{N,M}(s)$ is the transfer function matrix of the notch filter, defined as:

$$G_{N,M}(s) = \begin{bmatrix}G_N(s) & 0\\ 0 & G_N(s)\end{bmatrix} \tag{3.26}$$

where:

$$G_N(s) = \frac{s^2 + 4\omega_0^2}{s^2 + \frac{2\omega_0}{Q}s + 4\omega_0^2} \tag{3.27}$$

As discussed in Section 2.2.1.1.2, this filter is tuned at $2\omega_0$ to decouple the positive and negative sequence components of the plant signals.

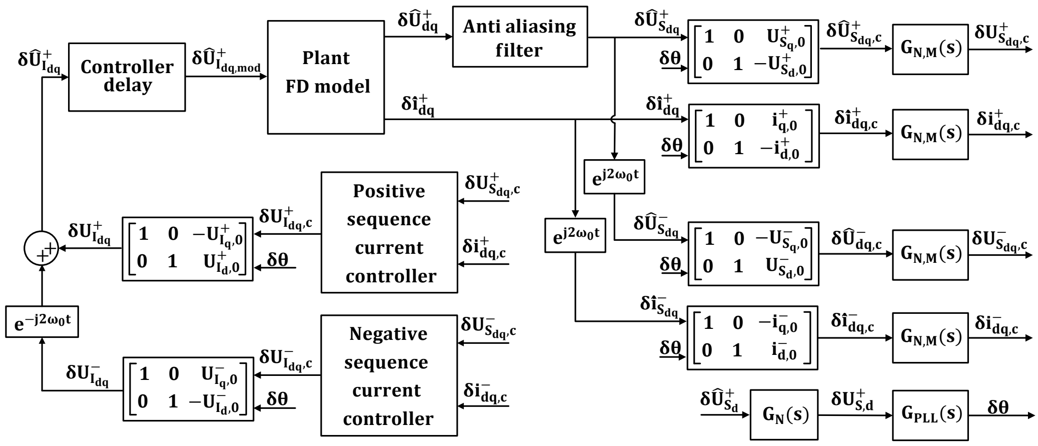

Figure 3.3: Block diagram of the system small-signal model, illustrating the frame alignments between the grid and the converter dq-frames.

3.1.1.3 Inner controller

In the following Section 3.1.1.3.1 the small-signal model of the positive sequence current controller is presented, while in Section 3.1.1.3.2, that of the negative sequence current controller is discussed.

3.1.1.3.1 Positive sequence current loop

As the positive sequence controller operates in the positive dq-frame, the derivation of its small-signal model is straightforward. In fact, thanks to the LTI property of this controller, its small-signal model is directly obtained from its block diagram, shown in Figure 2.11. The resulting block diagram of such small-signal model is illustrated in Figure 3.4, where the frame alignment terms between the grid and the converter dq-frames have also been included. In particular:

$$\delta\theta_M(s) = \begin{bmatrix} \delta\theta(s) & 0 \\ 0 & \delta\theta(s) \end{bmatrix} \tag{3.28}$$

$$G_{PI,M}(s) = \begin{bmatrix} G_{PI}(s) & 0 \\ 0 & G_{PI}(s) \end{bmatrix} = \begin{bmatrix} k_{p,I} + \frac{k_{i,I}}{s} & 0 \\ 0 & k_{p,I} + \frac{k_{i,I}}{s} \end{bmatrix} \tag{3.29}$$

$$G^{+}_{VFF,M}(s) = \begin{bmatrix} G^{+}_{VFF}(s) & 0 \\ 0 & G^{+}_{VFF}(s) \end{bmatrix} = \begin{bmatrix} \frac{1}{1+\tau_p s} & 0 \\ 0 & \frac{1}{1+\tau_p s} \end{bmatrix} \tag{3.30}$$

$$G^{+}_{C,M}(s) = \begin{bmatrix} 0 & -\omega_0 L_f \\ \omega_0 L_f & 0 \end{bmatrix} \tag{3.31}$$

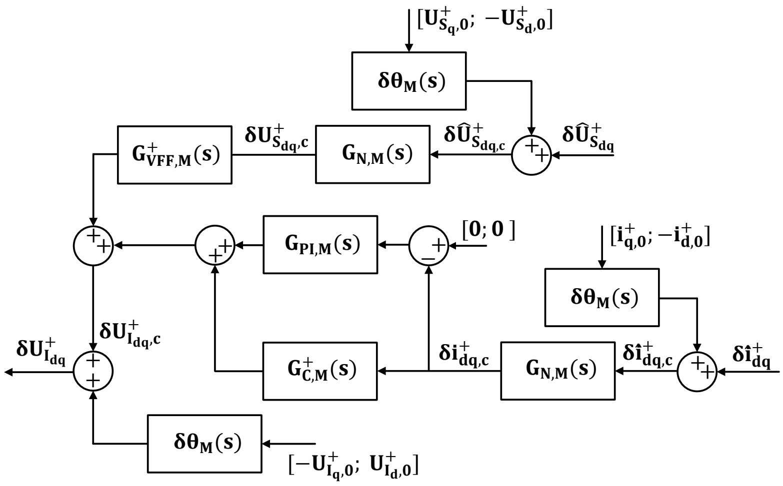

Figure 3.4: Block diagram of the small-signal model of the positive sequence current control loops, implemented in the converter positive dq-frame.

3.1.1.3.2 Negative sequence current loop

The derivation of the small-signal model of the negative sequence current controller in the negative dq-frame is straightforward. In fact, thanks to the LTI property of the controller, it can be derived directly from its block diagram shown in Figure 2.13. The resulting block diagram of such small-signal model is illustrated in Figure 3.5, where the frame alignment terms between the grid and the converter dq-frames have also been included.

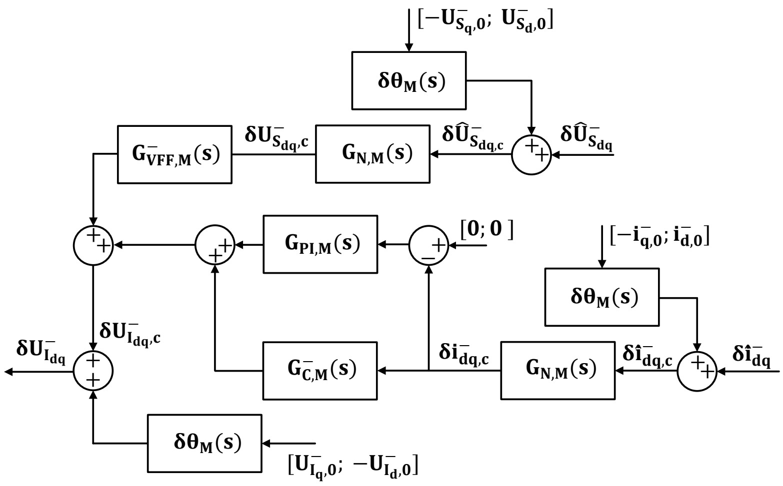

Figure 3.5: Block diagram of the small-signal model of the negative sequence current control loops, implemented in the converter negative *dq*-frame.

In particular:

$$G^-_{VFF,M}(s) = \begin{bmatrix} G^-_{VFF}(s) & 0 \\ 0 & G^-_{VFF}(s) \end{bmatrix} = \begin{bmatrix} \frac{1}{1+\tau_n s} & 0 \\ 0 & \frac{1}{1+\tau_n s} \end{bmatrix} \tag{3.32}$$

$$G^-_{C,M}(s) = \begin{bmatrix} 0 & \omega_0 L_f \\ -\omega_0 L_f & 0 \end{bmatrix} \tag{3.33}$$

As the small-signal model of the system is implemented in the positive *dq*-frame, the small-signal model of the negative sequence controller, defined by the block diagram in Figure 3.5, needs projecting onto the positive *dq*-frame. For this purpose, the methodology described in Appendix C.2.1 is applied, which consists in mapping the dynamics of the negative sequence current controller onto the positive *dq*-frame. The technique is summarised in Figure 3.6. $G_M(s)$ represents a generic transfer function matrix defined in the negative *dq*-frame and has the structure given in (C.24) and reported for convenience in (3.34):

$$G_M(s) = \begin{bmatrix} G(s) & 0 \\ 0 & G(s) \end{bmatrix} \tag{3.34}$$

$\hat{G}_M(s)$ is its corresponding expression in the positive dq-frame. Its expression is derived in Appendix C.2.1 and is provided in (3.35):

$$\hat{G}_M(s) = \begin{bmatrix} \frac{1}{2}[G(s-2j\omega_0)+G(s+2j\omega_0)] & \frac{1}{2}j[G(s+2j\omega_0)-G(s-2j\omega_0)] \\ \frac{1}{2}j[G(s-2j\omega_0)-G(s+2j\omega_0)] & \frac{1}{2}[G(s-2j\omega_0)+G(s+2j\omega_0)] \end{bmatrix} \quad (3.35)$$

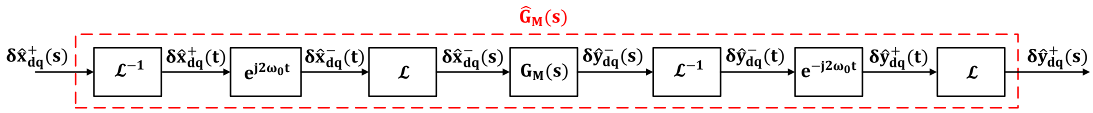

Figure 3.6: Translation of a negative dq-frame transfer function matrix $G_M(s)$, defined in (3.34), onto the positive dq-frame.

The signals $\delta\hat{x}^+_{dq}(t)$ and $\delta\hat{y}^+_{dq}(t)$ respectively represent the positive dq-frame expressions of $\delta x^-_{dq}(t)$ and $y^-_{dq}(t)$, which are defined in the negative dq-frame.

The method requires the calculation of the corresponding positive dq-frame expressions of each of the transfer function matrices in Figure 3.5. Hence, for the transfer function matrices $G_{PI,M}(s)$, $G^-_{VFF,M}(s)$, $\delta\theta_M(s)$, $G_{N,M}(s)$, respectively defined by (3.29), (3.32), (3.28) and (3.26), based on (3.35), their equivalent expressions in the positive dq-frame, $\hat{G}_{PI,M}(s)$, $\hat{G}^-_{VFF,M}(s)$, $\delta\hat{\theta}_M(s)$ and $\hat{G}_{N,M}(s)$, are:

$$\hat{G}_{PI,M}(s) = \begin{bmatrix} k_{p,PI} + \frac{k_{I,PI}s}{s^2+4\omega_0^2} & \frac{2\omega_0 k_{I,PI}s}{s^2+4\omega_0^2} \\ -\frac{2\omega_0 k_{I,PI}s}{s^2+4\omega_0^2} & k_{p,PI} + \frac{k_{I,PI}s}{s^2+4\omega_0^2} \end{bmatrix} \quad (3.36)$$

$$\hat{G}^-_{VFF,M}(s = \begin{bmatrix} \frac{\tau_n s+1}{\tau_n^2 s^2+1+2\tau_n s+(2\tau_n\omega_0)^2} & \frac{2\tau_n\omega_0}{\tau_n^2 s^2+1+2\tau_n s+(2\tau_n\omega_0)^2} \\ -\frac{2\tau_n\omega_0}{\tau_n^2 s^2+1+2\tau_n s+(2\tau_n\omega_0)^2} & \frac{\tau_n s+1}{\tau_n^2 s^2+1+2\tau_n s+(2\tau_n\omega_0)^2} \end{bmatrix} \quad (3.37)$$

$$\delta\hat{\theta}_M(s) = \begin{bmatrix} \frac{1}{2}[\delta\theta(s-2j\omega_0)+\delta\theta(s+2j\omega_0)] & \frac{1}{2}j[\delta\theta(s+2j\omega_0)-\delta\theta(s-2j\omega_0)] \\ \frac{1}{2}j[\delta\theta(s-2j\omega_0)-\delta\theta(s+2j\omega_0] & \frac{1}{2}[\delta\theta(s-2j\omega_0)+\delta\theta(s+2j\omega_0)] \end{bmatrix} \quad (3.38)$$

$$\hat{G}_{N,M}(s) = \begin{bmatrix} \frac{s^4+\frac{2\omega_0}{Q}s^3+16\omega_0^2 s^2+\frac{16\omega_0^3}{Q}s}{s^4+(\frac{2\omega_0}{Q})^2 s^2+\frac{4\omega_0}{Q}s^3+16\omega_0^2 s^2+\frac{32\omega_0^3}{Q}s+\frac{16\omega_0^4}{Q^2}} & \frac{-\frac{4\omega_0^2}{Q}s^2}{s^4+(\frac{2\omega_0}{Q})^2 s^2+\frac{4\omega_0}{Q}s^3+16\omega_0^2 s^2+\frac{32\omega_0^3}{Q}s+\frac{16\omega_0^4}{Q^2}} \\ \frac{\frac{4\omega_0^2}{Q}s^2}{s^4+(\frac{2\omega_0}{Q})^2 s^2+\frac{4\omega_0}{Q}s^3+16\omega_0^2 s^2+\frac{32\omega_0^3}{Q}s+\frac{16\omega_0^4}{Q^2}} & \frac{s^4+\frac{2\omega_0}{Q}s^3+16\omega_0^2 s^2+\frac{16\omega_0^3}{Q}s}{s^4+(\frac{2\omega_0}{Q})^2 s^2+\frac{4\omega_0}{Q}s^3+16\omega_0^2 s^2+\frac{32\omega_0^3}{Q}s+\frac{16\omega_0^4}{Q^2}} \end{bmatrix} \tag{3.39}$$

The resulting block diagram of the small-signal model of the negative sequence current controller, implemented in the positive dq-frame is shown in Figure 3.7.

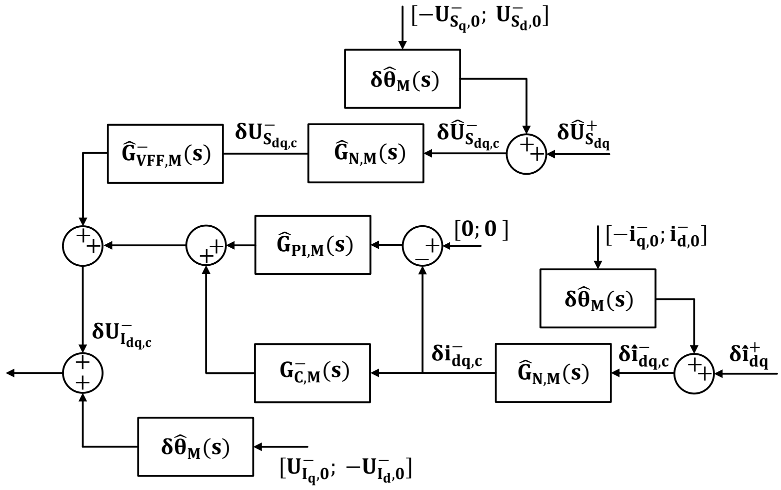

Figure 3.7: Block diagram of the small-signal model of the negative sequence control loops, implemented in the converter positive dq-frame.

3.1.1.4 Anti-aliasing filter

The anti-aliasing filter applied on the measured plant voltage operates in the abc-frame and, therefore, needs mapping onto the positive grid dq-frame (see Figure 2.20).

The transfer function models of the employed notch and LPF filters are $G_{AFn}(s)$ and $G_{LPF}(s)$, respectively defined in (E.4) and (E.6). It is emphasised that these filters operate equally and independently on each phase of the measured U voltage. Therefore, the anti-aliasing filter, acting on the three phases of U, can be described analytically introducing the transfer function matrices $G_{AFn,M}(s)$ and $G_{LPF,M}(s)$, defined as:

$$G_{AFn,M}(s) = \begin{bmatrix} G_{AFn}(s) & 0 & 0 \\ 0 & G_{AFn}(s) & 0 \\ 0 & 0 & G_{AFn}(s) \end{bmatrix} \tag{3.40}$$

$$G_{LPF,M}(s) = \begin{bmatrix} G_{LPF}(s) & 0 & 0 \\ 0 & G_{LPF}(s) & 0 \\ 0 & 0 & G_{LPF}(s) \end{bmatrix} \tag{3.41}$$

An equivalent dq-frame formulation of $G_{AFn,M}(s)$ and $G_{LPF,M}(s)$ is derived. For this purpose, the technique illustrated in Appendix C.2.2 is applied, which describes how to map an abc-frame diagonal transfer function matrix, defined as in (C.35), onto the positive dq-frame. It is worth noticing that such mapping technique is equivalent to the one illustrated in Figure 3.6, where the frame rotation terms are now equal to $e^{\pm j\omega_0 t}$ instead of $e^{\pm j2\omega_0 t}$ (see Figure 3.8).

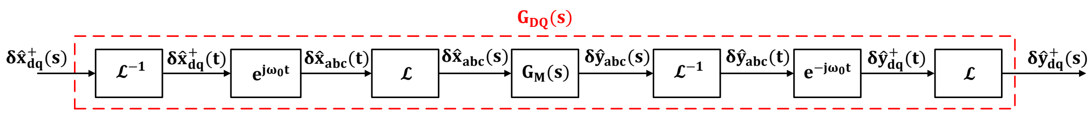

Figure 3.8: Translation of an abc-frame transfer function matrix $G_M(s)$, defined as in (C.35), onto the positive dq-frame transfer function $G_{DQ}(s)$.

The resulting dq-frame expressions $G_{AFn,DQ}(s)$ and $G_{LPF,DQ}(s)$, respectively corresponding to $G_{AFn,M}(s)$ and $G_{LPF,M}(s)$, are:

$$G_{AFn,DQ}(s) = \begin{bmatrix} G_{AFn,dd}(s) & G_{AFn,dq}(s) \\ G_{AFn,qd}(s) & G_{AFn,qq}(s) \end{bmatrix} \tag{3.42}$$

$$G_{LPF,DQ}(s) = \begin{bmatrix} G_{LPF,dd}(s) & G_{LPF,dq}(s) \\ G_{LPF,qd}(s) & G_{LPF,qq}(s) \end{bmatrix} \tag{3.43}$$

where:

$$
\begin{aligned}
G_{AFn,dd}(s) &= G_{AFn,qq}(s) \\
&= \frac{s^4 + \frac{\omega_n}{Q}s^3 + (2\omega_0^2 + 2\omega_n^2)s^2 + \frac{\omega_n\omega_0^2+\omega_n^3}{Q}s + (\omega_0^2 - \omega_n^2)^2}{s^4 + \frac{2\omega_n}{Q}s^3 + (\frac{\omega_n^2}{Q^2} + 2\omega_0^2 + 2\omega_n^2)s^2 + \frac{2\omega_n\omega_0^2+2\omega_n^3}{Q}s + (\omega_0^2 - \omega_n^2)^2 + \frac{\omega_0^2\omega_n^2}{Q^2}} \\
G_{AFn,dq}(s) &= -G_{AFn,qd}(s) \\
&= \frac{-\frac{\omega_n\omega_0}{Q}(s^2 + \omega_0^2 - \omega_n^2)}{s^4 + \frac{2\omega_n}{Q}s^3 + (\frac{\omega_n^2}{Q^2} + 2\omega_0^2 + 2\omega_n^2)s^2 + \frac{2\omega_n\omega_0^2+2\omega_n^3}{Q}s + (\omega_0^2 - \omega_n^2)^2 + \frac{\omega_0^2\omega_n^2}{Q^2}}
\end{aligned}
\tag{3.44}
$$

$$
\begin{aligned}
G_{LPF,dd}(s) = G_{LPF,qq}(s) &= \frac{\tau_f s + 1}{\tau_f^2 s^2 + 1 + 2\tau_f s + (\tau_f\omega_0)^2} \\
G_{LPF,dq}(s) = -G_{LPF,qd}(s) &= \frac{\tau_f\omega_0}{\tau_f^2 s^2 + 1 + 2\tau_f s + (\tau_f\omega_0)^2}
\end{aligned}
\tag{3.45}
$$

The corresponding block diagram of the dq-frame small-signal model of the anti-aliasing filter is illustrated in Figure 3.9. $\delta\hat{U}^+_{dq}$ and $\delta\hat{U}^+_{S_{dq}}$ are the small-signal perturbations of $\hat{U}^+_{dq}$ and $\hat{U}^+_{S_{dq}}$ around their steady-state values $\hat{U}^+_{dq,0}$, $\hat{U}^+_{S_{dq},0}$. The signal notation used in (2.13) has been applied.

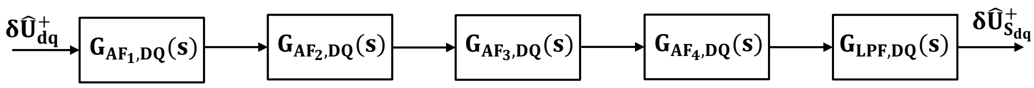

Figure 3.9: Equivalent block diagram of the small-signal model of the anti-aliasing filter, in the positive dq-frame.

The Bode plots of the elements of the anti-aliasing filter transfer function matrix, derived in the positive dq-frame, are reported in Figure C.6 in Appendix C.2.2.

3.1.1.5 Controller delay

A further element of the controller scheme shown in Figure 2.20, which has been modelled in the abc-frame, is the controller delay. Similarly to what has been done for the anti-aliasing filter, the diagonal transfer function matrix $G_{D,M}(s)$ is defined to model the delay in the *abc*-frame:

$$G_{D,M}(s) = \begin{bmatrix} G_D(s) & 0 & 0 \\ 0 & G_D(s) & 0 \\ 0 & 0 & G_D(s) \end{bmatrix} \tag{3.46}$$

where $G_D(s)$ is defined in (2.20). Applying the same procedure used for the anti-aliasing filter, $G_{D,M}(s)$ is mapped onto the dq-frame according to the theory described in Appendix C.2.2. The resulting dq-frame expression $G_{D,DQ}(s)$, associated to $G_{D,M}(s)$, is:

$$G_{D,DQ}(s) = \begin{bmatrix} e^{-sT_d}cos(\omega_0 T_d) & e^{-sT_d}sin(\omega_0 T_d) \\ -e^{-sT_d}sin(\omega_0 T_d) & e^{-sT_d}cos(\omega_0 T_d) \end{bmatrix} \tag{3.47}$$

The equivalent block diagram of the small-signal model of the controller delay, implemented in the dq-frame, is illustrated in Figure 3.10. $\delta\hat{U}^+_{I_{dq}}$ and $\delta\hat{U}^+_{I_{dq},D}$ are the small-signal perturbations of, respectively, $\hat{U}^+_{I_{dq}}$ and $\hat{U}^+_{I_{dq},D}$ around their steady-state values.

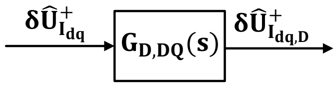

Figure 3.10: Equivalent block diagram of the small-signal model of the controller delay, in the positive dq-frame.

3.1.1.6 Outer controller

The small-signal model of the active power controller is presented in Section 3.1.1.6.1, while that of the voltage regulator is presented in Section 3.1.1.6.2.

3.1.1.6.1 Active power loop

The derivation of the small-signal model of the power loop requires the linearisation of (2.15). This results in the following small-signal equation:

$$\delta P(t) = \frac{3}{2}[\delta i^{+}_{d,c} U^{+}_{S_d,0} + i^{+}_{d,0} \delta U^{+}_{S_d,c} + \delta i^{+}_{q,c} U^{+}_{S_q,0} + i^{+}_{q,0} \delta U^{+}_{S_q,c}] \tag{3.48}$$

where $\delta P(t)$ is the small-signal perturbation around the steady-state value P_0. The resulting block diagram of the small-signal model of the power loop is shown in Figure 3.11, where $G_{PI,P}(s)$ is:

$$G_{PI,P}(s) = k_{p,P} + \frac{k_{i,P}}{s} \tag{3.49}$$

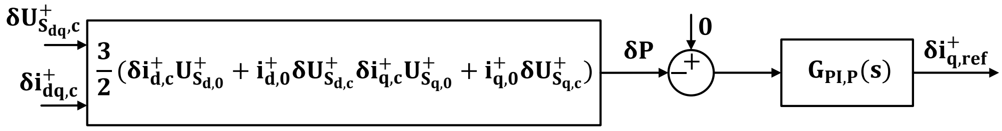

Figure 3.11: Block diagram of the active power loop small-signal model.

3.1.1.6.2 Voltage loop

The derivation of the small-signal model of the voltage loop requires the linearisation of (2.16). This results in the following small-signal equation:

$$\delta \hat{U}_S(t) = \frac{U^{+}_{S_d,0}}{\sqrt{[U^{+}_{S_d,0}]^2 + [U^{+}_{S_q,0}]^2}} \delta U^{+}_{S_d,c} + \frac{U^{+}_{S_q,0}}{\sqrt{[U^{+}_{S_d,0}]^2 + [U^{+}_{S_q,0}]^2}} \delta U^{+}_{S_q,c} \tag{3.50}$$

where $\delta \hat{U}_S(t)$ is the small-signal perturbation around the steady-state value $\hat{U}_{S,0}$. The resulting block diagram of the small-signal model of the power loop is shown in Figure 3.12, where $G_{PI,V}(s)$ is:

$$G_{PI,V}(s) = k_{p,V} + \frac{k_{i,V}}{s} \tag{3.51}$$

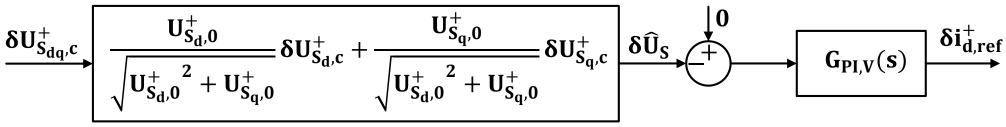

Figure 3.12: Block diagram of the voltage loop small-signal model.

3.1.2 Electrical system

The theory to define the small-signal model of the electrical system associated to the considered turbine-grid system described in Section 2.1.3 is presented as follows.

The equations of such electrical system are in the *abc*-frame, thereby they need to be referred to the positive *dq*-frame. This projection from the *abc*- to the *dq*- is discussed in Appendix C.12, and consists in deriving a *dq*-frame state space representation of the electrical system.

As the grid only contains linear passive components (see (C.3)), the A_u, B_u and C_u matrices in (C.5) are constant, i.e. they do not vary with the system operating point. By indicating with $\delta\vec{x}_u(t)$, $\delta\vec{x}_d(t)$, $\delta\vec{u}(t)$ and $\delta\vec{y}(t)$ the small-signal perturbations respectively corresponding to $\vec{x}_u(t)$, $\vec{x}_d(t)$, $\vec{u}(t)$ and $\vec{y}(t)$ (see (C.4) for their definitions), the following relations can be formulated:

$$\begin{aligned} \vec{x}_u(t) &= \vec{x}_{u,0} + \delta\vec{x}_u(t) \\ \vec{u}(t) &= \vec{u}_0 + \delta\vec{u}(t) \\ \vec{y}(t) &= \vec{y}_0 + \delta\vec{y}(t) \end{aligned} \tag{3.52}$$

where $\vec{x}_{u,0}$, $\vec{u}_0$ and $\vec{y}_0$ are the steady-state values of $\vec{x}_u(t)$, $\vec{u}(t)$ and $\vec{y}(t)$, taken at the system operating point.

As the resulting electrical system model is LTI, based on (C.4) and (C.5), its small-signal state-space model can be formulated as:

$$\begin{cases} \frac{d\delta\vec{x}_u(t)}{dt} = A_u\delta\vec{x}_u(t) + B_u\delta\vec{u}(t), \\ \delta\vec{y}(t) = C_u\delta\vec{x}_u(t) \end{cases} \tag{3.53}$$

In particular:

$$\delta\vec{u}(t) = \begin{bmatrix} \delta\hat{U}^{+}_{I_d,mod}(t) \\ \delta\hat{U}^{+}_{I_q,mod}(t) \\ \delta\hat{U}^{+}_{g_d}(t) \\ \delta\hat{U}^{+}_{g_q}(t) \end{bmatrix} ; \delta\vec{y}(t) = \begin{bmatrix} \delta\hat{i}^{+}_{d}(t) \\ \delta\hat{i}^{+}_{q}(t) \\ \delta\hat{U}^{+}_{d}(t) \\ \delta\hat{U}^{+}_{q}(t) \end{bmatrix} ; \tag{3.54}$$

It is worth mentioning that in the carried out analyses is has been assumed that $\delta\hat{U}^{+}_{g_{dq}}(t) = 0$.

3.1.3 Complete small-signal model

The block diagram of the complete small-signal model of the considered turbine-grid system is shown in Figure 3.13.

3.2 Validation of the small-signal model

In this Section, the derived small-signal models are validated against MATLAB/Simulink TD model simulations and experimental data.
Validation tests have been carried out for the four current loops of the controller (the i^{+}_{d}, the i^{+}_{q}, the i^{-}_{d} and i^{-}_{q} loops in Figure 2.20), and for the outer loops (the active power and the voltage regulators). The validation of inner loops is presented in Section 3.2.1, that of the outer loops in Section 3.2.2.

3.2.1 Inner controller

The validation tests of the inner current loops have been carried out considering the turbine-grid model described in Section 2.1.3 and the laboratory prototype system described in Section 2.3.2.3. For the former system, the system parameters detailed in Table 2.1 have been applied. For the latter one, those listed in Table 2.8 have been used. The controller scheme in Figure 2.20 has been considered (i.e. with no outer loops).
In these tests, while for the turbine-grid system the associated small-signal model has been validated against its corresponding TD model, the small-signal model of the laboratory prototype system has been validated both against its TD model and against

experimental data.

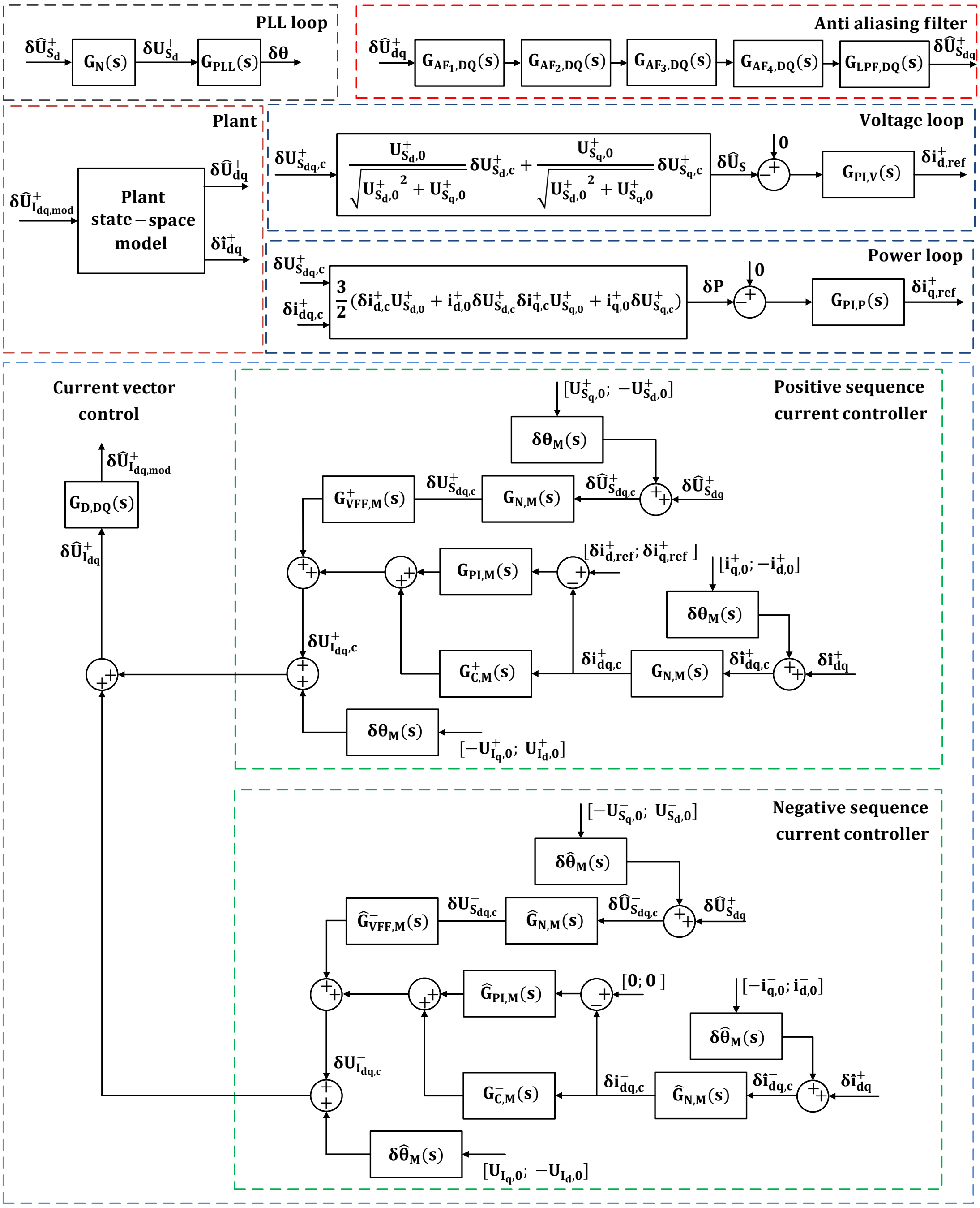

Figure 3.13: Block diagram of the complete small-signal model of the turbine-grid system.

As mentioned, the frequency responses of the closed-loop transfer functions of the four current loops have been considered. These are indicated as $G^+_{i,d}(j2\pi f)$, $G^+_{i,q}(j2\pi f)$, $G^-_{i,d}(j2\pi f)$ and $G^-_{i,q}(j2\pi f)$ for the i^+_d, the i^+_q, the i^-_d and the i^-_q loops, respectively. Their analytical expressions have been calculated from the small-signal models.

Thereafter, these frequency responses have been derived from time-domain simulations of the corresponding TD models. In these simulations, a small-signal sinusoidal perturbation has been added to the reference value of the tested current loop. The case of the i^+_q loop test is described as follows. Equivalent tests have been executed for the other three current loops.

By indicating with $i^+_{q,ref}(t)$ the perturbed reference signal of the q^+ loop, in the carried out simulations this has been defined as:

$$i^+_{q,ref}(t) = i^+_{q_{ref},0} + \delta i^+_{q,ref} cos(2\pi f_p t) \tag{3.55}$$

where $i^+_{q_{ref},0}$ is the steady-state value, $\delta i^+_{q,ref}$ is the amplitude of the applied small-signal perturbation, equal to 0.2 A, while f_p is its frequency.

The spectrum of the resulting perturbed feedback signal $i^+_q(t)$ has been analysed. This was characterized by a component at f_p, having a magnitude $\delta \hat{i}^+_q(f_p)$ and a phase $\gamma^+_q(f_p)$. Hence, the frequency response $G^+_{i,q}(j2\pi f_p)$ has been calculated as:

$$|G^+_{i,q}(j2\pi f_p)| = \frac{\delta \hat{i}^+_q(f_p)}{\delta i^+_{q,ref}}, \angle(G^+_{i,q}(j2\pi f_p)) = \gamma^+_q(f_p) \tag{3.56}$$

The test has been repeated varying the frequency f_p of the applied perturbation, thus carrying out a frequency sweep test. This has allowed the derivation of the TD model frequency response $G^+_{i,q}(j2\pi f)$.

As mentioned, equivalent tests have been repeated for the other three current loops of the system, and the corresponding $G^+_{i,d}(j2\pi f)$, $G^-_{i,d}(j2\pi f)$ and $G^-_{i,q}(j2\pi f)$ TD model frequency responses have been derived.

An equivalent methodology has been applied to derive the experimental frequency response data of the four current loops of the considered laboratory prototype.

The results of the validation tests are illustrated in Figures 3.14 and 3.15 for the turbine-grid interface and for the laboratory prototype inverter-grid interface, respectively. For the former interface, an operating point corresponding to $i^+_{q,ref} = 2000$ A, $i^+_{d,ref} = i^-_{q,ref} = i^-_{d,ref} = 0$ A has been considered. For the latter interface, an operating point corresponding to $i^+_{q,ref} = 5$ A, $i^+_{d,ref} = i^-_{q,ref} = i^-_{d,ref} = 0$ A has been tested.
Based on the shown results, a substantial accuracy of the tested small-signal models has been verified.

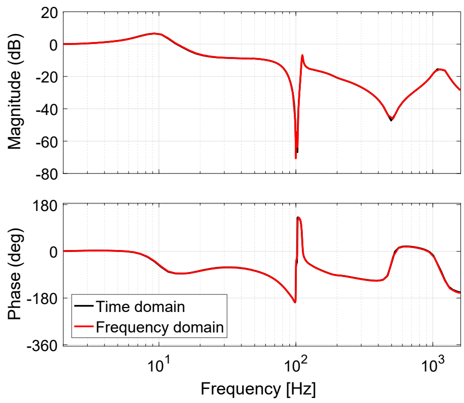

(a) $G^+_{i,d}(j2\pi f)$

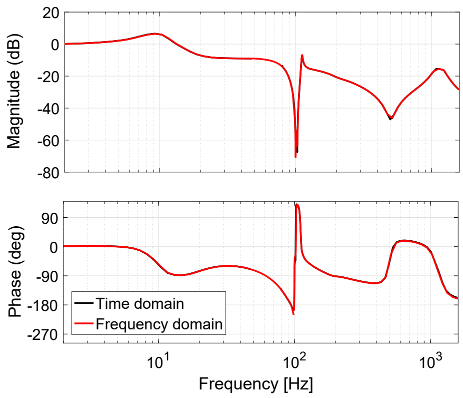

(b) $G^+_{i,q}(j2\pi f)$

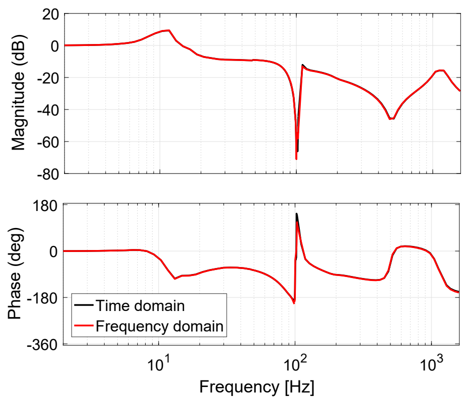

(c) $G^-_{i,d}(j2\pi f)$

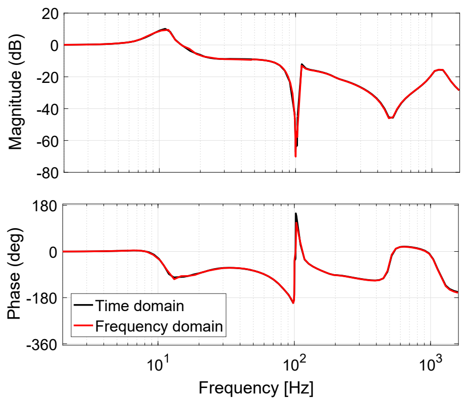

(d) $G^-_{i,q}(j2\pi f)$

Figure 3.14: Comparison between the frequency responses of the closed loop transfer functions of the four controller current loops of the modelled turbine-grid interface. The results obtained with the FD model are compared to those of the corresponding TD model.

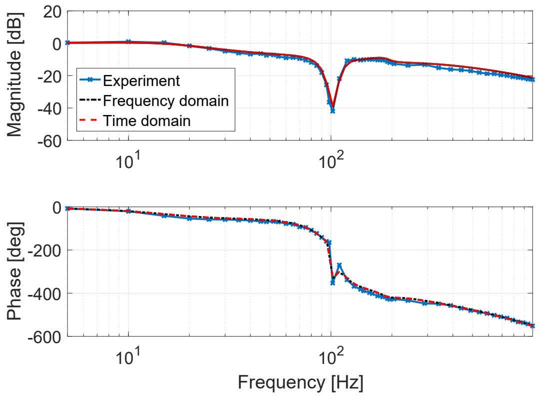

(a) $G^{+}_{i,d}(j2\pi f)$

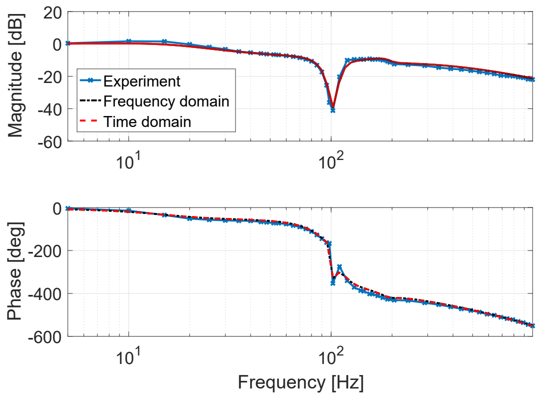

(b) $G^{+}_{i,q}(j2\pi f)$

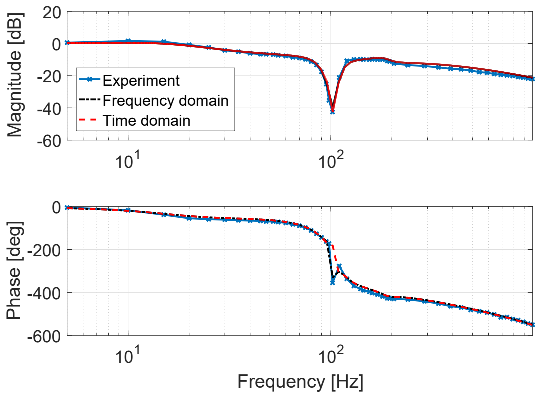

(c) $G^{-}_{i,d}(j2\pi f)$

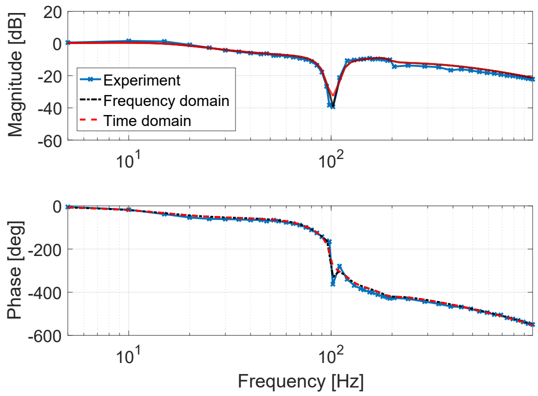

(d) $G^{-}_{i,q}(j2\pi f)$

Figure 3.15: Comparison between the frequency responses of the closed loop transfer functions of the four controller current loops of the built laboratory prototype inverter-grid interface described in Section 2.3.2.3. The results obtained with the FD model are compared to those of the corresponding TD model, as well as to experimental data.

3.2.2 Outer controller

In order to validate the accuracy of the derived small-signal model of the outer loops, the laboratory prototype inverter-grid interface described in Section 2.3.2.3 has been used. In these tests, the system and controller parameters detailed in Table 2.9 have been used (considering the scenario with SCR= 1.9). The controller scheme in Figure 2.20 has been considered, where the outer loops shown in Figures 2.15 and 2.16 have been added.

The frequency responses of the closed-loop transfer functions of the active power controller and of the voltage controller have been considered. These are respectively indicated as $G_P(j2\pi f)$, and $G_V(j2\pi f)$. Their analytical expressions have been calculated from the derived small-signal model of the considered inverter-grid interface. On the other hand, the laboratory prototype has been tested to obtain these frequency responses experimentally. In these tests, a small-signal sinusoidal perturbation has been added to the reference value of the tested loop. The case of the power loop test is described as follows. By indicating with $P_{ref}(t)$ the perturbed reference signal of the power loop, in the executed tests this has been defined as:

$$P_{ref}(t) = P_{ref,0} + \delta P_{ref} cos(2\pi f_p t) \tag{3.57}$$

where $P_{ref,0}$ is the steady-state value, δP_{ref} is the amplitude of the applied small-signal perturbation, equal to 100 W, while f_p is its frequency.
The spectrum of the resulting perturbed feedback signal $P(t)$ has been analysed. This was characterized by a component at f_p, with a magnitude $\delta \hat{P}(f_p)$ and a phase $\gamma_P(f_p)$. Hence, the frequency response $G_P(j2\pi f_p)$ has been calculated as:

$$|G_P(j2\pi f_p)| = \frac{\delta \hat{P}(f_p)}{\delta P_{ref}}, \angle(G_P(j2\pi f_p)) = \gamma_P(f_p) \tag{3.58}$$

The test has been repeated varying the frequency f_p of the applied perturbation, carrying out a frequency sweep test. This has allowed the derivation of the experimental frequency response $G_P(j2\pi f)$. An equivalent test has been repeated for the voltage loop, allowing the derivation of the experimental $G_V(j2\pi f)$ frequency response. In this case, the sinusoidal voltage perturbation $\delta \hat{U}_{ref}$ added to $\hat{U}_{ref}$ had an amplitude of 2 V. The results of the validation tests are illustrated in Figure 3.16. In these tests, an operating point characterized by $\hat{U}_{ref} = 1$ pu and $P_{ref} = 0.8$ pu has been considered. Based on the shown results, a substantial accuracy of the outer loops small-signal models has been verified.

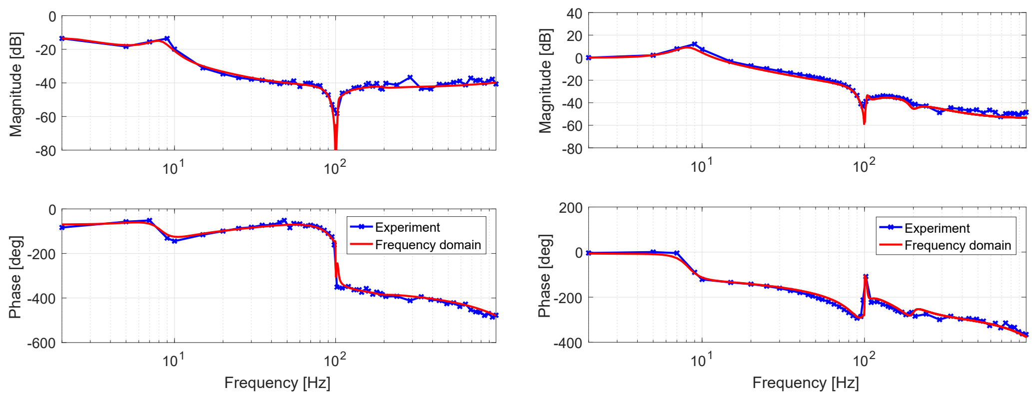

(a) $G_P(j2\pi f)$ (b) $G_V(j2\pi f)$

Figure 3.16: Comparison between the frequency responses of the closed loop transfer functions of the outer loops of the built laboratory prototype inverter-grid interface described in Section 2.3.2.3. The results obtained with the FD model are compared to the experimental data.

3.3 Chapter Summary

The theory used to derive a dq-frame small-signal model of the inverter-grid system discussed in Chapter 2 has been presented. Among the methodologies described to represent each element of the modelled system in the positive dq-frame, emphasis has been given on the technique used for the negative sequence current controller. The accuracy of the applied theory has been verified experimentally making use of the built scaled-down laboratory prototype of the studied system.

Chapter 4

Impedance-based stability study

Based on the theory described in Chapter 3, a small-signal model of the studied wind farm-grid system has been derived. This has been used to carry out the study of its stability applying the methodology presented in this Chapter.

As discussed in Section 2.2.1, the implementation of the controller in the *dq*-frame is advantegous for the controller design, especially as it allows to exploit the capability of PI regulators to track constant reference signals [58]. The applied converter control scheme shown in Figure 2.20 results in a MIMO small-signal model of the inverter-grid interface. This makes the study of its stability performance a complex task, especially because of the existing coupling between the *d*- and *q*-axis feedback control loops (see Figures 2.20 and 3.13). Taking inspiration from the impedance-based stability criterion [54], the so-called sequence-frame, which will also be named *pn*-frame in the following Sections, has been chosen to study the system stability. The used approach requires a representation of the inverter-grid interface small-signal model in terms of electrical impedances defined in the sequence-frame. The inverter is modelled as a controlled current source and is therefore represented by its Norton equivalent, while the grid is described in terms of its Thévenin equivalent (see Figure 4.1) [54]. The advantage of such impedance based stability study is the possibility of applying SISO control theory, thanks to the substantial decoupling between the positive and the negative sequence impedances of the circuit in Figure 4.1b. This enables to consider the resulting sequence-frame second order MIMO small-signal model of the system as two decoupled

SISO models, and, therefore, to use well-known tools such as the gain and the phase margin to assess the system relative stability [79], [55], [54].
In order to apply this methodology, a technique is needed to describe the converter dynamics in the sequence-frame. This has been done by making use of the definition of the small-signal converter admittance [54]. Such admittance is the output small-signal admittance of the inverter and includes the line reactor connected in series to its AC terminals (Z_f in Figure 4.1). It allows to quantify the effect of the converter controller on the measured voltage U and current i signals.

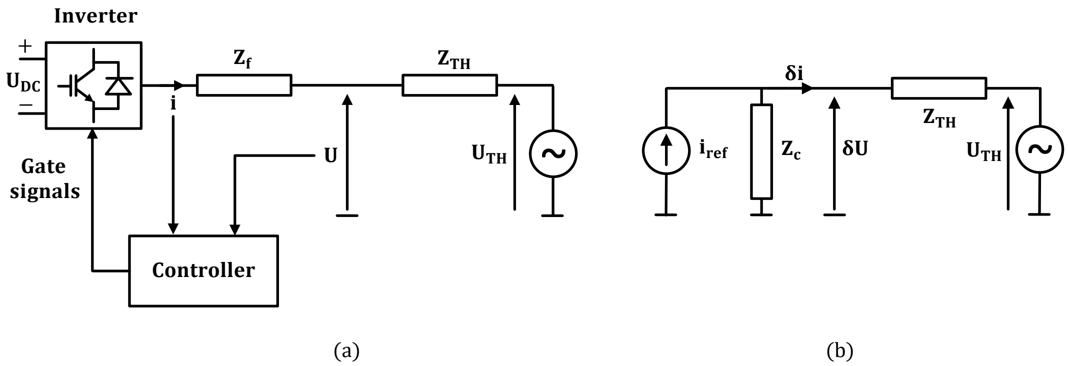

Figure 4.1: (a) Inverter-grid interface. (b) Equivalent small-signal circuit representation, used for the stability study.

In the applied methodology, the small-signal converter admittance has been first calculated in the dq-frame an then mapped onto the sequence-frame. By doing so, it has been possible to build the desired link between the dq-frame, where the controller is implemented, and the pn-frame, where stability is studied. It is worth highlighting that the equations used in this work to express the dq-frame small-signal admittance (or impedance) in the sequence-frame differ from similar formula published in the literature, which instead relate the dq-frame small-signal converter admittance either to its modified sequence-frame [60] or to its $\alpha\beta$-frame [97] formulations.
The employed equations allow a systematic calculation not only of the positive and the negative sequence terms of the small-signal converter admittance, but also of the coupling existing between them. Such coupling results from the converter controller

action on the measured voltage U and current i signals. In [60], how this coupling is related to any asymmetry in the d- and q- axes control loops, for instance caused by the PLL loop, or the voltage/power (outer) loops or the DC link voltage controller, is highlighted.

The system is said to be Mirror Frequency Decoupled (MFD) when there is a perfect symmetry between the d- and q- axes control loops, which results in zero coupling terms in the small-signal converter admittance [60]. In the carried out study, such MFD property of the inverter-grid interface system has been investigated for different controller schemes.

Despite the fact that these coupling terms are assumed negligible and therefore ignored in the impedance-based stability criterion [54], they have been of interest in the literature. Significant results have been found in [13], where it is shown that neglecting these coupling terms can lead to a wrong stability assessment when the PLL bandwidth is increased. Hence, by making use of the defined small-signal converter admittance, a stability study systematic methodology, which includes the mentioned coupling terms, has been defined. The method has been applied to the study of the wind farm resonances and its accuracy has been verified experimentally.

The impact of the cross-coupling terms on the stability assessment of the system has been further investigated, evaluating the property of diagonal dominance of the inverter-grid system in the sequence-frame [93]. A criterion capable of indicating whether such coupling is relevant or not to the stability analysis is presented. It indicates how the verification of the diagonal dominant property of the system is essential to justify the omission of the aforementioned coupling terms in the application of the impedance-based stability criterion [54]. A scenario where the inverter is connected to a weak grid and the diagonal dominance property is not verified is presented, proving, both analytically and experimentally, how in this circumstance the coupling terms should be taken into account for a correct judgement of the system stability.

Thereafter, by exploiting the mentioned diagonal dominance property of the system, a stability margin definition based on perturbation theory is introduced [63]. Compared to the SISO gain and phase margins, which require to neglect the coupling terms of the converter admittance, the presented stability margin takes such coupling into account, thus providing a safer and more conservative evaluation of the system stability robustness.

The Chapter is organised as follows. In Section 4.1, the methodology to calculate the small-signal converter admittance in the sequence-frame is described. In particular, in Section 4.1.3, a validation of this method is provided, experimentally proving its effectiveness regardless of the applied converter control schemes, and thus confirming the generality of its use. In these tests, specifically designed controller configurations have been considered to verify the MFD property of the system in the sequence-frame. In Section 4.2, how the small-signal converter admittance is used to carry out the stability study of the system is illustrated. A systematic technique to study the system stability, which includes the mentioned coupling in the small-signal converter admittance, is presented and applied to the analysis of the wind farm resonances. The results of the study are validated both against those obtained with the corresponding TD model of the wind farm-grid system, and against experimental data obtained with the built laboratory prototype where the investigated unstable dynamics have been reproduced. In Section 4.3, the study of the diagonal dominance property of the system in the sequence-frame is presented and used to infer whether the coupling terms of the small-signal converter admittance should be included or not in the stability study. The theoretical analysis is validated experimentally by considering the scenario of the built inverter prototype connected to a weak grid, with the outer active power and voltage regulators included in the control scheme. Finally, in Section 4.4, a stability margin which takes such coupling terms into account is introduced. Its effectiveness to quantify the relative stability of the system is validated experimentally and compared to that of the SISO stability margins used in the impedance-based stability criterion.

4.1 Calculation of the small-signal converter admittance

The small-signal converter admittance is calculated based on the small-signal model of the converter controller, whose dynamics are linearised at an operating point. This admittance also includes the coupling reactor interfacing the inverter to the rest of the electrical system.

The small-signal converter admittance is defined as the transfer function $Y_C(s)$ from the small-signal voltage $\delta U(s)$ to the small-signal inverter current $\delta i(s)$ (see Figure 4.2 where U_0 and i_0 represent the steady-state values of U and i, at the system operating point):

$$Y_C(s) = -\frac{\delta i(s)}{\delta U(s)} \tag{4.1}$$

It is pointed out that in (4.1), the current signal is taken to be positive when flowing out of the inverter AC terminals.

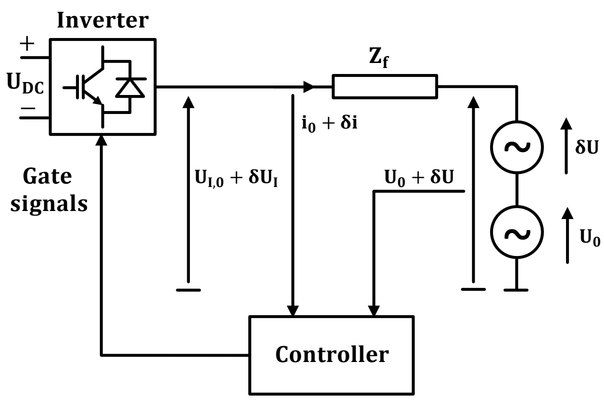

Figure 4.2: Schematic diagram for the calculation of the converter impedance.

The converter admittance is first calculated in the dq-frame and then mapped onto the pn-frame. These calculations will be discussed in the following Sections 4.1.1 and 4.1.2, respectively.

4.1.1 Converter admittance in the dq-frame

In order to calculate the dq-frame small-signal converter admittance $Y_{C,DQ}(s)$, the small-signal model of the inverter electrical system in Figure 4.2 is derived, where the control scheme is the one in Figure 2.20. The derivation of the dq-frame small-signal state-space representation of such inverter electrical system is reported in Appendix C.1.4. Thereby, the analytical expression of the small-signal converted admittance

$Y_{C,DQ}(s)$ is calculated as the closed-loop transfer function from $\delta\hat{U}^+_{dq}(s)$ to $-\delta\hat{i}^+_{dq}(s)$ (see Figure C.5 where these signals have been marked in red):

$$Y_{C,DQ}(s) = -\frac{\delta\hat{i}^+_{dq}(s)}{\delta\hat{U}^+_{dq}(s)} = \begin{bmatrix} Y_{C,dd}(s) & Y_{C,dq}(s) \\ Y_{C,qd}(s) & Y_{C,qq}(s) \end{bmatrix} \tag{4.2}$$

where $\delta\hat{i}^+_{dq}(s) = \mathcal{L}\{\delta\hat{i}^+_{dq}(t)\}$ and $\delta\hat{U}^+_{dq}(s) = \mathcal{L}\{\delta\hat{U}^+_{dq}(t)\}$.

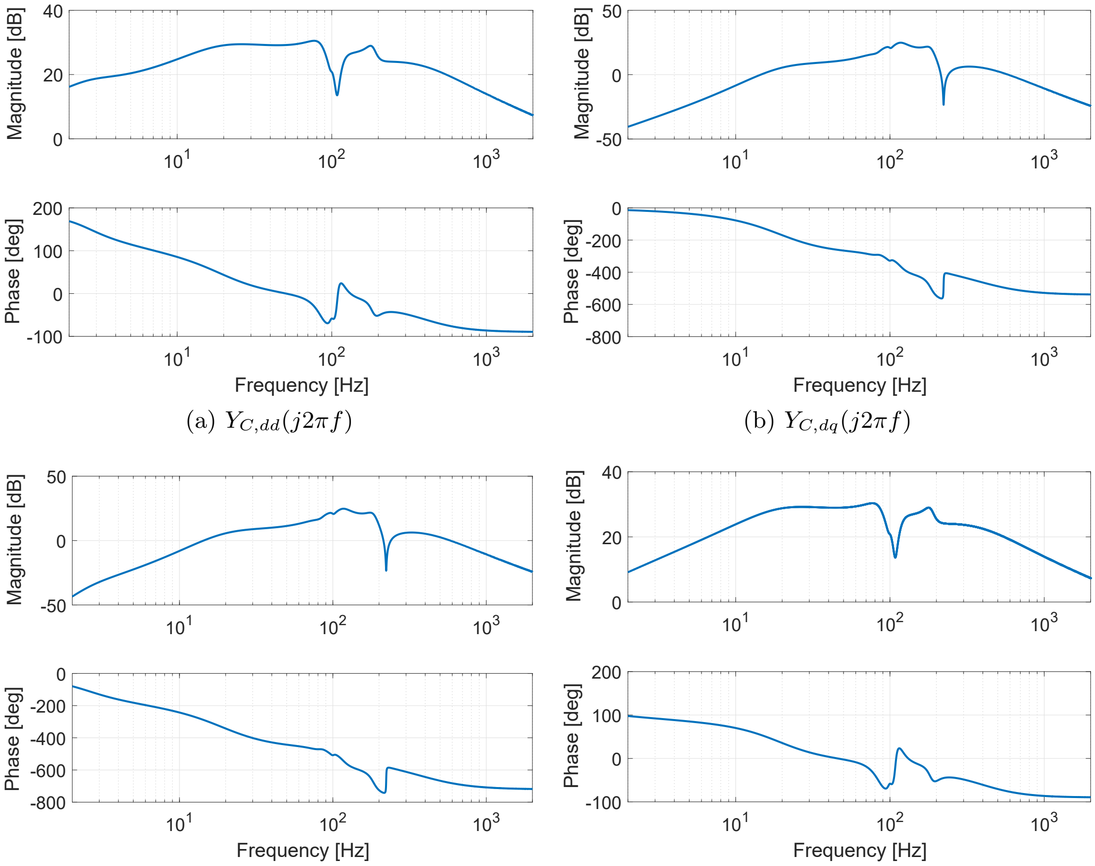

(a) $Y_{C,dd}(j2\pi f)$ (b) $Y_{C,dq}(j2\pi f)$

(c) $Y_{C,qd}(j2\pi f)$ (d) $Y_{C,qq}(j2\pi f)$

Figure 4.3: Frequency responses of the four elements of the $Y_{C,DQ}(j2\pi f)$ matrix calculated for the inverter modelled in the turbine-grid interface described in Section 2.1.3.

Figure 4.3 shows the calculated frequency responses of the admittance terms of the $Y_{C,DQ}(s)$ matrix calculated for the inverter modelled in the turbine-grid interface described in Section 2.1.3. These terms have been calculated for an operating point characterized by $i^+_{q,ref} = 2000$ A, $i^+_{d,ref} = i^-_{q,ref} = i^-_{d,ref} = 0$ A. It is worth noticing how the diagonal terms $Y_{C,dd}(j2\pi f)$ and $Y_{C,qq}(j2\pi f)$ demonstrate inductive characteristics at higher frequencies and how significant the amplitude of the cross coupling terms $Y_{C,dq}(j2\pi f)$ and $Y_{C,qd}(j2\pi f)$ is within the frequency range of the controller bandwidth (i.e. at frequencies less than 200 Hz).

In the following Section the methodology used to map $Y_{C,DQ}(s)$ onto the sequence-frame is described.

4.1.2 Converter admittance in the *pn*-frame

The methodology used to derive the *pn*-frame small-signal converter admittance terms from its *dq*-frame formulation is based on the application of a set of equations. Compared to alternative techniques presented in the literature, see for example [55], [13], this method is applicable in a systematic way, regardless of the converter controller scheme.

The transformations that map three-phase electrical signals from one mathematical frame to another are summarised in Figure 4.4 [99], [100] together with the related frames.

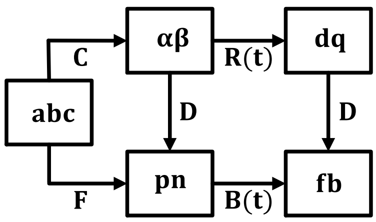

Figure 4.4: Diagram of the standard frames employed to describe three-phase electrical signals analytically, and matrix transformations relating one frame to the other.

In particular, C is the Clarke transform defined in (B.8), $R(t)$ is the rotation matrix formulated in (B.15), F is the Fortescue transform [101], whose definition is given in (C.63). Finally, the $B(t)$ and D transformations are defined in (C.44) and (C.45), respectively [99].

The *pn*-frame small-signal admittance terms are related to the elements of the matrix

$Y_{C,DQ}(s)$ in (4.2) as:

$$\begin{aligned}
Y_{C,pp}(s) &= \frac{1}{2}[Y_{C,qq}(s-j\omega_0) - jY_{C,dq}(s-j\omega_0) + jY_{C,qd}(s-j\omega_0) + Y_{C,dd}(s-j\omega_0)],\\
Y_{C,pn}(s) &= \frac{1}{2}[Y_{C,qq}(s-j\omega_0) - jY_{C,dq}(s-j\omega_0) - jY_{C,qd}(s-j\omega_0) - Y_{C,dd}(s-j\omega_0)],\\
Y_{C,np}(s) &= \frac{1}{2}[Y_{C,qq}(s+j\omega_0) + jY_{C,dq}(s+j\omega_0) + jY_{C,qd}(s+j\omega_0) - Y_{C,dd}(s+j\omega_0)],\\
Y_{C,nn}(s) &= \frac{1}{2}[Y_{C,qq}(s+j\omega_0) + jY_{C,dq}(s+j\omega_0) - jY_{C,qd}(s+j\omega_0) + Y_{C,dd}(s+j\omega_0)]
\end{aligned} \tag{4.3}$$

Moreover, the following equations relate the $\delta i_{pn}(s)$ and $\delta U_{pn}(s)$ signals:

$$\begin{aligned}
\delta i_p(s) &= -Y_{C,pp}(s)\delta U_p(s) - Y_{C,pn}(s)\delta U_n(s-2j\omega_0)\\
\delta i_n(s) &= -Y_{C,np}(s)\delta U_p(s+2j\omega_0) - Y_{C,nn}(s)\delta U_n(s)
\end{aligned} \tag{4.4}$$

which can be rewritten in a matrix format as:

$$\begin{aligned}
\begin{bmatrix} \delta i_p(s) \\ \delta i_n(s-2j\omega_0) \end{bmatrix} &= -Y_{C,PN}(s) \begin{bmatrix} \delta U_p(s) \\ \delta U_n(s-2j\omega_0) \end{bmatrix}\\
&= -\begin{bmatrix} Y_{C,pp}(s) & Y_{C,pn}(s) \\ Y_{C,np}(s-2j\omega_0) & Y_{C,nn}(s-2j\omega_0) \end{bmatrix} \begin{bmatrix} \delta U_p(s) \\ \delta U_n(s-2j\omega_0) \end{bmatrix}
\end{aligned} \tag{4.5}$$

$Y_{C,PN}(s)$ represents the *pn*-frame small-signal converter admittance matrix and the terms $Y_{C,pp}(s)$, $Y_{C,pn}(s)$, $Y_{C,np}(s)$ and $Y_{C,nn}(s)$ are the *pn*-frame small-signal converter admittance terms.

The derivation of equations (4.3)-(4.4) can be found in Appendix C.3.

It is worth noticing that (4.3)-(4.4) have been derived without making any assumption on the terms of the $Y_{C,DQ}(s)$ matrix. In this regard, such equations are generic and can therefore be applied for any arbitrarily defined *dq*-frame small-signal converter admittance matrix. This implies that such methodology to map the small-signal converter admittance from the *dq*- to the *pn*-frame is applicable regardless of the converter controller scheme.

It is worth mentioning that swapping the roles between voltage and current in (C.48), analogous relations equivalent to (4.3)-(4.4) can be formulated in terms of the small-signal converter impedance terms.

Equations (4.4) indicate that the input-output relationship between $\delta i_{pn}(s)$ and $\delta U_{pn}(s)$ is not decoupled in the *pn*-frame owing to the presence of the cross-coupling terms $Y_{C,pn}(s)$ and $Y_{C,np}(s)$. Such coupling between the positive and negative sequence signals involves a frequency shift of $\pm 2f_0$, with $f_0 = \frac{\omega_0}{2\pi}$. While a positive sequence small-signal voltage at frequency $\hat{f}$ generates a small-signal current signal with both a positive sequence component at $\hat{f}$ and a negative sequence component at $\hat{f} - 2f_0$, a negative sequence small-signal voltage at $\hat{f}$ gives rise to a small-signal current with both a negative sequence component at $\hat{f}$ and a positive sequence component at $\hat{f} + 2f_0$.

The particular case when such coupling effect disappears is when the converter controller is designed so that $Y_{C,qq}(s) = Y_{C,dd}(s)$ and $Y_{C,qd}(s) = -Y_{C,dq}(s)$, which requires the *d*- and *q*-axis control loops of the converter controller to be symmetric. Such a symmetric system is said to be Mirror Frequency Decoupled (MFD), according to the definition provided in [60]. While the MFD property of the inverter controller is broken by elements such as the PLL loop, the outer power and voltage regulators or the the DC link controller, standard tuning of these loops typically makes the cross-coupling terms $Y_{C,pn}(s)$ and $Y_{C,np}(s)$ have a sigificantly smaller magnitude than that of the $Y_{C,pp}(s)$ and $Y_{C,nn}(s)$ terms. This typically justifies the decision to neglect them in the application of the impedance based-stability criterion [54].

A more in depth analysis of these coupling terms and, in particular of how they impact the stability study is presented in Section 4.3, where a criterion to infer whether such coupling is relevant or not to the stability assessment of the system is presented. This is based on the analysis of the diagonal dominance property of the inverter-grid system in the sequence-frame.

4.1.3 Validation of the methodology

A validation of the presented methodology to map the converter admittance from the *dq*- to the *pn*-frame is presented as follows. In Section 4.1.3.1, the *pn*-frame small-signal converter admittance terms derived from the TD model of the turbine-grid system described in Section 2.1.3 are compared to the corresponding terms calculated with (4.3)-(4.4). Thereafter, in Section 4.1.3.2, an experimental validation of these equations is provided. By making use of the built laboratory prototype, specifically designed tests have been carried out both to prove the general applicability of (4.3)-(4.4), and to verify the conditions that make the system MFD.

4.1.3.1 Validation against time-domain simulations

The *pn*-frame small-signal converter admittance terms of the inverter system modelled in Section 2.1.3 have been calculated with equations (4.3)-(4.4), applying the methodology described in Section 4.1. The frequency responses of these admittance terms have been compared to those derived from time-domain simulations of the TD model of such inverter system.

In order to derive the $Y_{C,pp}(j2\pi f)$ and $Y_{C,np}(j2\pi(f-2f_0))$ terms from the inverter interface TD model, a small-signal positive sequence voltage $\delta U^+(t)$ has been added to $U_0(t)$ (see Figure 4.2), where $U_0(t)$ is:

$$\begin{aligned} U_{0,a}(t) &= U^+_{S_q,0} cos(2\pi f_0 t) \\ U_{0,b}(t) &= U^+_{S_q,0} cos(2\pi f_0 t - \frac{2}{3}\pi) \\ U_{0,c}(t) &= U^+_{S_q,0} cos(2\pi f_0 t - \frac{4}{3}\pi) \end{aligned} \tag{4.6}$$

$U^+_{S_q,0}$ is the voltage at the system operating point. In particular, the operating point characterized by $i^+_{q,ref} = 2000$ A, $i^+_{d,ref} = i^-_{q,ref} = i^-_{d,ref} = 0$ has been considered in this validation test. The added voltage perturbation has been defined as:

$$\begin{aligned} \delta U^+_a(t) &= \delta U_0 cos(2\pi f_p t) \\ \delta U^+_b(t) &= \delta U_0 cos(2\pi f_p t - \frac{2}{3}\pi) \\ \delta U^+_c(t) &= \delta U_0 cos(2\pi f_p t - \frac{4}{3}\pi) \end{aligned} \tag{4.7}$$

where δU_0 is the amplitude of the small-signal perturbation, while f_p is its frequency. The corresponding deviation $\delta i(t)$ on the steady-state inverter current $i_0(t)$ has been considered and its spectral components have been analysed. These consisted of a positive sequence component $\delta i^{+}_{pp}(j2\pi f_p)$ and of a negative sequence component $\delta i^{-}_{np}(j2\pi(f_p-2f_0))$. Thereby, $Y_{C,pp}(j2\pi f_p)$ and $Y_{C,np}(j2\pi(f_p-2f_0))$ have been calculated as:

$$\begin{aligned} Y_{C,pp}(j2\pi f_p) &= \frac{|\delta i^{+}_{pp,a}(j2\pi f_p)|}{\delta U_0}\angle\delta i^{+}_{pp,a}(j2\pi f_p) \\ Y_{C,np}(j2\pi(f_p-2f_0)) &= \frac{|\delta i^{-}_{np,a}(j2\pi(f_p-2f_0))|}{\delta U_0}\angle\delta i^{-}_{np,a}(j2\pi(f_p-2f_0)) \end{aligned} \tag{4.8}$$

Similarly, in order to calculate the $Y_{C,nn}(j2\pi f)$ and $Y_{C,pn}(j2\pi(f+2f_0))$ terms, a small-signal negative sequence voltage $\delta U^{-}(t)$ has been added to $U_0(t)$, defined as:

$$\begin{aligned} &\delta U^{-}_a(t) = \delta U_0 cos(2\pi f_p t) \\ &\delta U^{-}_b(t) = \delta U_0 cos(2\pi f_p t + \frac{2}{3}\pi) \\ &\delta U^{-}_c(t) = \delta U_0 cos(2\pi f_p t + \frac{4}{3}\pi) \end{aligned} \tag{4.9}$$

In this case, the corresponding deviation $\delta i(t)$ on the inverter current consisted of a negative sequence component $\delta i^{-}_{nn}(j2\pi f_p)$ and of a positive sequence component $\delta i^{+}_{pn}(j2\pi(f_p+2f_0))$. Thereby, $Y_{C,nn}(j2\pi f_p)$ and $Y_{C,pn}(j2\pi(f_p+2f_0))$ have been calculated as:

$$\begin{aligned} Y_{C,nn}(j2\pi f_p) &= \frac{|\delta i^{-}_{nn,a}(j2\pi f_p)|}{\delta U_0}\angle\delta i^{-}_{nn,a}(j2\pi f_p) \\ Y_{C,pn}(j2\pi(f_p+2f_0)) &= \frac{|\delta i^{+}_{pn,a}(j2\pi(f_p+2f_0))|}{\delta U_0}\angle\delta i^{+}_{pn,a}(j2\pi(f_p+2f_0)) \end{aligned} \tag{4.10}$$

These time domain simulations have been repeated for f_p varying in the [1 Hz, 2 kHz] range, thus carrying out a frequency sweep test. This allowed the derivation of the TD model frequency responses $Y_{C,pp}(j2\pi f)$, $Y_{C,pn}(j2\pi(f+2f_0))$, $Y_{C,np}(j2\pi(f-2f_0))$, $Y_{C,nn}(j2\pi f)$.

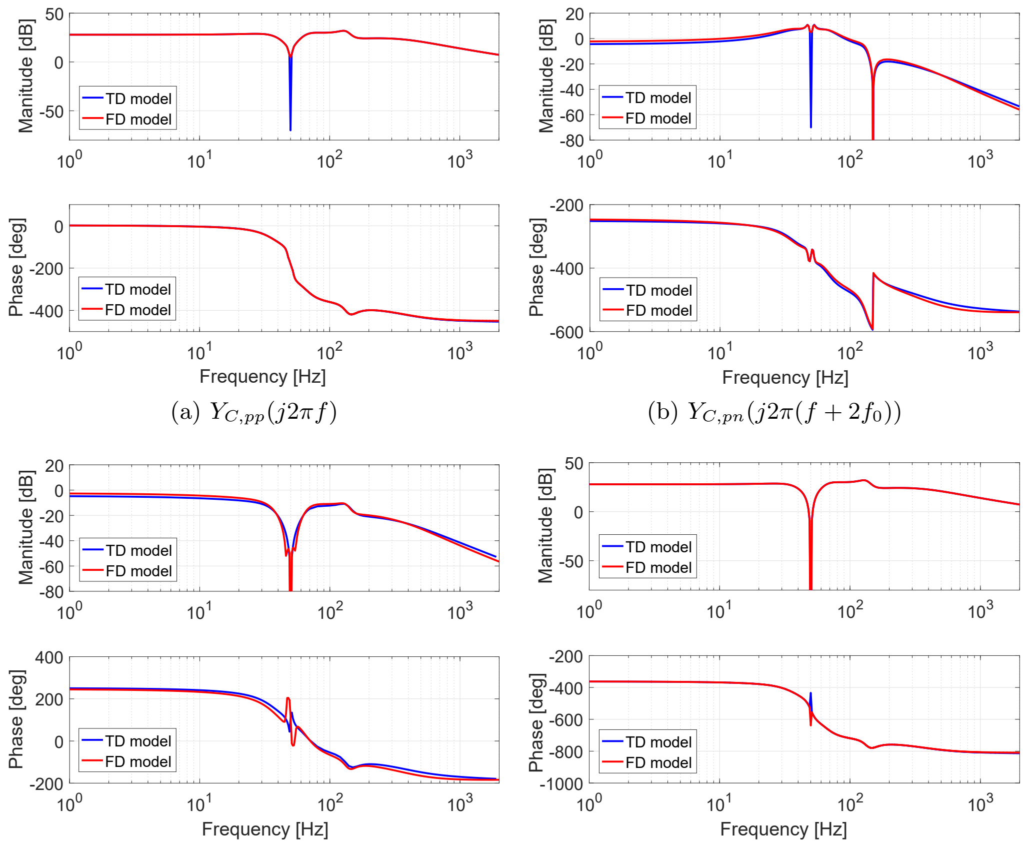

(a) $Y_{C,pp}(j2\pi f)$ (b) $Y_{C,pn}(j2\pi(f+2f_0))$

(c) $Y_{C,np}(j2\pi(f-2f_0))$ (d) $Y_{C,nn}(j2\pi f)$

Figure 4.5: Frequency responses of the small-signal converter admittance terms of $Y_{C,PN}(s)$, for the inverter interface modelled in Section 2.1.3. A comparison is shown between the results calculated with (4.3) and those derived from time domain simulations of the corresponding inverter interface TD model.

Figure 4.5 compares such results with those calculated with (4.3)-(4.4), which are based on the small-signal model of the inverter interface. As it can be seen, similarly to the dq-frame admittance terms $Y_{C,dd}(s)$ and $Y_{C,qq}(s)$, the pn-frame diagonal terms $Y_{C,pp}(s)$ and $Y_{C,nn}(s)$ also show an inductive nature in the higher frequency range, which is attributed to the presence of the coupling reactor Z_f. It is noticed how the magnitude of the pn-frame coupling terms $Y_{C,pn}(j2\pi(f+2f_0))$ and $Y_{C,np}(j2\pi(f-2f_0))$ is much smaller than that of the dq-frame coupling terms $Y_{dq}(j2\pi f)$ and $Y_{qd}(j2\pi f)$ (see Figure 4.3), in line with the studies presented in [54], [60], [13].

4.1.3.2 Validation against experimental data

In order to validate equations (4.3-4.4) experimentally, a series of tests have been carried out making use of the built laboratory inverter prototype. These tests have been designed both to illustrate how such equations can be applied effectively regardless of the employed converter control scheme and to investigate the MFD property of the system [60]. In all of these tests, the inverter has been connected to a resistive load, according to the electrical diagram shown in Figure 2.26. Different control schemes have been tested, which are based on the block diagram shown in Figure 2.20. As in these tests the inverter is not connected to the grid, the PLL loop has been disabled and the controller angle $\theta(t)$ has been calculated with (E.28). The used system parameters are those detailed in Table 2.7. The derived *pn*-frame small-signal frequency response admittance matrix $Y_{m,PN}(2j\pi f)$ is that resulting from the series combination of the converter and the load admittances, and has the following matrix format, which is based on (4.5):

$$Y_{m,PN}(2j\pi f) = \begin{bmatrix} Y_{m,pp}(2j\pi f) & Y_{m,pn}(2j\pi f) \\ Y_{m,np}(2j\pi(f-2f_0)) & Y_{m,nn}(2j\pi(f-2f_0)) \end{bmatrix} \tag{4.11}$$

It is emphasized how equations (4.3-4.4) are valid for any small-signal admittance definable within the electrical system. This justifies why the experimental tests have been carried out for the admittance matrix (4.11), rather than considering the small-signal converter admittance $Y_{C,PN}(s)$ defined in (4.5). In fact, as a matter of fact, with the equipment available in the used laboratory set-up, it was not possible to derive $Y_{C,PN}(s)$ experimentally.

In order to calculate the analytical expression of (4.11), the methodology described in Section 4.1 has been applied. The small-signal model of the built prototype has been derived based on the method discussed in Chapter 3. Thereby, the frequency response of the *dq*-frame small-signal admittance matrix $Y_{m,DQ}(2j\pi f)$ has been obtained from the closed-loop transfer function $Y_{m,DQ}(s)$ from $\delta\hat{U}^+_{I_{dq}}(s)$ to $\delta i^+_{dq}(s)$ (see Figure 3.13), setting $s = j2\pi f$:

$$Y_{m,DQ}(j2\pi f) = \frac{\delta i^{+}_{dq}(j2\pi f)}{\delta \hat{U}^{+}_{I_{dq}}(j2\pi f)} = \begin{bmatrix} Y_{m,dd}(j2\pi f) & Y_{m,dq}(j2\pi f) \\ Y_{m,qd}(j2\pi f) & Y_{m,qq}(j2\pi f) \end{bmatrix} \tag{4.12}$$

It is worth mentioning that in the small-signal model used in this calculation, the plant state-space model has been derived based on (C.17). Finally, the corresponding *pn*-frame terms of $Y_{m,PN}(j2\pi f)$ have been calculated based on equations (4.3)-(4.4). The same terms have been derived experimentally according to the procedure described in Appendix E.3, which is summarised as follows. A positive/negative sequence small-signal three-phase perturbation has been added to the *abc*-frame PWM modulation functions of the converter. Such modulation functions represent the reference signals of the applied SVM modulation technique [73], and are calculated by the controller algorithm as described in Appendix A. The frequency of the added perturbation has been varied in the [5 Hz, 990 Hz] range, thus carrying out a frequency sweep test. In each iteration of the test, the small-signal perturbation has been applied for 1s whilst the system is at steady-state and, simultaneously, the corresponding measured converter current i has been recorded locally in the control board. As a PWM asymmetrical sampling technique has been used in these tests, with a converter switching frequency of 2.5 kHz, the i data recorded during each iteration of the test is composed of 5000 samples. Thereafter, such recorded data has been exported into MATLAB to analyse their spectral composition. In particular, by having 5000 current samples for each test iteration, sampled at 5 kHz, the frequency spectrum of the collected data has been calculated with a resolution of 1 Hz. The results of the carried out spectral analysis have allowed the calculation of the experimental *pn*-frame small-signal admittance frequency response $Y_{m,PN}(2j\pi f)$.

Three different scenarios have been tested, each having a different controller scheme, as detailed in Table 4.1. It is worth mentioning that in scenario 1, as only the positive sequence controller is active, the notch filters in the controller block diagram in Figure 2.20, which have been used to decouple the positive and the negative sequence components of the measured plant signals, have been disabled.

Table 4.1: Tested controller configurations.

Scenario	Positive sequence current loop	Negative sequence current loop	Power loop
1	Included	Not included	Not included
2	Included	Included	Not included
3	Included	Included	Included

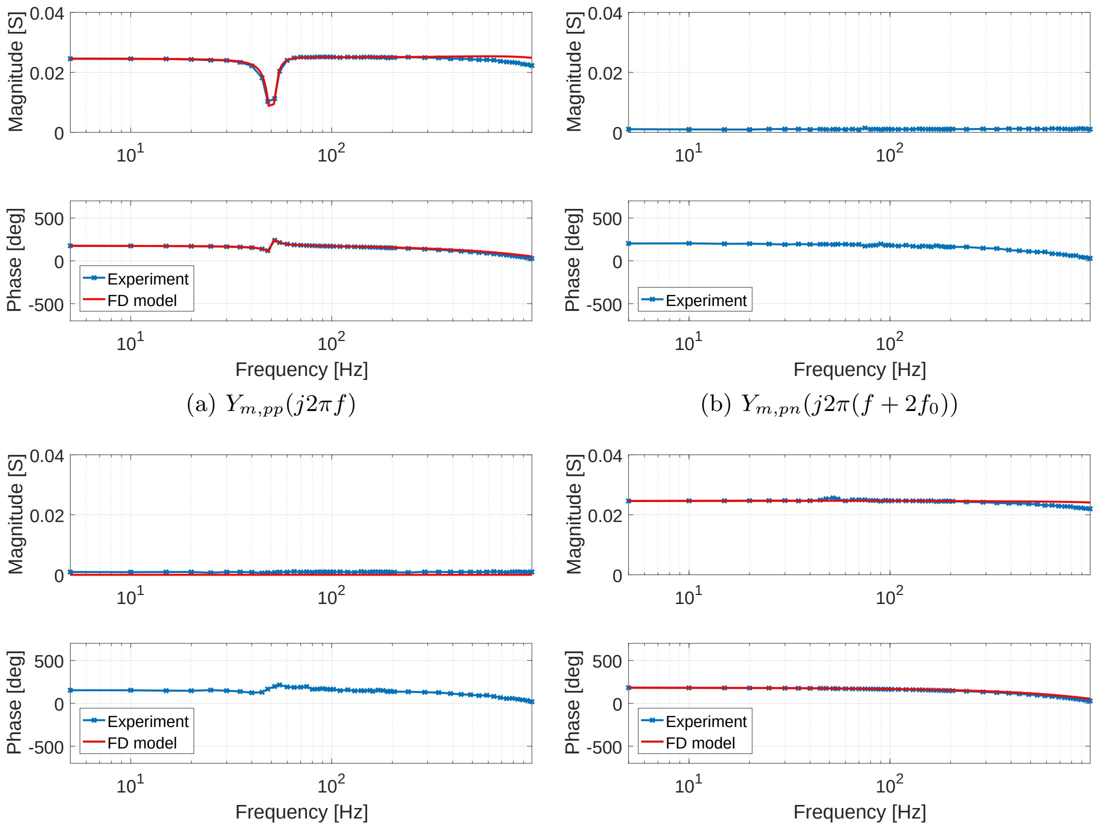

(a) $Y_{m,pp}(j2\pi f)$ (b) $Y_{m,pn}(j2\pi(f+2f_0))$

(c) $Y_{m,np}(j2\pi(f-2f_0))$ (d) $Y_{m,nn}(j2\pi f)$

Figure 4.6: Admittance terms of $Y_{m,PN}(j2\pi f)$ (scenario 1).

In scenarios 1 and 2, an operating point characterized by $i^+_{q,ref} = 2$ A, $i^+_{d,ref} = i^-_{q,ref} = i^-_{d,ref} = 0$ A has been chosen, while in scenario 3 an operating point determined by $P_{ref} = 200$ W has been tested, keeping $i^+_{d,ref}$, $i^-_{q,ref}$ and $i^-_{d,ref}$ equal to zero. In Figures 4.6-4.8 the experimental results are compared with those obtained from the built small-signal model of the system, for scenarios 1-3 respectively. The plots indicate an overlap between the theoretical calculations and experimental data, hence confirming the accuracy of the applied methodology, as well as the generality of its use.

In both scenarios 1 and 2, if it assumed that the plant impedances are balanced then the system becomes MFD, as the d- and q- axis control loops are symmetric [60]. In fact, under these conditions, $Y_{m,dq}(s) = -Y_{m,qd}(s)$ and $Y_{m,dd}(s) = Y_{m,qq}(s)$, making $Y_{m,pn}(s) = Y_{m,np}(s) = 0$ (see equations (4.4)). However, non-zero coupling terms were measured, with an amplitude of about 1 mS across the whole range of considered frequencies (see Figure 4.6b, 4.6c, 4.7b and 4.7c where the cross-coupling terms calculated by the small-signal model are not shown and equal to 0). This discrepancy between the theoretical and the experimental results is attributed to a small imbalance in the plant impedances of the laboratory test rig as well as to measurement tolerances.

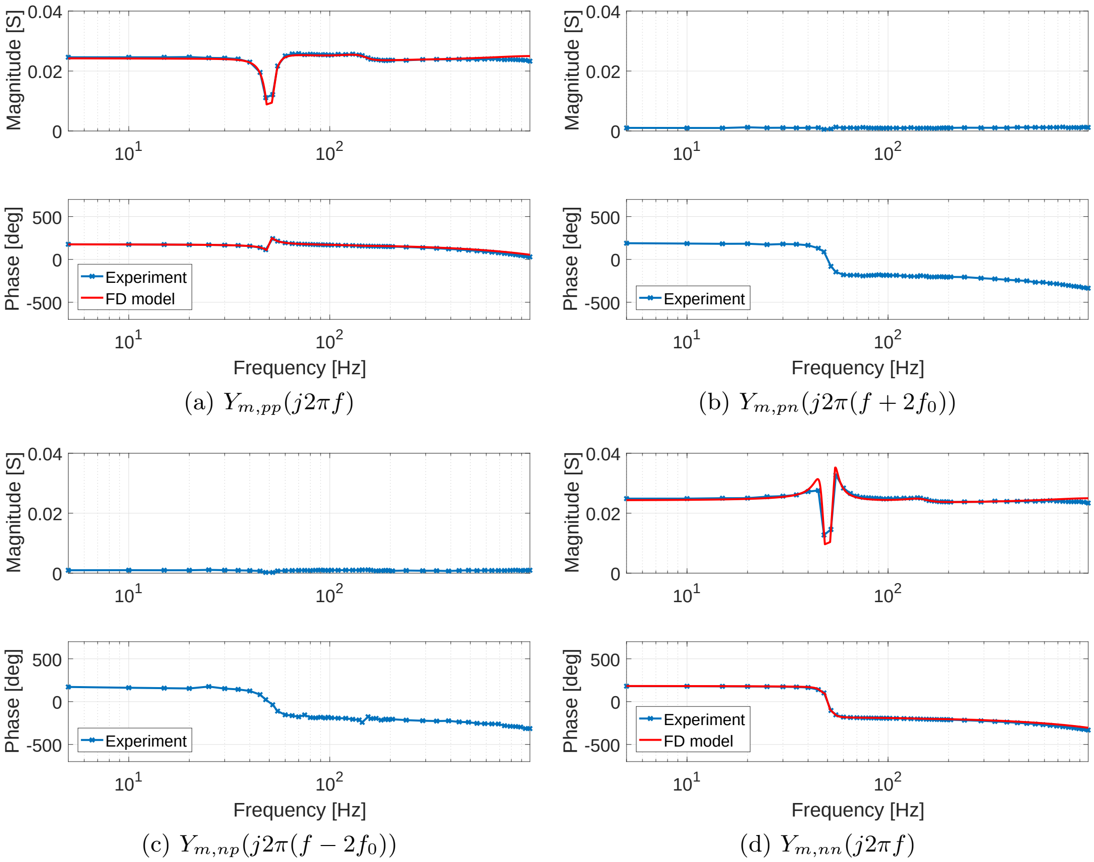

(a) $Y_{m,pp}(j2\pi f)$

(b) $Y_{m,pn}(j2\pi(f + 2f_0))$

(c) $Y_{m,np}(j2\pi(f - 2f_0))$

(d) $Y_{m,nn}(j2\pi f)$

Figure 4.7: Admittance terms of $Y_{m,PN}(j2\pi f)$ (scenario 2).

Comparing the results from these 2 scenarios, it can be seen that the effect of the negative sequence current controller is mainly observed in the negative sequence admittance term $Y_{m,nn}(j2\pi f)$, with its magnitude being strongly reduced at frequencies close to 50 Hz in scenario 2 (see Figure 4.7d), while revealing a substantially constant trend in scenario 1 (see Figure 4.6d).

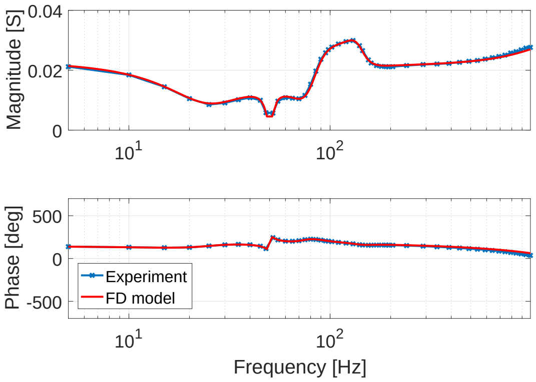

(a) $Y_{m,pp}(j2\pi f)$

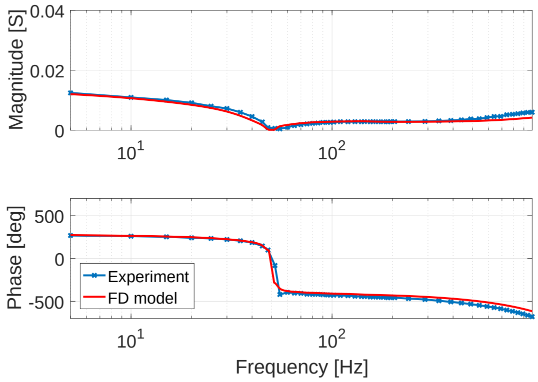

(b) $Y_{m,pn}(j2\pi(f+2f_0))$

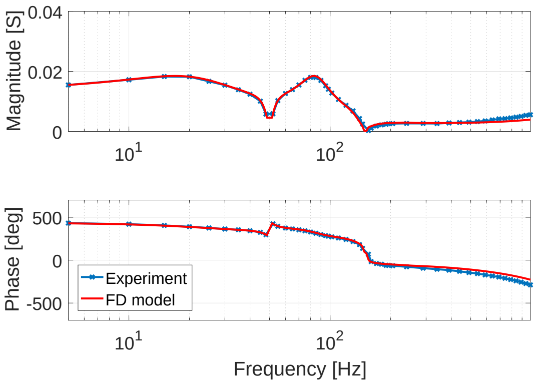

(c) $Y_{m,np}(j2\pi(f-2f_0))$

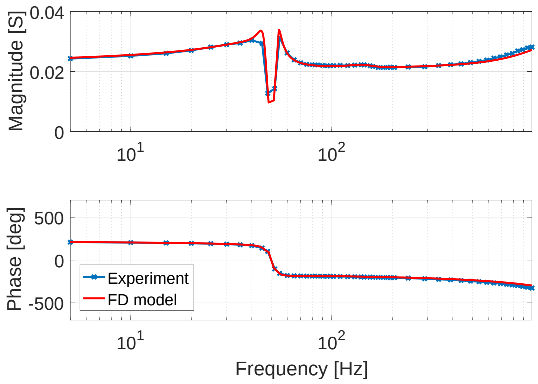

(d) $Y_{m,nn}(j2\pi f)$

Figure 4.8: Admittance terms of $Y_{m,PN}(j2\pi f)$ (scenario 3).

In scenario 3 the dq-symmetry of the controller has been broken by the activated power regulator, as this only operates on the q^+ control loop. Thereby, the system is no longer MFD, as confirmed by the larger magnitude of the coupling terms $Y_{m,pn}(j2\pi(f+2f_0))$ and $Y_{m,np}(j2\pi(f-2f_0))$ (see Figures 4.8b and 4.8c). In addition to this, comparing scenario 3 with scenarios 1 and 2, the impact of the power loop is mostly observable on the $Y_{m,pp}(j2\pi f)$ positive sequence term (as a result of its action being confined to the q^+ axis control loop).

4.2 Impedance based stability analysis

The *pn*-frame small-signal converter admittance calculated with the technique described in Section 4.1 has been used to assess the stability of the converter-grid system applying an impedance-based approach inspired by [54]. Thanks to the technique used to calculate the *pn*-frame small-signal converter admittance, the coupling terms of such admittance have been taken into account in the used stability study, unlike the method in [54].

The technique is based on the representation of the small-signal model of the converter-grid interface as an electrical circuit. The converter is modelled as a current source represented by its Norton equivalent, while the grid is described in terms of its Thévenin equivalent. Such circuit is shown in Figure 4.9, where $Z_{C,PN}(s)$ is the small-signal converter impedance while $Z_{TH,PN}(s)$ is the small-signal grid Thévenin impedance. It is worth mentioning that all the quantities are defined in the *pn*-frame. In more detail, $Z_{C,PN}(s) = Y_{C,PN}^{-1}(s)$, with $Y_{C,PN}(s)$ defined by (4.5). Based on (4.4), and under the assumption that the plant impedances are perfectly balanced, the $Z_{TH,PN}(s)$ impedance has been formulated as:

$$Z_{TH,PN}(s) = \begin{bmatrix} Z_{TH,pp}(s) & 0 \\ 0 & Z_{TH,nn}(s - 2j\omega_0) \end{bmatrix} \tag{4.13}$$

where $Z_{TH,pp}(s) = Z_{TH,nn}(s) = Z_{TH}(s)$, with $Z_{TH}(s)$ representing the *abc*-frame phase impedance [64].

Based on the diagram in Figure 4.9, the following set of equations are written:

$$\begin{aligned} \delta U_{pn}(s) &= Z_{TH,PN}(s)\delta i_{pn}(s) + U_{TH,pn}(s) \\ \delta U_{pn}(s) &= Z_{C,PN}(s)[i_{ref,pn}(s) - \delta i_{pn}(s)] \end{aligned} \tag{4.14}$$

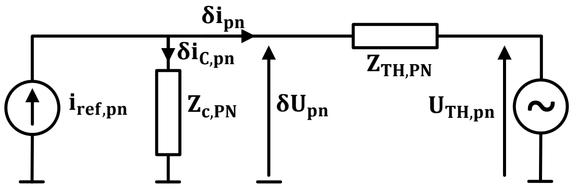

Figure 4.9: Small-signal impedance-based model of the inverter-grid interface.

Hence, $\delta i_{pn}(s)$ is formulated as:

$$\begin{aligned}\delta i_{pn}(s) = [Y_{TH,PN}(s)Z_{C,PN}(s)] \cdot [I + Y_{TH,PN}(s)Z_{C,PN}]^{-1} i_{ref,pn}(s) \\ - Y_{TH,PN}(s) \cdot [I + Y_{TH,PN}(s)Z_{C,PN}]^{-1} U_{TH,pn}(s)]\end{aligned} \tag{4.15}$$

where I is the 2×2 identity matrix, while $Y_{TH,PN}(s) = Z^{-1}_{TH,PN}(s)$. Based on (4.15), the feedback loop system shown in Figure 4.10 is drawn, whose open-loop gain $L_{PN}(s)$ is:

$$L_{PN}(s) = Y_{TH,PN}(s)Z_{C,PN}(s) \tag{4.16}$$

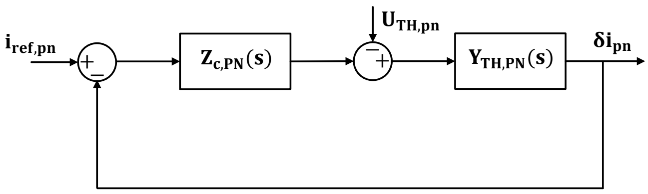

Figure 4.10: Feedback loop system equivalent to the circuit in Figure 4.9.

The Generalised Nyquist Criterion (GNC) has been applied to study the stability of the system [68]. It is pointed out that, as the converter is designed to be stable with an ideal grid [54], the converter admittance $Y_{C,PN}(s)$ has no poles in the Right Half Plan (RHP). Similarly, $Z_{TH,PN}(s)$ does not have poles in the RHP as the grid is designed to behave stably when connected to an ideal inverter. However, $Y_{C,PN}(s)$ might have RHP zeros [69], which would be RHP poles of $Z_{C,PN}(s)$. Hence, the matrix $L_{PN}(s)$ might have RHP poles, which must be taken into account when applying the GNC to

$I + L_{PN}(s)$ [24].

Based on these considerations, the $\hat{L}_{PN}(s) = L_{PN}^{-1}(s)$ matrix has been instead used in the stability study. From (4.5), (4.13), this is calculated as:

$$\begin{aligned}
\hat{L}_{PN}(s) &= L_{PN}^{-1}(s) = (Y_{TH,PN}(s) Z_{C,PN}(s))^{-1} \\
&= Z_{C,PN}^{-1}(s) Y_{TH,PN}^{-1}(s) = Y_{C,PN}(s) Z_{TH,PN}(s) \\
&= \begin{bmatrix} Y_{C,pp}(s) & Y_{C,pn}(s) \\ Y_{C,np}(s-2j\omega_0) & Y_{C,nn}(s-2j\omega_0) \end{bmatrix} \begin{bmatrix} Z_{TH,pp}(s) & 0 \\ 0 & Z_{TH,nn}(s-2j\omega_0) \end{bmatrix} \\
&= \begin{bmatrix} Y_{C,pp}(s) Z_{TH,pp}(s) & Y_{C,pn}(s) Z_{TH,nn}(s-2j\omega_0) \\ Y_{C,np}(s-2j\omega_0) Z_{TH,pp}(s) & Y_{C,nn}(s-2j\omega_0) Z_{TH,nn}(s-2j\omega_0) \end{bmatrix}
\end{aligned} \tag{4.17}$$

According to the previous considerations, $\hat{L}_{PN}(s)$ does not have poles in the RHP. The GNC has been applied to $I + \hat{L}_{PN}(s)$. It is worth mentioning that this is equivalent to applying the Generalised Inverse Nyquist Criterion (GINC) to $I + L_{PN}(s)$ [69].

The condition to verify if the system in Figure 4.10 is absolute stable therefore is as follows. By indicating with $\lambda_i(s)$ the eigenvalues of $\hat{L}_{PN}(s)$ and with $\mathcal{D}$ the Nyquist contour [102], if and only if the polar plots of $1 + \lambda_i(s)$ on the complex plane do not encircle the (0,0) point, with $s \in \mathcal{D}$, $i = 1, 2$, then the system is stable.

This criterion has been applied in the stability assessment of the studied wind farm-grid system, as discussed in the following Section.

4.2.1 Analysis of the wind farm resonances

The stability methodology discussed in Section 4.2 has been used to analyse the wind farm resonance stability problem investigated in this work, and in particular to assess the stability of the wind farm-grid system modelled in Section 2.1.4.

In order to verify the effectiveness of such methodology, the results of this stability study have been verified using time-domain simulations of the corresponding TD model of the wind farm-grid system. Thereafter, making use of the laboratory prototype of the inverter-grid interface described in Section 2.3.2.1, where such type of cable

due resonance has been reproduced, an experimental verification of the stability study methodology has been carried out.
In Section 4.2.1.1, the stability study of the wind farm-grid system is described, while in Section 4.2.1.2, the mentioned experimental validation is presented.

4.2.1.1 Stability assessment

The stability of the aggregated model of the wind farm grid system described in Section 2.1.4, whose equivalent circuit is illustrated in Figure 2.9, has been studied. In order to apply the methodology described in Section 4.2, based on the theory presented in Chapter 3, a small-signal model of such wind farm-grid system has been derived. Hence, the *pn*-frame small-signal converter admittance of the N-scaled aggregated turbine interface has been calculated.

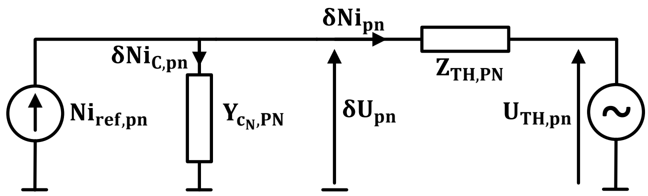

Figure 4.11: Small-signal equivalent circuit of the wind farm-grid interface.

Such small-signal model of the system has been represented in the sequence-frame in terms of an electrical circuit. The N-scaled aggregated turbine interface has been represented by its Norton equivalent, while a Thévenin equivalent has been used to represent the grid interface. Such representation of the system is illustrated in Figure 4.11.
$Y_{C_N,PN}(s)$ is the *pn*-frame small-signal converter admittance of the N-scaled turbine interface, which also includes the N-scaled reactor impedance $Z_{f_N}(s)$, while $Z_{TH,PN}(s)$ is the equivalent *pn*-frame impedance seen by the aggregated turbine interface. This therefore includes the $Z_{SYS}(s)$ impedance as well as the N-scaled impedances $Z_{PWM_N}(s)$ and $Z_{t_N}(s)$ in Figure 2.9.
As discussed in Section 2.1.4, in the applied wind farm aggregation technique it has been assumed that the N operating turbines are all generating their rated power, i.e.

they share the same operating point. Hence, the converter admittance of the N-scaled turbine $Y_{C_N,PN}(s)$ has been calculated as $NY_{C,PN}(s)$, where $Y_{C,PN}(s)$ is the converter admittance of the individual turbine, calculated with the method described in Section 4.1, and having the format in (4.5). In the carried analysis, it has also been assumed that all the plant impedances are balanced. Hence, the $Z_{TH,PN}(s)$ matrix has been formulated as in (4.13) [64].

It is worth highlighting that in the baseline design of the converter controller scheme employed in the turbines of the studied wind farm, a symmetrical regular sampling technique is used. As it will be discussed in more detail in Chapter 5, by affecting the magnitude of controller delay, such choice of the sampling technique is seen to be relevant to the wind farm resonance issue.

Having calculated $Y_{C_N,PN}(s)$ and $Z_{TH,PN}(s)$, the stability of the system has been studied applying the GNC to $I + \hat{L}_{PN}(s)$, with $\hat{L}_{PN}(s) = Y_{C_N,PN}(s)Z_{TH,PN}(s)$, according to the method described in Section 4.2. The resulting Nyquist plots are shown in Figure 4.12 as a function of the number of operating turbines N. They show that the system becomes unstable when more turbines are active and in particular when $N \geq 15$.

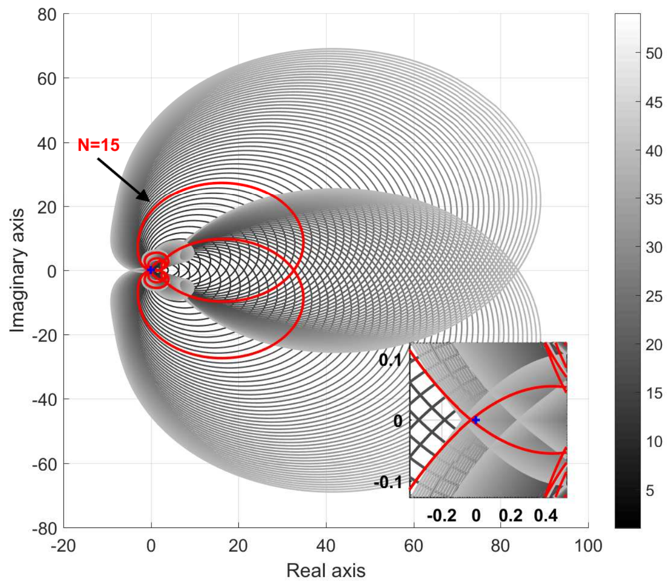

Figure 4.12: Nyquist plot of $I + \hat{L}_{PN}(s)$ for different values of the number of operating turbines N, with $1 \leq N \leq 54$.

The Bode plots of the eigenvalues of $\hat{L}_{PN}(s)$, $\lambda_1(j2\pi f)$ and $\lambda_2(j2\pi f)$, are shown for different N values in Figure 4.13 and 4.14, respectively. It can be noticed that for $N = 15$ a undamped resonance at $f_r \approx 344.3$ Hz occurs, as $|\lambda_1(j2\pi f_r)| > 1$, $|\lambda_2(j2\pi f_r)| > 1$ and $\angle\lambda_1(j2\pi f_r) = \angle\lambda_2(j2\pi f_r) = -540°$. Increasing the value of N, this resonance moves to lower frequencies in the close range of f_r. The plots reveal how the presence of these resonances is caused by the large phase loss of both $\angle\lambda_1(j2\pi f)$ and $\angle\lambda_2(j2\pi f)$ in the [300 Hz, 600 Hz] range, where the $Y_{TH,PN}(s)$ has a series resonance (see Fig. 2.10). This excessive phase loss is attributed to the controller delay, as it will be further discussed in the next Chapter.

It is noticed that at higher values of N an additional resonance is observed in the lower frequency range, at ≈ 59.5 Hz (see Figure 4.14). This is attributed to the larger magnitude of the small-signal converter admittance $Y_{C_N,PN}(s)$ when N is increased, which eventually introduces weak grid issues. When discussing the FVFF mitigation technique, in Chapter 5, it will be shown how such solution not only improves damping of the higher frequency resonances, but also helps alleviate such weak grid problems.

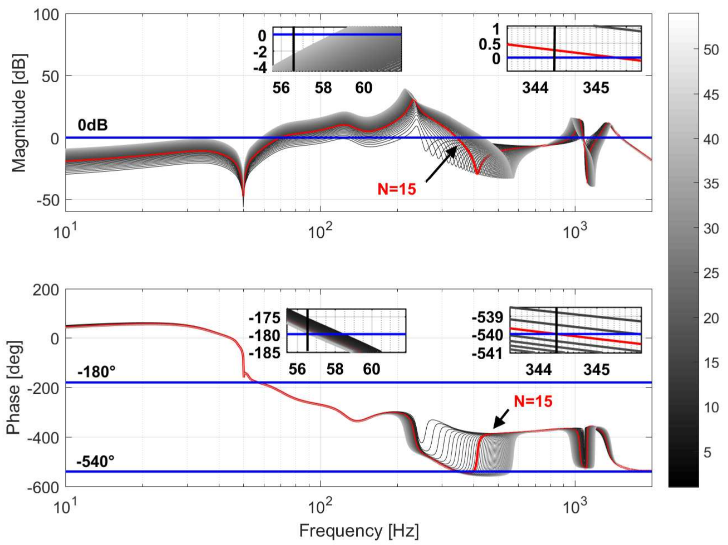

Figure 4.13: Bode plot of the eigenvalue $\lambda_1(2\pi f)$ of $\hat{L}_{PN}(s)$ for different values of the number of operating turbines N.

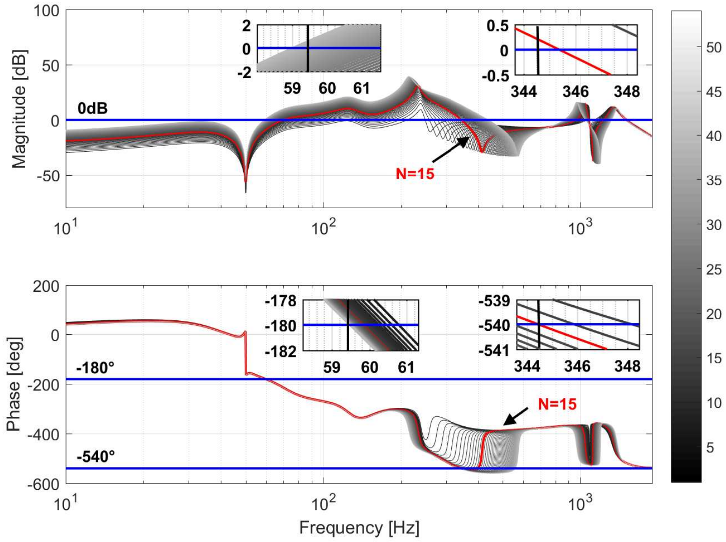

Figure 4.14: Bode plot of the eigenvalue $\lambda_2(2\pi f)$ of $\hat{L}_{PN}(s)$ for different values of the number of operating turbines N.

The analytical results of the stability study have been confirmed by the carried out time domains simulations of the built TD model of the wind farm-grid interface.

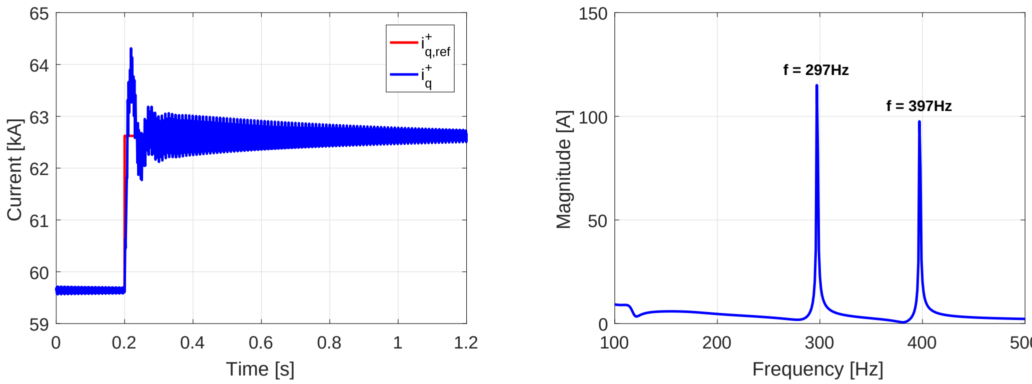

(a) (b)

Figure 4.15: (a) Simulated step response of the i_q^+ control loop for the aggregated TD model of the wind farm-grid system, with $N = 14$. (b) Magnitude spectrum of the step response transient.

Figure 4.15a shows the i_q^+ loop step response of the system for a 5 % increase in the $i_{q,ref}^+$ set-point, with $N = 14$. The spectral analysis of the recorded transient response reveals two components at 297 Hz and 397 Hz. They respectively correspond to a positive and a negative sequence mode at 347 Hz in the *abc*-frame. Such mode becomes divergent when $N > 14$, giving rise to instability.

These results show an accurate match between the resonance value predicted by the stability study and the one resulting by the time-domain simulations, which has allowed a verification of the accuracy of the applied stability assessment methodology.

4.2.1.2 Experimental verification

An experimental verification of the applied stability study technique is presented as follows.

The laboratory prototype inverter-grid interface described in Section 2.3.2.1 has been used, where a cable-due resonance of the same type of those analysed in this work has been reproduced (see Figure 2.25). In this test, the controller scheme in Figure 2.20 has been applied and a PWM symmetrical regular sampling technique has been used. In other words, the same baseline design of the converter controller employed in the studied wind farm-grid has been considered.

The results of the carried out test are reported in Figure 4.16a where the measured i_q^+ feedback signal is shown for a staircase-like increase of the corresponding $i_{q,ref}^+$ set-point. The observed divergent transient confirms the instability of the system as i_q^+ increases to 7 A, with the current eventually driven to zero by an over-current protection switch activated by the controller. The spectral analysis of this divergent transient is illustrated in Figure 4.16b, indicating the presence of two predominant components at 625 Hz and 725 Hz in the *dq*-frame. These respectively correspond to a positive and a negative sequence mode at 675 Hz in the *abc*-frame.

These experimental data have been verified analytically by studying the stability of the system with the methodology illustrated in Section 4.2. The resulting Nyquist plots of $I + \hat{L}_{PN}(s)$ are shown in Figure 4.17, indicating the instability of the system. The operating point corresponding to the rated power of the inverter has been considered to generate these results.

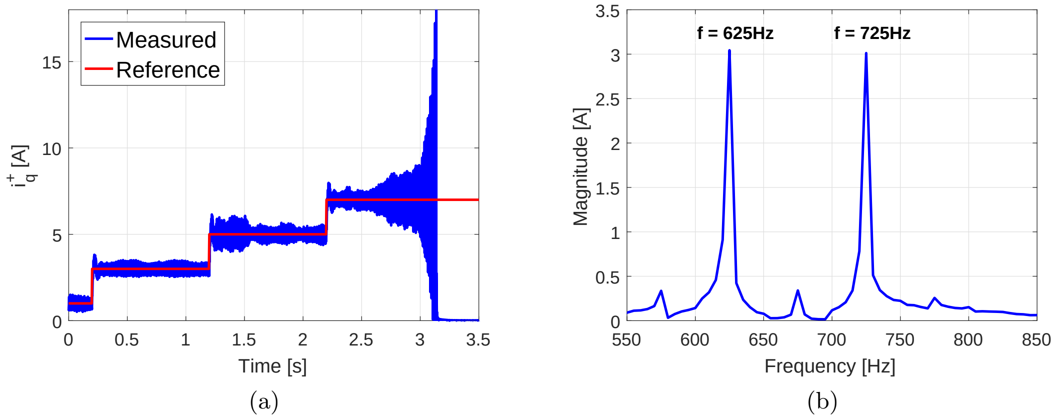

Figure 4.16: Test results of the tested inverter-grid interface described in Section 2.3.2.1. The baseline controller scheme shown in Figure 2.20 has been applied, using a PWM symmetrical regular sampling technique; (a) Recorded i_q^+ trend for a staircase-like change in the $i_{q,ref}^+$ set-point. (b) Magnitude spectrum of the divergent transient.

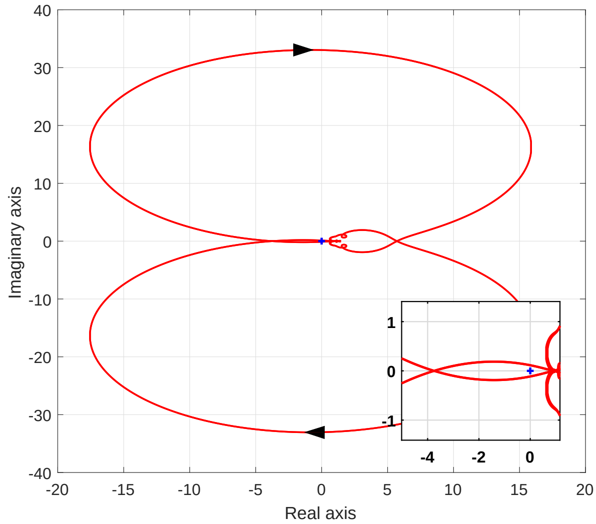

Figure 4.17: Nyquist plots of $I + \hat{L}_{PN}(s)$ for the system described in Section 2.3.2.1, considering its operating at rated power.

The corresponding Bode plots of the eigenvalues $\lambda_1(j2\pi f)$ and $\lambda_2(j2\pi f)$ of $\hat{L}_{PN}(s)$ are respectively shown in Figure 4.18 and 4.19. They confirm that the system resonance is at $f_r = 675$ Hz, as $|\lambda_1(j2\pi f_r)| > 1$, $|\lambda_2(j2\pi f_r)| > 1$ and $\angle\lambda_1(j2\pi f_r) = \angle\lambda_2(j2\pi f_r)| = -180°$, hence validating the effectiveness of the used stability analysis methodology. It can be noticed that the instability is again caused by the excessive phase loss of the eigenvalue functions in the frequency range where the cable due resonance occurs. As previously discussed, this effect is attributed to the controller delay. This aspect will be further investigated in Chapter 5, where the mitigation techniques proposed to overcome such resonance issue are presented.

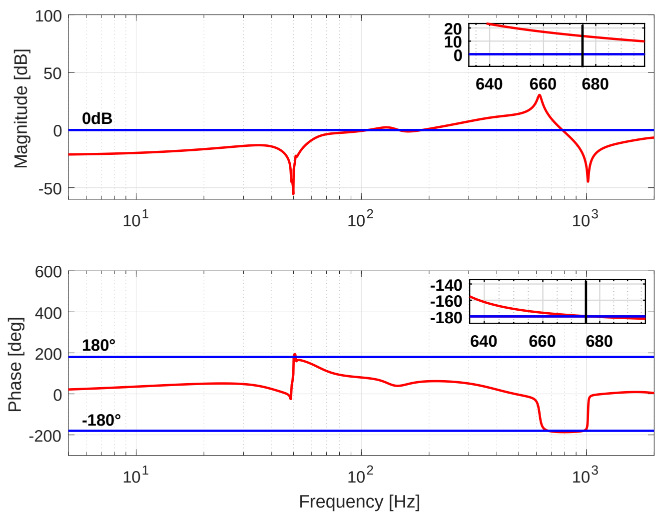

Figure 4.18: Bode plots of the eigenvalue $\lambda_1(2\pi f)$ of $\hat{L}_{PN}(s)$ for the system described in Section 2.3.2.1, considering its operating at rated power.

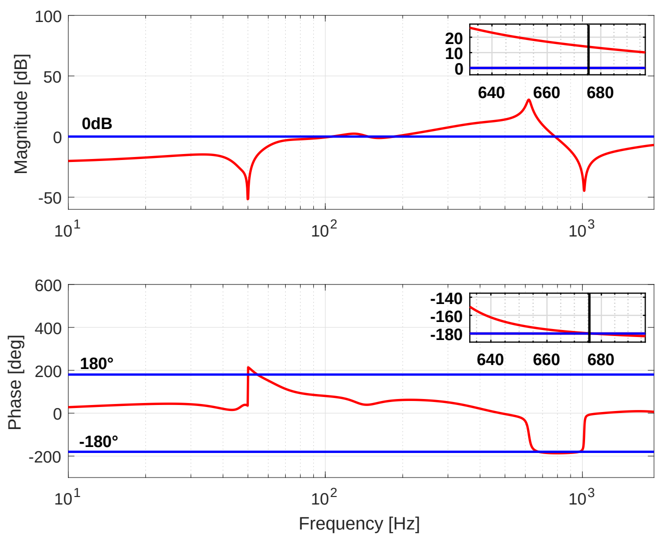

Figure 4.19: Bode plots of the eigenvalue $\lambda_2(2\pi f)$ of $\hat{L}_{PN}(s)$ for the system described in Section 2.3.2.1, considering its operating at rated power.

4.3 Effect of the converter admittance coupling on the stability study

A study of the effect of the *pn*-frame small-signal converter admittance coupling terms on the stability study of the inverter-grid system is presented as follows.

A claimed advantage of the impedance-based stability criterion [54] is the possibility to simplify the stability study by treating the converter-grid interconnection, as two decoupled SISO systems [55], [65]. This simplification derives from the assumed decoupling of the small-signal converter impedance in the sequence-frame [54]. A further advantage of this approach is that SISO concepts such as phase and gain margins, which are intuitive and easily interpretable indexes to quantify the stability performance of the system [103], can be applied. However, the existence of coupling in the *pn*-frame small-signal converter impedance has been proved in [60], where the MFD property of the converter system is introduced and associated to the structure of the converter control scheme. The verification of this property has been investigated in Section 4.1.3.2, confirming how asymmetries in the *dq*-axes control loops generate non-zero coupling terms in the *pn*-frame small-signal converter admittance. Significant results are presented in [13], where it is shown that neglecting such coupling terms can lead to a wrong stability assessment when the PLL bandwidth is increased.

Along the line of these studies, a criterion to infer whether such coupling is relevant or not to the stability study of the inverter-grid system is presented. This is based on the verification of the property of diagonal dominance of such system in the sequence-frame. The application of this criterion to a case study of an inverter connected to a grid with different SCR values is illustrated. It is shown how in the weak grid scenario the diagonal dominance property may be lacking, hence necessitating to take the small-signal converter admittance coupling terms into account for an accurate stability study. Experimental data will also be included to support the analytical results.

4.3.1 Study of the system diagonal dominance

The presented criterion to assess whether sequence-frame converter admittance coupling terms are relevant or not to the stability analysis of the inverter-grid system is based on the assessment of the diagonal dominance property of such system in the sequence-frame. The results illustrated in [63], where the stability robustness of diagonally dominant systems is studied, are applied. These are based on the Strictly Diagonal Dominance (SDD) property of a transfer function matrix [93] and on the related Gershgorin's theorem [104]. One of the key results of [63] is the derivation of a sufficient condition for the stability of a diagonally dominant system. This requires to verify that the matrix $I + \hat{L}_{PN}(s)$ is SDD over the Nyquist contour $\mathcal{D}$, where $\hat{L}_{PN}(s)$ is defined by (4.17). The verification of the SDD property therefore requires to verify that over the Nyquist contour $\mathcal{D}$:

$$\begin{aligned} &|1 + \hat{L}_{1,1}(s)| > |\hat{L}_{1,2}(s)| \\ &|1 + \hat{L}_{2,2}(s)| > |\hat{L}_{2,1}(s)| \end{aligned} \tag{4.18}$$

where $\hat{L}_{1,1}(s)$, $\hat{L}_{1,2}(s)$, $\hat{L}_{2,1}(s)$, $\hat{L}_{2,2}(s)$ are the elements of the $\hat{L}_{PN}(s)$ matrix.

In particular, when (4.18) is verified, then a sufficient condition for the stability of the system described by $L_{PN}(s)$ is that the characteristic loci of $I+\hat{L}_{D,PN}(s)$ satisfy the GNC [68], [63], where $\hat{L}_{D,PN}(s)$ corresponds to the $\hat{L}_{PN}(s)$ matrix with the off-diagonal terms set to zero:

$$\hat{L}_{D,PN}(s) = \begin{bmatrix} \hat{L}_{1,1}(s) & 0 \\ 0 & \hat{L}_{2,2}(s) \end{bmatrix} \tag{4.19}$$

It can therefore be concluded that if the system is SDD (i.e. (4.18) is true) the stability assessment of the system can be carried out by ignoring the cross-coupling terms of the small-signal converter admittance/impedance, which are therefore irrelevant to the stability analysis. The system can be treated as two decoupled SISO systems, in line with the impedance-based stability criterion [54]. However, if (4.18) is not verified, then such cross-coupling terms should be considered. Thereby, the GNC should be applied to $I + \hat{L}_{PN}(s)$. The presented results have been derived by studying the row diagonal dominance of $I + \hat{L}_{PN}(s)$. The same results would be obtained by assessing the column diagonal dominance of $I + \hat{L}_{PN}(s)$ [63], [93].

4.3.2 Case study: VSC connected to a grid with different SCR

The criterion described in Section 4.3.1 has been applied to the case study of a VSC connected either to a strong or a weak grid. The study has been used to show how the verification or not of the SDD property of the system can correctly indicate whether the coupling terms of the *pn*-frame small-signal converter admittance are relevant or not to the stability analysis.

4.3.2.1 Description of the system

The laboratory prototype inverter-grid system described in Section 2.3.2.3 has been used for this study. The grid inductance has been varied to reproduce a strong and a weak grid scenarios, respectively having a SCR of 5.2 and 1.9. The controller scheme in Figure 2.20 has been used, with the addition of both the power and voltage regulators, whose block diagrams are shown in Figures 2.15 and 2.16, respectively.
The current controller has been tuned applying the IMC method [87], [58] and has a bandwidth of $\approx$ 300 Hz. A different value of the PLL bandwidth has been chosen for the strong and weak grid scenarios, respectively equal to 25 Hz (in accordance with [97]) and 1.9 Hz. The lower value has been selected to stabilise the system dynamics under weak grid conditions, as discussed in [105]. Finally, the outer power and voltage loops have been tuned to have a bandwidth at least ten times lower than that of the inner current loop [58]. The system and controller parameters are those listed in Table 2.9.

4.3.2.2 Experimental results

The laboratory prototype has been tested for a staircase-like increase of the power loop set-point P_{ref} from 0.4 pu until 1 pu, while the reference value $\hat{U}_{ref}$ of the voltage loop has been kept equal to 1 pu. The set-points of the negative sequence current controller, $i^{-}_{d,ref}$ and $i^{-}_{q,ref}$, have been set to 0 pu. Figure 4.20a and 4.20b show the experimental results for the strong and the weak grid scenarios respectively, indicating that the system performs stably for both grid conditions. These results are compared to those obtained via the stability analysis, which is presented in the next Section.

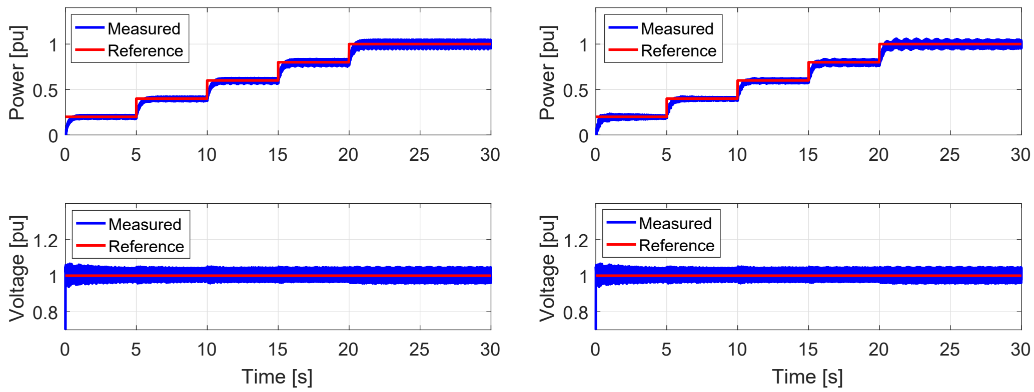

(a) (b)

Figure 4.20: Tested operation of the grid-connected VSC laboratory prototype; (a) SCR = 5.2; (b) SCR = 1.9.

4.3.2.3 Stability assessment

The stability of the system has been evaluated for the same operating points tested experimentally. For each of these operating points, a small-signal model of the inverter-grid system has been derived, applying the theory described in Chapter 3. Thereby, these FD models have been used to carry out the stability study of the system, based on the technique described in Section 4.2, as well as to assess the system SDD property, based on (4.18).

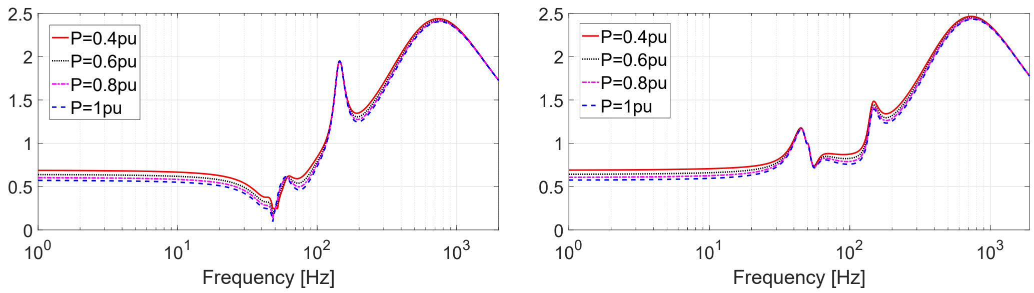

(a) $|1 + \hat{L}_{1,1}(j2\pi f)| - |\hat{L}_{1,2}(j2\pi f)|$ (b) $|1 + \hat{L}_{2,2}(j2\pi f)| - |\hat{L}_{2,1}(j2\pi f)|$

Figure 4.21: Verification of the diagonal dominance property of the system for the scenario with SCR = 5.2 (strong grid).

The results of the verification of the system SDD property are shown in Figure 4.21 and 4.22, for the strong and the weak grid cases respectively. They indicate that the system is not diagonal dominant only in the latter weak grid scenario, as can be seen in the [48 Hz, 62 Hz] range (see Figure 4.22a).

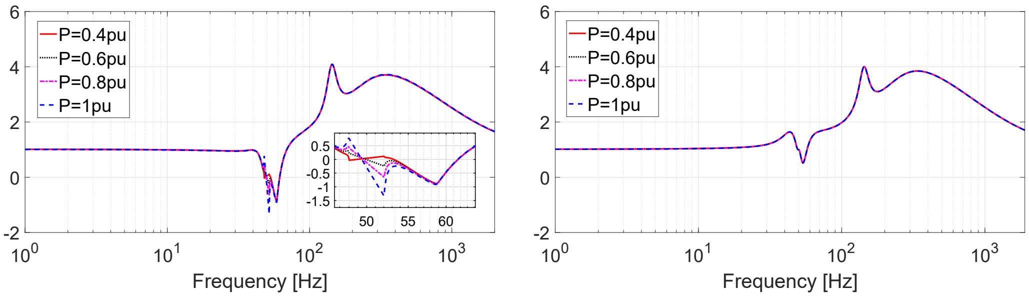

(a) $|1+\hat{L}_{1,1}(j2\pi f)| - |\hat{L}_{1,2}(j2\pi f)|$ (b) $|1+\hat{L}_{2,2}(j2\pi f)| - |\hat{L}_{2,1}(j2\pi f)|$

Figure 4.22: Verification of the diagonal dominance property of the system for the scenario with SCR = 1.9 (weak grid).

Consequently, according to the theory described in Section 4.3.1, the cross-coupling terms of the small-signal converter admittance are irrelevant to the stability study only in the strong grid case, thanks to the SDD property of the system. This is confirmed by the Nyquist plots of $I + \hat{L}_{PN}(s)$ and $I + \hat{L}_{D,PN}(s)$, respectively shown in Figure 4.23a and 4.23b, which both indicate a stable feedback system.

On the other hand, in the weak grid scenario, as the system is not SDD, it is necessary to include the aforementioned coupling terms in the stability study. Otherwise a wrong stability judgement might be made. In fact, while the Nyquist plots of $I + \hat{L}_{PN}(s)$, shown in Figure 4.24a, correctly confirm the system stability, those of $I + \hat{L}_{D,PN}(s)$, shown in Figure 4.24b, indicate instability. The difference between these Nyquist plots is highlighted by the Bode plots of the eigenvalues of $\hat{L}_{PN}(s)$ and $\hat{L}_{D,PN}(s)$, reported in Figure 4.25. The case of the operating point with $P_{ref} = 1$ pu is illustrated. It is worth noticing how such difference is confined in the same range of frequencies where the system is not SDD (see Fig. 4.22a).

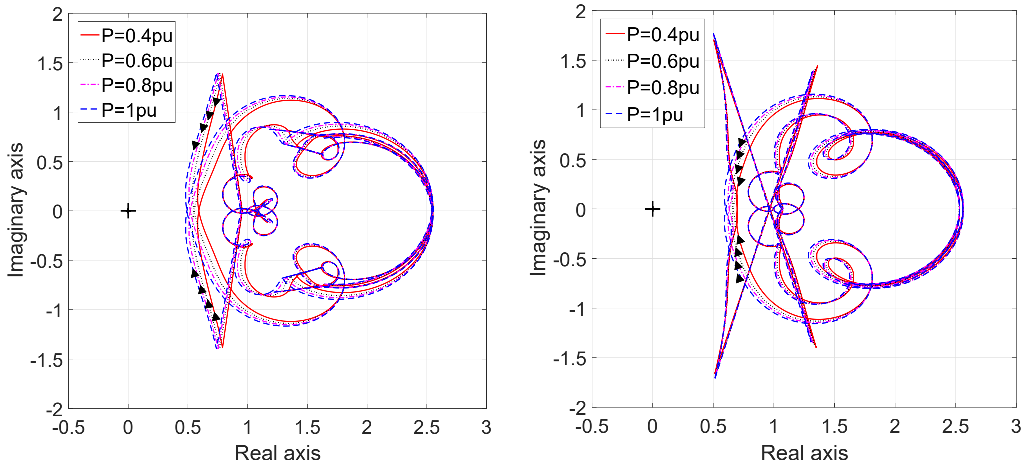

(a) (b)

Figure 4.23: Nyquist plots of $I + \hat{L}_{PN}(s)$ (a) and $I + \hat{L}_{D,PN}(s)$ (b) for the system with SCR = 5.2.

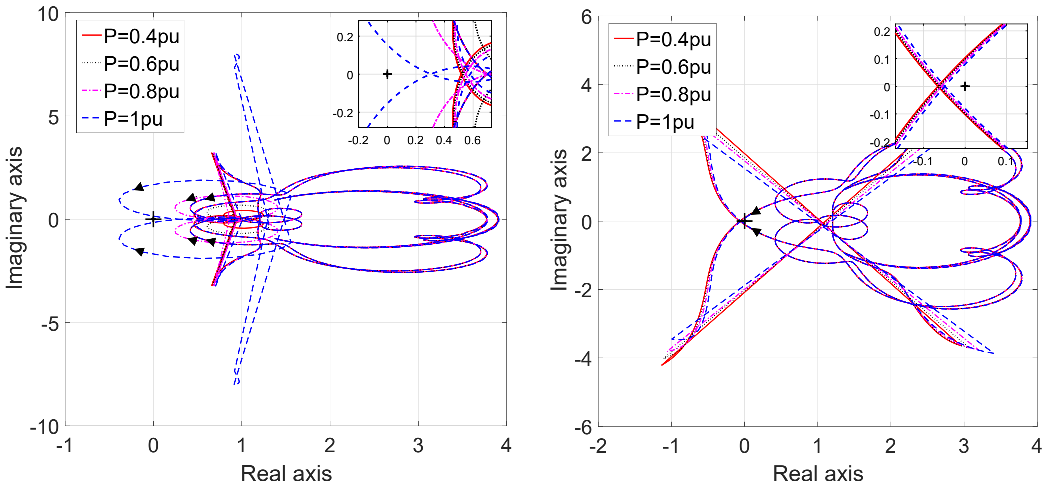

(a) (b)

Figure 4.24: Nyquist plots of $I + \hat{L}_{PN}(s)$ (a) and $I + \hat{L}_{D,PN}(s)$ (b) for the system with SCR = 1.9.

The results of the presented study case indicate that the coupling terms of the small-signal converter admittance can become relevant to the stability study, especially when multiple causes of asymmetry in dq-axes control loops are present, as in the investigated case where these are due both to the PLL loop and to the outer loops. As such, neglecting these coupling terms should not be an a priori assumption, as proposed in the impedance-based stability criterion [54]. The study of the system SDD property has been presented as a valuable tool to verify whether such coupling terms are significant or not to the stability analysis.

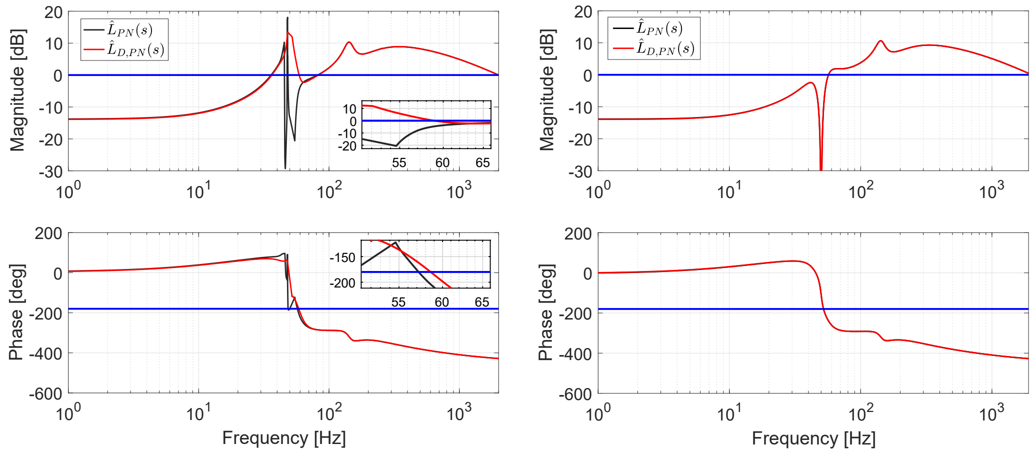

(a) (b)

Figure 4.25: Comparison between the Bode plots of the eigenvalues $\lambda_1(j2\pi f)$ (a) and $\lambda_2(j2\pi f)$ (b) of $\hat{L}_{PN}(s)$ and $\hat{L}_{D,PN}(s)$ for $P_{ref} = 1$ pu, $\hat{U}_{ref} = 1$ pu, with SCR $= 1.9$.

4.4 Study of the system relative stability

Besides the study of the system absolute stability, another important aspect is the assessment of the system relative stability [106]. This typically aims to calculate numerical quantities, the so-called stability margins, which indicate how robust the stability is against uncertainties in the system. Such uncertainties may for example arise from modelling errors, parameter variations or from unmodeled nonlinearities [103].

As aforementioned, by assuming that the positive and the negative sequence small-signal converter impedances/admittances are decoupled, the system is treated as two separate SISO systems [54]. Therefore, SISO tools such as the gain and the phase margin can be applied to evaluate the relative stability of the system. However, as discussed, non-zero coupling terms exist in the pn-frame small-signal converter impedance [60], and, as illustrated in Section 4.3, these terms might be relevant to the stability study. The inclusion of such coupling in the relative stability study of the system requires the identification of MIMO stability margins, whose definitions are not as straightforward and intuitive as in the SISO scenario [103]. Different approaches have been presented in the control literature [107]. The critical direction theory is proposed in [108], according to which at any frequency there is one specific vectorial direction of the applied perturbation which is relevant to the system stability. The structured singular-value method is proposed in [109], where a framework is built to generalise SISO stability margin definitions. Another attempt is the MIMO version of the circle theorem [103], whose effectiveness to assess the robustness of the system against different sources of uncertainty has been proved. The special case of diagonal dominant systems [93] is advantegeous, as more intuitive and graphically visualizable stability margin definitions are possible [103].

Based on previous studies published in the control literature on diagonally dominant systems [63], [103], [110], a perturbation norm based stability margin which exploits the SDD property of the converter-grid system in the sequence-frame is introduced.

Compared to the SISO gain and phase margin figures, which, as mentioned, ignore the cross-coupling terms of the small-signal converter impedance/admittance, the proposed stability margin takes such terms into account. The result is a safer and more conservative evaluation of the system stability robustness.

The presented stability margin is defined in the following Section 4.4.1, while its utilisation will be illustrated in Section 4.4.2 considering the case of a VSC connected to a weak grid.

4.4.1 Perturbation norm stability margin

Based on the results presented in [63], when the $I + \hat{L}_{PN}(s)$ matrix is SDD, i.e. (4.18) are true, then the following strictly positive quantity d_∞ can be defined as:

$$d_\infty = \min_{i=1,2;j\neq i}(|1 + \hat{L}_{i,i}(s)| - |\hat{L}_{i,j}(s)|) \tag{4.20}$$

with $s \in \mathcal{D}$. As demonstrated in [63], the value of d_∞ is interpreted as the maximum multiplicative perturbation $\delta L_{PN}(s)$ the system can stand without losing the closed-loop stability (see Figure 4.26):

$$d_\infty = \sup_{s \in \mathcal{D}} ||\delta L_{PN}(s)||_\infty \tag{4.21}$$

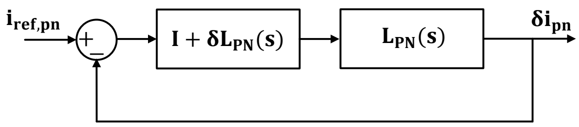

Figure 4.26: Feedback loop system with applied multiplicative perturbation $\delta L_{PN}(s)$.

For this reason, d_∞ is named perturbation norm stability margin. By drawing the Gershgorin discs [104] of the SDD matrix $I + \hat{L}_{PN}(s)$ in the complex plane, which correspond to the regions where the eigenvalues of $I + \hat{L}_{PN}(s)$ lie, the circle centred on the (0,0) point and having a radius equal to d_∞ can be identified, which is tangent to the Gershgorin discs. Such circle is indicated as the perturbation norm circle. The quantity d_∞ therefore represents the minimum (normed) distance between the (0,0) point of the complex plan and the mentioned discs. A similar graphical interpretation of d_∞ can be found in [111]. It is worth mentioning that if the matrix $I + \hat{L}_{PN}(s)$ is not SDD, the resulting value of d_∞ would be negative, indicating that it is not possible to define the perturbation norm circle. As discussed in Section 4.4.2, negative values of d_∞ indicate that the stability performance of the system is likely to be poor, with less damped dynamics.

The introduced d_∞ margin can be related to the SISO gain and phase margins, calculated by application of the impedance-based stability criterion [54]. In the following discussion, these will respectively be indicated as GM^+_{SISO} and PM^+_{SISO} for the positive sequence and GM^-_{SISO} and PM^-_{SISO} for the negative sequence.

As shown in Figure 4.27, by definition of SISO phase margin [94], the intersection between the perturbation norm circle and the unit circle allows to calculate the equivalent minimum SISO phase margin GM_{d_∞} of the system, associated to d_∞. Similarly, by definition of SISO gain margin [94], the intersection between the perturbation norm circle and the negative real axis allows to obtain the equivalent minimum SISO gain margin of the system, GM_{d_∞}, associated to d_∞.

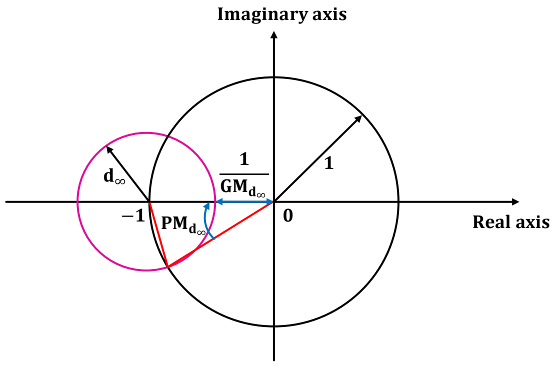

Figure 4.27: Graphical equivalence between d_∞ and SISO gain and phase margins, GM and PM respectively.

These minimum quantities can be calculated as:

$$\begin{aligned} GM_{d_\infty}[dB] &= 20\log_{10}\left(\frac{1}{1-min\{1,d_\infty\}}\right) \\ PM_{d_\infty}[deg] &= \frac{360}{\pi}\arcsin\left(\frac{min\{2,d_\infty\}}{2}\right) \end{aligned} \tag{4.22}$$

Therefore, the value of d_∞ allows a derivation of the minimum equivalent SISO stability margins of the system. It is highlighted that (4.22) can be applied only if the system is SDD, i.e. $d_\infty > 0$.

4.4.2 Case study: VSC connected to a weak grid

For the purpose of illustrating how the stability margin (4.20) can be used to assess the stability robustness of an inverter-grid system, a case study of an inverter connected to a weak grid has been considered, assessing how damping of the system dynamics varies with its operating point.

4.4.2.1 Description of the system

The laboratory prototype inverter-grid system described in Section 2.3.2.3 has been considered. The employed converter control scheme is the one shown in Figure 2.20. In this case, both the negative sequence current controller and the notch filters used to decouple the positive and negative sequence components of the measured plant signals, have been disabled. The system and control parameters are those detailed in Table 2.10. Such an ad hoc controller design has enabled the reproduction of an illustrative scenario for using the stability margin (4.20). It is worth noticing that by utilising a bigger grid inductance, the studied scenario is that of a weak grid (with a SCR of 1.9).

4.4.2.2 Stability assessment

In the carried out stability assessment, four operating points of the system have been considered. These are defined by the set-points values of the d- and q- axis current loops, $i^+_{q,ref}$ and $i^+_{d,ref}$ respectively, detailed in Table 4.2.
Figures 4.28a and 4.28b show the results of the verification of the conditions in (4.18), for the first and the second rows of the $I + \hat{L}_{PN}(s)$ matrix, respectively. As it can be seen, the system is SDD for all the tested operating points, but for OP_4. As such, according to the theory presented in Section 4.4.1, the resulting perturbation norm stability margin d_∞ is positive only for OP_1, OP_2 and OP_3.

Table 4.2: Positive sequence current loop set-points for the considered operating points for the system.

Operating Point (OP)	$i^+_{q,ref}$	$i^+_{d,ref}$
OP_1	3 A	0 A
OP_2	4 A	0 A
OP_3	5 A	0 A
OP_4	6 A	0 A

The stability of the system has been assessed by applying the Generalised Nyquist Criterion (GNC) to $I+\hat{L}_{PN}(s)$ [94], as discussed in Section 4.2. As discussed in Section 4.2, as $\hat{L}_{PN}(s)$ is open-loop stable [69], in order to verify the absolute stability of the system, it is enough to verify that the characteristic loci of $I + \hat{L}_{PN}(s)$ do not encircle the (0,0) point of the complex plane.
Detailed views of the Nyquist plots of $I + \hat{L}_{PN}(s)$ are shown in Figure 4.29, for the considered operating points. The associated Gershgorin discs are also shown. For the operating points OP_1, OP_2 and OP_3 it has been possible to draw the perturbation norm circle, thanks to the SDD property of the system which makes $d_\infty > 0$. Contrarily, as for OP_4 such property is not verified, the resulting Gershgorin discs encircle the (0,0) point (see Figure 4.29d). The reduction in the size of the perturbation circle, seen in

Figures 4.29a, 4.29b, and 4.29c, indicate that, despite of the fact that the system is absolute stable, its relative stability decreases as $i^+_{q,ref}$ increases.
For the calculated d_∞ values, the corresponding equivalent minimum SISO margins have been derived, based on (4.22). These have been compared to the SISO stability margins obtained by application of the the impedance based stability-criterion [54], i.e. neglecting the off-diagonal terms of $\hat{L}_{PN}(s)$.
The Bode plots of $\hat{L}_{1,1}(j2\pi f)$ and $\hat{L}_{2,2}(j2\pi f)$ are respectively shown in Figures 4.30a and 4.30b for the considered operating points. From these plots, the aforementioned stability margins GM^+_{SISO}, PM^+_{SISO}, GM^-_{SISO} and PM^-_{SISO} have been calculated.

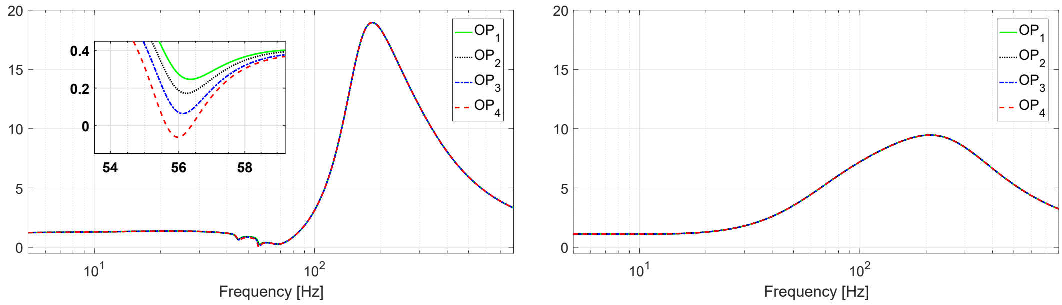

(a) $|1+\hat{L}_{1,1}(j2\pi f)| - |\hat{L}_{1,2}(j2\pi f)|$ (b) $|1+\hat{L}_{2,2}(j2\pi f)| - |\hat{L}_{2,1}(j2\pi f)|$

Figure 4.28: Verification of the diagonal dominance property of the system for the different operating points taken into considerations.

Table 4.3 compares the obtained stability margins figures. These data indicate that the critical resonance frequency of the system is at ≈ 57 Hz. As it can be seen, the SISO gain margin GM^+_{SISO} decreases as $i^+_{q,ref}$ increases, indicating a poorer relative stability of the system at higher current levels. This is also confirmed by the corresponding reduction in d_∞, and then by the loss of the system SDD property for OP_4, which makes d_∞ negative.
The SISO figures associated to the calculated d_∞ stability margin indicate its conservative feature. Such conservativeness relies on the significance of d_∞ [63]. As mentioned, d_∞ is interpreted as the upper limit of the perturbation $\delta L_{PN}(s)$ that can be applied to the system without making it unstable. In general, $\delta L_{PN}(s)$ is not diagonal, as such it can affect both the positive and the negative sequence control loops simultaneously.

Both because d_∞ is calculated taking into account the off-diagonal terms of $\hat{L}_{PN}(s)$ (see (4.20)), and because it considers any generic perturbation applied on the system (i.e. also non diagonal perturbations), such stability margin is more conservative than the SISO stability margins used in the impedance-based stability criterion [54]. By taking the coupling between the positive and negative sequence small-signal converter admittance into account, a safer measure of the system relative stability is therefore obtained.

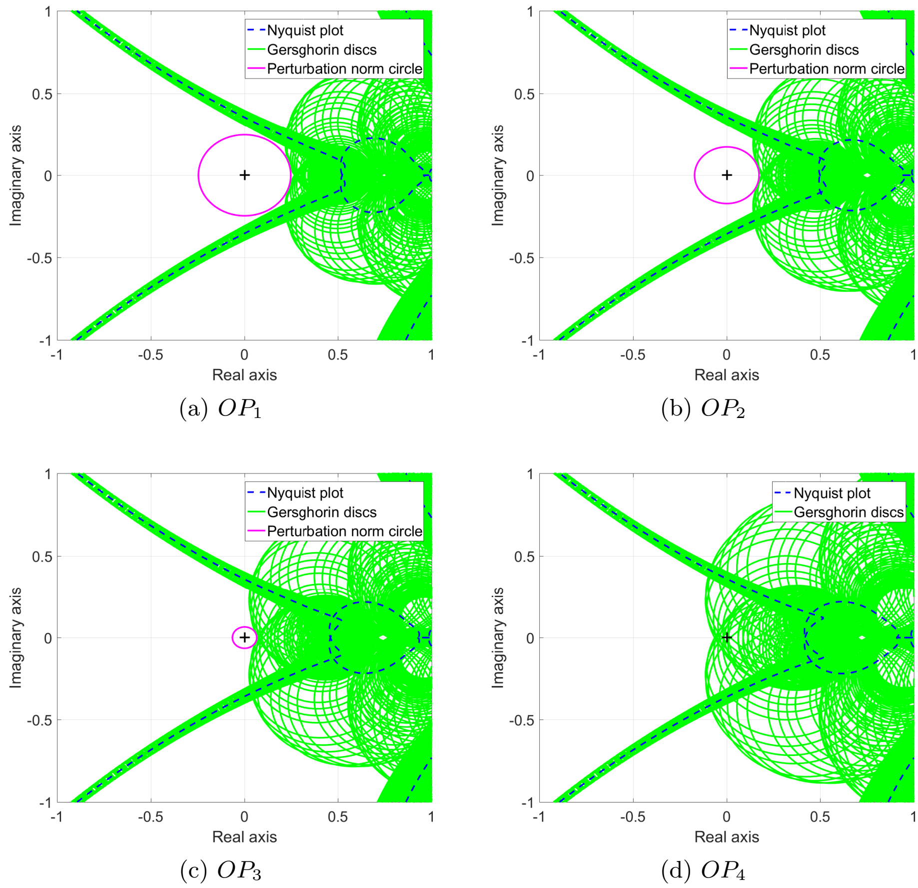

(a) OP_1 (b) OP_2

(c) OP_3 (d) OP_4

Figure 4.29: Nyquist plots and perturbation norm circle of the system for the different operating points taken into considerations.

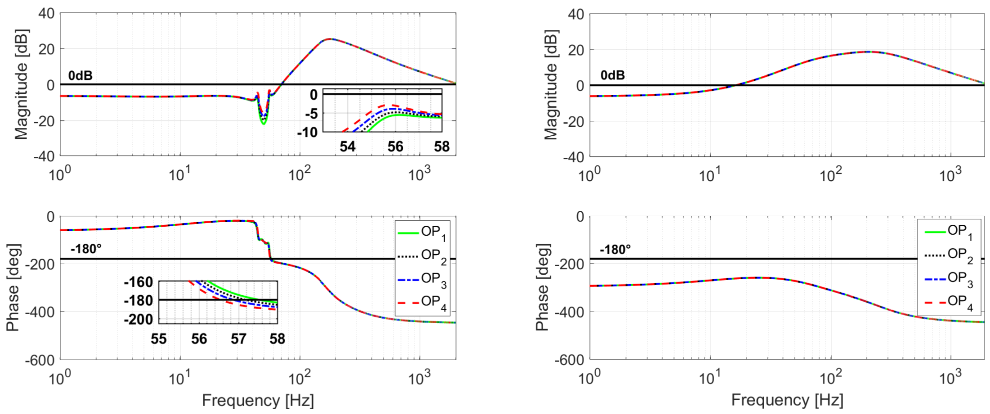

(a) (b)

Figure 4.30: Bode plots of $\hat{L}_{1,1}(j2\pi f)$ (a) and $\hat{L}_{2,2}(j2\pi f)$ (b) for the different operating points taken into considerations.

Table 4.3: Comparison between the SISO stability margins calculated with the impedance-based stability criterion (GM^+_{SISO}, FM^+_{SISO}, GM^-_{SISO}, PM^-_{SISO}) and the alternative figures based on the study of the system diagonal dominance (d_∞ and its equivalent SISO quantities GM_{d_∞} and PM_{d_∞}).

OP	GM^+_{SISO} **[dB]**	PM^+_{SISO} **[deg]**	GM^-_{SISO} **[dB]**	GM^-_{SISO} **[deg]**	d_∞	GM_{d_∞}**[dB]**	PM_{d_∞} **[deg]**
OP_1	6.2 (at 57.5 Hz)	19 (at 70.2 Hz)	∞	83 (at 16 Hz)	0.25	≥ 2.5	≥ 14.4
OP_2	5.7 (at 57.2 Hz)	19 (at 70.1 Hz)	∞	83 (at 16 Hz)	0.17	≥ 1.6	≥ 9.8
OP_3	4.8 (at 56.9 Hz)	19 (at 70.1 Hz)	∞	83 (at 16 Hz)	0.07	≥ 0.6	≥ 4
OP_4	3.9 (at 56.6 Hz)	19 (at 70 Hz)	∞	83 (at 16 Hz)	< 0	-	-

4.4.2.3 Experimental results

The analytical results presented in Section 4.4.2.2 have been verified experimentally making use of the laboratory prototype of the studied system.

The system has been tested for a staircase-like increase of the $i^+_{q,ref}$ set-point from 3A up to 7A. The recorded data are shown in Figure 4.31a.

A spectral analysis of each of the four step-response transients occurring during the ΔT_1, ΔT_2, ΔT_3 and ΔT_4 periods highlighted in Figure 4.31a is shown in Figure 4.31b. As it can be seen, these transients present a spectral peak at ≈ 6 Hz in the dq-frame, which corresponds to a positive-sequence mode at ≈ 56 Hz in the abc-frame. The magnitude of this spectral peak increases with $i^+_{q,ref}$, indicating less damping of the system dynamics at higher current generation levels, in line with the results of the presented analytical study. The presence of smaller spectral peaks at $\approx$ 106 Hz, which indicate the existence of a negative-sequence mode at $\approx$ 56 Hz in the *abc*-frame, is attributed to small imbalance in the electrical impedances.

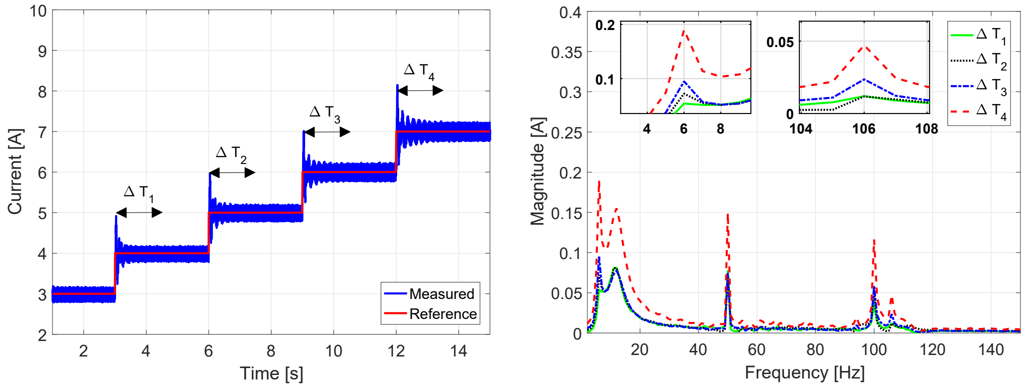

(a) (b)

Figure 4.31: (a) Recorded response of $i_q^+(t)$ for a staircase-like increase of $i_{q,ref}^+(t)$ from 3A to 7A. (b) Magnitude spectra of the recorded transients, occurring during the ΔT_1,ΔT_2, ΔT_3 and ΔT_4 periods.

These experimental data are therefore in agreement with the carried out analytical study, with a substantial overlap between the critical resonance frequency predicted theoretically ($\approx$ 57 Hz) and the one verified experimentally ($\approx$ 56 Hz). They therefore verify the effectiveness of the introduced stability margin to quantify the relative stability of the system.

4.5 Chapter Summary

The notion of small-signal converter admittance has been introduced. A systematic methodology to derive its expression in the sequence-frame has been presented and verified experimentally, proving its effectiveness regardless of the converter controller scheme. A framework to assess the stability of the system in the sequence-frame has been defined, which, compared to the impedance-based stability criterion [54], takes into account the existing coupling between the positive and the negative sequence converter admittance terms. Such methodology has been applied to assess the stability of the studied wind farm system and its accuracy has been verified experimentally. The study

has highlighted that in the connection between a wind farm and the grid both a high frequency resonance and a weak grid effect are likely to occur, the former caused by the parasitic capacitance of the installed cables and lines, the latter caused by the larger equivalent small-signal converter admittance of the wind farm.
A criterion to infer whether the mentioned coupling is relevant or not to the stability study has been presented. This is based on the evaluation of the diagonal dominance property of the impedance-based small-signal model of the system in the sequence-frame. It has been shown how such property might be lacking in the scenario of a converter connected to the weak grid. A stability margin that takes such coupling into account has been introduced. Its effectiveness has been verified experimentally, and its more conservative feature compared to the SISO stability margins used in the impedance-based stability criterion [54] has been highlighted.

Chapter 5

Wind farm resonances: mitigation techniques

The stability assessment of the studied wind farm system, presented in Section 4.2.1, has shown how the electrical resonances caused by the cables and lines connecting the wind farm to the grid generate instability when a greater number of turbines are operating. These resonances strongly depend on the wind farm layout and operating point, as well as on the cable/line parameters [40], [8], thus making the proposed solutions applicable on a case-by-case scenario, as discussed in Section 1.2.

Compared to the existing approaches, generic mitigation techniques which do not rely either on the knowledge of the wind farm electrical specifics or on parameter tuning are presented in this Chapter.

The stability study carried out has also highlighted the greater risk with weak grid problems. It will be shown how one of the proposed strategies, the Fast Voltage Feed-Forward (FVFF) technique, is also beneficial to such weak grid issues.

The presented mitigation techniques aim to reduce the phase loss of the eigenvalues of $\hat{L}_{PN}(s)$, calculated for the modelled wind farm-grid system and shown in Figures 4.13-4.14, in Section 4.2.1.1. Such excessive phase loss, which is particularly evident in the range of frequencies where the wind farm resonances occur, is attributed to the discrete controller delay.

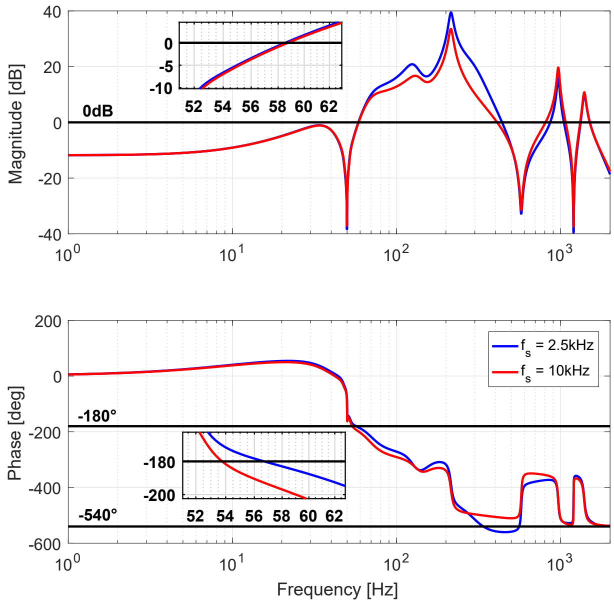

Figure 5.1: Bode plot of the eigenvalue $\lambda_1(2\pi f)$ of $\hat{L}_{PN}(s)$ for different values of the switching frequency f_s, with $N = 54$.

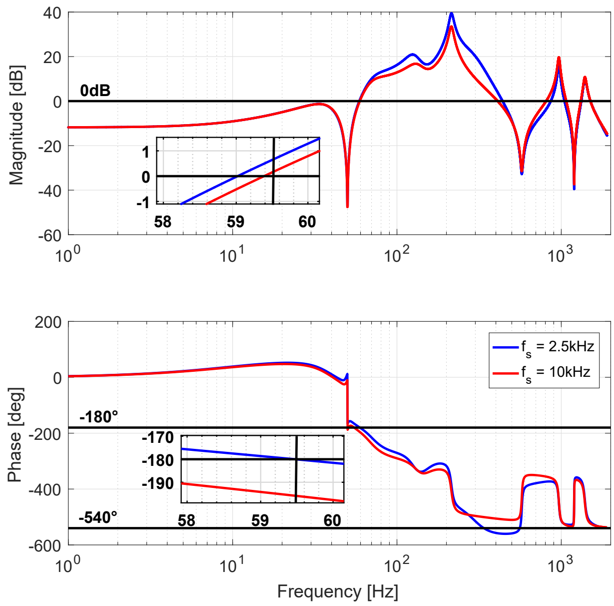

Figure 5.2: Bode plot of the eigenvalue $\lambda_2(2\pi f)$ of $\hat{L}_{PN}(s)$ for different values of the switching frequency f_s, with $N = 54$.

A confirmation of the impact of the controller delay on such phase loss effect is provided in Figures 5.1 and 5.2 where, for the grid-connected wind farm system discussed in Section 4.2.1, the Bode plots of the eigenvalues of $\hat{L}_{PN}(s)$ are drawn for two different converter switching frequencies, $f_s = 2.5$ kHz and $f_s = 10$ kHz. The case with $N = 54$ operating turbines is shown. As it can be seen, when f_s is increased, the mentioned phase loss is reduced as a consequence of the lower equivalent delay of the controller [91] (see equation (2.19)). The stabilising effect of using a higher switching frequency of the inverter is confirmed by the corresponding Nyquist plots of $I + \hat{L}_{PN}(s)$, shown in Figure 5.3. However, such a strategy would be detrimental for the inverter efficiency, and, for this reason, would not be feasible in a real application [71].

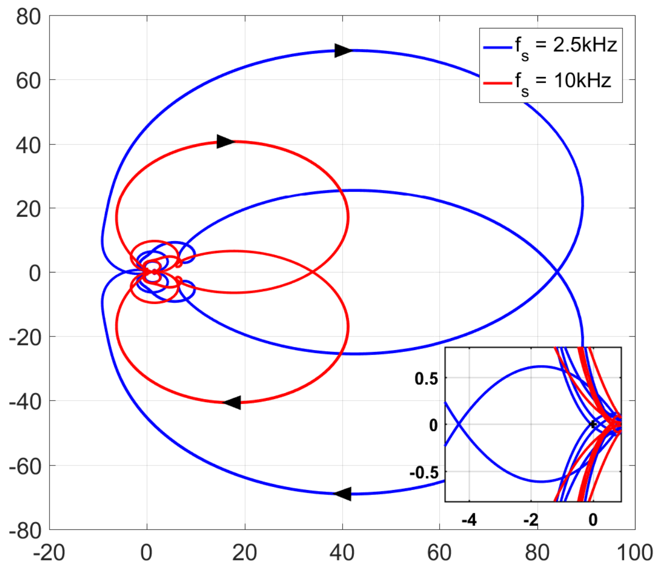

Figure 5.3: Nyquist plot of $I + \hat{L}_{PN}(s)$ for different values of the switching frequency f_s, with $N = 54$.

Alternative methods to compensate for the controller delay have been proposed in the literature and typically consist in adding a tuned filter in the inverter control system. However, this solution is able to compensate for the delay effect only at a specific design frequency [58], and therefore is not able to cope effectively with the variability of the wind farm resonance frequencies, which change with the wind farm topology and operating point. Also, the technique of adding filters in the converter control scheme has in general been seen to have an effectiveness significantly dependant on the wind farm design [29], [34], [42], [44], [46]. For this reason this approach has not been pursued.

On the other hand, this work has been focusing on reducing the controller delay by changing the hardware implementation of the controller algorithm. The aim has been to make a more efficient use of the hardware resources to tackle the problem, without increasing the converter switching frequency. A straightforward way to reduce the controller delay, by modifying the execution of the controller algorithm, would be to change the PWM regular sampling method, from symmetrical, which is the technique used in the baseline controller scheme of the studied wind farm, to asymmetrical (see Appendix A for the description of these PWM sampling methods). In fact, this would allow a reduction of the controller delay by 50 % [71]. However, such beneficial effect may not be enough to achieve the desired stability performance (this aspect will be discussed in more detail in Section 5.2.2.1). Thereby, two more techniques have been designed to reduce the controller delay further.

The first proposed strategy aims to reduce the delay on the voltage feed-forward term of the controller scheme (see Figure 2.20), and for this reason it has been named FVFF. The second one aims to reduce the delay associated to the current loop calculations, and, for this reason, it has been named Reduced Current Delay (RCD) strategy.

The implementation of these techniques has been made possible by the more recent availability of control boards with two processor cores, such as the TMS320F28377D control board by Texas Instrument, or the ZC706 control board by Xilinx. The latter model has been used in this work. By making use of two microprocessors, it has been possible to double the processing power of the control board, and therefore to execute different sections of the controller algorithm simultaneously.

A description of the designed hardware implementation of the controller is provided in Section 5.1, where the baseline execution of the controller algorithm is presented. Both the FVFF and the RCD strategies will modify such a baseline execution, with the purpose of minimising the delay of the controller action. One processor is used to sample the plant signals, while the other one is used to execute the vector control algorithm. The possibility of oversampling of the U voltage signal will be exploited by the FVFF

strategy. The use of FPGA modules will be exploited by the RCD strategy and will allow to adjust, in a scale of nanoseconds, the converter PWM pattern currently being applied to modulate the inverter AC voltage.
The FVFF technique is presented in Section 5.2. Its hardware implementation is described and its stabilising effect is validated both analytically and experimentally. Moreover, it will be shown how this strategy is also beneficial to weak grid issues. Thereafter, in Section 5.3, the RCD strategy is presented. It will be shown how the optimal performance of the controller is obtained when both of these strategies are used, which therefore represents the final design proposed by this work.

5.1 Controller hardware implementation

The controller has been implemented making use of the Xilinx Zynq-7000 ZC706 evaluation board. The board is composed of a Processing System (PS) section, where two ARM® Cortex™-A9 MPCore™ processors are included, and of a Programmable Logic (PL) section, based on FPGA technology [112]. The two sections can operate simultaneously, exchanging data and control signals.
A schematic block diagram of the controller hardware implementation is represented in Figure 5.4. Both ARM® processors have been used, which will be referred to as Processor 1 (P1) and Processor 2 (P2) in the following description.
In this design, the two processors of the PS section are used to execute the controller algorithm, while FPGA modules implemented in the PL section control the operation of the ADC/DAC board as well as generate the PWM pattern delivered to the converter's gate driver.
The controller operation is synchronized to two clocks, both implemented in the PL section. The main clock triggers P2 by generating an interrupt every T_{sample}. This is equal to $\frac{1}{f_s}$ if symmetrical sampling is used, or $\frac{1}{2f_s}$ in case of asymmetrical sampling [71]. The second clock, at $f_{OS} = 100$ kHz, is derived from the main clock and controls both the operation of P1, by sending an interrupt every $T_{OS} = \frac{1}{f_{OS}} = 10\ \mu$s, and that of the ADC driver, activating sampling of the plant signals.

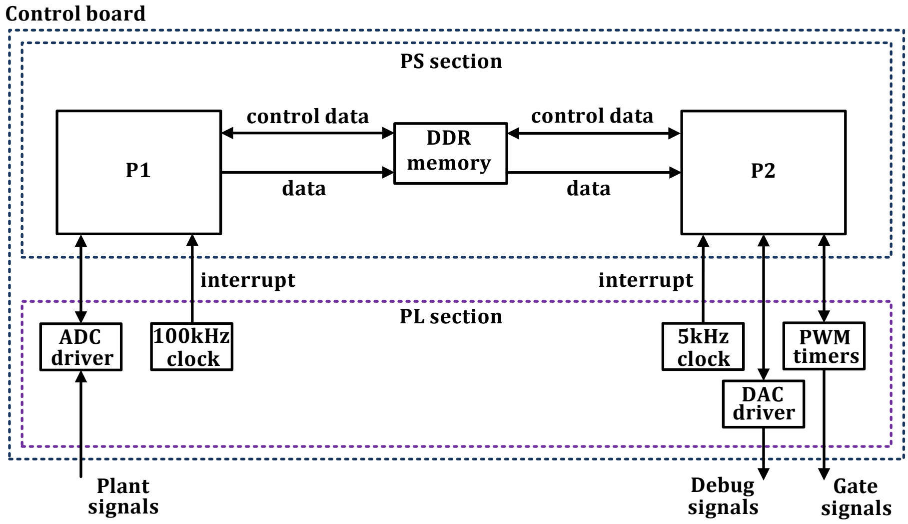

Figure 5.4: Block diagram of the controller hardware implementation.

The notation detailed in Table 5.1 is used for the time variable.

Table 5.1: Notation used for the time variable

Symbol	Description	Sampling time
t	continuous time	-
t_k	discrete time	T_{sample}
$\bar{t}_n$	discrete time	T_{OS}

Figure 5.5 shows a time diagram of the baseline execution of the controller algorithm. The k^{th} sampling period $[t_k, t_{k+1}]$ is shown, with $p = T_{sample} f_{OS}$.
P1 reads the DC voltage U_{DC} and the inverter current i at $t = t_k$ (i.e. at the beginning of each T_{sample} period), and the AC voltage U at $t = \bar{t}_n, \bar{t}_{n+1}, \bar{t}_{n+2}, ..., \bar{t}_{n+p}$, i.e. every T_{OS}. While no filter is applied on the i current and on the U_{DC} voltage signals, the anti-aliasing filter discussed in Section 2.2.1.4 is applied by P1 on U. The operations executed by P1 have been indicated as "S" in the timing diagram. By making use of the shared DDR memory (see Figure 5.4), P1 provides P2 with the sampled plant signals, namely $U_S[k]$=$U_S(t_k)$, $i_S[k] = i_S(t_k)$ and $U_{DC}[k] = U_{DC}(t_k)$), every T_{sample}. It is worth mentioning that the whole data set is sent to P2 a $\Delta\hat{T}$ time after the acquisition of the plant signals (which occurs at $t = t_k$). $\Delta\hat{T}$ is the time it takes P1 to execute its

"S" algorithm.

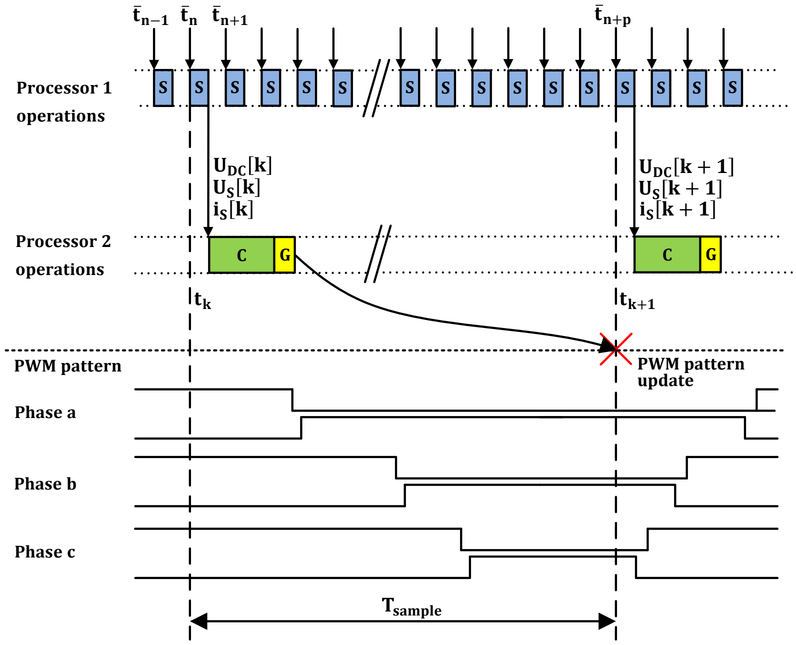

Figure 5.5: Timing diagram of the baseline controller operation.

The calculations carried out by P2 consist in the vector control algorithm (operations "C") and in the calculation of the PWM timers (operations "G"). Such PWM pattern is delivered to the inverter switches at $t = t_{k+1}$, i.e. at the beginning of the next sampling period. This shows the T_{sample} delay between the instant when the plant signals are measured and the moment when the resulting PWM pattern is delivered. The proposed mitigation techniques aim to reduce such delay.
A summary of the operations executed by the controller is provided in Table 5.2, where their execution time has also been specified. A detailed description of the digital implementation of the controller algorithm can be found in Appendix E.

Table 5.2: Summary of the operations executed by the controller algorithm.

Operations	Processor	Execution time	Notes
S	P1	7 μs	Sampling + Anti-aliasing filter on AC voltage
C	P2	23 μs	Vector control algorithm
G	P2	6 μs	Calculation of the PWM pattern

5.2 FVFF strategy

The first mitigation method is presented as follows. In Section 5.2.1 the operation of the FVFF technique is described. In Sections 5.2.2 and 5.2.3 its benefits on the controller performance will be proven theoretically and experimentally.

5.2.1 Description of the technique

The FVFF strategy consists in a revision of the way the voltage feed-forward term of the converter current controller contributes to the control action (see the control scheme in Figure 2.20). In order to maximise the damping capabilities of this term [58], this strategy aims to make such term as close as possible to the latest sample of the measured voltage U. In order to do so, the FVFF strategy modifies the baseline hardware implementation of the controller algorithm, discussed in Section 5.1.

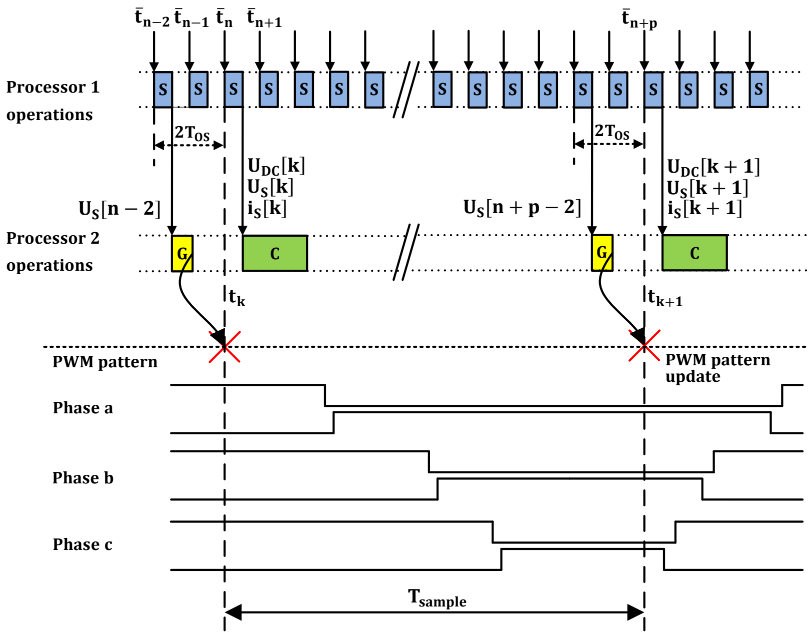

Figure 5.6: Timing diagram of the controller operation with the FVFF strategy.

The timing diagram illustrating the operation of the FVFF technique is shown in Figure 5.6. While in the baseline controller operation the voltage signal used in the feed-forward term is the one sampled at the beginning of each switching period (i.e. the

signal $U_S[k]$ in Figure 5.6), in the proposed strategy the latest voltage sample available during the present sampling period $[t_k, t_{k+1}]$ is instead utilised.
A practical constraint in the implementation of this strategy is the hardware processing time needed to execute the "S" and "G" operations. Based on the execution times detailed in Table 5.2, it takes $\approx$ 13 μs to complete the "S" and "G" calculations. Therefore, the latest voltage sample that can be used to calculate the Voltage Feed-Forward (VFF) within the present sampling period $[t_k, t_{k+1}]$, is the one read a $2T_{OS}$ time before its end ($U_S[n+p-2]$ in Fig. 5.6). By using this latest sample it has been possible to reduce the controller delay affecting the feed-forward term from the T_{sample} value of the baseline design down to $2T_{OS}$.

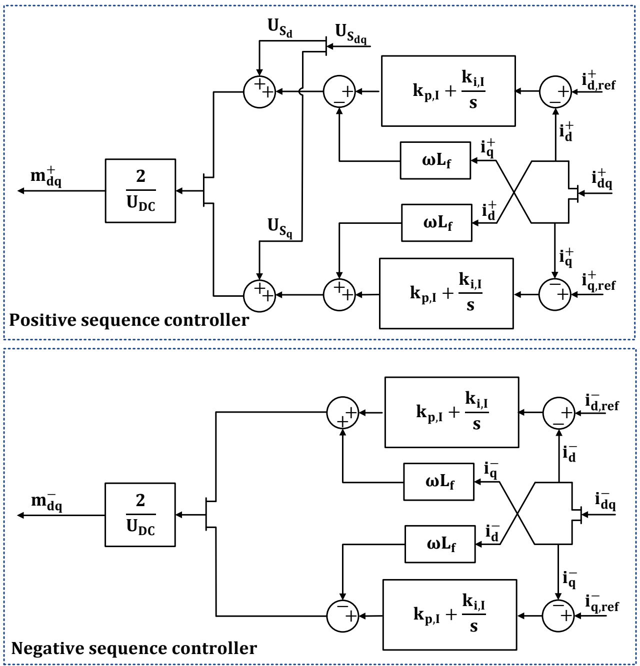

Figure 5.7: Block diagram of the current controller in the proposed FVFF strategy.

A modification has also been applied on the current control loops. Considering the controller scheme in Figure 2.20, the low pass filter employed in the feed-forward term of the current controllers has been removed. In fact, despite the fact that it allows an attenuation of the higher harmonics of the measured voltage, this filter causes a significant phase lag on the measured U signal, which curbs the damping properties of the feed-forward term. Figure 5.7 illustrates the revised version of such control loops, where it can be seen how the feed-forward term $U_{S_{dq}}$ now directly contributes to define the outputs of the positive sequence current loop. It is worth highlighting that the $U_{S_{dq}}$ signal includes both the positive and the negative sequence components of the measured U voltage.

The effect of the FVFF strategy on the stability of the studied wind farm system will be shown in the following Section 5.2.2. Thereafter, an experimental verification of its effectiveness will be provided in Section 5.2.3.

5.2.2 Effect of the FVFF strategy on the wind farm resonances

The impact of the FVFF strategy on the stability performance of the wind farm system described in Section 4.2.1 has been verified. The new Nyquist plots of $I + \hat{L}_{PN}(s)$ are shown in Figure 5.8, indicating that the system is now stable for any considered number N of operating turbines (see Figure 4.12 for comparison with the baseline controller). These results have been obtained considering a PWM symmetrical sampling technique.

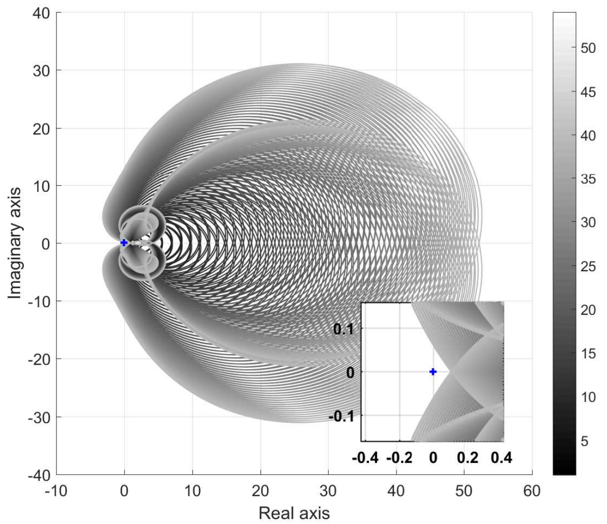

Figure 5.8: Nyquist plot of $I + \hat{L}_{PN}(s)$ for different values of the number of operating turbines N, considering the revised controller design where the FVFF strategy has been implemented.

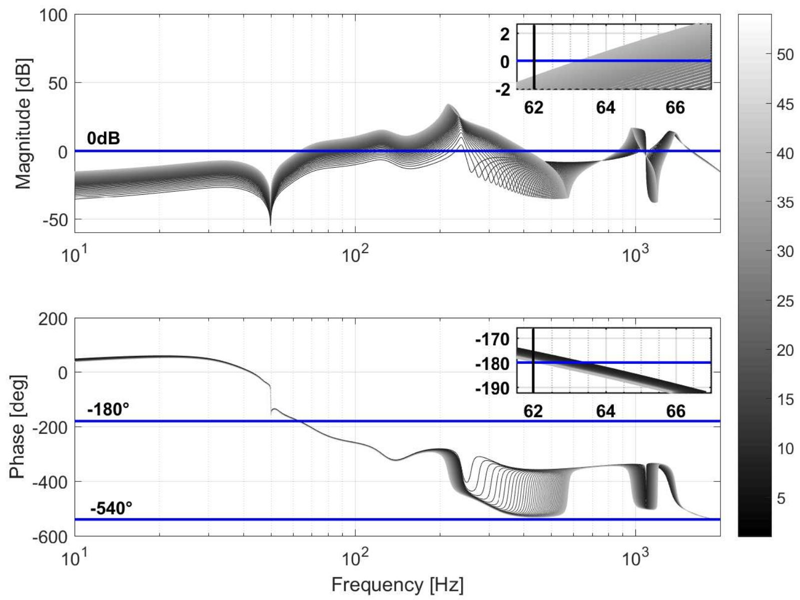

Figure 5.9: Bode plot of the eigenvalue $\lambda_1(2\pi f)$ of $\hat{L}_{PN}(s)$ for different values of the number of operating turbines N, considering the revised controller design where the FVFF strategy has been implemented.

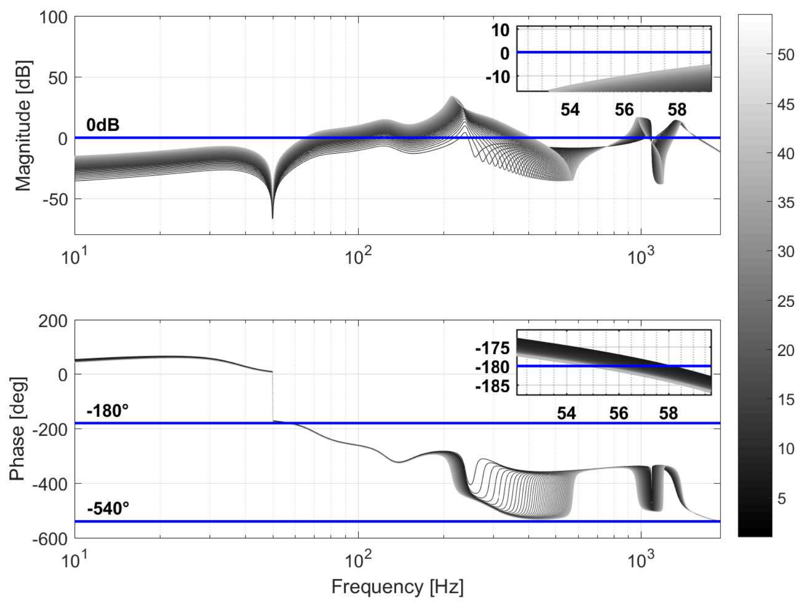

Figure 5.10: Bode plot of the eigenvalue $\lambda_2(2\pi f)$ of $\hat{L}_{PN}(s)$ for different values of the number of operating turbines N, considering the revised controller design where the FVFF strategy has been implemented.

Such stabilising effect of the FVFF term derives from its impact on the phase of the system eigenvalues $\lambda_1(j2\pi f)$ and $\lambda_2(j2\pi f)$, as shown in their Bode plots in Figures 5.9 and 5.10, respectively. Thanks to the reduced phase loss achieved in the [300 Hz, 600 Hz] frequency range, the wind farm resonances are counteracted effectively making the system stable. It is highlighted how the FVFF strategy also improves the system dynamics in the lower frequency range, mitigating the weak grid issues observed in the range of 60 Hz for higher N values (see Figure 4.14 and the related comments in Section 4.2.1.1).

5.2.2.1 Impact of the PWM sampling method

In this Section effect of the PWM sampling technique on the stability performance of the studied wind farm system is considered. In particular, the scenarios where an asymmetrical sampling is used either with or without the FVFF strategy are compared to the controller scheme analysed in the previous Section (i.e. the one where the FVFF strategy is used with symmetrical sampling).

The resulting Nyquist plots are shown in Figure 5.11. The case with $N = 54$ is shown which corresponds to the most critical operating condition for the wind farm. As it can be seen from these plots, changing the PWM technique of the baseline controller from symmetric to asymmetric PWM is not sufficient to stabilise the system dynamics. This is confirmed by the Bode plots of the eigenvalues $\lambda_1(j2\pi f)$ and $\lambda_2(j2\pi f)$ of $\hat{L}_{PN}(j\omega)$, shown in Figures 5.12 and 5.13 respectively. As it can be seen, the phase loss of these functions is still too high in the [1000 Hz, 1200 Hz] range, i.e. in the frequency range of the second group of resonance of $Y_{TH}(s)$ (see Figure 2.10), making the system unstable. This confirms the need to design alternative methods to mitigate the effect of the controller delay further.

Comparing the two configurations where the FVFF strategy is employed, it can be observed how the benefit of using a PWM asymmetrical sampling technique is mostly in the higher frequency range, where the effect of the controller delay becomes more significant. An improvement can also be noticed in the [50 Hz, 70 Hz] range, with the low frequency resonance due to the weak grid effect becoming better damped.

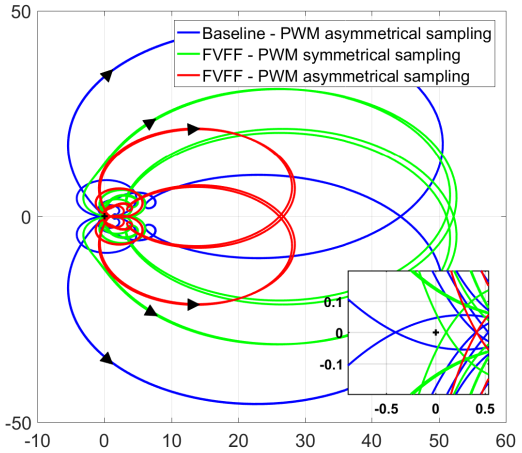

Figure 5.11: Comparison between the Nyquist plots of $I + \hat{L}_{PN}(s)$ for the scenarios where the FVFF strategy is combined with either a symmetrical or an asymmetrical sampling technique and the one where the baseline controller is used with asymmetrical sampling. The case with $N = 54$ is shown.

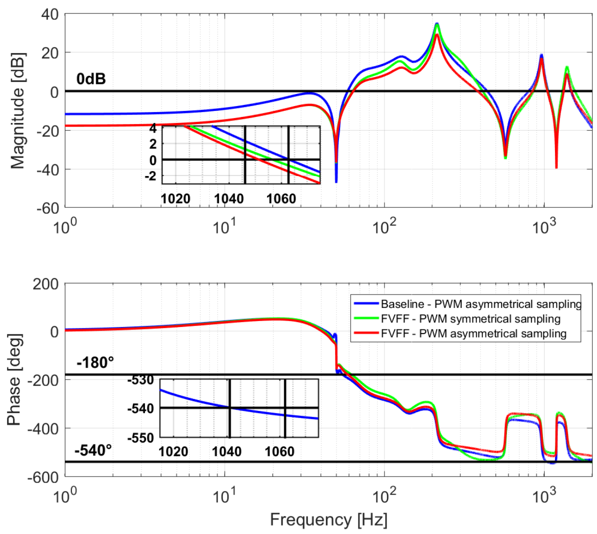

Figure 5.12: Comparison between the Bode plots of the eigenvalue $\lambda_1(2\pi f)$ of $\hat{L}_{PN}(s)$ for the scenarios where the FVFF strategy is combined with either a symmetrical or an asymmetrical sampling technique and the one where the baseline controller is used with asymmetrical sampling. The case with $N = 54$ is shown.

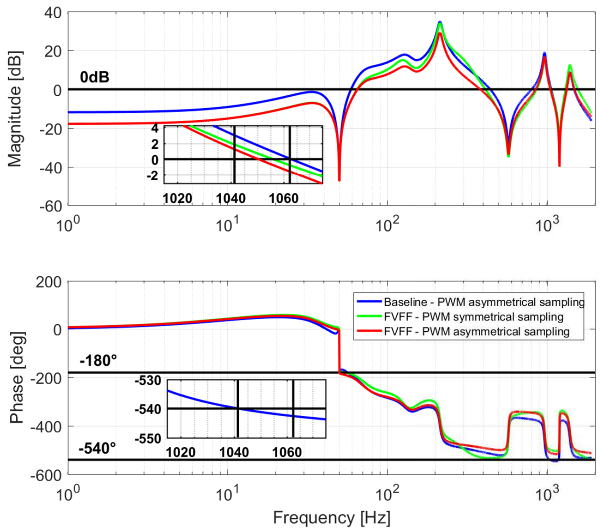

Figure 5.13: Comparison between the Bode plots of the eigenvalue $\lambda_2(2\pi f)$ of $\hat{L}_{PN}(s)$ for the scenarios where the FVFF strategy is combined with either a symmetrical or an asymmetrical sampling technique and the one where the baseline controller is used with asymmetrical sampling. The case with $N = 54$ is shown.

As expected, the improvement on the stability performance obtained by combining the asymmetrical sampling method with the FVFF strategy is confirmed by the stability margins of the system, calculated based on the methodology described in Section 4.4, and detailed in Table 5.3. The figures confirm the instability of the configuration where the baseline controller is used with an asymmetrical sampling method, and indicate how the weak grid effect ultimately becomes the critical aspect that limits the system stability performance, when the FVFF strtegy is combined with asymmetrical sampling. It is worth mentioned that when the FVFF strategy is used with symmetrical sampling it is not possible to calculate the d_∞ perturbation norm, as the system is not diagonally dominance (i.e. the conditions (4.18) are not verified).

The results of the stability study are aligned with those obtained with the corresponding TD model of the wind farm-grid system, as shown in the Figure 5.14. The step response of the q^+ current loop is shown for a 5 % increase in the $i^+_{q,ref}$ set-point. As it can be seen, in both the scenarios where either the symmetrical or the asymmetrical sampling technique is combined with the FVFF strategy, the system is stable.

Table 5.3: Analysis of the wind farm system relative stability for the control designs where the FVFF strategy is combined either with symmetrical or with asymmetrical sampling and for the configuration where the baseline controller is used with asymmetrical sampling. The case with $N = 54$ is shown.

Control strategy	GM^{+}_{SISO} [dB]	PM^{+}_{SISO} [deg]	GM^{-}_{SISO} [dB]	GM^{-}_{SISO} [deg]	d_{∞} -	$GM_{d_{\infty}}$ [dB]	$PM_{d_{\infty}}$ [deg]
Baseline - PWM symm.	-3 (at 1041 Hz)	-2.7(1063 Hz)	-3 (at 1041 Hz)	-2.7(1063 Hz)	< 0	-	-
FVFF - PWM symm.	0.8 (at 62 Hz)	3.5 (at 63 Hz)	12.6 (at 55 Hz)	7.7 (412 Hz)	< 0	-	-
FVFF - PWM asymm	5 (at 59 Hz)	19 (at 64 Hz)	47 (at 51 Hz)	34 (at 65 Hz)	0.132	≥ 1.23	≥ 7.6

However, a lower overshoot is observed in the latter scenario, conforming the increased damping of the system dynamics assured by this design, in line with the results of the presented stability study, as shown in Figure 5.11.

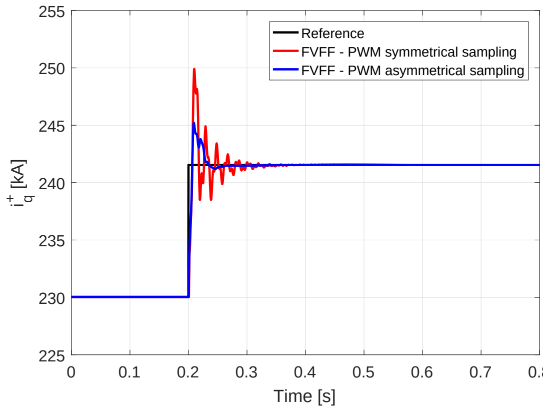

Figure 5.14: Simulated step response of the i_q^+ control loop, making use of the TD model of the wind farm-grid system. The case with $N = 54$ is shown.

5.2.3 Experimental verification

The effectiveness of the FVFF strategy to stabilise the system dynamics has been verified experimentally. Both its capability to counteract the higher frequency resonances caused by the parasitic capacitance of the cables, and its benefit on weak grid issues have been verified, as it will be shown in the following Sections 5.2.3.1 and 5.2.3.2, respectively. The laboratory prototype of the inverter-grid interconnection has been used for these tests. The collected experimental data have been backed up by corresponding results obtained from the stability study of the tested system configurations.

5.2.3.1 Influence on the high frequency resonance

In order to verify the effect of the FVFF term on the high frequency resonance, the laboratory prototype inverter-grid system described in Section 2.3.2.1 has been used. The test described in Section 4.2.1.2 has been repeated making use of the new controller design, where the FVFF strategy has been implemented. Both cases where either symmetrical or asymmetrical sampling is used have been tested, with a switching frequency of 2.5 kHz (see Table 2.6). The results are shown in Figure 5.15, which confirm the beneficial effect of the FVFF strategy on the system stability performance, in both of the tested configurations (see Figure 4.16a for comparison with the baseline controller design).

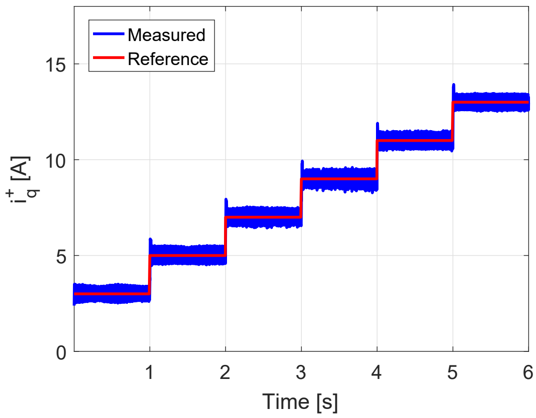

(a)

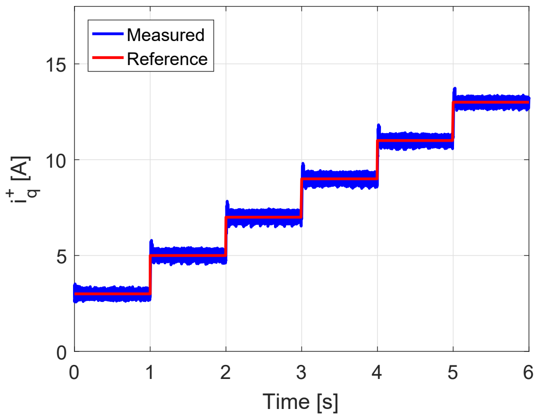

(b)

Figure 5.15: Recorded i_q^+ trend for a staircase-like change in the $i_{q,ref}^+$ set-point, making use of the FVFF strategy; (a) PWM symmetrical sampling; (b) PWM asymmetrical sampling.

The associated Nyquist plots are shown in Figure 5.16, which confirm the stability of the system when the FVFF strategy is utilised. The operating point corresponding to the rated power of the inverter has been considered to generated these results. Thanks to the diagonal dominance property of the test rig system being satisfied, it has also been possible to calculate the corresponding perturbation norm stability margins and draw the corresponding circles, shown in the same Figure 5.16.

The Bode plots of the system eigenvalues are shown in Figures 5.17 and 5.18, respectively. They indicate how in the higher frequency range, where the resonance occurs, the FVFF term has a beneficial effect on the phase loss of both $\lambda_1(j2\pi f)$ and $\lambda_2(j2\pi f)$. As expected, a further improvement is obtained when the asymmetrical PWM sampling technique is used.

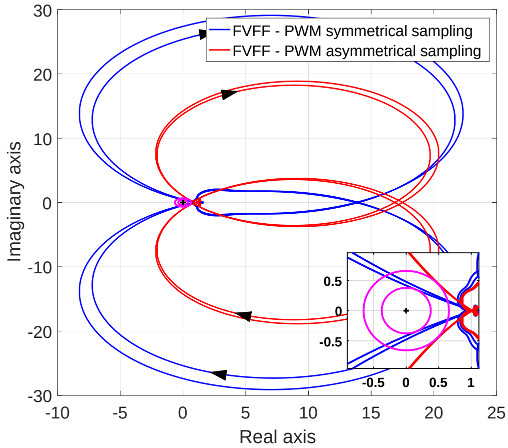

Figure 5.16: Nyquist plot of $I+\hat{L}_{PN}(s)$ for the laboratory tested system, for the scenarios where the FVFF strategy is combined with either a symmetrical or an asymmetrical sampling technique.

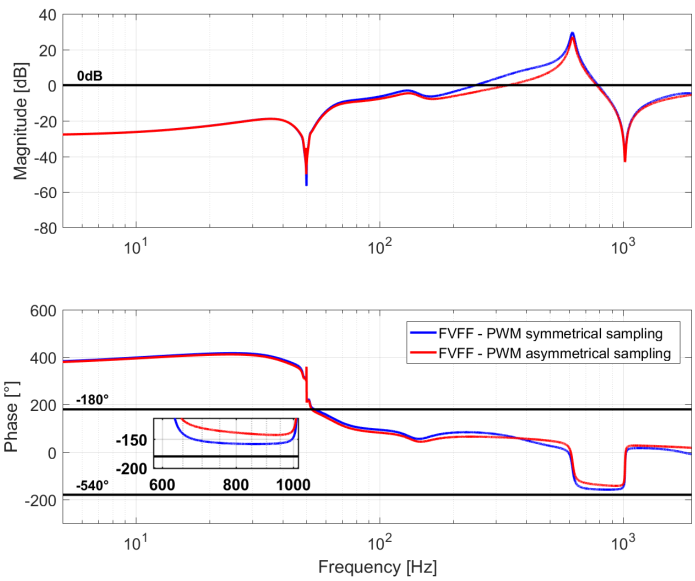

Figure 5.17: Bode plot of the eigenvalue $\lambda_1(j2\pi f)$ of $\hat{L}_{PN}(s)$ for the scenarios where the FVFF strategy is combined with either a symmetrical or an asymmetrical sampling technique.

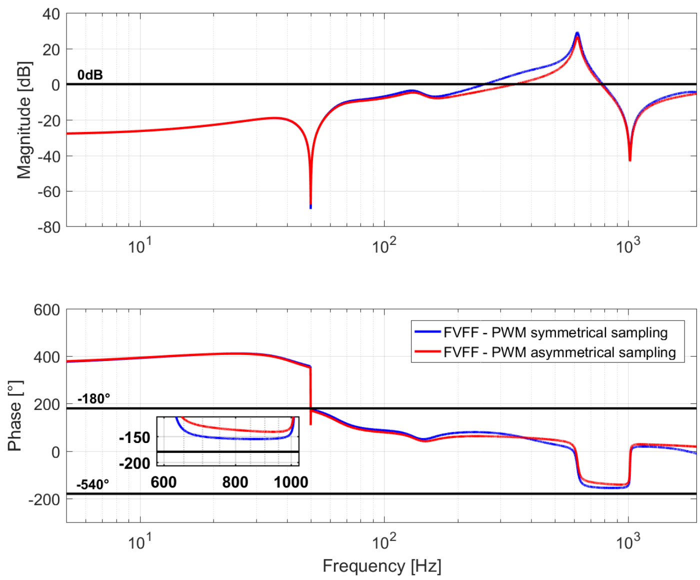

Figure 5.18: Bode plot of the eigenvalue $\lambda_2(j2\pi f)$ of $\hat{L}_{PN}(s)$ for the scenarios where the FVFF strategy is combined with either a symmetrical or an asymmetrical sampling technique.

The resulting stability margins of the system, calculated with the methodology described in Section 4.4, are detailed in Table 5.4. These confirm how a better performance is obtained when the FVFF strategy is used together with the PWM asymmetrical sampling technique.

Table 5.4: Stability margins for the tested laboratory prototype

Control strategy	GM^+_{SISO} **[dB]**	PM^+_{SISO} **[deg]**	GM^-_{SISO} **[dB]**	GM^-_{SISO} **[deg]**	d_∞ -	GM_{d_∞} **[dB]**	PM_{d_∞} **[deg]**
FVFF - PWM symm.	22.9 (at 54 Hz)	22.4 (at 788 Hz)	57 (at 51 Hz)	25.3 (at 786 Hz)	0.38	≥ 4.15	≥ 21.9
FVFF - PWM asymm.	25.7 (at 52.5 Hz)	42.8 (at 776 Hz)	55 (at 51 Hz)	43.4 (at 773 Hz)	0.66	≥ 9.4	≥ 38.5

5.2.3.2 Influence on the weak grid effect

This study has revealed how the connection of a wind farm to the grid is likely to give rise to a lower frequency resonance associated to a weak grid effect. In this Section, the experimental results verifying the beneficial effect the FVFF strategy has on this resonance are presented, comparing the performance of the baseline controller scheme, shown in Figure 2.20, to that of the revised one where the FVFF strategy is

implemented. In these tests, a switching frequency of 2.5 kHz has been used with an asymmetrical PWM regular sampling technique. The test-rig configuration described in Section 2.3.2.3 has been used, where the grid SCR has been varied by modifying the size of the grid inductance L_g, hence reproducing weak grid conditions. The controller parameters listed in Table 2.11 have been utilised.
The results of the tests where the baseline controller is used are shown in Figure 5.19.

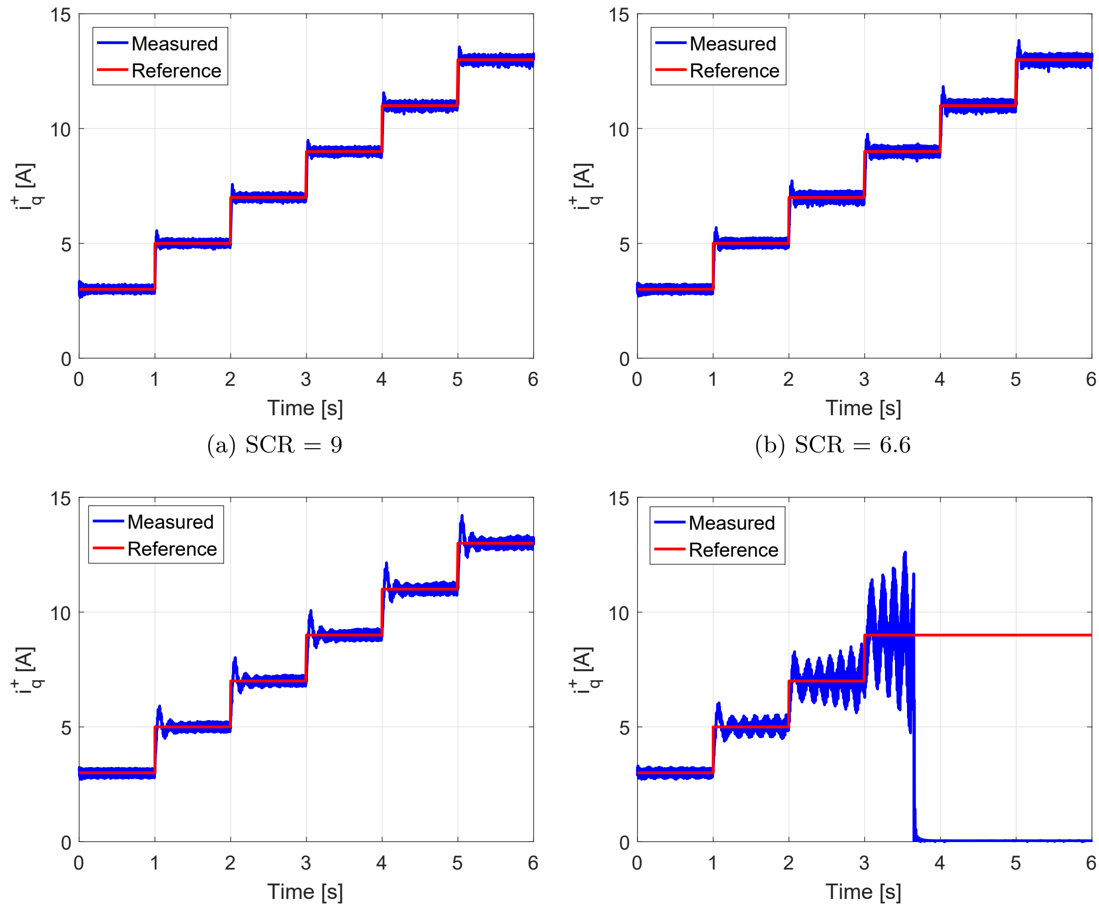

(a) SCR = 9

(b) SCR = 6.6

(c) SCR = 4.5

(d) SCR = 3.4

Figure 5.19: Recorded i_q^+ trend for a staircase-like change in the $i_{q,ref}^+$ set-point for different values of the grid SCR. The baseline controller has been tested.

As it can be seen, increasing the value of the grid inductance, the system dynamics become less and less damped, until when the system becomes unstable for a grid SCR ≤ 3.4. A spectral analysis of the divergent transient shown in Figure 5.19d is shown in

Figure 5.20, which indicates the presence of two components at 7.5 Hz and 107.5 Hz, respectively corresponding to a positive sequence component and a negative sequence component at 57.5 Hz in the *abc*-frame.

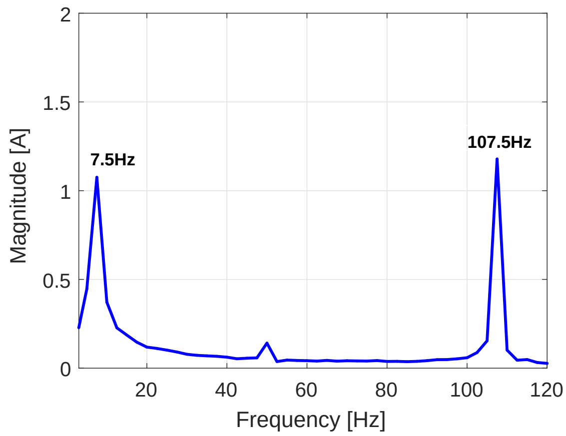

Figure 5.20: Magnitude spectrum of the divergent transient in Figure 5.19d

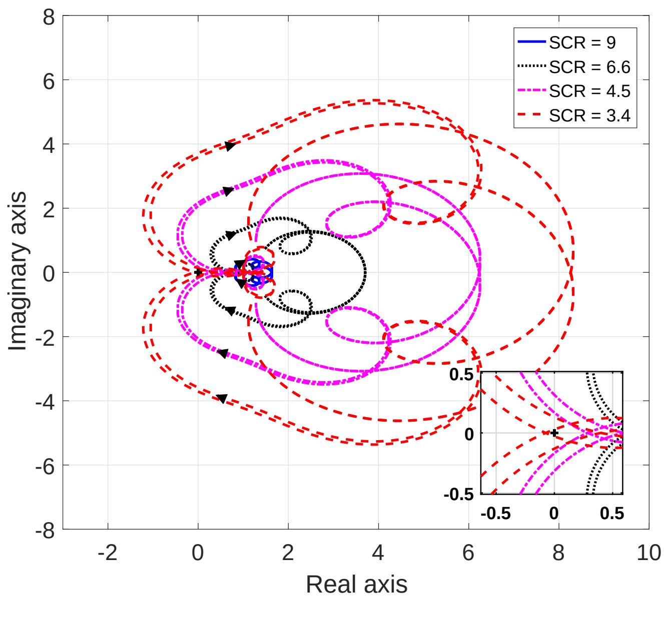

Figure 5.21: Nyquist plot of $I + \hat{L}_{PN}(s)$ for the laboratory tested system, where the baseline controller is used.

These experimental results are confirmed by those of the system stability study. The corresponding Nyquist plots are shown in Figure 5.21, confirming the instability of the system for SCR ≤ 3.4. The operating point corresponding to the rated power of the inverter has been considered to generated these results. The Bode plots of the system eigenvalues $\lambda_1(j2\pi f)$ and $\lambda_2(j2\pi f)$ are shown in Figure 5.22 and 5.23, respectively.

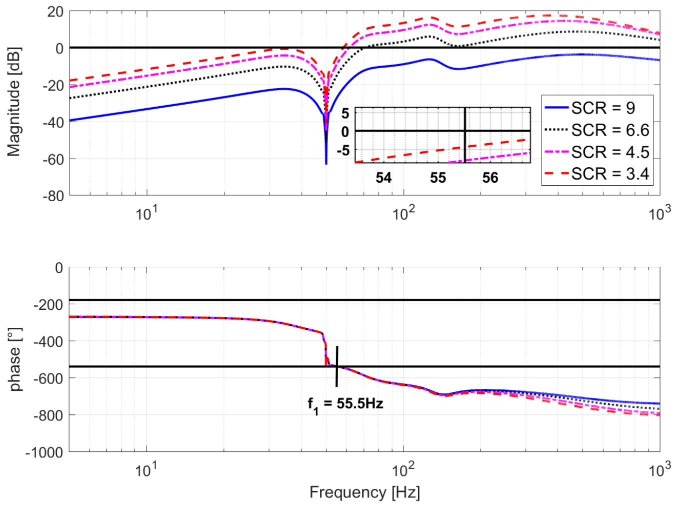

Figure 5.22: Bode plot of the eigenvalue $\lambda_1(j2\pi f)$ of $\hat{L}_{PN}(s)$ for the laboratory tested system, where the baseline controller is applied.

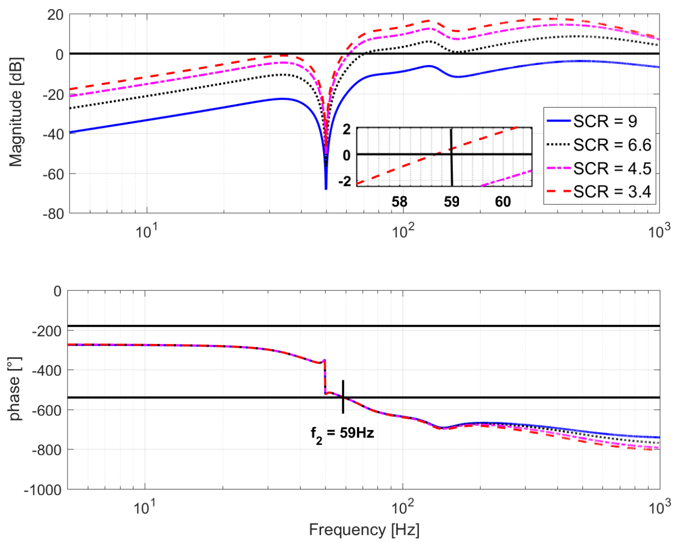

Figure 5.23: Bode plot of the eigenvalue $\lambda_2(j2\pi f)$ of $\hat{L}_{PN}(s)$ for the laboratory tested system, where the baseline controller is applied.

As it can be seen, an undamped negative sequence mode at $f_2 = 59$ Hz is predicted as $\angle\lambda_2(j2\pi f_2) = -540°$ (i.e. $-3 \cdot 180°$) and $|\lambda_2(j2\pi f_2)| > 1$. A substantial match with the frequency of the resonance observed in the test is found. The existence of a positive sequence component at 57.5 Hz, which results from the experimental data, is attributed to imbalance in the grid impedance.

The test has been repeated applying the new controller scheme, where the FVFF strategy has been implemented. As it can be seen from the experimental data shown in Figure 5.24, the system now behaves stably when the grid SCR is > 1.6, hence confirming the beneficial effect of the FVFF strategy on weak grid issues.

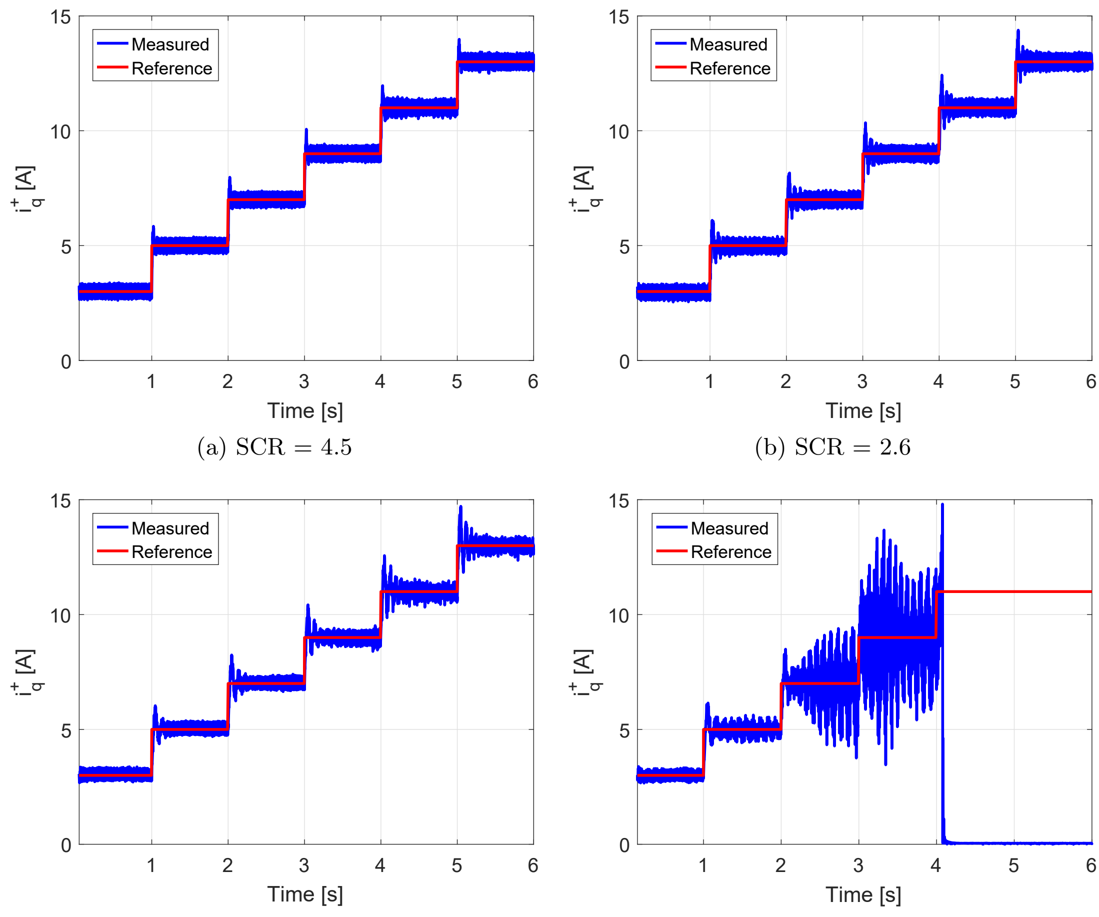

Figure 5.24: Recorded i_q^+ trend for a staircase-like change in the $i_{q,ref}^+$ set-point for different values of grid inductance. The control scheme implementing the FVFF strategy has been tested.

Figure 5.25 shows the magnitude spectrum of the divergent transient in Figure 5.24d, which indicates the presence of two components at 10 Hz and 110 Hz. These are respectively associated to a positive and a negative sequence component at 60 Hz in the *abc*-frame.

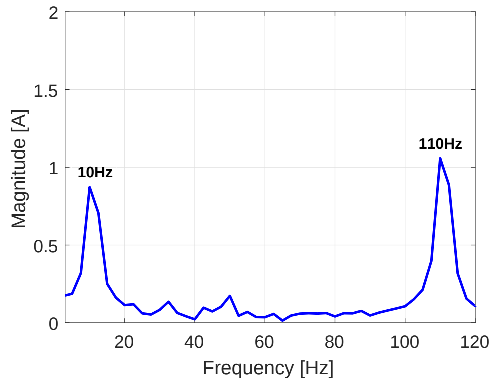

Figure 5.25: Magnitude spectrum of the divergent transient in Figure 5.24d.

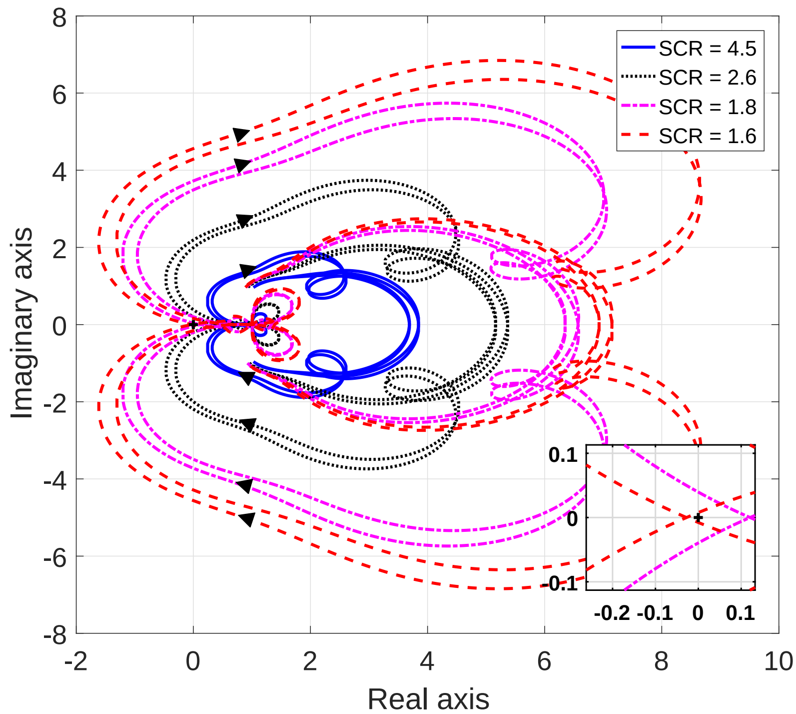

Figure 5.26: Nyquist plot of $I + \hat{L}_{PN}(s)$ for the laboratory tested system, where the FVFF strategy is applied.

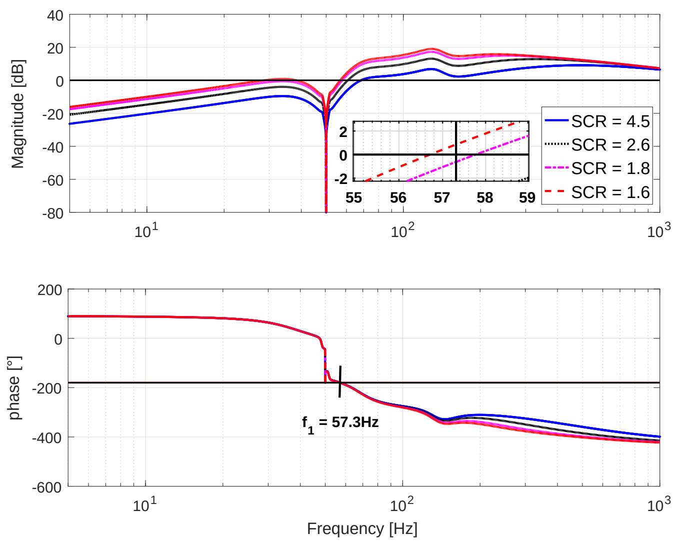

Figure 5.27: Bode plot of the eigenvalue $\lambda_1(j2\pi f)$ of $\hat{L}_{PN}(s)$ for the laboratory tested system, where the FVFF strategy is applied.

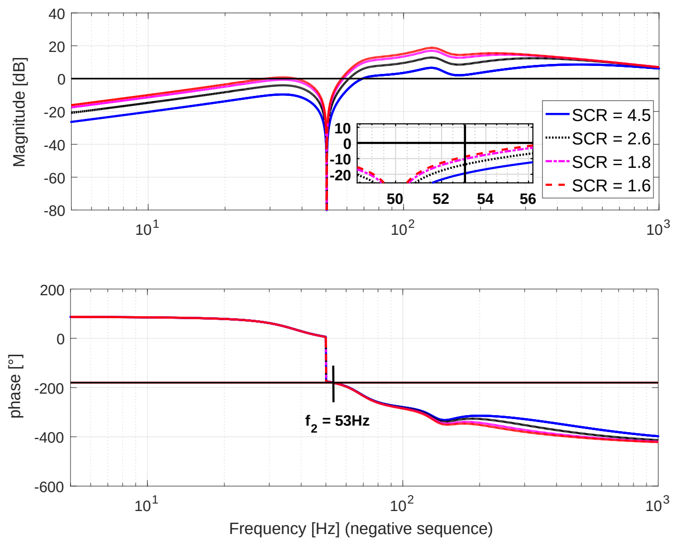

Figure 5.28: Bode plot of the eigenvalue $\lambda_2(j2\pi f)$ of $\hat{L}_{PN}(s)$ for the laboratory tested system, where the FVFF strategy is applied.

The experimental data are in line with the results of the stability study. As it can be seen from the new Nyquist plots of the system, shown in Figure 5.26, stable dynamics are confirmed when the grid SCR is > 1.6. The Bode plots of the system eigenvalues

$\lambda_1(j2\pi f)$ and $\lambda_2(j2\pi f)$ are shown in Figures 5.27 and 5.28, respectively. The presence of an undamped positive sequence mode at $f_1 = 57.3$ Hz is predicted, with a substantial match with the frequency of the experimentally observed resonance. The existence of a negative sequence component at 60 Hz, which results from the experimental data, is attributed to imbalance in the grid impedance.

In conclusion, the tests have allowed a confirmation of the capability of the FVFF strategy to mitigate weak grid issues. In fact, for the test-rig configuration used in the tests, while with the baseline controller the system dynamics have been seen to become unstable for a grid SCR ≤ 3.4, when the FVFF strategy is employed the system becomes unstable only for a SCR ≤ 1.6.

5.3 RCD strategy

The second designed mitigation technique, named the RCD strategy is presented as follows. In Section 5.3.1, the technique is described, and a verification of its functionality is provided experimentally. Thereafter, in Section 5.3.2, its capability to mitigate the wind farm resonance issue is shown highlighting how an optimal performance of the controller is possible when this technique is used in combination with the FVFF term. Such solution is therefore seen as the optimal design suggested by this work, and experimental results will be used to support this conclusion. A sensitivity analysis will also be presented to verify the robustness of this design against changes in the wind farm resonance frequencies.

5.3.1 Description of the technique

The strategy takes an approach similar to the one applied by the FVFF technique, where the latest available AC voltage sample contributes to the definition of the PWM pattern used to control the converter (see the timing diagram in Figure 5.6). In this case, the aim is the utilisation of the latest available measured signals (both current and voltage) to adjust the PWM signals being applied in the current sampling period to modulate the inverter AC voltage. In the implementation of this strategy, an asymmetrical sampling technique has been assumed, with a switching frequency of 2.5 kHz. Two different timing diagrams are defined to describe the operation of the RCD strategy. One, illustrated in Figure 5.29, refers to the case when the RCD strategy operates without the FVFF term. The other, shown in Figure 5.31, applies when both the RCD and the FVFF techniques are active. To explain these timing diagrams, the operations executed in the generic $[t_k, t_{k+1}]$ sampling period will be described as follows.

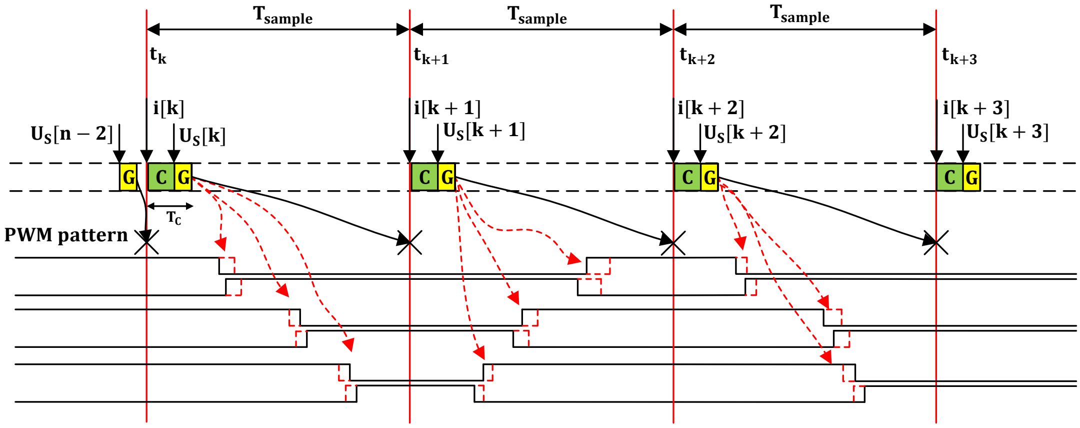

Figure 5.29: Timing diagram illustrating the operation of the RCD technique, when it operates without the FVFF term.

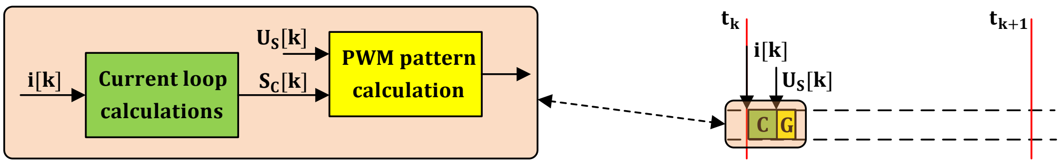

Figure 5.30: Operations executed in the RCD strategy in the $[t_k, t_{k+1}]$ sampling period, when it operates without the FVFF term.

The key point of the RCD strategy is that the gate signals delivered at $t = t_k$ are revised in view of the PWM pattern calculated with the voltage and current samples read at the same t_k time. Because of this correction, shown by red dashed lines in Figures 5.29 and 5.31, the final PWM pattern applied during the $[t_k, t_{k+1}]$ sampling period may no longer result from the AC signals read at time t_{k-1}, but from their values read at t_k. In other words, if the converter switches have not already changed their on/off status, then the results of the controller algorithm are used in the current sample window to review the PWM pattern currently being delivered, instead of being used only in the next sampling window. This therefore allows the elimination of the

T_{sample} delay associated to the discrete sampling of the voltage and current signals.

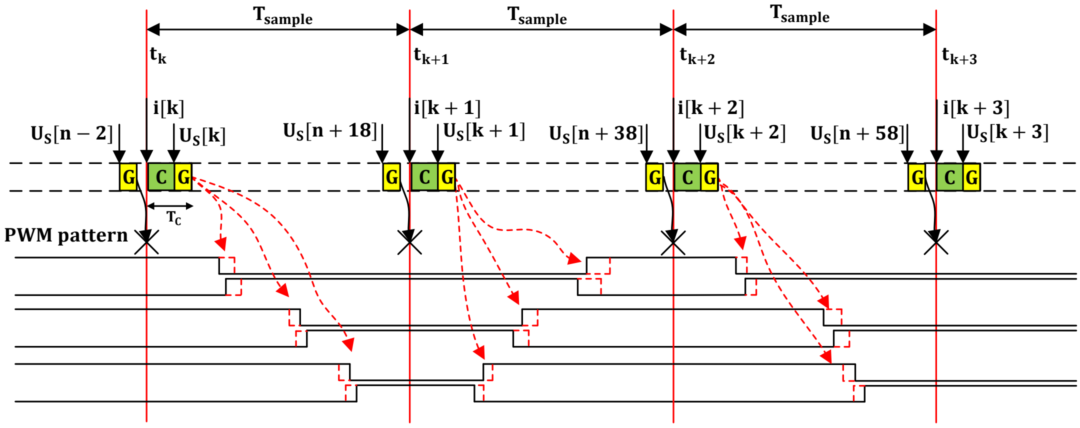

Figure 5.31: Timing diagram illustrating the operation of the RCD technique, when it operates in combination with the FVFF term.

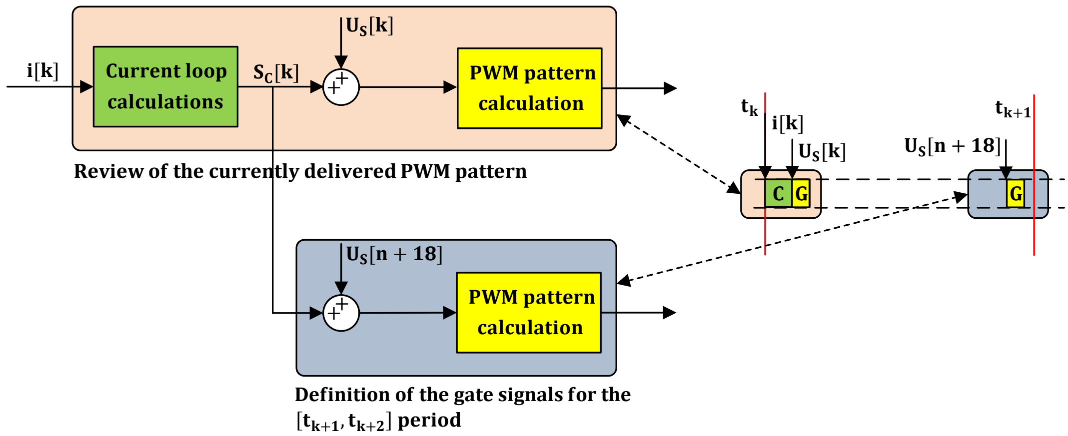

Figure 5.32: Operations executed in the RCD strategy in the $[t_k, t_{k+1}]$ sampling period, when it operates with the FVFF term.

The implementation of this strategy has required a revision of the hardware implementation of the controller algorithm described in Section 5.2. In particular, in the upgraded design, the AC voltage U is still sampled by P1 while the AC inverter current i and the inverter DC voltage U_{DC} are sampled by P2 (see Table 5.5). An optimisation of the ”C” algorithm has been also been carried out to reduce its execution time (this aspect will be discussed in more detail later on).

Table 5.5: Summary of the operations executed by the controller algorithm, when the RCD strategy is used.

Operations	Processor	Execution time	Notes
S	P1	7 μs	AC voltage sampling + Anti-aliasing filter
C	P2	5 μs	Current and DC voltage sampling + Vector control algorithm
G	P2	6 μs	Calculation of the PWM pattern

The result of calculations "C" is based on the inverter AC current sampled at time t_k (see Figures 5.29 and 5.31) and has been indicated as $S_{C,k}$ in Figure 5.30 and 5.32, where the operations associated to the timing diagrams in Figures 5.29 and 5.31 are respectively illustrated. The $S_{C,k}$ data is then combined with the voltage feed-forward term $U_S[k]$, which is provided to P2 by P1 and consists in the AC plant voltage sampled at $t = t_k$, and filtered by the anti-aliasing filter.
When the RCD strategy is used without the FVFF term, the $S_{C,k}$ data is combined with $U_S[k]$ according to the current controller scheme in Figure 2.20. On the other hand, when the FVFF strategy is also used, $S_{C,k}$ is combined with $U_S[k]$ as detailed in the current controller scheme in Figure 5.7.
Once $S_{C,k}$ is combined with $U_S[k]$, the resulting modulation depth is used to calculate the PWM pattern used to update the gate signals delivered in the current sampling window. Based on the execution times detailed in Table 5.5, with the "C" execution time reduced to 5 μs thanks to a carried out optimization of its algorithm, the total time needed for carry out the PWM pattern update is $T_c = 13$ μs.
Finally, only when the FVFF is also active, the $S_{C,k}$ data are then combined with $U_S[n+18]$ to derive the initial version of the PWM pattern that will be delivered in the next $[t_{k+1}, t_{k+2}]$ sampling period (see Figure 5.32). Otherwise, the PWM pattern used to review the currently delivered gate signals will also provide the initial gate signals timers used in the following $[t_{k+1}, t_{k+2}]$ sampling period.

The process of reviewing the currently delivered PWM pattern is based on the principle that only the converter switches that have not changed their status during the initial T_c period can have their turn-on/turn-off times being reviewed. The occurrence of such early switching events depends both on the duration of the T_c period and on the amplitude of the SVM modulation functions. The ideal situation would be that none of the converter switches have changed their status during the mentioned T_c period, so that all of their turn-on/turn-off times can be updated in a straightforward manner. As it will be discussed in Section 5.3.1.2, this condition would also be beneficial for the harmonics content of the modulated converter voltage. Hence, it would be desirable to reduce the calculation time T_c as much as possible (which justifies the need to optimise the execution of the "C" algorithm) as well as to operate the converter with lower PWM modulation depths (this notion will be discussed in more detail in Section 5.3.1.2).

Depending on which and on how many of the converter switches have changed their status during the T_c period, the implemented RCD algorithm operates differently. Its ultimate aim is to review the PWM pattern currently delivered without altering the fundamental component of the modulated line voltage, defined by the PWM pattern being reviewed. The execution of the algorithm depends on W, which is the number of converter legs whose switching devices have changed their status during the T_c period. The currently applied PWM pattern is then updated only if the switching devices of no more than one leg have already switched their on/off status (i.e. only if $W \leq 1$), as illustrated in Figure 5.33.

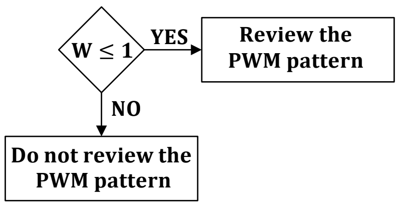

Figure 5.33: Illustration of the operation of the RCD algorithm.

If none of the converter devices have switched during the T_c period (i.e. $W = 0$), all of them will have their PWM timers being reviewed. On the other hand, if either one or both of the switches of any one of the three converter legs have already switched during T_c (i.e. $W = 1$), only the PWM timers of the switches belonging to the other two legs will be updated, as their IGBT modules have not switched yet. The leg where at least one of its two IGBT modules has changed its status during T_c will be indicated as $\hat{x}$ in the following description, with $\hat{x} = a, b, c$. In more detail, when $W = 1$, the PWM on/off timers of the other two legs are replaced by the new reviewed timers after that these are adjusted. This preliminary correction of the new timers depends on when the IGBT modules of leg $\hat{x}$ have switched. Such correction is done not to alter the fundamental component of the modulated line voltage. Finally, when $W \geq 2$, the currently applied PWM pattern is not modified, as any carried out modification would alter the desired line voltage.

If $W = 0$, i.e. no switching activity has occurred during the T_c period, two possible cases may occur, indicated as $W_{0,1}$ and $W_{0,2}$.

An example of scenario $W_{0,1}$ is illustrated in Figure 5.34. In this case, according to the new PWM pattern calculated at $t = t_k + T_c$, the switches will change their state at a time t, with $t_k + T_c < t < t_{k+1}$, i.e. sometime within the present T_{sample} window after $t_k + T_c$. The currently applied PWM pattern is therefore simply replaced by the new pattern calculated at $t = t_k + T_c$.

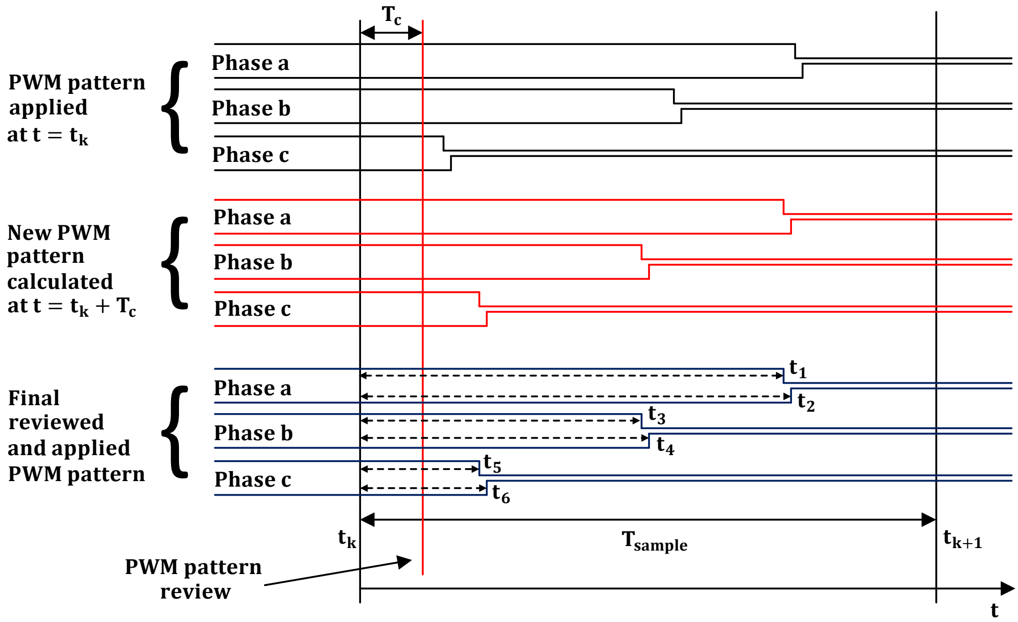

Figure 5.34: Illustration of the operation of the RCD algorithm, case $W_{0,1}$

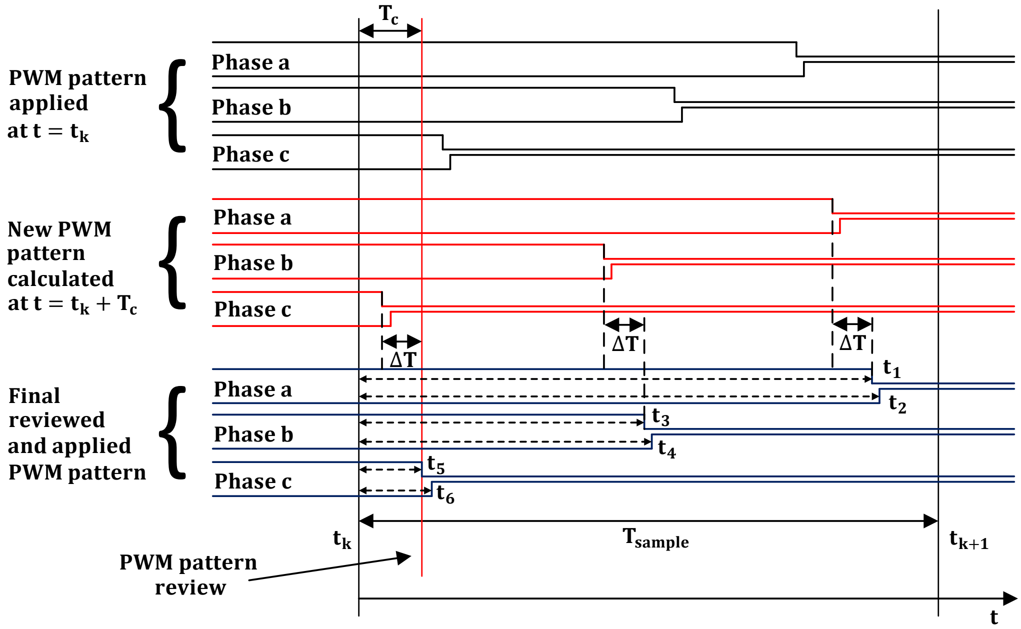

Figure 5.35: Illustration of the operation of the RCD algorithm, case $W_{0,2}$

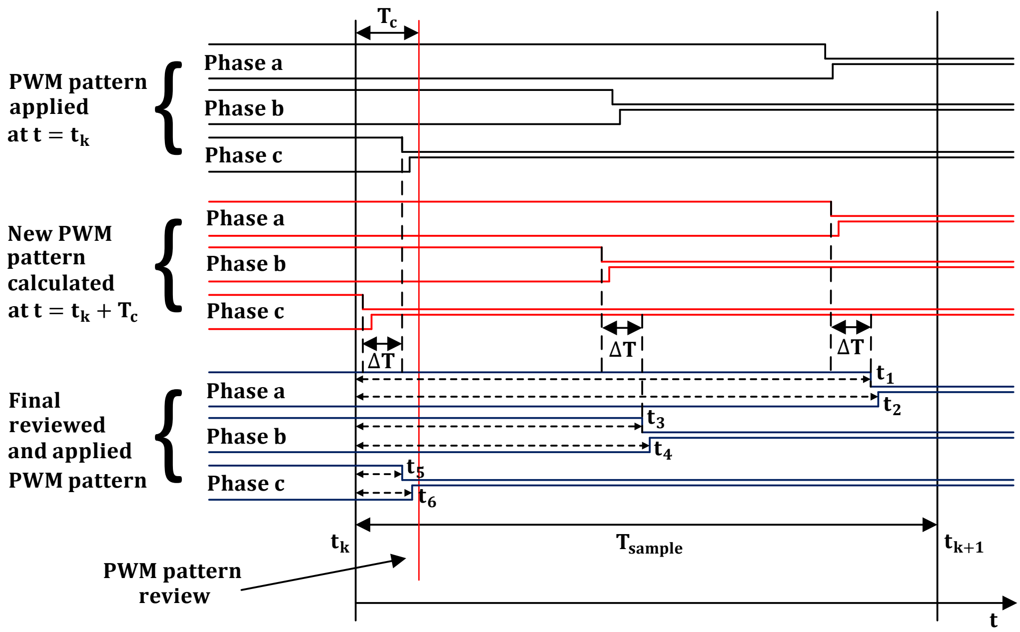

Figure 5.36: Illustration of the operation of the RCD algorithm, case $W_{1,1}$

The scenario $W_{0,2}$ occurs when, according to the new PWM pattern calculated at

$t = t_k + T_c$, the switches of one leg should already have switched at a time t, with $t_k < t < t_k + T_c$. An example of this case is shown in Figure 5.35 where, according to the new pattern, such condition occurs for the switches of phase c. Consequently, these two IGBT modules are switched immediately (i.e. at $t = t_k + T_c$, keeping the constraint on the dead-time). As they have switched with a ΔT delay compared to the time when they were supposed to change their state, such ΔT delay is added to the PWM timers of the IGBT modules of the other two legs, in order to maintain the same modulated line voltage, as previously discussed.
If $W = 1$, i.e. the switches of only one converter leg have already changed their on/off status during the T_c period, two other possible scenarios may occur, referred to as $W_{1,1}$ and $W_{1,2}$.

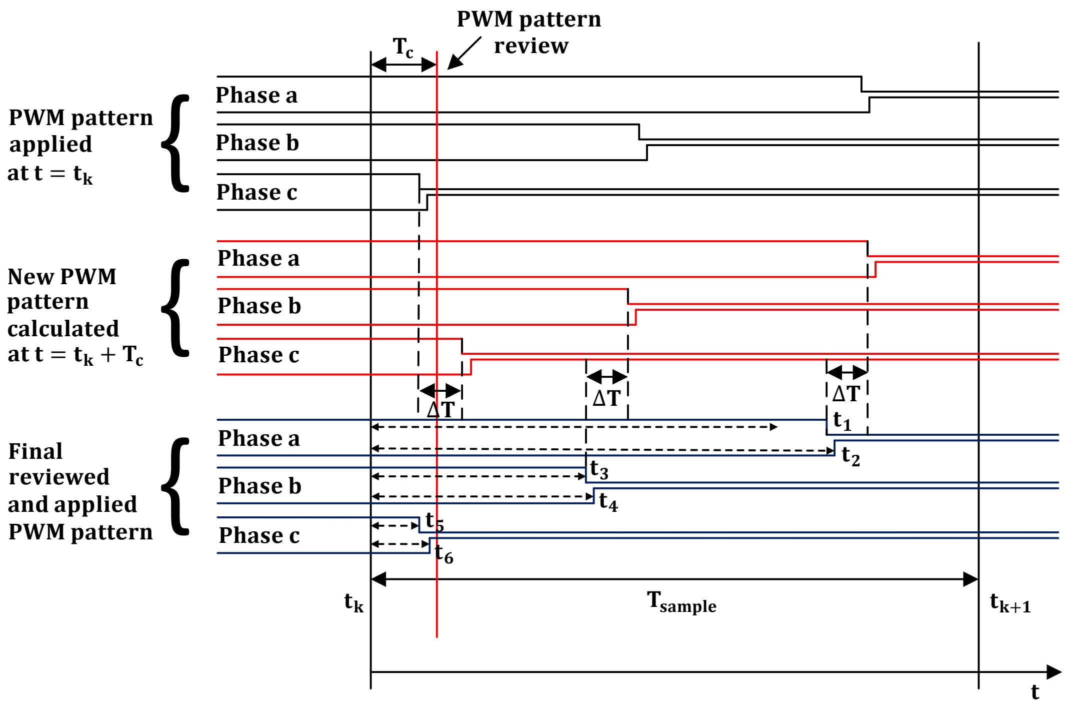

Figure 5.37: Illustration of the operation of the RCD algorithm, case $W_{1,2}$

In scenario $W_{1,1}$, according to the new PWM pattern, the IGBT modules that have already changed their status should have switched at an earlier time, as shown in Figure 5.36. In this example, at the time when the new PWM pattern is available, the switches of phase c have already switched. However, according to the new pattern, these switches should have switched a ΔT time earlier. In other words, these switches have changed their state with a delay equal to ΔT. This ΔT time is then added to the PWM timers of the IGBTs of the other two legs, again to maintain the same modulated line voltage.

Finally, the complementary $W_{1,2}$ scenario occurs when, according to the new PWM pattern, the switches that have already changed their status should have switched at a later time, as shown in Figure 5.37. In this example, at the time when the new PWM pattern is available, the switches of phase c have already switched. However, according to the new pattern, these switches should have switched a ΔT time later. In other words, these switches have changed their state a ΔT time earlier. This ΔT time is then subtracted from the PWM timers of the IGBTs of the other two legs, once again to maintain the same modulated line voltage.

It is worth mentioning that in scenarios $W_{0,2}$, $W_{1,1}$ and $W_{1,2}$, the RCD algorithm also verifies that by modifying the PWM timers of the switches that have not changed their status yet, their final PWM timers t_i are such that $T_k + T_c < t_i < T_k + T_{sample}$, with $i = 1, 2, ...6$. If this condition is not verified, the PWM pattern is not reviewed. The technique used to calculate the PWM timers is described in Appendix E.2.4.

The occurrence of the above listed cases depends both on the T_c calculation time and on the amplitude of the SVM modulation functions $m_x[k]$, with $x = a, b, c$. In fact, operating at higher modulation depths makes the switching activity of the IGBT modules start at earlier times during each T_{sample} window, therefore impacting on the execution of the RCD algorithm. In more detail, the verification of the different scenarios with $W = 0, 1, 2$ can be related to the SVM modulation depth $\hat{m}[k]$, calculated as:

$$\hat{m}[k] = \frac{\sqrt{3}}{2} M[k] = \frac{\sqrt{3}}{2} \sqrt{m_d^2[k] + m_q^2[k]}, \tag{5.1}$$

where $m_d[k]$ and $m_q[k]$ are the resulting dq-frame modulation signals generated by the controller algorithm. It is then possible to identify the critical value of $\hat{m}[k]$, indicated as $\hat{m}_c$, for which the RCD algorithm will operate with $W = 0$. This is related to the T_c calculation time as:

$$\hat{m}_c = -\frac{2T_c}{T_{sample}} + 1 \tag{5.2}$$

where in (5.2) $0 \leq T_c \leq \frac{T_{sample}}{2}$. In particular, for the achieved calculation time, $T_c = 13$ μs, $\hat{m}_c$ is 0.87 (see Figure 5.38a). It is worth mentioning that this result depends on the shape of the modulation functions.

When $\hat{m}[k] > 0.87$, at any time t_k, no more then one of the three phases of the SVM modulation functions, phase $\hat{x}$, will have an amplitude higher than 0.87. Hence, under this operating condition, only the converter leg corresponding to phase $\hat{x}$ will experience a switching activity during the initial T_c time of the $[t_k, t_{k+1}]$ sampling period, i.e. at a time t with $t_k < t \leq t_k + T_c$. This will cause the RCD algorithm to operate with $W = 1$. Finally, it is pointed out that the case with $W = 2$ never occurs with $T_c \leq 13$ μs (see Figure 5.38b, where the most critical scenario with $\hat{m}[k] = 1$ is illustrated). By satisfying such condition on the T_c calculation time, it is therefore assured that the implemented RCD algorithm will always succeed in updating the currently delivered PWM pattern, regardless of the converter operating point.

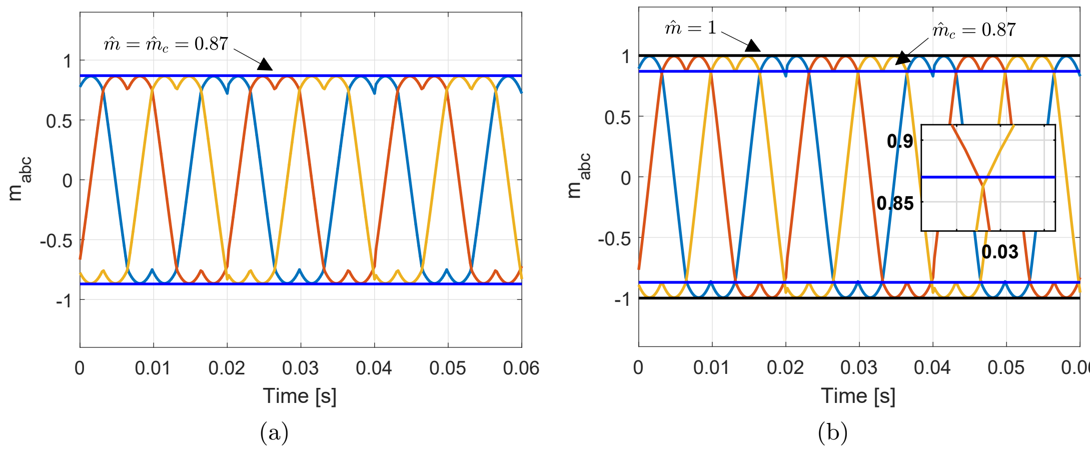

Figure 5.38: (a) Converter SVM modulation functions for (a) $\hat{m}[k] = \hat{m}_c$ and (b) $\hat{m}[k] = 1 > \hat{m}_c$.

5.3.1.1 Experimental verification

The operation of the RCD algorithm has been tested with the laboratory test-rig described in Section 2.3.2.3, making use of the system and controllers parameters detailed in Table 2.12.

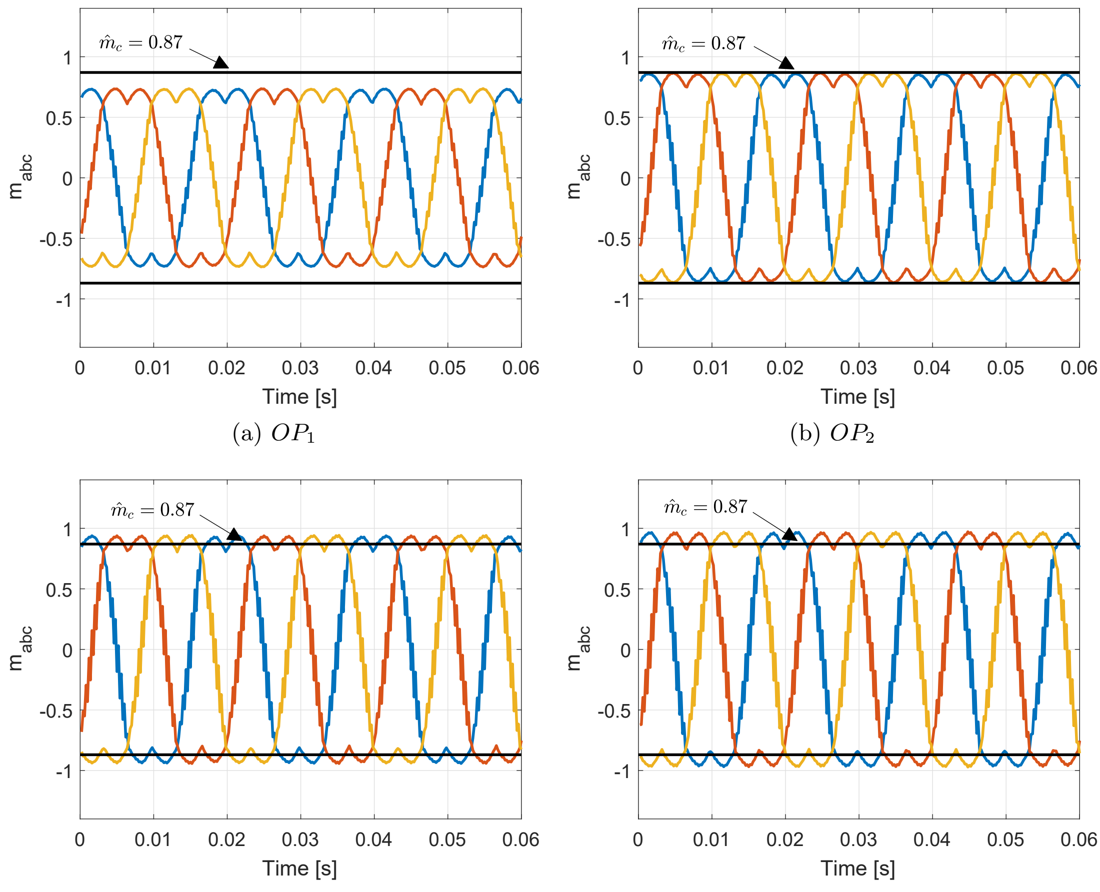

(a) OP_1 (b) OP_2 (c) OP_3 (d) OP_4

Figure 5.39: Recorded SVM modulation functions generated by the controller prototype for the different operating points listed in Table 5.6.

Different operating points of the system have been tested in order to verify the functionality of the RCD algorithm both for $\hat{m}[k] \leq 0.87$ (i.e. when only the scenario with $W = 0$ occurs) and for $\hat{m}[k] > 0.87$ (i.e when both cases with $W = 0$ and $W = 1$ occur). Higher SVM modulation depths have been obtained increasing the set-point of the i_d^+ loop, in other words increasing the amount of reactive power injected into the grid. The tested operating points are listed in Table 5.6. The resulting modulation functions recorded from the carried out tests are shown in Figure 5.39, for the considered operating points. Testing the prototype with higher SVM modulation depths has been avoided not to incur in over-modulation.

Table 5.6: Operating points tested to verify the functionality of the RCD algorithm.

Operating point	$i^{+}_{q,ref}$	$i^{+}_{d,ref}$	$i^{-}_{q,ref}$	$i^{-}_{d,ref}$	$\hat{m}[k]$
OP_1	4 A	0 A	0 A	0 A	0.73
OP_2	4 A	5 A	0 A	0 A	0.87
OP_3	4 A	8 A	0 A	0 A	0.91
OP_4	4 A	9 A	0 A	0 A	0.97

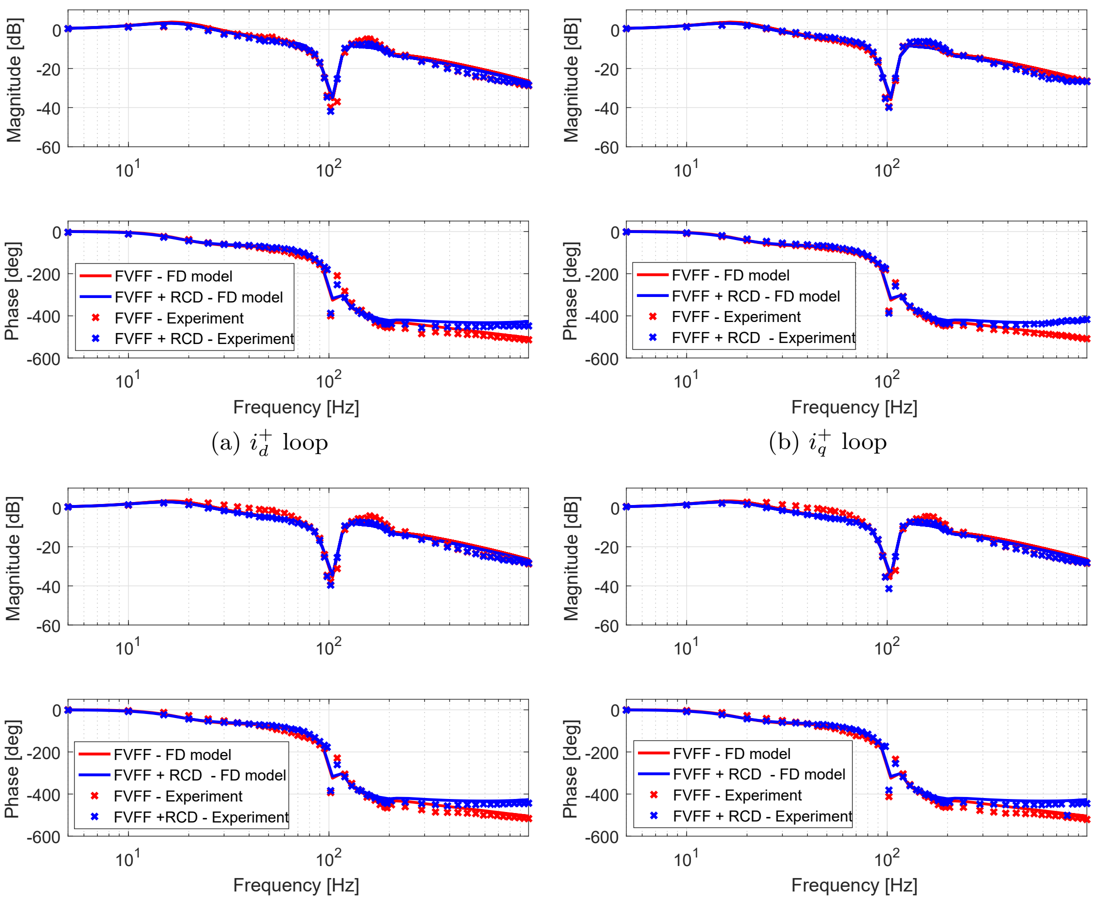

(a) i_d^+ loop (b) i_q^+ loop

(c) i_d^- loop (d) i_q^- loop

Figure 5.40: Comparison between current loop frequency responses either obtained experimentally or with the system FD model. The case corresponding to the operating point OP_1 in Table 5.6 is illustrated.

Figures 5.40, 5.41, 5.42, 5.43 show the closed loop frequency responses of the current controller loops, for the operating points OP_1, OP_2, OP_3 and OP_4, respectively. The results obtained from the system small-signal model are contrasted to the experimental data. The controller scheme where only the FVFF term is implemented is compared to the configuration where the RCD algorithm is also active. In the small-signal models, in order to reproduce the effect of the RCD strategy, the T_{sample} delay of the current loop has been eliminated. In other words, the controller delay T_d defined in (2.19) has been set to $0.5T_{sample}$, which is attributed to the Sample & Hold effect of the PWM generation [91].

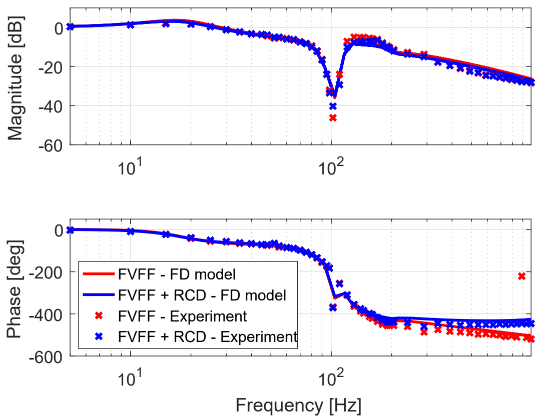

(a) i_d^+ loop

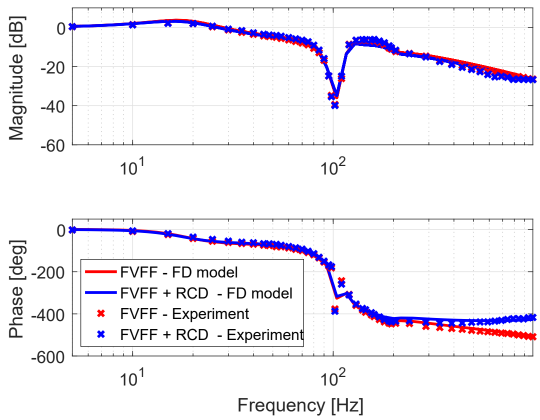

(b) i_q^+ loop

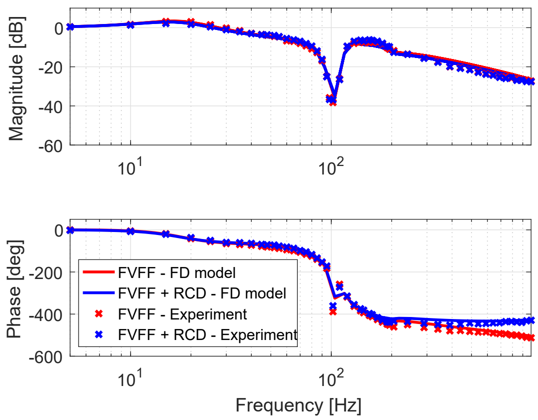

(c) i_d^- loop

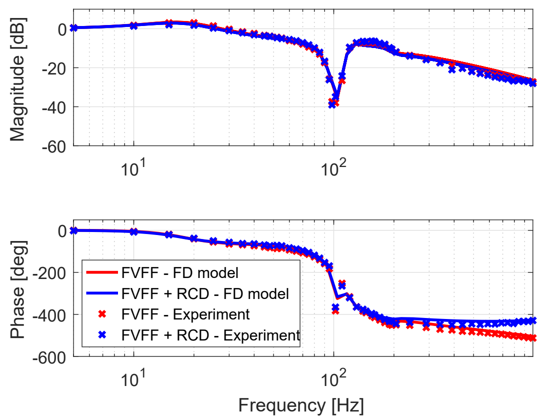

(d) i_q^- loop

Figure 5.41: Comparison between current loop frequency responses either obtained experimentally or with the system FD model. The case corresponding to the operating point OP_2 in Table 5.6 is illustrated.

Figures 5.40 and 5.41 show the cases with a modulation depth $\hat{m}$ of 0.73 and 0.87 respectively, which makes the RCD algorithm operate with $W = 0$. On the other hand, Figures 5.42 and 5.43 show the cases with $\hat{m}$ equal to 0.91 and 0.97 respectively, where both conditions $W = 0$ and $W = 1$ may occur.

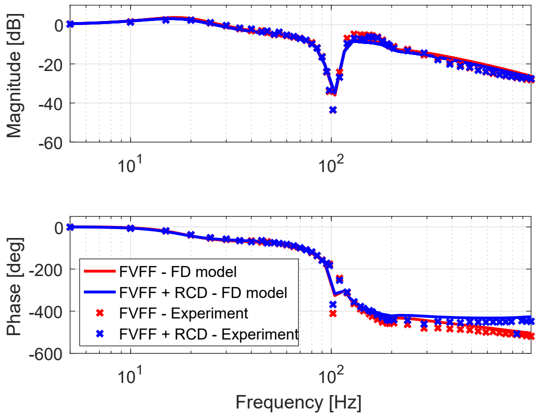

(a) i_d^+ loop

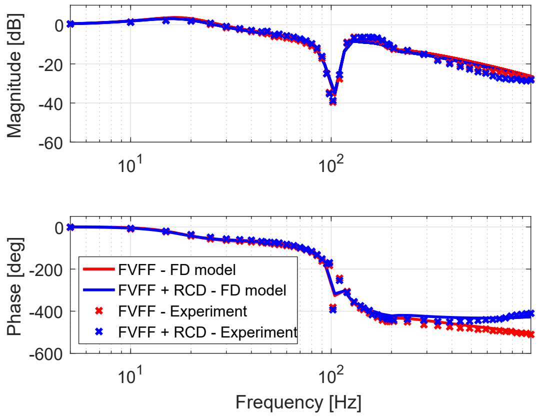

(b) i_q^+ loop

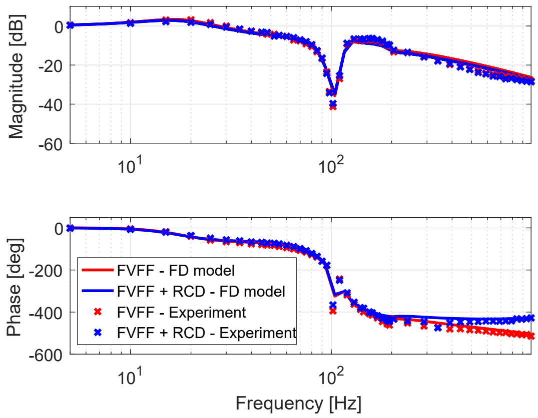

(c) i_d^- loop

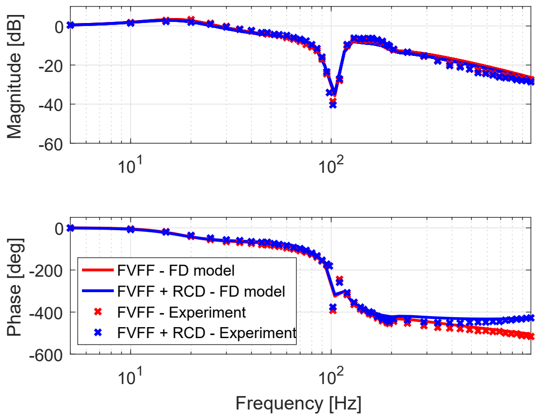

(d) i_q^- loop

Figure 5.42: Comparison between current loop frequency responses either obtained experimentally or with the system FD model. The case corresponding to the operating point OP_3 in Table 5.6 is illustrated.

The plots show a substantial overlap between the results from the small-signal (FD) model and the experimental data. For all the considered operating points, the relevant difference between the two controller schemes is seen in the reduction of the phase loss in the higher frequencies range. Such phase loss reduction is attributed to the elimination of the T_{sample} delay in the controller operation, which therefore confirms the effectiveness of the RCD algorithm.

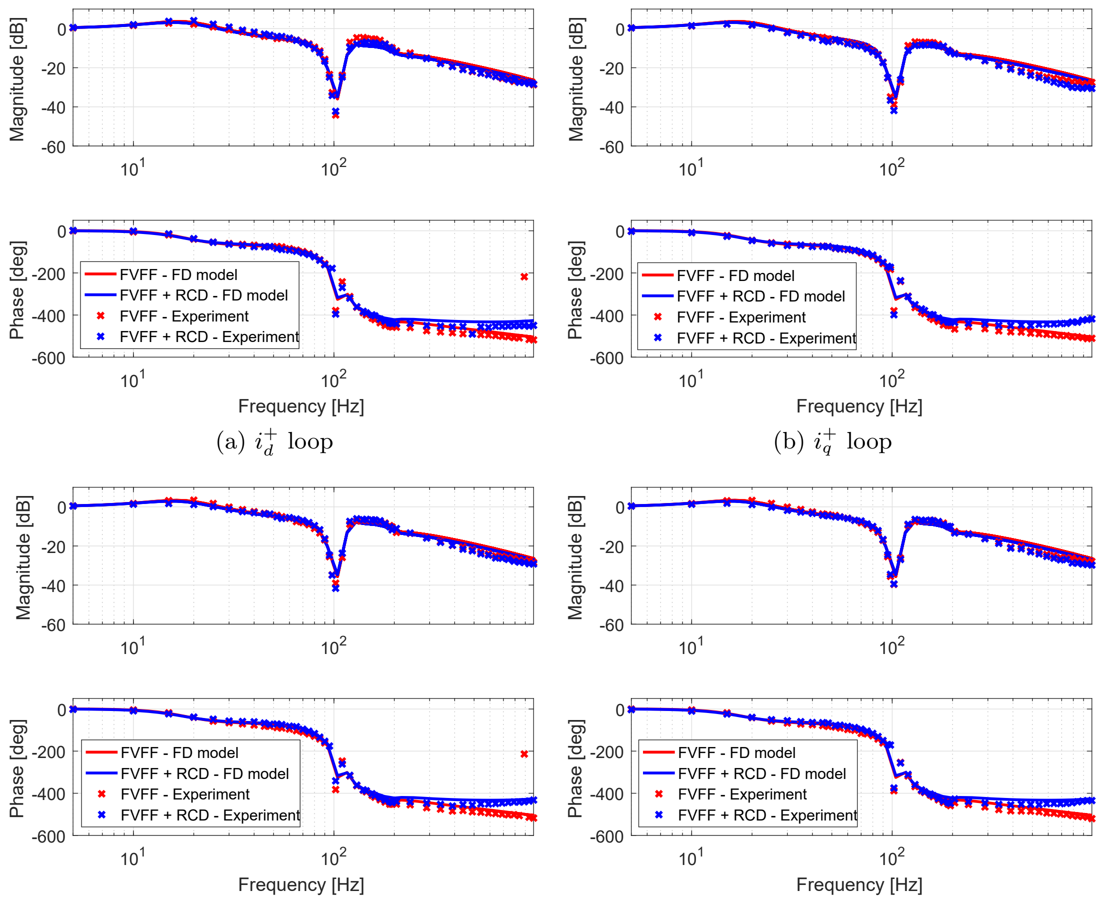

(a) i_d^+ loop (b) i_q^+ loop (c) i_d^- loop (d) i_q^- loop

Figure 5.43: Comparison between current loop frequency responses either obtained experimentally or with the system FD model. The case corresponding to the operating point OP_4 in Table 5.6 is illustrated.

5.3.1.2 Effect on the harmonics of the modulated voltage

The review of the PWM pattern delivered during the current sampling period, applied according to the described RCD method, has an impact on the harmonics of the inverter modulated AC voltage, as it will be discussed in this Section.

In order to evaluate such effect, the RCD algorithm has been implemented in MATLAB/Simulink, and the operation of the inverter with and without the use of the RCD technique has been simulated for different PWM modulation depths $\hat{m}$. From the simulation results, the harmonic content of the modulated voltage has been assessed, comparing the scenario where the RCD strategy is used to the one where it is not applied. These simulations have been carried out with the inverter connected to a passive RL load through its coupling reactor, and with the inverter feedback controller disabled (see Figure 5.44). The system parameters used in this analysis are detailed in Table 5.7.

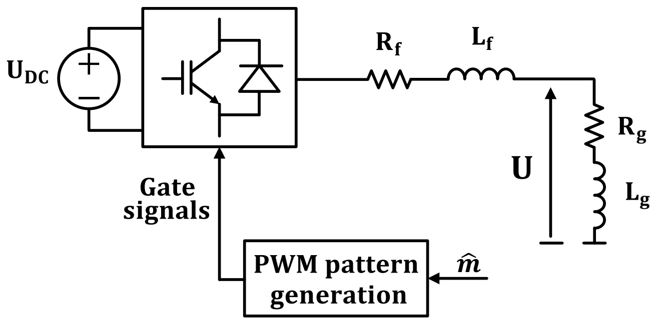

Figure 5.44: Symulink based model used to assess the impact of the RCD algorithm on the harmonics of the modulated voltage signal.

Table 5.7: System parameters associated to scheme in Figure 5.44.

Electrical Parameters	**Value**
Fundamental frequency	50 Hz
Grid Inductance L_g	0.1 mH
Grid Resistance R_g	0.1 Ω
Coupling Inductance L_f	2.5 mH
Coupling Resistance R_f	0.1 Ω
Inverter DC voltage	3000 V

Figure 5.45 shows the results obtained from the carried simulations for different values of the modulation depth $\hat{m}$. As it can be seen, the RCD strategy does not alter the harmonic content of the U voltage as long as the modulation depth is lower than 0.87. This indicates that when operating in scenario $W_{0,1}$, i.e. when the currently applied PWM pattern is simply replaced by its updated version (see Figure 5.34), there is no effect on the harmonics of the modulated inverter voltage . However, at higher modulation depths, an impact on the voltage harmonics can be observed. This is attributed to the occurrence of scenarios $W_{0,2}$, $W_{1,1}$ and $W_{1,2}$, and in particular to the preliminary correction applied on the new calculated PWM pattern before this is

applied (see Figures 5.35, 5.36 and 5.37).

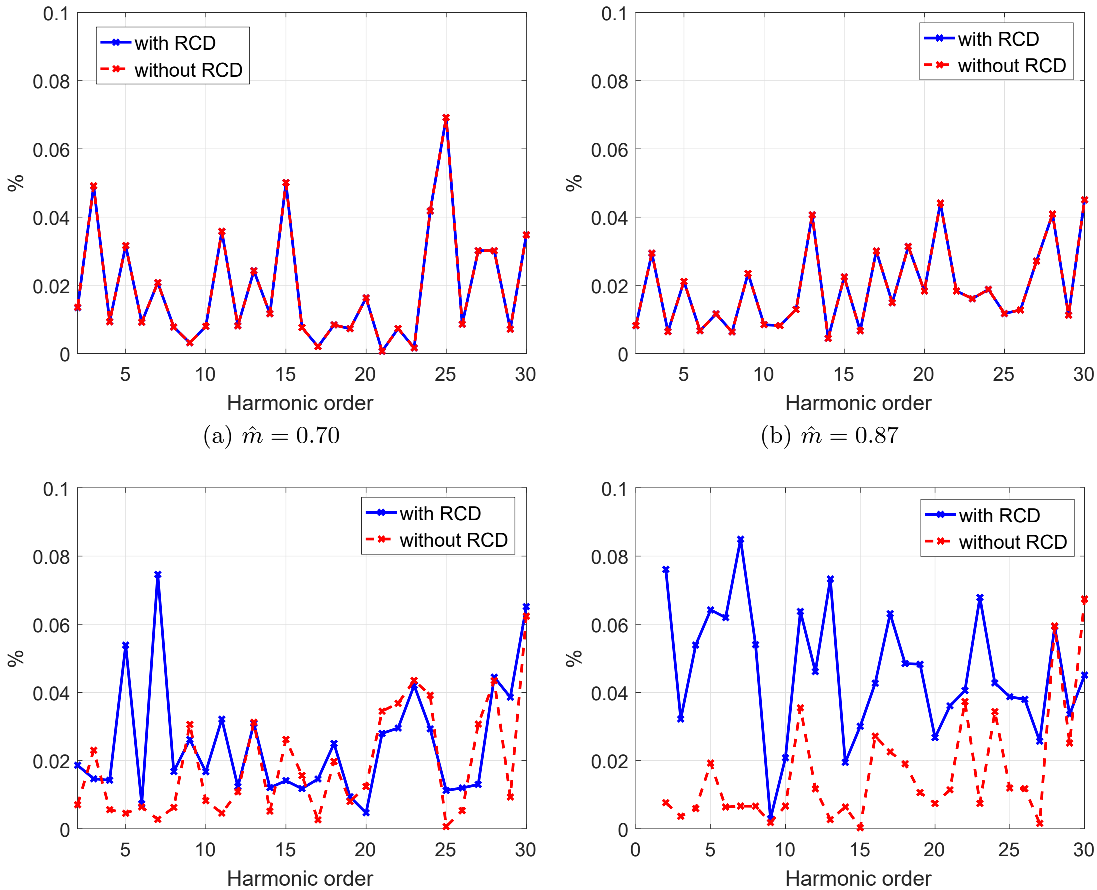

(a) $\hat{m} = 0.70$ (b) $\hat{m} = 0.87$ (c) $\hat{m} = 0.95$ (d) $\hat{m} = 1$

Figure 5.45: Comparison between the harmonic components of the modulated U voltage in Figure 5.44. The cases with $m_{depth} = 0.70, 0.87, 0.95, 1$ are shown, with $T_c = 13$ μs.

These results are also confirmed in Figure 5.46 where the Total Harmonic Distortion (THD) of the U voltage is shown for different modulation depths $\hat{m}$. For this calculation the harmonics up to the 30^{th} order have been considered, according to the following equation [113]:

$$THD[\%] = \frac{\sqrt{\sum_{n=2}^{30}(\hat{U}_{a,n})^2}}{\hat{U}_{a,1}} \times 100 \tag{5.3}$$

where $\hat{U}_{a,n}$ is the RMS voltage magnitude of the n^{th} harmonic of $U_a(t)$.

As it can be seen, the RCD algorithm has no impact on the voltage THD, as long as $\hat{m} \leq 0.87$. On the other hand, at higher modulation depths, the voltage THD increases when the RCD algorithm is in action. The worst case scenario occurs with $\hat{m} = 1$, with the THD becoming approximately 0.15 % higher. Based on these results, it can be stated that the beneficial effect of the RCD strategy on the delay performance of the controller operation comes at the cost of a lower quality of the modulated AC voltage, when operating at higher PWM modulation depths.

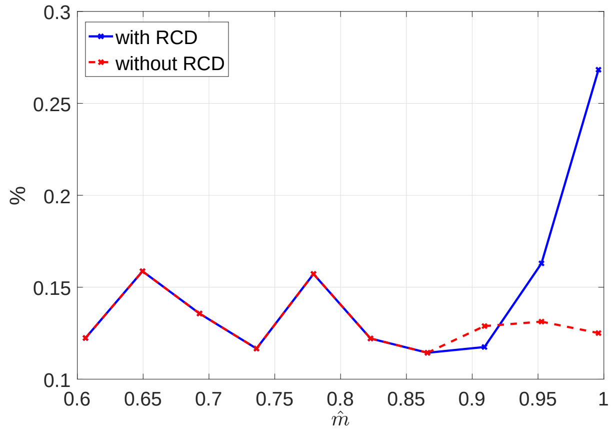

Figure 5.46: Comparison between the THD of the modulated U voltage as a function of $\hat{m}$. The cases where the RCD algorithm is either used or not are contrasted, with $T_c = 13$ μs.

5.3.2 Effect of the RCD strategy on the wind farm resonances

The effect of the RCD strategy on the stability performance of the wind farm system described in Section 2.1.4 has been evaluated. In this analysis, the use of a PWM asymmetrical sampling technique has been assumed. Figures 5.47 and 5.48 show the resulting Nyquist plots of $I + \hat{L}_{PN}(s)$ for the cases where the RCD is strategy operates without or with the FVFF term, respectively. As it can be seen, in both scenarios the system is stable for any number N of operating turbines, with $1 \leq N \leq 54$. The corresponding Bode plots of the system eigenvalues, $\lambda_1(j2\pi f)$ and $\lambda_2(j2\pi f)$, are reported in Figures 5.49 and 5.50 for the scenario where the RCD technique operates without the FVFF strategy, and in Figures 5.51 and 5.52 for the scenario where both the RCD and the FVFF techniques are used. As it can be seen, in the higher frequency range, the reduction on the phase loss of the eigenvalue functions is expectedly maximized when both strategies are in action.

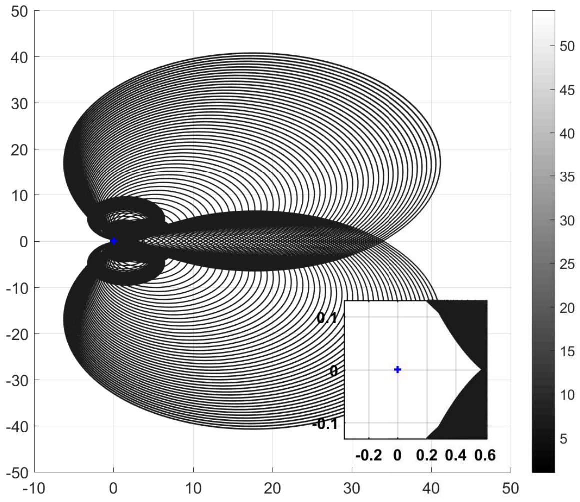

Figure 5.47: Nyquist plot of $I + \hat{L}_{PN}(s)$ for different values of the number of operating turbines N, considering the revised controller where only the RCD strategy is implemented.

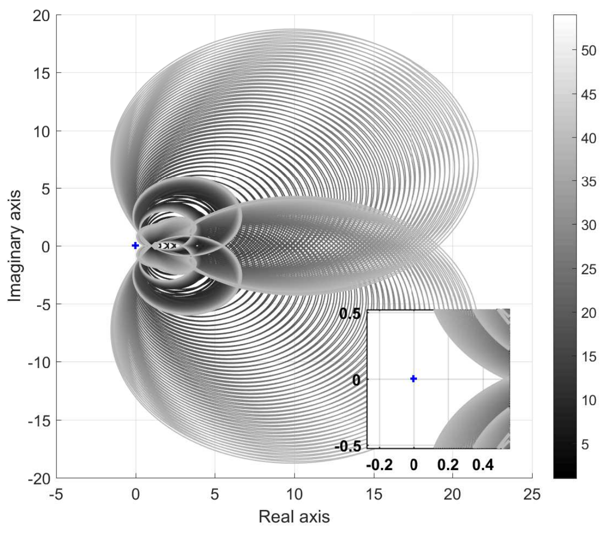

Figure 5.48: Nyquist plot of $I + \hat{L}_{PN}(s)$ for different values of the number of operating turbines N, considering the revised controller where both the RCD and the FVFF strategies are implemented.

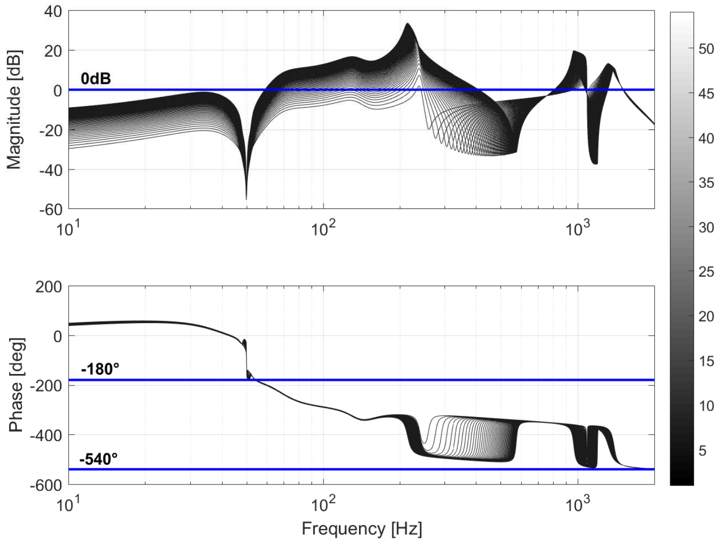

Figure 5.49: Bode plot of the eigenvalue $\lambda_1(2\pi f)$ of $\hat{L}_{PN}(s)$ for different values of the number of operating turbines N, considering the revised controller where only the RCD strategy is implemented.

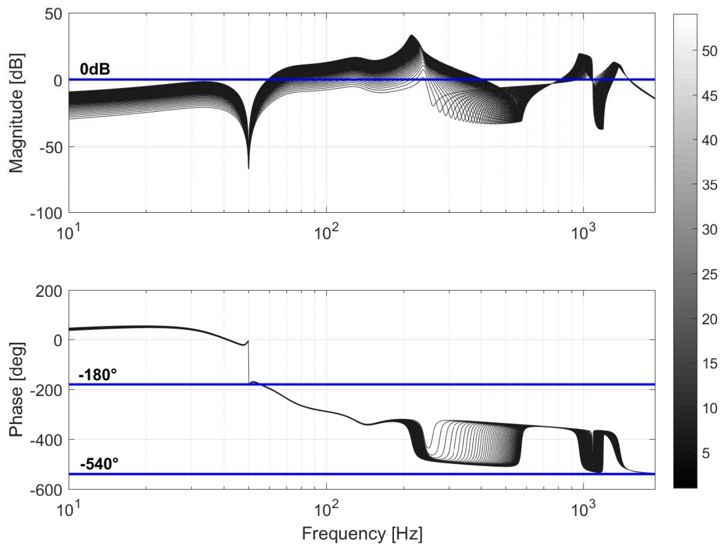

Figure 5.50: Bode plot of the eigenvalue $\lambda_2(2\pi f)$ of $\hat{L}_{PN}(s)$ for different values of the number of operating turbines N, considering the revised controller where only the RCD strategy is implemented.

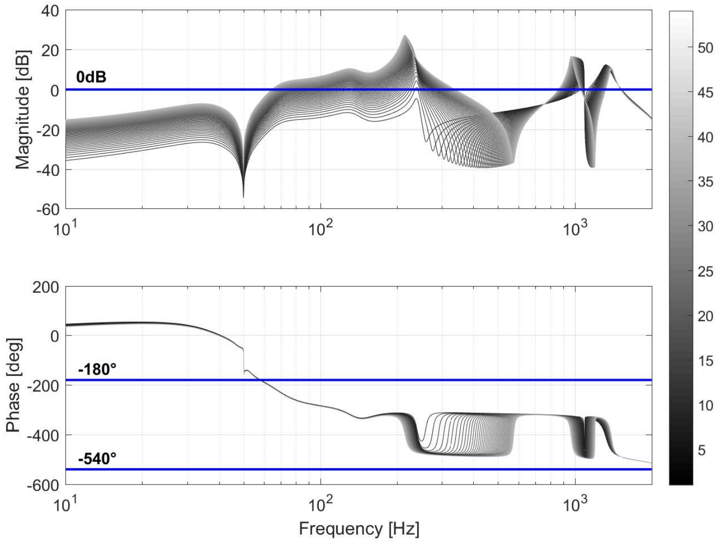

Figure 5.51: Bode plot of the eigenvalue $\lambda_1(2\pi f)$ of $\hat{L}_{PN}(s)$ for different values of the number of operating turbines N, with the revised controller where both the RCD and the FVFF strategies are implemented.

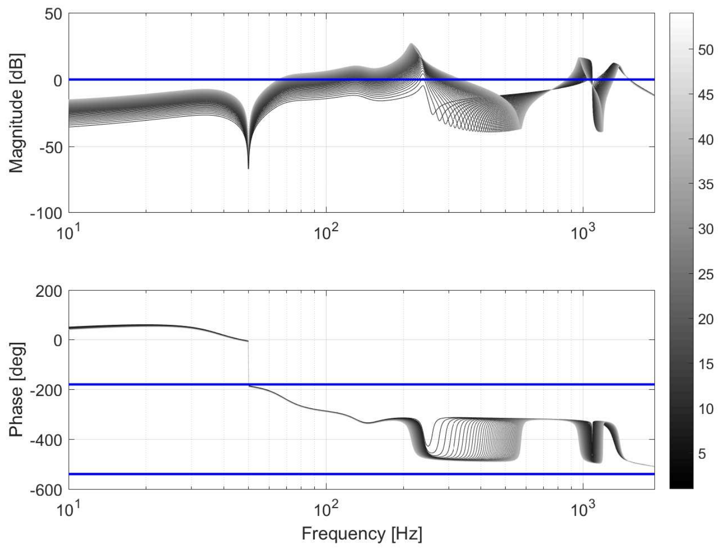

Figure 5.52: Bode plot of the eigenvalue $\lambda_2(2\pi f)$ of $\hat{L}_{PN}(s)$ for different values of the number of operating turbines N, with the revised controller where both the RCD and the FVFF strategies are implemented.

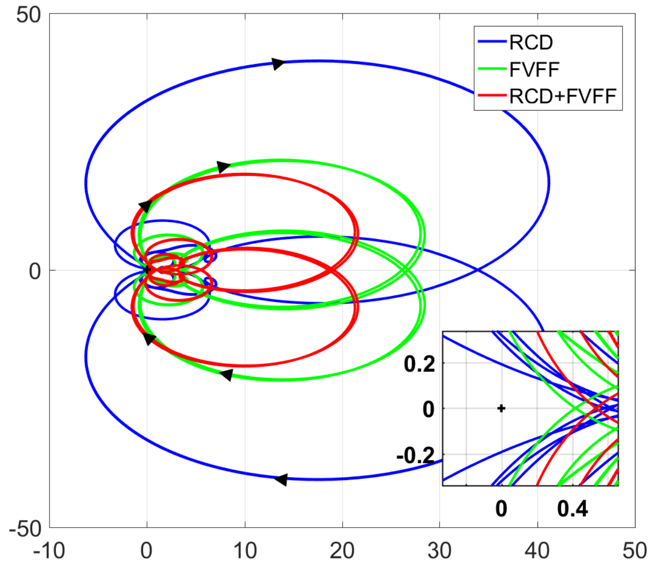

Figure 5.53: Comparison between the Nyquist plots of $I+\hat{L}_{PN}(s)$. The different control schemes proposed in the study are compared. $N = 54$.

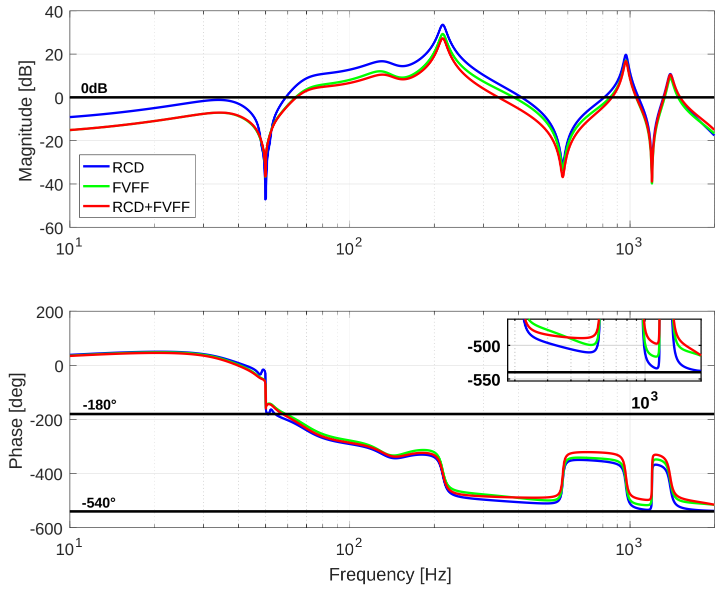

Figure 5.54: Comparison between the Bode plots of the eigenvalue $\lambda_1(j2\pi f)$ of $\hat{L}_{PN}(s)$. The different control schemes proposed in the study are compared. $N = 54$.

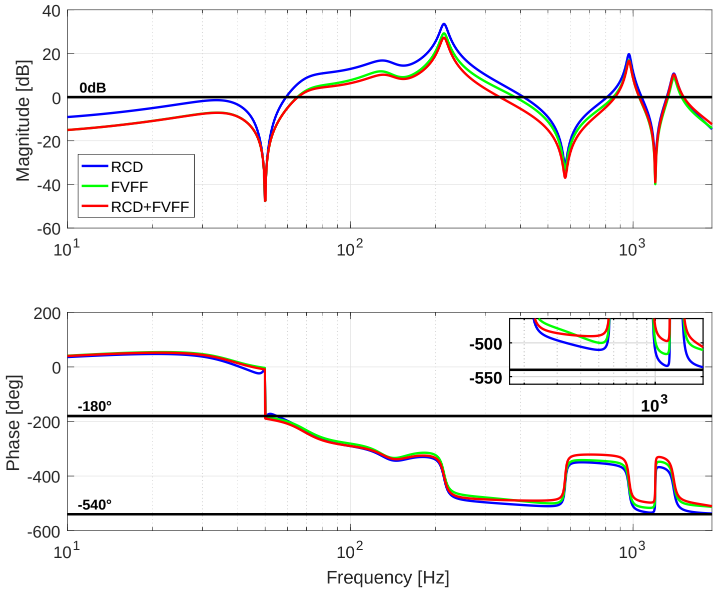

Figure 5.55: Comparison between the Bode plots of the eigenvalue $\lambda_2(j2\pi f)$ of $\hat{L}_{PN}(s)$. The different control schemes proposed in the study are compared. $N = 54$.

A comparison among the proposed controller schemes has been carried for the case with $N = 54$, i.e. in the most critical operating conditions of the wind farm, when it is generating its rated power. The resulting Nyquist plots are shown in Figure 5.53, while the Bode plots of the system eigenvalues are reported in Figures 5.54 and 5.55. The results show that the FVFF strategy is more effective than the RCD strategy on reducing the phase loss of the eigenvalues of $\hat{L}_{PN}(j\omega)$ in the range of frequencies where the wind farm resonances occur. In addition to this, the plots show that the FVFF term reduces the magnitude of the eigenvalues of $\hat{L}_{PN}(j\omega)$ in the lower frequency range, which confirms the damping properties of such a strategy. This is seen as acting to mitigate weak grid issues.

The results of the study of the system relative stability are detailed in Table 5.8. When only the RCD strategy is used, the mitigation of the high frequency cable resonance is less effective, as the low phase margin data obtained in the higher frequency range indicates. When the FVFF strategy is applied, the high frequency resonances are counteracted more effectively, making the weak grid effect critical in the system stability performance. Thanks to the diagonal dominance property of the system being satisfied, it has also been possible to calculate the d_∞ stability margin introduced in Section 4.4. Its values confirm the conservativeness of this figure, which is particularly evident for the two scenarios where the FVFF term is active.

Table 5.8: Analysis of the wind farm system relative stability for $N = 54$.

Control strategy	GM^+_{SISO} **[dB]**	PM^+_{SISO} **[deg]**	GM^-_{SISO} **[dB]**	GM^-_{SISO} **[deg]**	d_∞ -	GM_{d_∞} **[dB]**	PM_{d_∞} **[deg]**
RCD	8.7 (at 54 Hz)	11 (at 1072 Hz)	7.5 (at 55 Hz)	11 (at 1072 Hz)	0.177	≥ 1.69	≥ 10.2
FVFF	5 (at 59 Hz)	19 (at 64 Hz)	47 (at 51 Hz)	34 (at 65 Hz)	0.132	≥ 1.23	≥ 7.6
FVFF + RCD	6.3 (at 58 Hz)	30 (at 65 Hz)	47 (at 51 Hz)	45 (at 65 Hz)	0.24	≥ 2.4	≥ 13.9

Overall, the results indicate that by combining the FVFF and the RCD strategies, both the high frequencies resonances and the weak grid effect are mitigated more effectively. This is in line with the simulation data obtained with the corresponding TD model of the studied wind farm system. As it can be seen from Figure 5.56, where the step response of the q^+ current loop is shown for a 5 % increase in the $i^+_{q,ref}$ set-point, a lower overshoot as well as more damped dynamics are achieved when the FVFF technique is combined with the RCD strategy.

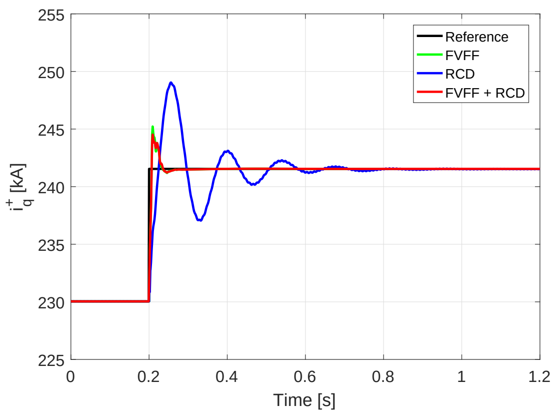

Figure 5.56: Simulated step responses of the i^+_q control loop, using the TD model of the studied wind farm system. The case with $N = 54$ operating turbines is shown. The different mitigation techniques presented in this work have been compared.

In conclusion, based on the stability margins detailed in Table 5.8, the best performing one is the scheme where both the FVFF and the RCD strategies are employed.

Such control scheme will be indicated as the optimal controller design in the following Sections.

5.3.2.1 Sensitivity analysis

A particular aspect of the wind farm electrical resonances is that their frequency strongly depends on the details of the cabling system of the wind park, as discussed in Chapter 1. Therefore, a desirable property of any proposed mitigation technique should be its robustness against any changes in the frequencies of these resonances.
In order to assess how well the proposed optimal control scheme can deal with such changes, the frequencies of the cable resonances of the studied wind farm have been varied. In more detail, the cable parameters listed in Table 2.2 have been altered to shift the resonance frequencies of the system admittance $Y_{TH}(s)$, shown in Figure 2.10, by approximately ±20%. The new resonance frequencies are detailed in Table 5.9, where these have been grouped in two ranges, indicated as FR_1 and FR_2. The resulting Bode plots of the modified $Y_{TH}(s)$ admittance are shown in Figure 5.57.

Table 5.9: Analysed ranges of resonances of the system admittance $Y_{TH}(s)$.

Scenario	FR_1 **[Hz]**	FR_2 **[Hz]**	Notes
M	[218, 477]	[952, 1108]	≈ 20 % lower than scenario B, see Figure 5.57a
B	[280, 575]	[1111, 1200]	Baseline scenario, see Figure 2.10
P	[341, 713]	[1573, 1590]	≈ 20 % higher than scenario B, see Figure 5.57b

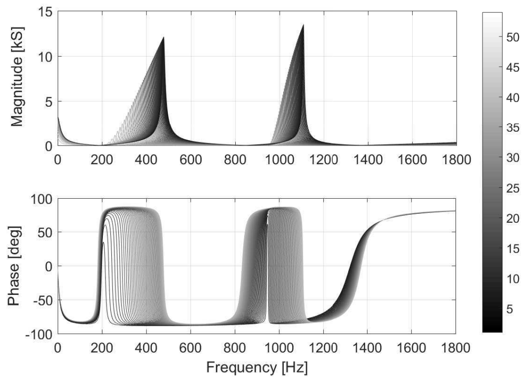

(a) Scenario M

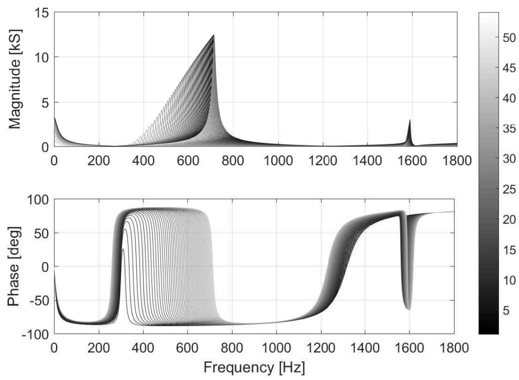

(b) Scenario P

Figure 5.57: Modified system admittance $Y_{TH}(s)$ in the carried out sensitivity analysis study.

As mentioned, the proposed optimal control strategy where both the RCD and the FVFF strategies are utilised is evaluated. The resulting Nyquist plots of the system are shown in Figure 5.58, which confirm that the system is stable in any of the reproduced scenarios. The corresponding Bode plots of the system eigenvalues are illustrated in Figures 5.59 and 5.60. As it can be seen, the phase performance of $\hat{L}_{PN}(j\omega)$ results substantially immune to the applied changes on the resonance frequencies. This therefore confirms the capability of the proposed optimal controller design to mitigate the wind farm resonances, regardless of the details of the wind farm cabling system.

The corresponding stability margins of the system are reported in Table 5.10. They confirm that the high frequency resonances are no longer critical to the system stability. The presence of a low frequency resonance, attributed to weak grid issues, is now the factor curbing the system stability performance. Its criticality is seen to increase when the wind farm resonances occur at lower frequencies.

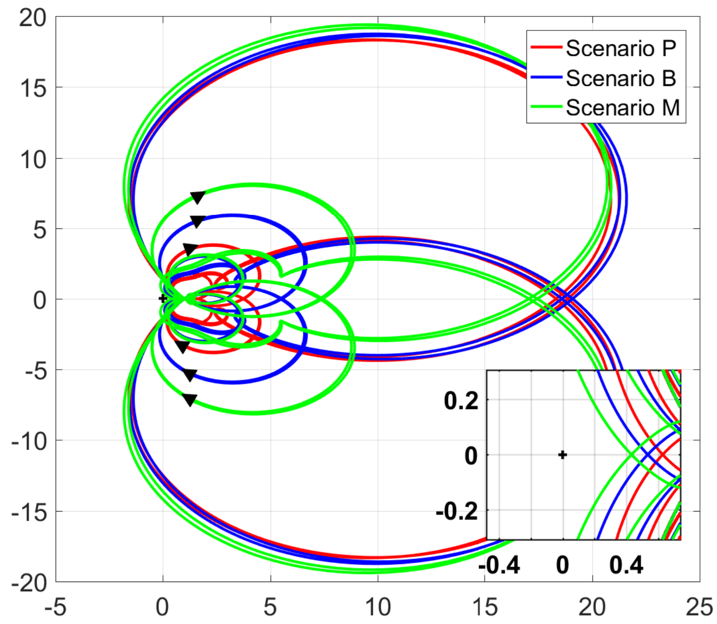

Figure 5.58: Comparison between the Nyquist plots of $I + \hat{L}_{PN}(s)$ for scenarios M, B and P. $N = 54$.

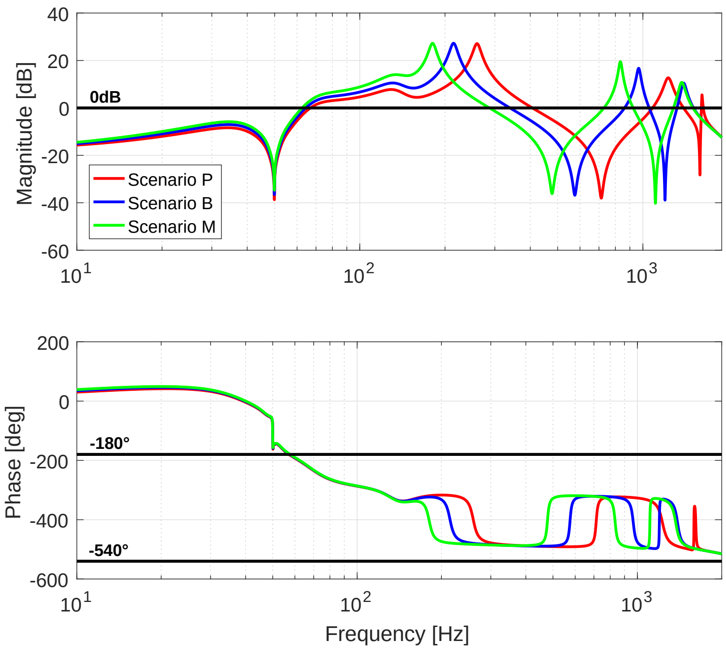

Figure 5.59: Comparison between the Bode plots of the eigenvalue $\lambda_1(j2\pi f)$ of $\hat{L}_{PN}(s)$ for scenarios M, B and P. $N = 54$.

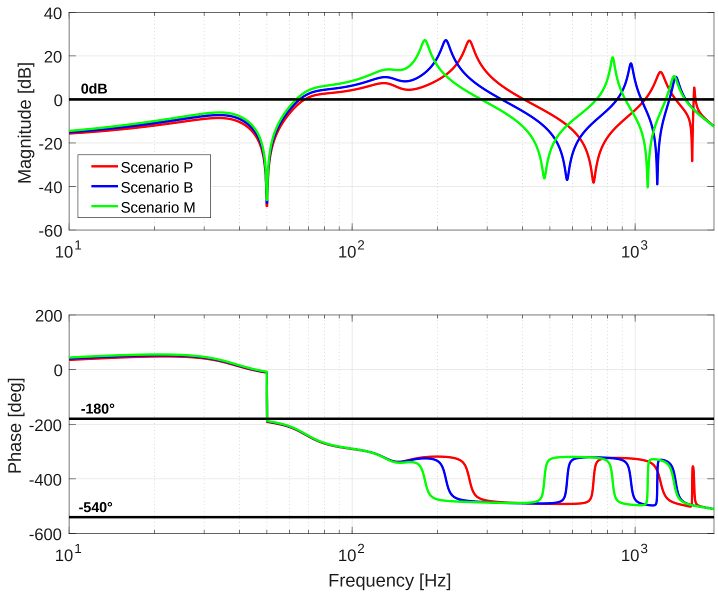

Figure 5.60: Comparison between the Bode plots of the eigenvalue $\lambda_2(j2\pi f)$ of $\hat{L}_{PN}(s)$ for scenarios M, B and P. $N = 54$.

Table 5.10: Sensitivity analysis: assessment of the system relative stability. $N = 54$.

Scenario	GM^{+}_{SISO} [dB]	PM^{+}_{SISO} [deg]	GM^{-}_{SISO} [dB]	GM^{-}_{SISO} [deg]	d_∞ -	GM_{d_∞} [dB]	PM_{d_∞} [deg]
M	5 (at 58 Hz)	22 (at 63 Hz)	47 (at 51 Hz)	38 (at 63.5 Hz)	0.132	≥ 1.23	≥ 7.6
B	6.3 (at 58 Hz)	30 (at 6 Hz)	47 (at 51 Hz)	45 (at 65 Hz)	0.242	≥ 2.4	≥ 13.9
P	8.1 (at 58 Hz)	42 (at 67 Hz)	47 (at 51 Hz)	56 (at 68 Hz)	0.352	≥ 3.8	≥ 20.3

5.3.2.2 Experimental verification

The effect of the RCD strategy on the cable due resonances has been verified experimentally, making use of the laboratory prototype described in Section 2.3.2.1. The same test described in Section 4.2.1.2 and 5.2.3.1 has been carried out, making use of a PWM asymmetrical sampling technique, with a switching frequency of 2.5 kHz.
A comparison among the experimental results obtained considering the three proposed mitigation strategies, namely the FVFF, the RCD and the FVFF+RCD techniques, is reported in Figure 5.61.

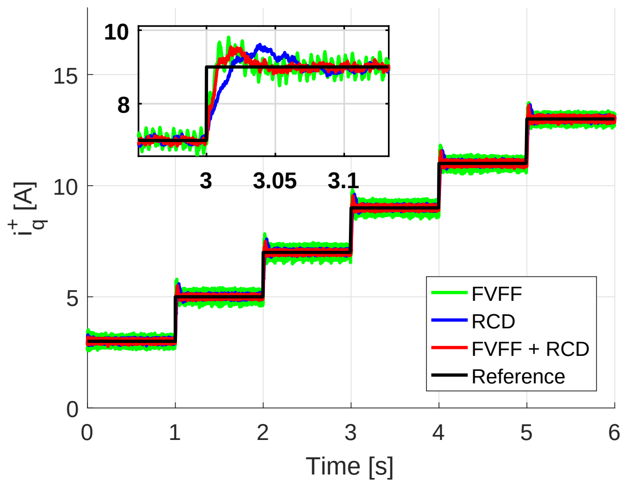

Figure 5.61: Comparison among the recorded i_q^+ trends for the considered control scheme configurations.

The results confirm that when the FVFF and the RCD strategies are combined the optimal stability perfomance is obtained, with the 10 % - 90 % rise time t_r, the 1 % settling time t_s and the Percentage Overshoot PO being reduced [25] (see Table 5.11).

As such, a faster control action with more damped system dynamics are obtained.

Table 5.11: Comparison between the step response parameters t_r, t_s and PO for the different controller schemes. These values have been derived from the step response occurring at $t = 3$ s in Figure 5.61

Control strategy	$t_r[ms]$	$t_s[ms]$	$PO[\%]$
RCD	≈16	≈70	≈30
FVFF	≈6	≈40	≈40
FVFF + RCD	≈7	≈40	≈20

Figure 5.62 shows the corresponding Nyquist plots of the system, comparing the proposed controller configurations. The operating point corresponding to the rated power of the inverter has been considered to generated these results. The associated Bode plots of the system eigenvalues are shown in Figures 5.63 and 5.64. These results confirm the previously mentioned observations that the FVFF term has a higher capability than the RCD algorithm to counteract the cable due high frequency resonances, and that the optimal performance is obtained when both the RCD and the FVFF strategies operate together.

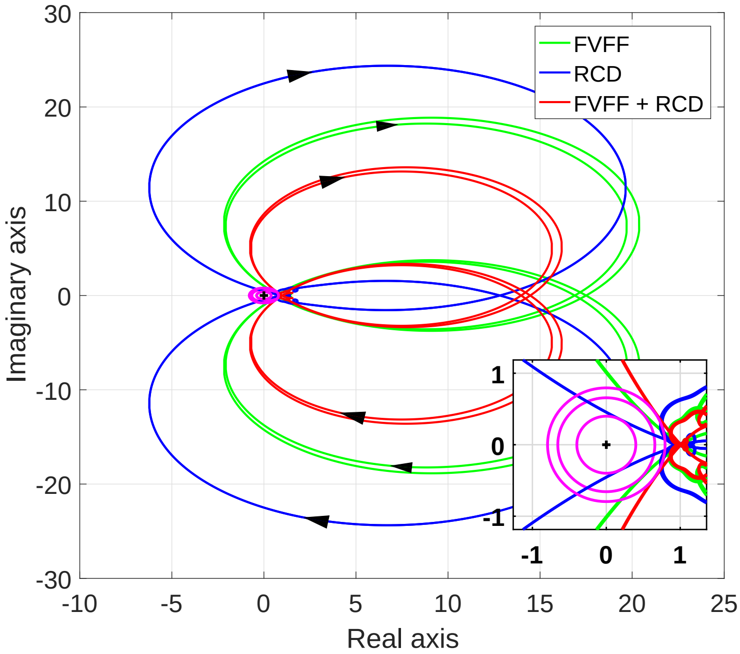

Figure 5.62: Nyquist plot of $I + \hat{L}_{PN}(s)$ for the laboratory tested system.

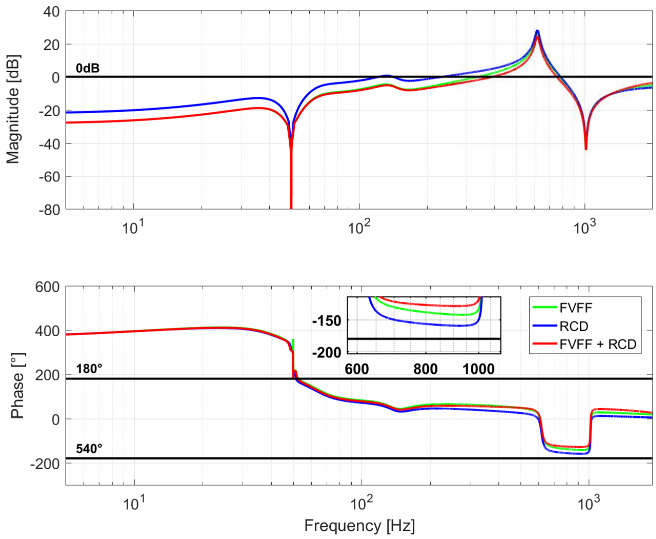

Figure 5.63: Bode plot of the eigenvalue $\lambda_1(j2\pi f)$ of $\hat{L}_{PN}(s)$ for the laboratory tested system.

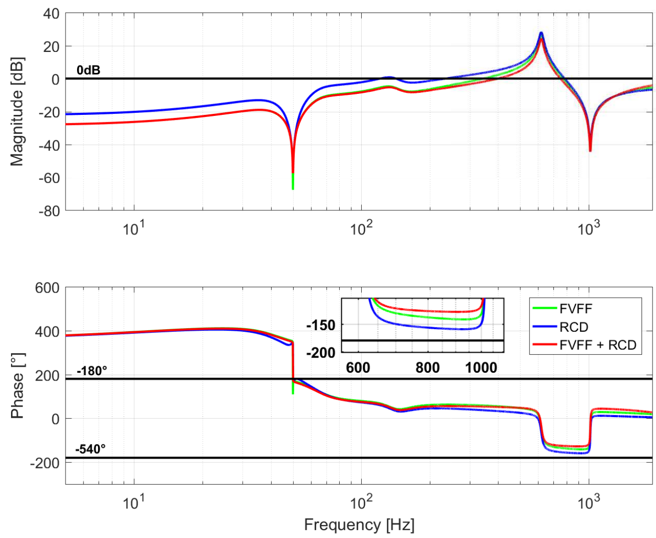

Figure 5.64: Bode plot of the eigenvalue $\lambda_2(j2\pi f)$ of $\hat{L}_{PN}(s)$ for the laboratory tested system.

These conclusions are in line with the corresponding system stability margin data detailed in Table 5.12. In particular, it can be seen how the phase margin figures increase significantly when the RCD and the FVFF strategies are combined. The results therefore are a further confirmation that such controller scheme is the optimal one among the proposed designs.

Table 5.12: Stability margins for the tested laboratory prototype. A comparison among the proposed mitigation techniques is presented.

Control strategy	GM^{+}_{SISO} **[dB]**	PM^{+}_{SISO} **[deg]**	GM^{-}_{SISO} **[dB]**	GM^{-}_{SISO} **[deg]**	d_{∞} -	$GM_{d_{\infty}}$ **[dB]**	$PM_{d_{\infty}}$ **[deg]**
RCD	25.4 (at 51.5 Hz)	24 (at 784 Hz)	29 (at 52 Hz)	24 (at 784 Hz)	0.4	≥ 4.44	≥ 23.1
FVFF	25.7 (at 52.8 Hz)	42.8 (at 776 Hz)	55 (at 50 Hz)	43.4 (at 774 Hz)	0.66	≥ 9.4	≥ 38.5
FVFF + RCD	26.2 (at 52.6 Hz)	55 (at 753 Hz)	57 (at 50 Hz)	55 (at 750 Hz)	0.79	≥ 13.56	≥ 46.5

5.4 Chapter summary

The significant role of the controller delay on the studied wind farm high frequency resonance problem has been identified. Two mitigation methods, the FVFF and the RCD strategies, have been designed to minimise such delay without increasing the switching frequency of the converter. Both techniques are based on a more efficient use of the hardware processing power available in modern control boards, and do not require either parameter tuning or a prior knowledge of the details of the wind farm design.
The FVFF strategy is based on using the latest AC voltage sample to determine the controller action, exploiting oversampling of such signal. It has been shown, both analytically and experimentally, how this strategy is beneficial not only to the high frequency resonance problem associated to the parasitic capacitance of the employed cables/lines, but also to weak grid issues.
The RCD strategy is based on adjusting the PWM pattern currently being delivered to the converter, based on the latest samples of the voltage and current signals. The capability of the RCD strategy of eliminating the sampling delay of the controller has been proven experimentally, highlighting how this comes at a cost of a higher harmonic content in the modulated inverter voltage when operating at higher modulation depths.
It has been shown that the optimal performance of the controller is obtained when both the FVFF and the RCD strategies are applied, which therefore represents the final controller design proposed by this work. Its robustness against changes in the frequencies

of the wind farm resonances has been verified, confirming the general applicability of the presented solution, regardless of the wind farm electrical specifics.

Chapter 6

Conclusions

6.1 General conclusions

In this thesis an analysis of the electrical resonances caused by the cables and lines connecting a wind farm to the grid has been carried out. The stability issues arising from the interaction between these resonances and the turbine's inverter controller have been reproduced, both in an analytical small-signal model of a wind farm-grid system where such issues were observed, and in a scaled-down prototype of a grid-connected VSC system. The relevant role of the parasitic capacitance of such cables and lines to the generation of these resonances has been confirmed, and the likelihood of potential weak grid issues has been identified.

In the modelling phase of the work, a technique has been defined to derive a unique small-signal model of the converter-grid system in the positive *dq*-frame. In particular, a methodology to project the dynamics of the inverter's negative sequence current controller from the negative to the positive *dq*-frame has been formulated. This has allowed the inclusion of the coupling between the positive and the negative sequence current controllers into the corresponding controller small-signal model, while such coupling is typically ignored in the modelling techniques published to date in the literature. A particular application of this projection technique consists in mapping transfer function models defined in the *abc*-frame onto the positive *dq*-frame.

A framework has been built to study the stability of the inverter-grid system in the sequence-frame, based on an impedance-based approach. For this purpose, a systematic methodology to calculate the sequence-frame small-signal converter admittance has been derived, and its accuracy and applicability regardless of the employed converter control scheme have been verified experimentally. A study of the existing coupling between the positive and the negative sequence components of the small-signal converter admittance has been carried out, verifying how this is affected by the employed converter control scheme, and in particular by asymmetries between the *d*- and the *q*-axis control loops. An experimental validation of the conditions that make the system Mirror Frequency Decoupled has been carried out.

An analytical technique to include the effect of these coupling terms into the stability study has been introduced, which has allowed to improve the accuracy of the stability study compared to the impedance-based stability criterion. Hence, a criterion to infer whether such coupling terms are relevant or not to the stability analysis has been presented, by assessing the property of diagonal dominance of the small-signal impedance-based model of the system in the sequence-frame. It has been shown how in the scenario of a VSC connected to a weak grid this coupling is likely to become relevant in a standard controller configuration where the active power and the voltage regulators are included in the converter control scheme. A stability margin definition that takes such coupling into account has been introduced. Its effectiveness has been verified experimentally, by considering the scenario of a VSC connected to a weak grid and evaluating how damping of the system dynamics varies with its operating point. It has been show how the presented stability margins offers a more conservative and safer analysis of the system relative stability compared to the gain and phase margin figure used in the impedance-based stability criterion.

The proposed stability study methodology has been applied to analyse the wind farm resonances of the considered wind farm-grid system. Its accuracy to predict the stability behaviour of the system has been verified experimentally making use of a laboratory inverter-grid prototype, where such type of cable due resonance issue has been reproduced. The analysis has indicated the central role of the controller delay in contributing towards unstable dynamics when such high frequency wind farm resonances are present.

Compared to the techniques proposed in the literature to address these instability problems, which need to be customised on a case-by-case basis and require an a priori knowledge of the wind farm specifics, a more generic and portable solution to the problem has been aimed by this work. The proposed techniques, the FVFF and the RCD strategies, differ from such standard methodologies as they do not require parameter tuning, nor the installation of additional equipment such as STATCOMs or reactive components. They are instead based on optimising the use of the processing power available in modern control boards, with the purpose of reducing the mentioned detrimental effect of the controller delay on the investigated problem. This has been done without altering the converter switching frequency, but making a more effective use of the voltage and current measurements taken from the plant. In particular, the implementation of the proposed techniques has required a revision of the standard implementation of the controller algorithm, making use of two processor cores instead of one.

The proposed FVFF technique has allowed to reduce the phase lag on the voltage feed forward term of the current controller. In this way, by oversampling the voltage signal, and by making use of its latest available sample to determine the controller action, it has been possible to maximise the damping capabilities of the controller. The effectiveness of this strategy to counteract the high frequency electrical resonances caused by the parasitic capacitance of the cables/lines, and to mitigate weak grid issues has been verified experimentally.

The designed RCD strategy has successfully eliminated the sampling delay of the controller, allowing a prompt controller action based on the latest voltage and current measurements. An experimental verification of its functionality and of its stabilising effect on the wind farm resonance problem has been carried out. The elimination of the sampling delay is seen to come at the cost of a potential higher harmonic generation in the modulated converter voltage, when this operates with higher modulation depths. It has been seen how this effect could be reduced by minimising the execution time of the controller algorithm.

In conclusion, the controller implementation where both the FVFF and the RCD strategies are used, has been proposed as the optimal design to boost the stability performance of the controller, making it more robust to changes in the wind farm resonances, as well as more immune to weak grid issues.

6.2 Author's contributions

The following contributions of this work are listed:

- A methodology to include the negative sequence current controller of the converter system in a unique small-signal model of such system, defined in the positive dq-frame.
- A set of equations to derive the small-signal converter admittance in the sequence-frame, in a systematic way, starting from equivalent data defined in the dq-frame.
- An analysis of the cross-coupling terms between the positive and the negative sequence terms of the small-signal converter admittance, verifying how different elements of the converter controller affect the Mirror Frequency Decoupled (MFD) property of the system.
- A criterion to infer whether such coupling terms should be included or not in the stability analysis of the converter-grid system, by evaluation of the diagonal dominance property of the small-signal impedance-based model of such system in the sequence-frame.
- The introduction of a perturbation norm stability margin to assess the relative stability of a converter-grid system. This exploits the mentioned property of diagonal dominance of the small-signal impedance-based model of such system in the sequence-frame, when this property is verified.
- The design of a FVFF strategy to reduce the phase lag on the voltage feed-forward term of the converter current controller, proving its effectiveness to counteract the high frequency wind farm resonance problem, as well as to mitigate weak grid issues.

- The design of a RCD strategy to eliminate the sampling delay of the converter controller.

6.3 Future work

The following items are identified as future work:

- Extend the developed methodology to calculate the *pn*-frame small-signal converter admittance to the cases of other converter topologies (e.g. Modular-Multilevel-Converter).
- Apply the presented stability study methodology to the cases where alternative converter control strategies are used (e.g. Virtual Synchronous Machine control).
- Further study on the anti-aliasing filter design, and evaluation of how such filter implementation affects the performance of the FVFF strategy.
- Further analyse the impact of the RCD strategy on the harmonics of the inverter modulated AC voltage and suggest possible mitigation methods.
- Improve the operation of the RCD strategy, by a further minimisation of the controller algorithm execution time.

Bibliography

[1] T. Burton, D. Sharpe, N. Jenkins, and E. Bossanyi, *Wind energy handbook.* John Wiley & Sons, 2001.

[2] Y. Kumar, J. Ringenberg, S. S. Depuru, V. K. Devabhaktuni, J. W. Lee, E. Nikolaidis, B. Andersen, and A. Afjeh, "Wind energy: Trends and enabling technologies," *Renewable and Sustainable Energy Reviews*, vol. 53, pp. 209–224, 2016.

[3] L. E. Jones, *Renewable energy integration: practical management of variability, uncertainty, and flexibility in power grids.* Academic Press, 2017.

[4] P. S. Georgilakis, "Technical challenges associated with the integration of wind power into power systems," *Renewable and Sustainable Energy Reviews*, vol. 12, no. 3, pp. 852–863, 2008.

[5] F. Blaabjerg, R. Teodorescu, M. Liserre, and A. V. Timbus, "Overview of control and grid synchronization for distributed power generation systems," *IEEE Transactions on industrial electronics*, vol. 53, no. 5, pp. 1398–1409, 2006.

[6] E. J. Coster, J. M. Myrzik, B. Kruimer, and W. L. Kling, "Integration issues of distributed generation in distribution grids," *Proceedings of the IEEE*, vol. 99, no. 1, pp. 28–39, 2011.

[7] C. Buchhagen, C. Rauscher, A. Menze, and J. Jung, "Borwin1 - first experiences with harmonic interactions in converter dominated grids," in *International ETG Congress 2015; Die Energiewende - Blueprints for the new energy age*, 2015.

[8] P. Brogan, "The stability of multiple, high power, active front end voltage sourced converters when connected to wind farm collector systems," in *Proc. EPE Wind Energy Chapter Seminar*, 2010.

[9] H. A. Mohammadpour, A. Ghaderi, and E. Santi, "Analysis of sub-synchronous resonance in doubly-fed induction generator-based wind farms interfaced with gate–controlled series capacitor," *IET Generation, Transmission & Distribution*, vol. 8, no. 12, pp. 1998–2011, 2014.

[10] A. E. Leon and J. A. Solsona, "Sub-synchronous interaction damping control for dfig wind turbines," *IEEE Transactions on Power Systems*, vol. 30, no. 1, pp. 419–428, 2015.

[11] A. Egea-Alvarez, S. Fekriasl, F. Hassan, and O. Gomis-Bellmunt, "Advanced vector control for voltage source converters connected to weak grids," *IEEE Transactions on Power Systems*, vol. 30, no. 6, pp. 3072–3081, 2015.

[12] L. Zhang, L. Harnefors, and H.-P. Nee, "Power-synchronization control of grid-connected voltage-source converters," *IEEE Transactions on Power systems*, vol. 25, no. 2, pp. 809–820, 2010.

[13] X. Wang, L. Harnefors, F. Blaabjerg, and P. C. Loh, "A unified impedance model of voltage-source converters with phase-locked loop effect," in *Energy Conversion Congress and Exposition (ECCE), 2016 IEEE*. IEEE, 2016, pp. 1–8.

[14] Ł. H. Kocewiak, J. Hjerrild, and C. L. Bak, "Wind turbine converter control interaction with complex wind farm systems," *IET Renewable Power Generation*, vol. 7, no. 4, pp. 380–389, 2013.

[15] E. Ebrahimzadeh, F. Blaabjerg, X. Wang, and C. L. Bak, "Modeling and identification of harmonic instability problems in wind farms," in *Energy Conversion Congress and Exposition (ECCE), 2016 IEEE*. IEEE, 2016, pp. 1–6.

[16] O. Anaya-Lara, D. Campos-Gaona, E. Moreno-Goytia, and G. Adam, *Offshore wind energy generation: control, protection, and integration to electrical systems.* John Wiley & Sons, 2014.

[17] P. Bresesti, W. L. Kling, R. L. Hendriks, and R. Vailati, "Hvdc connection of offshore wind farms to the transmission system," *IEEE Transactions on energy conversion*, vol. 22, no. 1, pp. 37–43, 2007.

[18] J. Glasdam, L. Zeni, M. Gryning, J. Hjerrild, L. Kocewiak, B. Hesselbaek, K. Andersen, T. Sørensen, M. Blanke, P. E. Sørensen *et al.*, "Hvdc connected offshore wind power plants: review and outlook of current research," in *Workshop on Large-scale Integration of Wind Power Into Power Systems*, 2013.

[19] F. Wang, L. Bertling, T. Le, A. Mannikoff, and A. Bergman, "An overview introduction of vsc-hvdc: State-of-art and potential applications in electric power systems," in *Cigrè International Symposium, Bologna, Italy, Sept. 2011.*, 2011.

[20] O. D. Adeuyi, "Grid connection of offshore wind farms through multi-terminal high voltage direct current networks," Ph.D. dissertation, Cardiff University, 2015.

[21] A. R. Jha, *Wind turbine technology.* CRC press, 2010.

[22] T. Burton, N. Jenkins, D. Sharpe, and E. Bossanyi, *Wind energy handbook.* John Wiley & Sons, 2011.

[23] K. M. Hasan, K. Rauma, A. Luna, J. I. Candela, and P. Rodriguez, "Harmonic resonance study for wind power plant," in *International Conference on Renewable Energies and Power Quality (ICREPQ'12)*, 2012.

[24] Q.-G. Wang, Z. Ye, W.-J. Cai, and C.-C. Hang, *PID control for multivariable processes.* Springer, 2008.

[25] W. Jacqueline, A. Johnson Michael, and K. Reza, "Control engineering: An introductory course," 2002.

[26] M. Bollen, S. Mousavi-Gargari, and S. Bahramirad, "Harmonic resonances due to transmission-system cables," in *The Renewable Energies and Power Quality Journal (RE&PQJ)*, no. 12, 2014.

[27] H. A. Brantsæter, "Harmonic resonance mode analysis and application for offshore wind power plants," Master's thesis, NTNU, 2015.

[28] Y. Sun, E. De Jong, J. Cobben, and V. Cuk, "Offshore wind farm harmonic resonance analysispart i: Converter harmonic model," in *PowerTech, 2017 IEEE Manchester*. IEEE, 2017, pp. 1–6.

[29] S. Jiang, S. Zhang, X. Lu, B. Ge, and F. Z. Peng, "Resonance issues and active damping in hvac grid-connected offshore wind farm," in *Energy Conversion Congress and Exposition (ECCE), 2013 IEEE*. IEEE, 2013, pp. 210–215.

[30] J. B. Glasdam, "Harmonics in offshore wind power plants employing power electronic devices in the transmission system," Ph.D. dissertation, Department of Energy Technology, Aalborg University, 2015.

[31] M. Altin, Ö. Göksu, R. Teodorescu, P. Rodriguez, B.-B. Jensen, and L. Helle, "Overview of recent grid codes for wind power integration," in *Optimization of Electrical and Electronic Equipment (OPTIM), 2010 12th International Conference on*. IEEE, 2010, pp. 1152–1160.

[32] I. M. de Alegría, J. Andreu, J. L. Martín, P. Ibanez, J. L. Villate, and H. Camblong, "Connection requirements for wind farms: A survey on technical requierements and regulation," *Renewable and Sustainable Energy Reviews*, vol. 11, no. 8, pp. 1858–1872, 2007.

[33] M. Bradt, B. Badrzadeh, E. Camm, D. Mueller, J. Schoene, T. Siebert, T. Smith, M. Starke, and R. Walling, "Harmonics and resonance issues in wind power plants," in *Transmission and Distribution Conference and Exposition (T&D), 2012 IEEE PES*. IEEE, 2012, pp. 1–8.

[34] F. Freijedo, S. Chaudhary, R. Teodorescu, J. M. Guerrero, C. L. Bak, Ł. H. Kocewiak, and C. F. Jensen, "Harmonic resonances in wind power plants: modeling, analysis and active mitigation methods," in *PowerTech, 2015 IEEE Eindhoven*. IEEE, 2015, pp. 1–6.

[35] M. P. Gryning, *Offshore Wind Park Control Assessment Methodologies to Assure Robustness: PhD Thesis*. Department of Electrical Engineering, Technical University of Denmark, 2015.

[36] L. Monjo, L. Sainz, J. Liang, and J. Pedra, "Study of resonance in wind parks," *Electric Power Systems Research*, vol. 128, pp. 30–38, 2015.

[37] K. Yang, "On harmonic emission, propagation and aggregation in wind power plants," Ph.D. dissertation, Luleå tekniska universitet, 2015.

[38] R. Zheng and M. Bollen, *Harmonic resonances associated with wind farms*. Luleå tekniska universitet, 2010.

[39] K. Rauma, "Electrical resonances and harmonics in a wind power plant," *Aalto University, master thesis, Finland*, 2012.

[40] L. H. Kocewiak, *Harmonics in large offshore wind farms*. Department of Energy Technology, Aalborg University, 2012.

[41] G. Shen, X. Zhu, J. Zhang, and D. Xu, "A new feedback method for pr current control of lcl-filter-based grid-connected inverter," *IEEE Transactions on Industrial Electronics*, vol. 57, no. 6, pp. 2033–2041, 2010.

[42] J. Dannehl, F. W. Fuchs, S. Hansen, and P. B. Thogersen, "Investigation of active damping approaches for pi-based current control of grid-connected pulse width modulation converters with lcl filters," *IEEE Transactions on Industry Applications*, vol. 46, no. 4, pp. 1509–1517, 2010.

[43] L. Harnefors, A. G. Yepes, A. Vidal, and J. Doval-Gandoy, "Passivity-based controller design of grid-connected vscs for prevention of electrical resonance instability." *IEEE Trans. Industrial Electronics*, vol. 62, no. 2, pp. 702–710, 2015.

[44] L. Harnefors, L. Zhang, and M. Bongiorno, "Frequency-domain passivity-based current controller design," *IET Power Electronics*, vol. 1, no. 4, pp. 455–465, 2008.

[45] J. C. Willems, "Dissipative dynamical systems part i: general theory," *Archive for rational mechanics and analysis*, vol. 45, no. 5, pp. 321–351, 1972.

[46] R. Pena-Alzola, M. Liserre, F. Blaabjerg, M. Ordonez, and T. Kerekes, "A self-commissioning notch filter for active damping in a three-phase lcl-filter-based grid-tie converter," *IEEE Trans. Power Electron.*, vol. 29, no. 12, pp. 6754–6761, 2014.

[47] G. Goertzel, "An algorithm for the evaluation of finite trigonometric series," *American Math. Monthly*, vol. 65, pp. 34–35, 1958.

[48] J. R. Wells, B. M. Nee, P. L. Chapman, and P. T. Krein, "Selective harmonic control: a general problem formulation and selected solutions," *IEEE Transactions on Power Electronics*, vol. 20, no. 6, pp. 1337–1345, 2005.

[49] M. S. Dahidah, G. Konstantinou, and V. G. Agelidis, "A review of multilevel selective harmonic elimination pwm: formulations, solving algorithms, implementation and applications," *IEEE Transactions on Power Electronics*, vol. 30, no. 8, pp. 4091–4106, 2015.

[50] H. Akagi, H. Fujita, and K. Wada, "A shunt active filter based on voltage detection for harmonic termination of a radial power distribution line," *IEEE Transactions on Industry Applications*, vol. 35, no. 3, pp. 638–645, 1999.

[51] H. Akagi, "Active harmonic filters," *Proceedings of the IEEE*, vol. 93, no. 12, pp. 2128–2141, 2005.

[52] H. Fujita, T. Yamasaki, and H. Akagi, "A hybrid active filter for damping of harmonic resonance in industrial power systems," *IEEJ Transactions on Industry Applications*, vol. 118, no. 10, pp. 1193–1200, 1998.

[53] X. Wang, F. Blaabjerg, M. Liserre, Z. Chen, J. He, and Y. Li, "An active damper for stabilizing power-electronics-based ac systems," *IEEE Transactions on Power Electronics*, vol. 29, no. 7, pp. 3318–3329, 2014.

[54] J. Sun, "Impedance-based stability criterion for grid-connected inverters," *IEEE Transactions on Power Electronics*, vol. 26, no. 11, pp. 3075–3078, 2011.

[55] M. Cespedes and J. Sun, "Impedance modeling and analysis of grid-connected voltage-source converters," *IEEE Transactions on Power Electronics*, vol. 29, no. 3, pp. 1254–1261, March 2014.

[56] M. Cheah-Mane, L. Sainz, J. Liang, N. Jenkins, and C. E. Ugalde-Loo, "Criterion for the electrical resonance stability of offshore wind power plants connected through hvdc links," *IEEE Transactions on Power Systems*, vol. 32, no. 6, pp. 4579–4589, 2017.

[57] E. Ebrahimzadeh, F. Blaabjerg, X. Wang, and C. L. Bak, "Efficient approach for harmonic resonance identification of large wind power plants," in *Power Electronics for Distributed Generation Systems (PEDG), 2016 IEEE 7th International Symposium on.* IEEE, 2016, pp. 1–7.

[58] A. Yazdani and R. Iravani, *Voltage-sourced converters in power systems: modeling, control, and applications.* John Wiley & Sons, 2010.

[59] L. Harnefors, X. Wang, A. G. Yepes, and F. Blaabjerg, "Passivity-based stability assessment of grid-connected vscsan overview," *IEEE Journal of emerging and selected topics in Power Electronics*, vol. 4, no. 1, pp. 116–125, 2016.

[60] A. Rygg, M. Molinas, C. Zhang, and X. Cai, "A modified sequence-domain impedance definition and its equivalence to the dq-domain impedance definition for the stability analysis of ac power electronic systems," *Journal of Emerging and Selected Topics In Power Electronics*, vol. 4, no. 4, pp. 1383–1396, 2016.

[61] M. Cespedes and J. Sun, "Renewable energy systems instability involving grid-parallel inverters," in *Applied Power Electronics Conference and Exposition, 2009. APEC 2009. Twenty-Fourth Annual IEEE.* IEEE, 2009, pp. 1971–1977.

[62] M. K. Bakhshizadeh, X. Wang, F. Blaabjerg, J. Hjerrild, Ł. Kocewiak, C. L. Bak, and B. Hesselbæk, "Couplings in phase domain impedance modeling of grid-connected converters," *IEEE Transactions on Power Electronics*, vol. 31, no. 10, pp. 6792–6796, 2016.

[63] L. Yeung and G. Bryant, "Robust stability of diagonally dominant systems," in *IEE Proceedings D (Control Theory and Applications)*, vol. 131, no. 6. IET, 1984, pp. 253–260.

[64] J. L. Kirtley, *Electric power principles: sources, conversion, distribution and use.* John Wiley & Sons, 2011.

[65] M. Céspedes and J. Sun, "Modeling and mitigation of harmonic resonance between wind turbines and the grid," in *Energy Conversion Congress and Exposition (ECCE), 2011 IEEE.* IEEE, 2011, pp. 2109–2116.

[66] Y. Yu, H. Li, Z. Li, and Z. Zhao, "Modeling and analysis of resonance in lcl-type grid-connected inverters under different control schemes," *Energies*, vol. 10, no. 1, p. 104, 2017.

[67] C. Zhang, X. Wang, and F. Blaabjerg, "Analysis of phase-locked loop influence on the stability of single-phase grid-connected inverter," in *Power Electronics for Distributed Generation Systems (PEDG), 2015 IEEE 6th International Symposium on.* IEEE, 2015, pp. 1–8.

[68] I. Postlethwaite, "A generalized inverse nyquist stability criterion," *International Journal of Control*, vol. 26, no. 3, pp. 325–340, 1977.

[69] B. Wen, D. Boroyevich, R. Burgos, P. Mattavelli, and Z. Shen, "Inverse nyquist stability criterion for grid-tied inverters," *IEEE Transactions on Power Electronics*, vol. 32, no. 2, pp. 1548–1556, 2017.

[70] P. C. Sen, *Principles of electric machines and power electronics.* John Wiley & Sons, 2007.

[71] N. Mohan, *Power electronics: a first course.* Wiley, 2011.

[72] F. Vasca and L. Iannelli, *Dynamics and control of switched electronic systems: advanced perspectives for modeling, simulation and control of power converters.* Springer, 2012.

[73] D. G. Holmes and T. A. Lipo, *Pulse width modulation for power converters: principles and practice.* John Wiley & Sons, 2003, vol. 18.

[74] G. L. Calzo, A. Lidozzi, L. Solero, and F. Crescimbini, "Lc filter design for on-grid and off-grid distributed generating units," *IEEE transactions on industry applications*, vol. 51, no. 2, pp. 1639–1650, 2014.

[75] Y. Feng, P. Tavner, and H. Long, "Early experiences with uk round 1 offshore wind farms." *Proceedings of the Institution of Civil Engineers: energy.*, vol. 163, no. 4, pp. 167–181, 2010.

[76] L. P. Kunjumuhammed, B. C. Pal, C. Oates, and K. J. Dyke, "The adequacy of the present practice in dynamic aggregated modeling of wind farm systems," *IEEE Transactions on Sustainable Energy*, vol. 8, no. 1, pp. 23–32, 2017.

[77] L. H. Kocewiak, J. Hjerrild, and C. L. Bak, "Wind turbine converter control interaction with complex wind farm systems," *IET Renewable Power Generation*, vol. 7, no. 4, pp. 380–389, 2013.

[78] S.-K. Chung, "A phase tracking system for three phase utility interface inverters," *IEEE Transactions on Power electronics*, vol. 15, no. 3, pp. 431–438, 2000.

[79] M. Cespedes and J. Sun, "Modeling and mitigation of harmonic resonance between wind turbines and the grid," in *Energy Conversion Congress and Exposition (ECCE), 2011 IEEE.* IEEE, 2011, pp. 2109–2116.

[80] K. J. Åström and T. Hägglund, *PID controllers: theory, design, and tuning.* Instrument society of America Research Triangle Park, NC, 1995, vol. 2.

[81] K. Ogata and Y. Yang, *Modern control engineering.* Prentice-Hall, 2002, vol. 4.

[82] D. Holmes, T. Lipo, B. McGrath, and W. Kong, "Optimized design of stationary frame three phase ac current regulators," *IEEE Transactions on Power Electronics*, vol. 24, no. 11, pp. 2417–2426, 2009.

[83] C. E. Shannon, "Communication theory of secrecy systems," *Bell system technical journal*, vol. 28, no. 4, pp. 656–715, 1949.

[84] A. Giles, L. Reguera, and A. Roscoe, "Optimal controller gains for inner current controllers in vsc inverters," 2015.

[85] W. Hurewicz and H. Wallman, *Dimension theory.* Princeton university press Princeton, 1948, vol. 1969.

[86] M. E. Van Valkenburg, *Analog filter design.* Holt, Rinehart, and Winston, 1982.

[87] M. Yazdanian and A. Mehrizi-Sani, "Internal model-based current control of therlfilter-based voltage-sourced converter," *IEEE Transactions on Energy Conversion*, vol. 29, no. 4, pp. 873–881, 2014.

[88] S.-J. Kweon, S.-H. Shin, S.-H. Jo, and H.-J. Yoo, "Reconfigurable high-order moving-average filter using inverter-based variable transconductance amplifiers," *IEEE Transactions on Circuits and Systems II: Express Briefs*, vol. 61, no. 12, pp. 942–946, 2014.

[89] S. W. Smith *et al.*, "The scientist and engineer's guide to digital signal processing," 1997.

[90] N. Mohan and T. M. Undeland, *Power electronics: converters, applications, and design.* John Wiley & Sons, 2007.

[91] B. P. McGrath, S. G. Parker, and D. G. Holmes, "High-performance current regulation for low-pulse-ratio inverters," *IEEE Transactions on Industry Applications*, vol. 49, no. 1, pp. 149–158, 2013.

[92] B. Terzić, G. Majić, and A. Slutej, "Stability analysis of three-phase pwm converter with lcl filter by means of nonlinear model," *Automatika*, vol. 51, no. 3, pp. 221–232, 2010.

[93] M. Johnson, "Diagonal dominance and the method of pseudodiagonalisation," in *Proceedings of the Institution of Electrical Engineers*, vol. 126, no. 10. IET, 1979, pp. 1011–1017.

[94] J. C. Doyle, B. A. Francis, and A. R. Tannenbaum, *Feedback control theory.* Courier Corporation, 2013.

[95] J. Hu, Y. Huang, D. Wang, H. Yuan, and X. Yuan, "Modeling of grid-connected dfig-based wind turbines for dc-link voltage stability analysis," *IEEE Trans. Sustain. Energy*, vol. 6, no. 4, pp. 1325–1336, 2015.

[96] B. Wen, D. Boroyevich, P. Mattavelli, Z. Shen, and R. Burgos, "Influence of phase-locked loop on input admittance of three-phase voltage-source converters," in *2013 Twenty-Eighth Annual IEEE Applied Power Electronics Conference and Exposition (APEC).* IEEE, 2013, pp. 897–904.

[97] X. Wang, L. Harnefors, and F. Blaabjerg, "Unified impedance model of grid-connected voltage-source converters," *IEEE Transactions on Power Electronics*, vol. 33, no. 2, pp. 1775–1787, 2018.

[98] N. P. Strachan and D. Jovcic, "Stability of a variable-speed permanent magnet wind generator with weak ac grids," *IEEE Transactions on Power Delivery*, vol. 25, no. 4, pp. 2779–2788, 2010.

[99] G. C. Paap, "Symmetrical components in the time domain and their application to power network calculations," *IEEE Transactions on power systems*, vol. 15, no. 2, pp. 522–528, 2000.

[100] D. C. White and H. H. Woodson, *Electromechanical energy conversion.* Wiley, 1959.

[101] W. V. Lyon, *Applications of the method of symmetrical components.* McGraw-Hill book company, inc., 1937.

[102] G. C. Goodwin, S. F. Graebe, and M. E. Salgado, "Control system design," *Upper Saddle River*, vol. 13, 2001.

[103] M. Safonov and M. Athans, "A multiloop generalization of the circle criterion for stability margin analysis," *IEEE Transactions on Automatic Control*, vol. 26, no. 2, pp. 415–422, 1981.

[104] Y.-T. Juang and C.-S. Shao, "Stability analysis of dynamic interval systems," *International Journal of Control*, vol. 49, no. 4, pp. 1401–1408, 1989.

[105] J. Z. Zhou, H. Ding, S. Fan, Y. Zhang, and A. M. Gole, "Impact of short-circuit ratio and phase-locked-loop parameters on the small-signal behavior of a vsc-hvdc converter," *IEEE Transactions on Power Delivery*, vol. 29, no. 5, pp. 2287–2296, 2014.

[106] R. C. Dorf and R. H. Bishop, *Modern control systems.* Pearson, 2011.

[107] S. Skogestad and I. Postlethwaite, *Multivariable feedback control: analysis and design.* Wiley New York, 2007, vol. 2.

[108] H. Latchman and O. Crisalle, "Exact robustness analysis for highly structured frequency-domain uncertainties," in *American Control Conference, Proceedings of the 1995*, vol. 6. IEEE, 1995, pp. 3982–3987.

[109] J. Doyle, "Analysis of feedback systems with structured uncertainties," in *IEE Proceedings D-Control Theory and Applications*, vol. 129, no. 6. IET, 1982, pp. 242–250.

[110] K. S. Ray and D. D. Majumder, "Application of circle criteria for stability analysis of linear siso and mimo systems associated with fuzzy logic controller," *IEEE Transactions on Systems, Man, and Cybernetics*, no. 2, pp. 345–349, 1984.

[111] D. Owens and A. Chotai, "Robust controller design for linear dynamic systems using approximate models," in *IEE Proceedings D (Control Theory and Applications)*, vol. 130, no. 2. IET, 1983, pp. 45–56.

[112] Xilinx, *ZC706 Evaluation Board for the Zynq-7000 XC7Z045 All Programmable SoC User Guide.* Xilinx Inc., 2016.

[113] F. De La Rosa, *Harmonics and power systems.* CRC press Boca Raton, 2006.

[114] M. P. Kazmierkowski, R. Krishnan, F. Blaabjerg, and J. Irwin, *Control in power electronics: selected problems.* Academic press, 2002.

[115] S. J. Orfanidis, *Introduction to signal processing.* Prentice-Hall, Inc., 1995.

[116] W. Duesterhoeft, M. W. Schulz, and E. Clarke, "Determination of instantaneous currents and voltages by means of alpha, beta, and zero components," *Transactions of the American Institute of Electrical Engineers*, vol. 70, no. 2, pp. 1248–1255, 1951.

[117] C. F. Van Loan, "Matrix computations (johns hopkins studies in mathematical sciences)," 1996.

[118] R. H. Park, "Two-reaction theory of synchronous machines generalized method of analysis-part i," *Transactions of the American Institute of Electrical Engineers*, vol. 48, no. 3, pp. 716–727, 1929.

[119] R. Teodorescu, M. Liserre, and P. Rodriguez, *Grid converters for photovoltaic and wind power systems.* John Wiley & Sons, 2011, vol. 29.

[120] R. N. Bracewell and R. N. Bracewell, *The Fourier transform and its applications.* McGraw-Hill New York, 1986, vol. 31999.

[121] Xilinx, *LogiCORE IP Processing System 7 v5.3.* Xilinx Inc., 2013.

[122] V. I. T. Association *et al.*, "American national standards institute, inc.,american national standard for fpga mezzanine card (fmc) standard, ansi standard ansi/vita 57.1-2008,(2008)."

[123] P. Consortium, "Pcie/104 and pci/104-express specification revision 3.0."

[124] Semikron, "Sevenpack igbt and mosfet driver skhi 71 (r) - datasheet," 2007.

[125] T. I. Incorporated, *SN74LVCC3245A Octal Bus Transceiver With Adjustable Output Voltage and 3-State Outputs*, 2017.

[126] Semikron, "Skm 75 gb 124 d - semitrans®m low loss igbt modules - thecnical specifications."

[127] LEM, "Lem voltage transducer lv 25-p - thecnical specifications," 2017.

[128] A. S. Sedra and K. C. Smith, *Microelectronic circuits.* New York: Oxford University Press, 1998.

[129] LEM, "Lem current transducer la 55-p - thecnical specifications," 2017.

[130] J. F. Chicharo, "Theory and application of (iir) adaptive notch filtering," 1989.

[131] S. Amen, P. Bilokon, A. Brinley-Codd, M. Fofaria, and T. Shah, "Numerical solutions of differential equations," *Imperial College London*, 2004.

Appendix A

Inverter AC voltage modulation

The theory applied to modulate the inverter AC voltage is presented in Section A.1, while the Space Vector Modulation (SVM) method, which has been used throughout the work, is discussed in Section A.2.

A.1 Inverter voltage modulation

The modulation of the three phase two level converter topology described in Section 2.1.1.1 is discussed as follows.

The inverter output voltage is regulated by a set of digital signals, the so-called Pulse Width Modulation (PWM) pattern. These signals alternatively change the turn-on and turn-off status of the inverter IGBT switches [72], with the purpose of obtaining the desired modulated voltage. The PWM pattern results from an algorithm which calculates the turn-on and turn-off times of the six inverter switches by comparing a set of per-unit reference voltages, the so-called modulation index functions m_{abc}, to a unique carrier signal. This typically is a triangular periodic waveform, whose frequency f_s is the switching frequency of the converter, and whose amplitude is in the range [-1, 1]. In this work, only the operation of the inverter under linear modulation conditions has been considered, therefore assuming that the modulation functions m_{abc} also lie in the [-1, 1] range [90].

Depending on the sampling strategy, namely natural sampling, regular symmetrical sampling and regular asymmetrical sampling, different PWM signals are obtained [73], shown in Figure A.1. In the natural sampling case, the modulation function and the carrier are continuously sampled. In the other two methods, which are used in practical hardware implementations, the comparison takes place at discrete times. In the symmetrical case, this occurs only when the carrier waveform has its minimum (or maximum) value, once every switching period $T_s = \frac{1}{f_s}$. Conversely, in the asymmetrical case, the comparison occurs twice per switching period, when the carrier is maximum and minimum. The modulation functions are therefore updated every T_{sample}, with $T_{sample} = \frac{T_s}{2}$. [73].

Taking into consideration the regular asymmetrical sampling technique, for a generic T_{sample} period $[t_k, t_{k+1}]$, by respectively indicating with $d_a[k]$, $d_b[k]$ and $d_c[k]$ the fractions of T_{sample} during which the switches Q_1, Q_3 and Q_5 are conducting during the $[t_k, t_{k+1}]$ interval (see Figure 2.2), these can be related to the values of $m_a[k]$, $m_b[k]$ and $m_c[k]$ as:

$$d_a[k] = \frac{m_a[k]+1}{2}, d_b[k] \quad = \frac{m_b[k]+1}{2}, d_c[k] = \frac{m_c[k]+1}{2} \tag{A.1}$$

Thereby, by considering the middle point of the DC link as the reference voltage, the average values $\hat{U}_{I,a}[k]$, $\hat{U}_{I,b}[k]$, $\hat{U}_{I,c}[k]$ of the inverter output voltages, calculated over the $[t_k, t_{k+1}]$ period, are [71], [72]:

$$\begin{aligned}
\hat{U}_{I,a}[k] &= \frac{2d_a - 1}{2} U_{DC} = m_a[k]\frac{U_{DC}}{2}, \\
\hat{U}_{I,b}[k] &= \frac{2d_b - 1}{2} U_{DC} = m_b[k]\frac{U_{DC}}{2}, \\
\hat{U}_{I,c}[k] &= \frac{2d_c - 1}{2} U_{DC} = m_c[k]\frac{U_{DC}}{2}
\end{aligned} \tag{A.2}$$

The linear relations (A.2) between the DC link voltage U_{DC} and the average inverter output voltages are valid for modulation indexes lying in the $[-1, 1]$ range, in other words under linear modulation conditions [71]. Equations (A.2) are at the basis of the average model of the inverter, used in this work (see Section 2.1.1.1).

Among the possible techniques that define the modulation functions, Space Vector Modulation (SVM) has been applied, because of its main advantage of assuring linear modulation over a wider range of values of the modulation indexes [73], as it will be discussed in the following Section A.2.

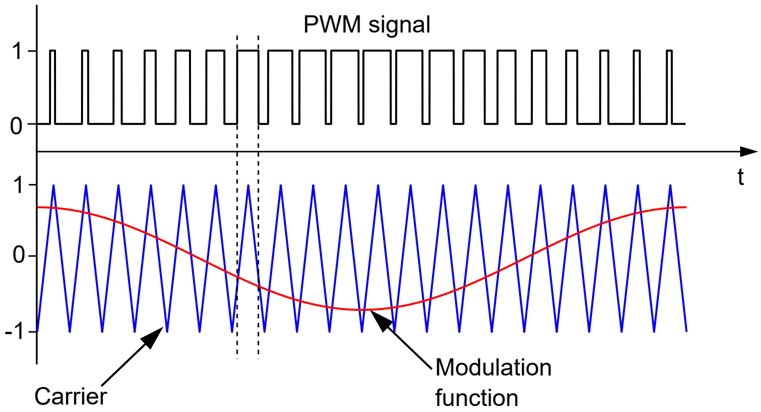

(a)

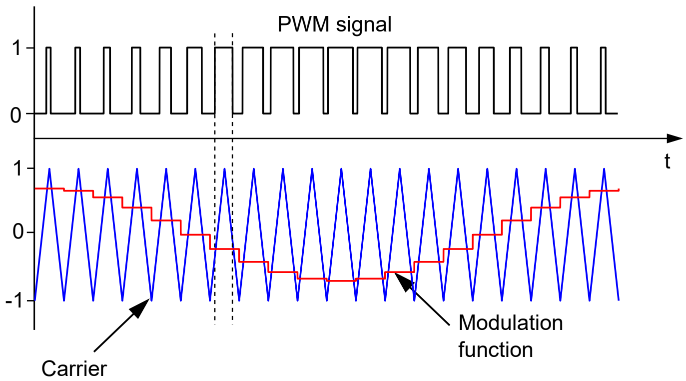

(b)

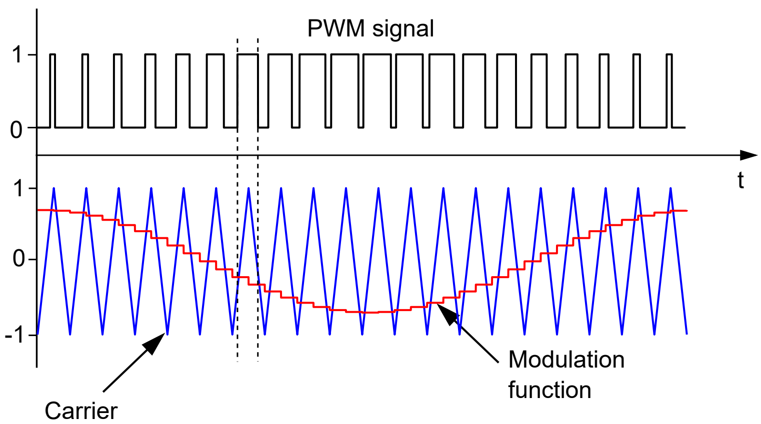

(c)

Figure A.1: Comparison among standard sampling strategies used to generate the PWM signal: (a) Natural sampling; (b) Regular symmetrical sampling (single edge); (c) Regular asymmetrical sampling (double edge).

A.2 Space Vector Modulation

The basic idea of this technique is to represent the desired inverter average output voltage $\hat{U}_{I,abc}[k]$ in (A.2) as a space vector $\vec{U}_I[k]$ in the $\alpha\beta$-frame (see Appendix B.1 for the definition of space vector). In particular, based on (B.7):

$$\vec{U}_I[k] = U_{I,\alpha}[k] + jU_{I,\beta}[k] \tag{A.3}$$

As the output terminal of each inverter leg can either be connected to the positive terminal of the inverter DC voltage (see Figure 2.2), or to its negative terminal, a digital value can be used to identify the two possible inverter leg output voltages (codified as 1 or 0 respectively). Thereby, the resulting three phase inverter voltage $U_{I,abc}$ can be identified as $U_{I,nmk}$ where n, m, k indicate the digital value, 0 or 1, for legs a, b, c respectively. Only 8 possible values can be taken by $U_{I,nmk}$, determining 8 corresponding base space vectors in the $\alpha\beta$-frame and indicated as $\vec{U}_{nmk}$ (see Figure A.2). The vectors $\vec{U}_{000}$ and $\vec{U}_{111}$ are the so-called zero vectors, which respectively correspond to the cases where the leg outputs are all connected to the negative terminal of the inverter DC input, or to its posititve terminal. The other six non-zero vectors have a magnitude equal to $\frac{2U_{DC}}{3}$ and divide the $\alpha\beta$ plane into 6 equal sectors, indicated as $S_{1,..,6}$ in the Figure A.2 [73]. U_{DC} is the inverter DC voltage.
Hence, the voltage $\vec{U}_I[k]$ in (A.3) can be described as a linear combination both of two of the six non-zero base vectors, depending on the sector where $\vec{U}_I[k]$ lies, and of the two zero base vectors. To give an example, if $\vec{U}_I[k]$ lies in sector S_1, it will be described as a combination of $\vec{U}_{100}$ and $\vec{U}_{110}$ and of the zero vectors. The two non-zero vectors used to describe $\vec{U}_I[k]$ are those limiting the sector where the $\vec{U}_I[k]$ is. Each of the selected base vectors is applied at the inverter output for a fraction of T_{sample} so that the resulting average inverter output over the T_{sample} period equals $\vec{U}_I[k]$. By indicating with $\vec{U}_L$ and $\vec{U}_R$ the two non-zero base vectors respectively leading and lagging $\vec{U}_I[k]$,

the following linear combination can be formulated:

$$\vec{U}_I[k] = k_L\vec{U}_L + k_R\vec{U}_R \tag{A.4}$$

where in (A.4) k_L and k_R are the fractions of T_{sample} during which the two base vectors $\vec{U}_L$ and $\vec{U}_R$ are respectively applied. In other words, the vector $\vec{U}_L$ is applied for a time $T_L = k_l T_{sample}$, while the vector $\vec{U}_R$ is applied for a time $T_R = k_r T_{sample}$, with:

$$T_L + T_R \leq T_{sample}$$

The remaining fraction of T_{sample} will be covered by the zero vectors $\vec{U}_{000}$ and $\vec{U}_{111}$, respectively applied for T_0 and T_1 periods. Among the different methods used to apply the zero vectors, their application before and after the non-zero vectors has been considered in this work [114].

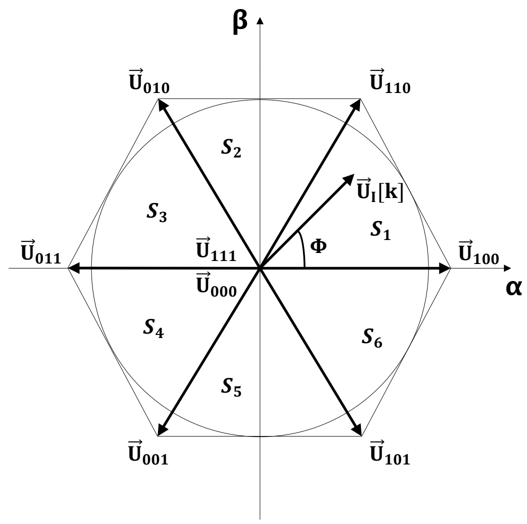

Figure A.2: Graphical representation of the SVM vectors

Taking into consideration the regular asymmetrical sampling strategy, the following Figure A.3 illustrates the operation of the SVM technique for a switching period $T_s =$

$2T_{sample}$.

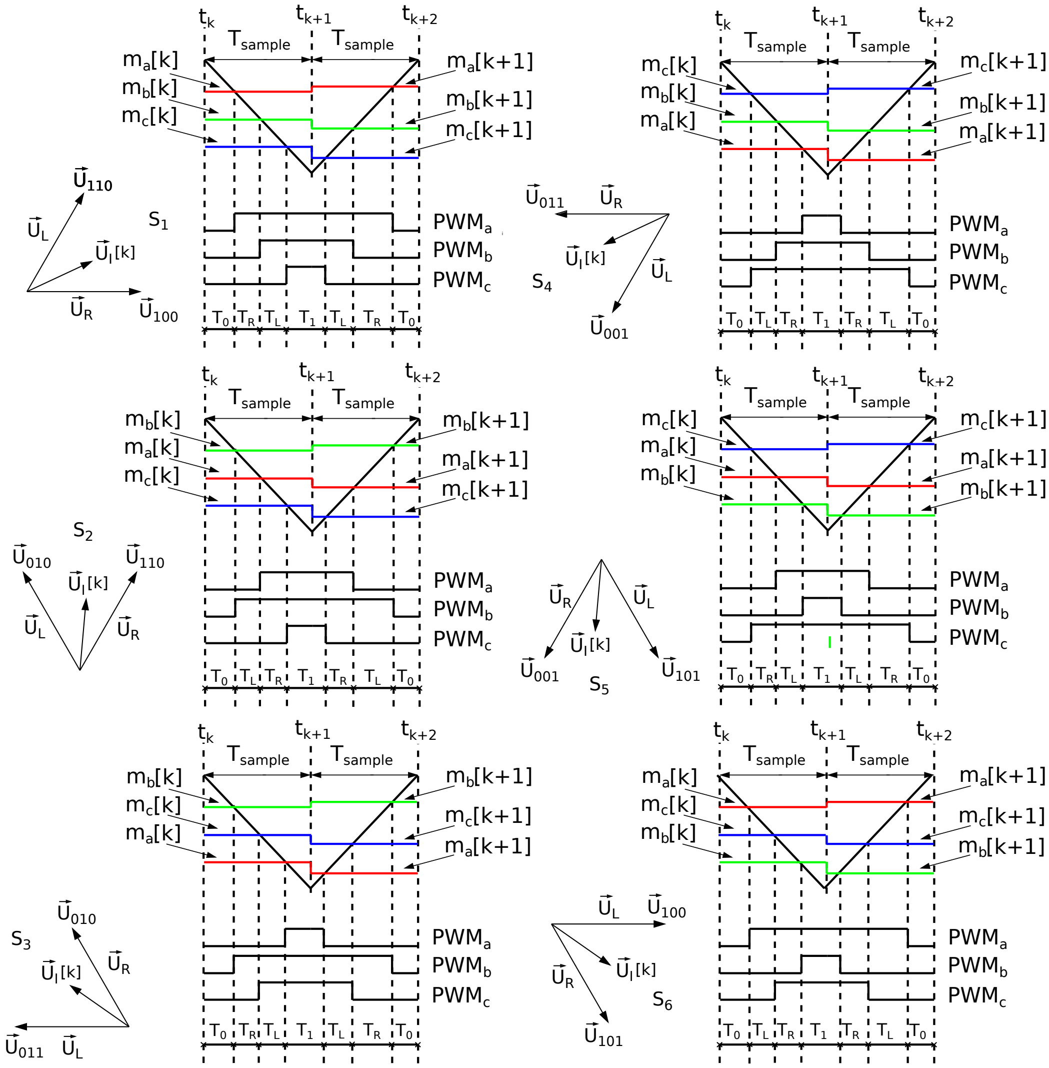

Figure A.3: Operation of the SVM algorithm.

The SVM modulation functions $m_{abc}[k]$ are applied by the inverter controller at $t = t_k$, i.e. at the beginning of the T_{sample} period. Hence, the corresponding PWM pattern associated to $m_{abc}[k]$ is applied in the $[t_k, t_{k+1}]$ interval. Based on (A.2), the following linear relation can be written between the modulated inverter voltage $\vec{U}_I[k]$ and the space vector $\vec{m}[k]$ associated to $m_{abc}[k]$:

$$\vec{U}_I[k] = \vec{m}[k]\frac{U_{DC}}{2} \tag{A.5}$$

An analytical expression of the SVM functions $m_{abc}[k]$ is calculated, which depends on the sector where the inverter voltage $\vec{U}_I[k]$ to be generated in the $[t_k,\, t_{k+1}]$ interval lies in. From (A.5), as this sector is the same one where $\vec{m}[k]$ lies, it can be identified by the $m_\alpha[k]$ and $m_\beta[k]$ components of $\vec{m}[k]$ in the $\alpha\beta$-frame, as detailed in Table A.1. The modulation functions $m_{abc}[k]$ are calculated as detailed in Table (A.2) where $M[k]$ is the module of the $\vec{m}[k]$ vector, calculated as $\sqrt{m_\alpha^2[k] + m_\beta^2[k]}$, while $\phi[k]$ is the angle between $\vec{U}_I[k]$ (or equivalently $\vec{m}[k]$) and the α axis, varying in the $[0, 2\pi]$ range (see Figure A.2).

Table A.1: Sector identification according to the SVM algorithm

1° Quadrant $m_\alpha[k] \geq 0$, $m_\beta[k] \geq 0$	$m_\beta[k] \leq \sqrt(3) m_\alpha[k]$ S_1	$m_\beta[k] > \sqrt(3) m_\alpha[k]$ S_2
2° Quadrant $m_\alpha[k] < 0$, $m_\beta[k] \geq 0$	$m_\beta[k] \leq -\sqrt(3) m_\alpha[k]$ S_3	$m_\beta[k] > -\sqrt(3) m_\alpha[k]$ S_2
3° Quadrant $m_\alpha[k] \leq 0$, $m_\beta[k] \leq 0$	$m_\beta[k] \geq \sqrt(3) m_\alpha[k]$ S_4	$m_\beta[k] < \sqrt(3) m_\alpha[k]$ S_5
4° Quadrant $m_\alpha[k] > 0$, $m_\beta[k] \leq 0$	$m_\beta[k] \geq -\sqrt(3) m_\alpha[k]$ S_6	$m_\beta[k] < -\sqrt(3) m_\alpha[k]$ S_3

It is worth noticing that, within the limits of linear modulation, the maximum lenght of $\vec{U}_I[k]$ which can be reproduced by this algorithm is equal to $\frac{U_{DC}}{\sqrt{3}}$, identifying the circular area in Figure (A.2). The corresponding maximum value of the modulations function is $\frac{2}{\sqrt{3}} \approx 1.15$, i.e. approximately 15 % higher than the maximum modulation indexes achievable when using sinusoidal reference functions. This is one of the main advantages of the SVM technique, which justifies its wide use in industrial applications [73].

Table A.2: $m_{abc}[k]$ modulation functions according to the SVM algorithm.

Sector	$m_{abc}[k]$	Sector	$m_{abc}[k]$
1	$m_a[k] = \frac{\sqrt(3)}{2}M[k]cos(\phi[k] - \frac{\pi}{6})$, $m_b[k] = \frac{3}{2}M[k]cos(\phi[k] - \frac{2}{3}\pi)$, $m_c[k] = \frac{\sqrt(3)}{2}M[k]cos(\phi[k] - \frac{7}{6}\pi)$	4	$m_a[k] = \frac{\sqrt(3)}{2}M[k]cos(\phi[k] - \frac{\pi}{6})$, $m_b[k] = \frac{3}{2}M[k]cos(\phi[k] - \frac{2}{3}\pi)$, $m_c[k] = \frac{\sqrt(3)}{2}M[k]cos(\phi[k] - \frac{7}{6}\pi)$
2	$m_a[k] = \frac{3}{2}M[k]cos(\phi[k])$, $m_b[k] = \frac{\sqrt(3)}{2}M[k]cos(\phi[k] - \frac{\pi}{2})$, $m_c[k] = \frac{\sqrt(3)}{2}M[k]cos(\phi[k] - \frac{3}{2}\pi)$	5	$m_a[k] = \frac{3}{2}M[k]cos(\phi[k])$, $m_b[k] = \frac{\sqrt(3)}{2}M[k]cos(\phi[k] - \frac{\pi}{2})$, $m_c[k] = \frac{\sqrt(3)}{2}M[k]cos(\phi[k] - \frac{3}{2}\pi)$
3	$m_a[k] = \frac{\sqrt(3)}{2}M[k]cos(\phi[k] + \frac{\pi}{6})$, $m_b[k] = \frac{\sqrt(3)}{2}M[k]cos(\phi[k] - \frac{5}{6}\pi)$, $m_c[k] = \frac{3}{2}M[k]cos(\phi[k] - \frac{4}{3}\pi)$	6	$m_a[k] = \frac{\sqrt(3)}{2}M[k]cos(\phi[k] + \frac{\pi}{6})$, $m_b[k] = \frac{\sqrt(3)}{2}M[k]cos(\phi[k] - \frac{5}{6}\pi)$, $m_c[k] = \frac{3}{2}M[k]cos(\phi[k] - \frac{4}{3}\pi)$

Appendix B

Definition of the dq-frame

In this Appendix the mathematical framework used to formulate the dq-frame used throughout this work will be presented. This is based on the phase space vector concept, defined in Section B.1 and on the Clarke and Park transformations, respectively discussed in Sections B.2 and B.3. Both a positive and a negative dq-frame will be defined, which are respectively used for the implementation of the positive and the negative sequence current controllers, discussed in Section 2.2.1.

B.1 Three phase space vector

The following abc-frame balanced signal $f_{abc}(t)$ is considered:

$$\begin{aligned} f_a(t) &= \hat{f}cos(\omega_0 t), \\ f_b(t) &= \hat{f}cos(\omega_0 t - \frac{2}{3}\pi), \\ f_c(t) &= \hat{f}cos(\omega_0 t - \frac{4}{3}\pi) \end{aligned} \tag{B.1}$$

where $\hat{f}$ is constant and represents the maximum amplitude of the phase signals, whereas $\omega_0 = 2\pi f_0$ is the frequency, with $f_0 = 50$ Hz. Equation (B.1) describes the ideal form of the plant signals in a power system operating at steady state conditions. The space vector $\vec{f}(t)$ is defined as [58]:

$$\vec{f}(t) = \frac{2}{3}[f_a(t) + e^{j\frac{2}{3}\pi} f_b(t) + e^{j\frac{4}{3}\pi} f_c(t)] \tag{B.2}$$

which, using Euler's formula [115], can be reformulated as:

$$\vec{f}(t) = \hat{f}e^{j\omega_0 t} \tag{B.3}$$

The space vector $\vec{f}(t)$ can be interpreted as a phasor vector rotating (anti-clockwise) in the complex plane at the rotational speed ω_0.
The expression (B.3) can be extended to the case when both the amplitude $\hat{f}$ and the frequency ω of the three phase signal are time-dependant:

$$\begin{aligned} f_a(t) &= \hat{f}(t)cos(\theta(t)), \\ f_b(t) &= \hat{f}(t)cos(\theta(t) - \frac{2}{3}\pi), \\ f_c(t) &= \hat{f}(t)cos(\theta(t) - \frac{4}{3}\pi) \end{aligned} \tag{B.4}$$

where $\theta(t)$ is:

$$\theta(t) = \int_0^t \omega(\tau)d\tau \tag{B.5}$$

$\omega(t)$ represents the time-dependent angular frequency of the three phase signal.
Hence, the general expression of the space vector can be formulated as:

$$\vec{f} = \hat{f}(t)e^{j\theta(t)} \tag{B.6}$$

It is worth mentioning that (B.1) and (B.4) indicate a positive sequence (balanced) signal, where phase b and c respectively lag phase a by $\frac{2}{3}\pi$ rad and $\frac{4}{3}\pi$ rad.

B.2 Stationary $\alpha\beta$-frame

The space vector introduced in the previous Section can be mapped onto a stationary two dimensional frame, whose axis are conventionally indicated as α and β [58]. This represents a complex plane reference frame in which the time-varying position of the rotating space vector is identified by its coordinates $f_\alpha(t)$ and $f_\beta(t)$:

$$\vec{f}(t) = f_\alpha(t) + jf_\beta(t) \tag{B.7}$$

In particular, $f_\alpha(t)$ and $f_\beta(t)$ can be calculated making use of the Clarke transform C [116]:

$$\begin{bmatrix} f_\alpha(t) \\ f_\beta(t) \end{bmatrix} = C \begin{bmatrix} f_a(t) \\ f_b(t) \\ f_c(t) \end{bmatrix} = \frac{2}{3} \cdot \begin{bmatrix} 1 & -\frac{1}{2} & -\frac{1}{2} \\ 0 & \frac{1}{2}\sqrt{3} & -\frac{1}{2}\sqrt{3} \end{bmatrix} \begin{bmatrix} f_a(t) \\ f_b(t) \\ f_c(t) \end{bmatrix} \tag{B.8}$$

The Figure B.1 represents the space vector $\vec{f}(t)$ in the defined stationary $\alpha\beta$-frame.

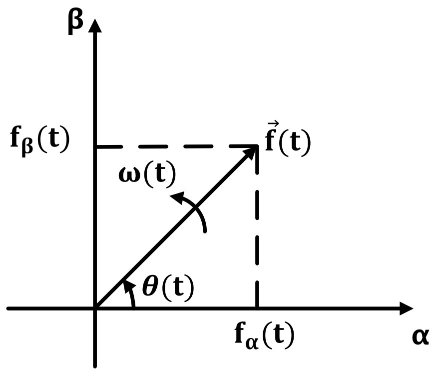

Figure B.1: Representation of the space vector $\vec{f}(t)$ in the $\alpha\beta$-frame.

B.3 Positive dq-frame

From the perspective of the controller designer, a convenient reference frame would be one where the space vector is represented by constant coordinates. In fact, this would allow to deal with AC signals as if they were DC quantities. For this purpose, a new set of coordinates of $\vec{f}(t)$ are defined, indicated as $f_d(t)$ and $f_q(t)$, such that [58]:

$$\vec{f}(t) = f_\alpha(t) + jf_\beta(t) = [f_d(t) + jf_q(t)]e^{j\epsilon(t)} \tag{B.9}$$

The $f_d(t)$ and $f_q(t)$ coordinates are defined in the so-called dq-frame, which is rotated by an angle $\epsilon(t)$ with respect to the stationary $\alpha\beta$-frame. In particular, $\epsilon(t)$ is defined as:

$$\epsilon(t) = \epsilon_0 + \int_0^{\tau} \omega(\tau) d\tau. \tag{B.10}$$

From (B.5), (B.10):

$$\frac{d\epsilon(t)}{dt} = \frac{d\theta(t)}{dt} = \omega(t) \tag{B.11}$$

Equation (B.10) implies that the dq-frame rotates at the same speed $\omega(t)$ of the space vector $\vec{f}(t)$. In particular, from equations (B.6), (B.9):

$$\begin{aligned} &\vec{f} = \hat{f}(t)e^{j\theta(t)} = [f_d(t) + jf_q(t)]e^{j\epsilon(t)} \Rightarrow \\ &\hat{f}(t)e^{j(\theta(t)-\epsilon(t))} = f_d(t) + jf_q(t) \Rightarrow \\ &\hat{f}(t)e^{-j\epsilon_0} = f_d(t) + jf_q(t) \Rightarrow \\ &\hat{f}(t) = [f_d(t) + jf_q(t)]e^{j\epsilon_0} \end{aligned} \tag{B.12}$$

Furthermore, if $\theta(t) = \omega_0 t$ then:

$$\begin{aligned} \frac{d\vec{f}(t)}{dt} &= \frac{d\{[f_d(t) + jf_q(t)]e^{j(\omega_0 t+\epsilon_0)}\}}{dt} = [\frac{df_d(t)}{dt} + j\frac{df_q(t)}{dt}]e^{(j\omega_0 t+\epsilon_0)} \\ &+ [f_d(t) + jf_q(t)]j\omega_0 e^{(j\omega_0 t+\epsilon_0)} = \\ &= \{[\frac{df_d(t)}{dt} - \omega_0 f_q(t)] + j[\frac{df_q(t)}{dt} + \omega_0 f_d(t)]\}e^{(j\omega_0 t+\epsilon_0)} \end{aligned} \tag{B.13}$$

Among the different possible orientations of the dq-frame, in the present work the one shown in Figure (B.2) has been chosen where the q-axis leads the d-axis by 90° and is aligned to the phase a of $\vec{f}(t)$ [81]. According to this orientation, ϵ_0 in (B.10), (B.12) is equal to $-\frac{\pi}{2}$. Thereby, from (B.12):

$$\vec{f} = [f_d(t) + jf_q(t)]e^{j(\theta(t)-\frac{\pi}{2})} \tag{B.14}$$

The $f_d(t)$ and $f_q(t)$ coordinates can be obtained from the $f_\alpha(t)$, $f_\beta(t)$ applying the $R(\theta(t))$ transformation, which is one version of the Givens rotations [117]:

$$\begin{bmatrix} f_d(t) \\ f_q(t) \end{bmatrix} = R(\theta(t)) \begin{bmatrix} f_\alpha(t) \\ f_\beta(t) \end{bmatrix} = \begin{bmatrix} sin(\theta(t)) & -cos(\theta(t)) \\ cos(\theta(t)) & sin(\theta(t)) \end{bmatrix} \begin{bmatrix} f_\alpha(t) \\ f_\beta(t) \end{bmatrix} \tag{B.15}$$

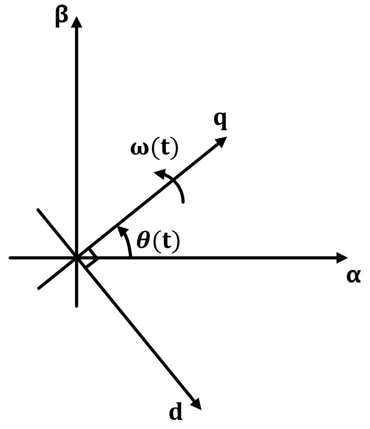

Figure B.2: Defined orientation of the dq-frame.

In order to highlight that the defined dq-frame rotates at the same frequency $\omega(t)$ of (B.4), which is a positive sequence signal, such rotating frame will also be indicated as positive sequence dq-frame, or simply positive dq-frame throughout the work. Combining the C and $R(\theta(t))$ transformations respectively defined in (B.8) and (B.15), a unique matrix transformation $T(\theta(t)) = R(\theta(t)) \cdot C$ can be formulated to map the three phase signal defined in (B.4) onto the positive dq-frame:

$$\begin{bmatrix} f_d(t) \\ f_q(t) \end{bmatrix} = T(\theta(t)) \begin{bmatrix} f_a(t) \\ f_b(t) \\ f_c(t) \end{bmatrix} = \frac{2}{3} \cdot \begin{bmatrix} sin(\theta(t)) & sin(\theta(t) - \frac{2}{3}\pi) & sin(\theta(t) - \frac{4}{3}\pi) \\ cos(\theta(t)) & cos(\theta(t) - \frac{2}{3}\pi) & cos(\theta(t) - \frac{4}{3}\pi) \end{bmatrix} \begin{bmatrix} f_a(t) \\ f_b(t) \\ f_c(t) \end{bmatrix} \tag{B.16}$$

Such transformation in (B.16) is the Park transform [118]. In particular, assuming that the three phase signal $f_{abc}(t)$ is defined as in (B.1) then the values of $f_d(t)$ and $f_q(t)$

become time-invariant. Such property of $T(\theta(t))$ is exploited in the implementation of the converter controller in the dq-frame, as discussed in Section 2.2.1.

The $f_{abc}(t)$ signal can be obtained from the dq-frame signal $f_{dq}(t)$ applying the transpose transform matrix $T^T(\theta(t))$:

$$\begin{bmatrix} f_a(t) \\ f_b(t) \\ f_c(t) \end{bmatrix} = T^T(\theta(t)) \begin{bmatrix} x_d(t) \\ x_q(t) \end{bmatrix} = \begin{bmatrix} sin(\theta(t)) & cos(\theta(t)) \\ sin(\theta(t) - \frac{2}{3}\pi) & cos(\theta(t) - \frac{2}{3}\pi) \\ sin(\theta(t) - \frac{4}{3}\pi) & cos(\theta(t) - \frac{4}{3}\pi) \end{bmatrix} \begin{bmatrix} f_d(t) \\ f_q(t) \end{bmatrix} \quad \text{(B.17)}$$

B.4 Negative dq-frame

In this Section, the case of mapping an unbalanced three phase signal on a rotating dq-frame is considered. This will lead to the introduction of the negative sequence dq-frame.

Unbalance in plant signals may for example be caused by fault grid conditions or simply by differences in the phase impedances of the electrical system [58]. Such unbalanced signals can be analytically described as a combination of a positive and a negative sequence signal. While the former has the form given in (B.1) and is characterized by a space vector rotating anti-clockwise at ω_0 in the $\alpha\beta$-frame, the latter is instead associated to a space vector rotating at ω_0 but in the opposite direction (i.e. clockwise), with phase b and c respectively leading phase a by $\frac{2}{3}\pi$ rad and $\frac{4}{3}\pi$ rad.

It is worth mentioning that three phase AC signals may also have a zero sequence component, where no phase shift occurs among the phases of the signal. However, such component may be present only when a 4 wire electrical connection which includes the neutral conductor is employed in the system. A 3 wire connection (i.e. without the neutral wire) has been applied in this work, as this represents common practice in real installations of grid-connected inverters [119], as such the zero sequence component has not been included in this study.

Based on the aforementioned considerations, a generic unbalanced signal $f_{abc}(t)$ signal can be described as [119]:

$$f_{abc}(t) = \begin{bmatrix} f_a(t) \\ f_b(t) \\ f_c(t) \end{bmatrix} = \hat{f}^+ \begin{bmatrix} cos(\omega_0 t) \\ cos(\omega_0 t - \frac{2}{3}\pi) \\ cos(\omega_0 t + \frac{2}{3}\pi) \end{bmatrix} + \hat{f}^{-1} \begin{bmatrix} cos(\omega_0 t) \\ cos(\omega_0 t + \frac{2}{3}\pi) \\ cos(\omega_0 t - \frac{2}{3}\pi) \end{bmatrix} \tag{B.18}$$

where the scenario of a signal with no other frequency harmonics has been considered. Despite the fact that $\hat{f}^+$ and $\hat{f}^-$ are assumed constant in (B.18), the theoretical results illustrated in this Section can be generalised to the more general case when these quantities are time-dependant. Based on the definition given in (B.2), the space vector corresponding to (B.18) is:

$$\vec{f}(t) = \vec{f}^+(t) + \vec{f}^-(t) = \hat{f}^+ e^{j\omega_0 t} + \hat{f}^- e^{-j\omega_0 t} \tag{B.19}$$

which highlights how this is composed of two components, $\vec{f}^+(t)$ and $\vec{f}^-(t)$, respectively associated to the positive and negative sequence components of $f_{abc}(t)$. Albeit both of them rotate at ω_0, the former moves anti-clockwise, the latter clockwise. Hence, an equivalent dq-frame can be defined for the negative sequence component of $f_{abc}(t)$. Such a frame would now be rotating at the same speed of $\vec{f}^-(t)$, i.e. at ω_0 (clockwise). It is named negative sequence dq-frame, or simply negative dq-frame. According to the used notation, $\vec{f}^-(t)$ can be expressed as:

$$\vec{f}^- = [f_d^- + jf_q^-]e^{-j(\theta(t)+\frac{\pi}{2})} \tag{B.20}$$

with $\theta(t) = \omega_0 t$. The signals f_d^- and f_q^- are the dq-components of $\vec{f}^-$ in the negative dq-frame. These are calculated by the same Park transform matrix in (B.16) where $\theta(t)$ is now replaced by $-\theta(t)$. A graphical representation of both the positive and negative sequence dq-frames is given in Figure B.3.

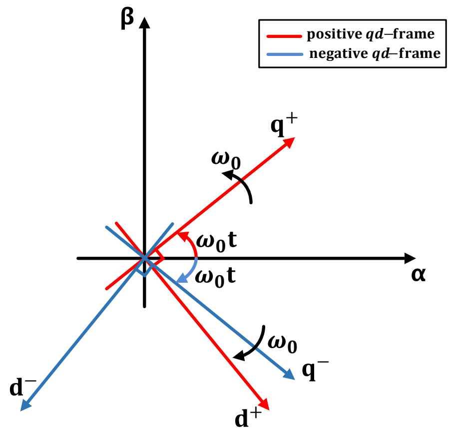

Figure B.3: Representation of the positive and negative dq-frames.

When mapping the $\vec{f}^{+}(t)$ space vector on the positive dq-frame its d- and q-components respectively are $\bar{f}_d^{+}$ and $\bar{f}_q^{+}$. Equivalently, when representing the $\vec{f}^{-}(t)$ space vector on the negative dq-frame the resulting components are $\bar{f}_d^{-}$ and $\bar{f}_q^{-}$. When the $\vec{f}$ space vector (B.19) is mapped either on the positive or on the negative dq-frame, its dq-components will be either $f_q^{+}(t)$, $f_q^{+}(t)$ or $f_q^{-}(t)$, $f_q^{-}(t)$, respectively. Their expressions are [58]:

$$\begin{aligned}
\begin{bmatrix} f_d^{+}(t) \\ f_q^{+}(t) \end{bmatrix} &= \begin{bmatrix} \bar{f}_d^{+} \\ \bar{f}_q^{+} \end{bmatrix} + \begin{bmatrix} cos(2\omega_0 t) & sin(2\omega_0 t) \\ -sin(2\omega_0 t) & cos(2\omega_0 t) \end{bmatrix} \begin{bmatrix} \bar{f}_d^{-} \\ \bar{f}_q^{-} \end{bmatrix}, \\
\begin{bmatrix} f_d^{-}(t) \\ f_q^{-}(t) \end{bmatrix} &= \begin{bmatrix} \bar{f}_d^{-} \\ \bar{f}_q^{-} \end{bmatrix} + \begin{bmatrix} cos(2\omega_0 t) & -sin(2\omega_0 t) \\ sin(2\omega_0 t) & cos(2\omega_0 t) \end{bmatrix} \begin{bmatrix} \bar{f}_d^{+} \\ \bar{f}_q^{+} \end{bmatrix}
\end{aligned} \tag{B.21}$$

It can be seen that such dq-frame components have both a DC element ($\bar{f}_d^{+}$, $\bar{f}_q^{+}$,$\bar{f}_d^{-}$, $\bar{f}_q^{-}$) and an oscillatory one. The latter, which is at $2\omega_0$, can be seen as a coupling effect between the positive and negative sequence components of $f_{abc}(t)$. This result affects the design of the converter current controller, which aims to control the positive and negative sequence components of the AC inverter current separately (see Section 2.2.1.1). Among the different methods suggested in the literature to remove this coupling effect [119], a notch filter tuned at $2\omega_0$ has been used in this work, as discussed in Section 2.2.1.1.2.

Appendix C

Mathematical derivations

C.1 State-space model of the electrical system in the *dq*-frame

In this Section, the derivation of the *dq*-frame state-space representations of the grid-inverter electrical system models used in the work is provided.

C.1.1 Electrical system in Figure 2.6

The *dq*-frame state-space model of the circuit illustrated in Figure (C.1) is derived, which is equal to the grid-inverter interface equivalent circuit shown in Figure 2.6.

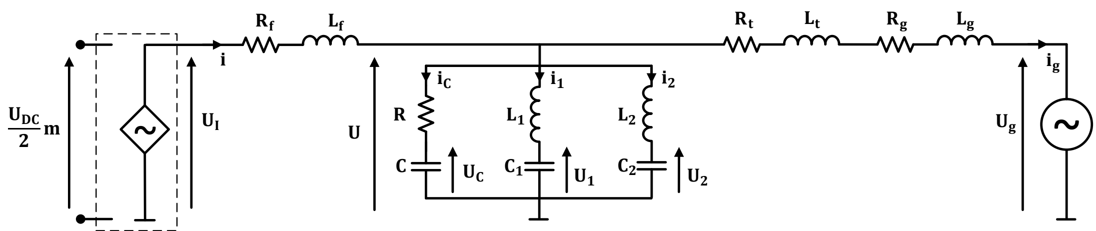

Figure C.1: One-line diagram of the turbine-grid model described in Section 2.1.3.

The set of equations (C.1) can be written, in the time domain, for the space vectors associated to the signals highlighted in the circuit. Such space vectors have been defined according to (B.14), with $\theta(t) = \omega_0 t$.

$$
\begin{aligned}
\vec{U}_I(t) &= \vec{U}(t) + R_\mathrm{f}\vec{i}(t) + L_f\frac{d\vec{i}(t)}{dt} \\
\vec{U}(t) &= \vec{U}_g(t) + (R_t + R_g)\vec{i}_g(t) + (L_t + L_g)\frac{d\vec{i}_g(t)}{dt} \\
\vec{U}(t) &= \vec{U}_2(t) + L_2\frac{d\vec{i}_2(t)}{dt} \\
\vec{U}(t) &= \vec{U}_1(t) + L_1\frac{d\vec{i}_1(t)}{dt} \\
\vec{i}_2(t) &= C_2\frac{d\vec{U}_2(t)}{dt} \\
\vec{i}_1(t) &= C_1\frac{d\vec{U}_1(t)}{dt} \\
\vec{i}_c(t) &= C\frac{d\vec{U}_c(t)}{dt}
\end{aligned}
\tag{C.1}
$$

It is highlighted that equations (C.1) define an LTI system, thus making the derivation of the state-space model straightforward [25]. Equations (C.1) are reformulated in terms of the *dq*-components of the signals. By making use of (B.13), the following equations (C.2) and (C.3) are obtained for the *d*- and *q*- components of the signals, respectively:

$$
\begin{aligned}
U_{I_d}(t) &= U_d(t) + R_f i_d(t) + L_f\frac{di_d(t)}{dt} - L_f\omega_0 i_q(t) \\
U_d(t) &= U_{g_d}(t) + (R_t + R_g)i_{g_d}(t) + (L_t + L_g)\frac{di_{g_d}(t)}{dt} - (L_t + L_g)\omega_0 i_{g_q}(t) \\
U_d(t) &= U_{2_d}(t) + L_2\frac{di_{2_d}(t)}{dt} - L_2\omega_0 i_{2_q}(t) \\
U_d(t) &= U_{1_d}(t) + L_1\frac{di_{1_d}(t)}{dt} - L_1\omega_0 i_{1_q}(t) \\
i_{2_d}(t) &= C_2\frac{dU_{2_d}(t)}{dt} - C_2\omega_0 U_{2_q}(t) \\
i_{1_d}(t) &= C_1\frac{dU_{1_d}(t)}{dt} - C_1\omega_0 U_{1_q}(t) \\
i_{c_d}(t) &= C\frac{dU_{c_d}(t)}{dt} - C\omega_0 U_{c_q}(t)
\end{aligned}
\tag{C.2}
$$

$$
\begin{aligned}
U_{I_q}(t) &= U_q(t) + R_f i_q(t) + L_f \frac{di_q(t)}{dt} + L_f \omega_0 i_d(t) \\
U_q(t) &= U_{g_q}(t) + (R_t + R_g) i_{g_q}(t) + (L_t + L_g) \frac{di_{g_q}(t)}{dt} + (L_t + L_g)\omega_0 i_{g_d}(t) \\
U_q(t) &= U_{2_q}(t) + L_2 \frac{di_{2_q}(t)}{dt} + L_2 \omega_0 i_{2_d}(t) \\
U_q(t) &= U_{1_q}(t) + L_1 \frac{di_{1_q}(t)}{dt} + L_1 \omega_0 i_{1_d}(t) \\
i_{2_q}(t) &= C_2 \frac{dU_{2_q}(t)}{dt} + C_2 \omega_0 U_{2_d}(t) \\
i_{1_q}(t) &= C_1 \frac{dU_{1_q}(t)}{dt} + C_1 \omega_0 U_{1_d}(t) \\
i_{c_q}(t) &= C \frac{dU_{c_q}(t)}{dt} + C \omega_0 U_{c_d}(t)
\end{aligned}
\tag{C.3}
$$

By defining the state variables $x_i(t)$, with $i = 1, ..., 14$, the input variables $u_j(t)$, with $j = 1, ..., 4$, and output variables $y_k(t)$, with $k = 1, ..., 4$, as detailed in (C.4), the state-space model (C.5) is found. In particular, $\vec{x}_u(t) = [x_1(t), ..., x_{14}(t)]$, $\vec{u}(t) = [u_1(t), ..., u_4(t)]$ and $\vec{y}(t) = [y_1(t), ..., y_4(t)]$ respectively are the state-, the input- and the output- (column) vectors.

$$
\begin{bmatrix} x_1(t) + jx_2(t) \\ x_3(t) + jx_4(t) \\ x_5(t) + jx_6(t) \\ x_7(t) + jx_8(t) \\ x_9(t) + jx_{10}(t) \\ x_{11}(t) + jx_{12}(t) \\ x_{13}(t) + jx_{14}(t) \end{bmatrix} = \begin{bmatrix} U_{2_d}(t) + jU_{2_q}(t) \\ U_{c_d}(t) + jU_{c_q}(t) \\ U_{1_d}(t) + jU_{1_q}(t) \\ i_{2_d}(t) + ji_{2_q}(t) \\ i_{1_d}(t) + ji_{1_q}(t) \\ i_d(t) + ji_q(t) \\ i_{g_d}(t) + ji_{g_q}(t) \end{bmatrix} ; \begin{bmatrix} u_1(t) + ju_2(t) \\ u_3(t) + ju_4(t) \end{bmatrix} = \begin{bmatrix} U_{I_d}(t) + jU_{I_q}(t) \\ U_{g_d}(t) + jU_{g_q}(t) \end{bmatrix} ;
$$

$$
\begin{bmatrix} y_{1_d}(t) + jy_{2_q}(t) \\ y_{3_d}(t) + jy_{4_q}(t) \end{bmatrix} = \begin{bmatrix} i_d(t) + ji_q(t) \\ U_d(t) + jU_q(t) \end{bmatrix} ; \tag{C.4}
$$

$$
\begin{cases} \frac{d\vec{x}_u(t)}{dt} = A_u \vec{x}_u(t) + B_u \vec{u}(t), \\ \vec{y}(t) = C_u \vec{x}_u(t) \end{cases} \tag{C.5}
$$

The matrices A_u, B_u and C_u are respectively provided in (C.6), (C.7) and (C.8).

$$A_u = \begin{bmatrix}
0 & \omega_0 & 0 & 0 & 0 & 0 & \frac{1}{C_2} & 0 & 0 & 0 & 0 & 0 & 0 & 0 \\
-\omega_0 & 0 & 0 & 0 & 0 & 0 & 0 & \frac{1}{C_2} & 0 & 0 & 0 & 0 & 0 & 0 \\
0 & 0 & 0 & \omega_0 & 0 & 0 & -\frac{1}{C} & 0 & -\frac{1}{C} & 0 & \frac{1}{C} & 0 & -\frac{1}{C} & 0 \\
0 & 0 & -\omega_0 & 0 & 0 & 0 & 0 & -\frac{1}{C} & 0 & -\frac{1}{C} & 0 & \frac{1}{C} & 0 & -\frac{1}{C} \\
0 & 0 & 0 & 0 & 0 & \omega_0 & 0 & 0 & \frac{1}{C_1} & 0 & 0 & 0 & 0 & 0 \\
0 & 0 & 0 & 0 & -\omega_0 & 0 & 0 & 0 & 0 & \frac{1}{C_1} & 0 & 0 & 0 & 0 \\
-\frac{1}{L_2} & 0 & \frac{1}{L_2} & 0 & 0 & 0 & -\frac{R}{L_2} & \omega_0 & -\frac{R}{L_2} & 0 & \frac{R}{L_2} & 0 & -\frac{R}{L_2} & 0 \\
0 & -\frac{1}{L_2} & 0 & \frac{1}{L_2} & 0 & 0 & -\omega_0 & -\frac{R}{L_2} & 0 & -\frac{R}{L_2} & 0 & \frac{R}{L_2} & 0 & -\frac{R}{L_2} \\
0 & 0 & \frac{1}{L_1} & 0 & -\frac{1}{L_1} & 0 & -\frac{R}{L_1} & 0 & -\frac{R}{L_1} & \omega_0 & \frac{R}{L_1} & 0 & -\frac{R}{L_1} & 0 \\
0 & 0 & 0 & \frac{1}{L_1} & 0 & -\frac{1}{L_1} & 0 & -\frac{R}{L_1} & -\omega_0 & -\frac{R}{L_1} & 0 & \frac{R}{L_1} & 0 & -\frac{R}{L_1} \\
0 & 0 & -\frac{1}{L_f} & 0 & 0 & 0 & \frac{R}{L_f} & 0 & \frac{R}{L_f} & 0 & -\frac{R+R_f}{L_f} & \omega_0 & \frac{R}{L_f} & 0 \\
0 & 0 & 0 & -\frac{1}{L_f} & 0 & 0 & 0 & \frac{R}{L_f} & 0 & \frac{R}{L_f} & -\omega_0 & -\frac{R+R_f}{L_f} & 0 & \frac{R}{L_f} \\
0 & 0 & \frac{1}{L_t} & 0 & 0 & 0 & -\frac{R}{L_t} & 0 & -\frac{R}{L_t} & 0 & \frac{R}{L_t} & 0 & -\frac{R+R_t}{L_t} & \omega_0 \\
0 & 0 & 0 & \frac{1}{L_t} & 0 & 0 & 0 & -\frac{R}{L_t} & 0 & -\frac{R}{L_t} & 0 & \frac{R}{L_t} & -\omega_0 & -\frac{R+R_t}{L_t}
\end{bmatrix} \tag{C.6}$$

$$B_u = \begin{bmatrix} 0 & 0 & 0 & 0 \\ 0 & 0 & 0 & 0 \\ 0 & 0 & 0 & 0 \\ 0 & 0 & 0 & 0 \\ 0 & 0 & 0 & 0 \\ 0 & 0 & 0 & 0 \\ 0 & 0 & 0 & 0 \\ 0 & 0 & 0 & 0 \\ 0 & 0 & 0 & 0 \\ 0 & 0 & 0 & 0 \\ \frac{1}{L_f} & 0 & 0 & 0 \\ 0 & \frac{1}{L_f} & 0 & 0 \\ 0 & 0 & -\frac{1}{L_t} & 0 \\ 0 & 0 & 0 & -\frac{1}{L_t} \end{bmatrix} \tag{C.7}$$

$$C_u = \begin{bmatrix} 0 & 0 & 0 & 0 & 0 & 0 & 0 & 0 & 0 & 0 & 1 & 0 & 0 & 0 \\ 0 & 0 & 0 & 0 & 0 & 0 & 0 & 0 & 0 & 0 & 0 & 1 & 0 & 0 \\ 0 & 0 & 1 & 0 & 0 & 0 & -R & 0 & -R & 0 & R & 0 & -R & 0 \\ 0 & 0 & 0 & 1 & 0 & 0 & 0 & -R & 0 & -R & 0 & R & 0 & -R \end{bmatrix} \tag{C.8}$$

C.1.2 Electrical system in Figure 2.27

The dq-frame state-space model of the circuit illustrated in Figure (C.2) is derived, which models the grid-inverter system shown in Figure 2.27. The set of equations (C.9) can be derived for the space vectors associated to the signals highlighted in the circuit. Such space vectors have been defined according to (B.14), with $\theta(t) = \omega_0 t$.

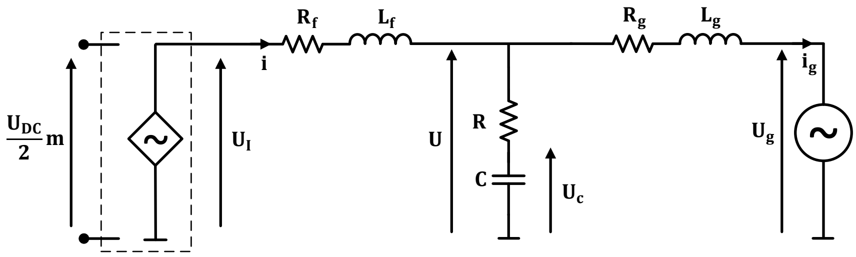

Figure C.2: One-line diagram of the laboratory prototype grid-converter interface model described in Section 2.3.2.3.

$$
\begin{aligned}
\vec{U}_I(t) &= \vec{U}(t) + R_f \vec{i}(t) + L_f \frac{d\vec{i}(t)}{dt} \\
\vec{U}(t) &= \vec{U}_g(t) + R_t \vec{i}_g(t) + L_t \frac{d\vec{i}_g(t)}{dt} \\
\vec{i}(t) &= \vec{i}_g(t) + C \frac{d\vec{U}_c(t)}{dt}
\end{aligned}
\tag{C.9}
$$

Equations (C.9) identify an LTI system, which makes the derivation of the state-space model straightforward. Applying the same procedure illustrated in Section C.1.1, (C.9) is mapped onto the dq-frame, resulting in the following set of equations for the dq-components of the signals. These equations have been obtained making use of (B.13).

$$
\begin{aligned}
U_{I_d}(t) &= U_d(t) + R_f i_d(t) + L_f \frac{di_d(t)}{dt} - L_f \omega_0 i_q(t) \\
U_{I_q}(t) &= U_q(t) + R_f i_q(t) + L_f \frac{di_q(t)}{dt} + L_f \omega_0 i_d(t) \\
U_d(t) &= U_{g_d}(t) + R_t i_{g_d}(t) + L_t \frac{i_{g_d}(t)}{dt} - L_t \omega_0 i_{g_q}(t) \\
U_q(t) &= U_{g_q}(t) + R_t i_{g_q}(t) + L_t \frac{i_{g_q}(t)}{dt} + L_t \omega_0 i_{g_d}(t) \\
i_d(t) &= i_{g_d}(t) + C \frac{dU_{c_d}(t)}{dt} - C \omega_0 U_{c_q}(t) \\
i_q(t) &= i_{g_q}(t) + C \frac{dU_{c_q}(t)}{dt} + C \omega_0 U_{c_d}(t)
\end{aligned}
\tag{C.10}
$$

By defining the state variables $x_i(t)$, with $i = 1, ..., 6$, the input variables $u_j(t)$, with $j = 1, ..., 4$, and output variables $y_k(t)$, with $k = 1, ..., 4$, as detailed in (C.11), the state-space model (C.12) can be found. In particular, $\vec{x}_d(t) = [x_1(t), ..., x_6(t)]$,

$\vec{u}(t) = [u_1(t), ..., u_4(t)]$, $\vec{y}(t) = [y_1(t), ..., y_4(t)]$ respectively are the state-, the input- and the output- (column) vectors.

$$\begin{bmatrix} x_1(t) + jx_2(t) \\ x_3(t) + jx_4(t) \\ x_5(t) + jx_6(t) \end{bmatrix} = \begin{bmatrix} U_{c_d}(t) + jU_{c_q}(t) \\ i_d(t) + ji_q(t) \\ i_{g_d}(t) + ji_{g_q}(t) \end{bmatrix}; \begin{bmatrix} u_1(t) + ju_2(t) \\ u_3(t) + ju_4(t) \end{bmatrix} = \begin{bmatrix} U_{I_d}(t) + jU_{I_q}(t) \\ U_{g_d}(t) + jU_{g_q}(t) \end{bmatrix};$$
$$\begin{bmatrix} y_1(t) + jy_2(t) \\ y_3(t) + jy_4(t) \end{bmatrix} = \begin{bmatrix} i_d(t) + ji_q(t) \\ U_d(t) + jU_q(t) \end{bmatrix}; \tag{C.11}$$

$$\begin{cases} \frac{d\vec{x}_d(t)}{dt} = A_d\vec{x}_d(t) + B_d\vec{u}(t), \\ \vec{y}(t) = C_d\vec{x}_d(t) \end{cases} \tag{C.12}$$

The matrices A_d, B_d and C_d are provided in (C.13).

$$A_d = \begin{bmatrix} 0 & \omega & \frac{1}{C} & 0 & -\frac{1}{C} & 0 \\ -\omega & 0 & 0 & \frac{1}{C} & 0 & -\frac{1}{C} \\ -\frac{1}{L_f} & 0 & -\frac{R_f+R}{L_f} & \omega & \frac{R}{L_f} & 0 \\ 0 & -\frac{1}{L_f} & -\omega & -\frac{R_f+R}{L_f} & 0 & \frac{R}{L_f} \\ \frac{1}{L_t} & 0 & -\frac{R}{L_t} & 0 & -\frac{R_t+R}{L_t} & \omega \\ 0 & \frac{1}{L_t} & 0 & -\frac{R}{L_t} & -\omega & -\frac{R_t+R}{L_t} \end{bmatrix};$$
$$B_d = \begin{bmatrix} 0 & 0 & 0 & 0 \\ 0 & 0 & 0 & 0 \\ \frac{1}{L_f} & 0 & 0 & 0 \\ 0 & \frac{1}{L_f} & 0 & 0 \\ 0 & 0 & -\frac{1}{L_t} & 0 \\ 0 & 0 & 0 & -\frac{1}{L_t} \end{bmatrix}; C_d = \begin{bmatrix} 0 & 0 & 0 & 0 & 1 & 0 \\ 0 & 0 & 0 & 0 & 0 & 1 \\ 1 & 0 & R & 0 & -R & 0 \\ 0 & 1 & 0 & R & 0 & -R \end{bmatrix}; \tag{C.13}$$

C.1.3 Electrical system in Figure 2.26

The dq-frame state-space model of the electrical system in Figure 2.26 is derived, which is modelled by the circuit shown in Figure C.3.

The set of equations (C.14) can be derived for the space vectors associated to the signals highlighted in the circuit. Such space vectors have been defined according to (B.14), with $\theta(t) = \omega_0 t$.

$$\begin{aligned} \vec{U}_I &= (R_f + R_L)\vec{i} + L_f \frac{d\vec{i}}{dt} \\ \vec{U} &= R_L \vec{i} \end{aligned} \tag{C.14}$$

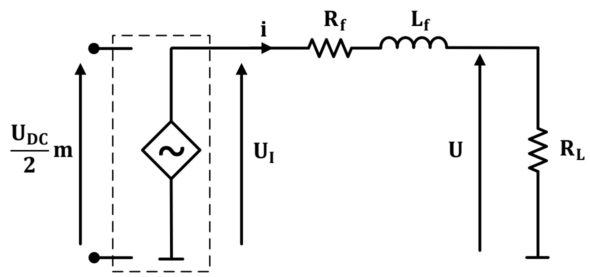

Figure C.3: One-line diagram of the linearised circuit modelling the electrical system in Figure 2.26.

Equations (C.14) identify an LTI system, which makes the derivation of the state-space model straightforward. Applying the same procedure illustrated in Sections C.1.1 and C.1.2, (C.14) is mapped onto the dq-frame making use of (B.13). The resulting following set of equations are formulated for the dq-components of the signals.

$$\begin{aligned} U_{I,d}(t) &= (R_f + R_L)i_d(t) + L_f \frac{di_d(t)}{dt} - L_f\omega_0 i_q(t) \\ U_{I,q}(t) &= (R_f + R_L)i_q(t) + L_f \frac{di_q(t)}{dt} + L_f\omega_0 i_d(t) \end{aligned} \tag{C.15}$$

By setting the state-vector $\vec{x}_l(t)$, the input-vector $\vec{u}(t)$ and the output-vector $\vec{y}(t)$

as:

$$\vec{x}_l(t) = \begin{bmatrix} i_d(t) \\ i_q(t) \end{bmatrix} ; \vec{u}(t) = \begin{bmatrix} U_{I_d}(t) \\ U_{I_q}(t) \end{bmatrix} ; \vec{y}(t) = \begin{bmatrix} i_d(t) \\ i_q(t) \\ U_d(t) \\ U_q(t) \end{bmatrix} ; \tag{C.16}$$

the following state-space model has been formulated for the circuit in Figure C.3:

$$\begin{cases} \frac{d\vec{x}_l(t)}{dt} = A_l\vec{x}_l(t) + B_l\vec{u}(t), \\ \vec{y}(t) = C_l\vec{x}_l(t) \end{cases} \tag{C.17}$$

where A_l, B_l and C_l are:

$$A_l = \begin{bmatrix} -\frac{R_f+R}{L_f} & \omega \\ -\omega & -\frac{R_f+R}{L_f} \end{bmatrix} ; B_l = \begin{bmatrix} \frac{1}{L_f} & 0 \\ 0 & \frac{1}{L_f} \end{bmatrix} ; C_l \quad = \begin{bmatrix} 1 & 0 \\ 0 & 1 \end{bmatrix} ; \tag{C.18}$$

C.1.4 Electrical system in Figure 4.2

The derivation of the dq-frame state-space small-signal model of the electrical system in Figure 4.2 is presented as follows.

As for the cases described in the previous Sections, an average model of the inverter is used. The resulting circuit modelling the electrical system in Figure 4.2 is shown in Figure C.4, where the coupling reactor Z_f has been modelled by the series connection of its inductance L_f and its parasitic resistance R_f. In order to derive the state-space representation of such system, the same methodology applied in Appendices C.1.1, C.1.2 and C.1.3 has been applied. Hence, the equations of the electrical system have been first defined in the abc-frame and then mapped onto the dq-frame.

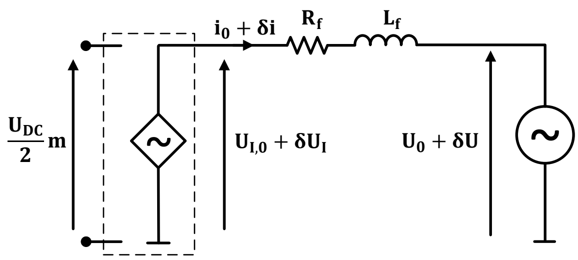

Figure C.4: One-line diagram of the linearised circuit modelling the electrical system in Figure 4.2.

Based on the LTI property of the system identified by the circuit in Figure C.4, and making use of the space-vector notation defined by (B.9), the following equation (C.19) is formulated, which relates the small-signal perturbation on the voltage across the reactor to the corresponding small-signal perturbation on its current:

$$\delta\vec{U}_I(t) - \delta\vec{U}(t) = R_f\delta\vec{i}(t) + L_f\frac{d\delta\vec{i}(t)}{dt} \tag{C.19}$$

Based on (B.13), (C.19) can be reformulated in the grid positive dq-frame as:

$$\begin{aligned} \delta U_{I,d}(t) - \delta U_d(t) &= R_f\delta i_d(t) + L_f\frac{d\delta i_d(t)}{dt} - L_f\omega_0\delta i_q(t) \\ \delta U_{I,q}(t) - \delta U_q(t) &= R_f\delta i_q(t) + L_f\frac{d\delta i_q(t)}{dt} + L_f\omega_0\delta i_d(t) \end{aligned} \tag{C.20}$$

Equations (C.20) can be expressed in a state-space format as:

$$\begin{cases} \frac{d\delta\vec{x}_f(t)}{dt} = A_f\delta\vec{x}_f(t) + B_f\delta\vec{u}(t), \\ \delta\vec{y}(t) = C_f\delta\vec{x}_f(t) + D_f\delta\vec{u}(t) \end{cases} \tag{C.21}$$

where:

$$\delta\vec{x}_f(t) = \begin{bmatrix} x_{f,1}(t) \\ x_{f,2}(t) \end{bmatrix} = \begin{bmatrix} \delta i_d(t) \\ \delta i_q(t) \end{bmatrix}; \delta\vec{u}(t) = \begin{bmatrix} \delta U_{I_d}(t) \\ \delta U_{I_q}(t) \\ \delta U_d(t) \\ \delta U_q(t) \end{bmatrix}; \delta\vec{y}(t) = \begin{bmatrix} \delta i_d(t) \\ \delta i_q(t) \\ \delta U_d(t) \\ \delta U_q(t) \end{bmatrix}; \tag{C.22}$$

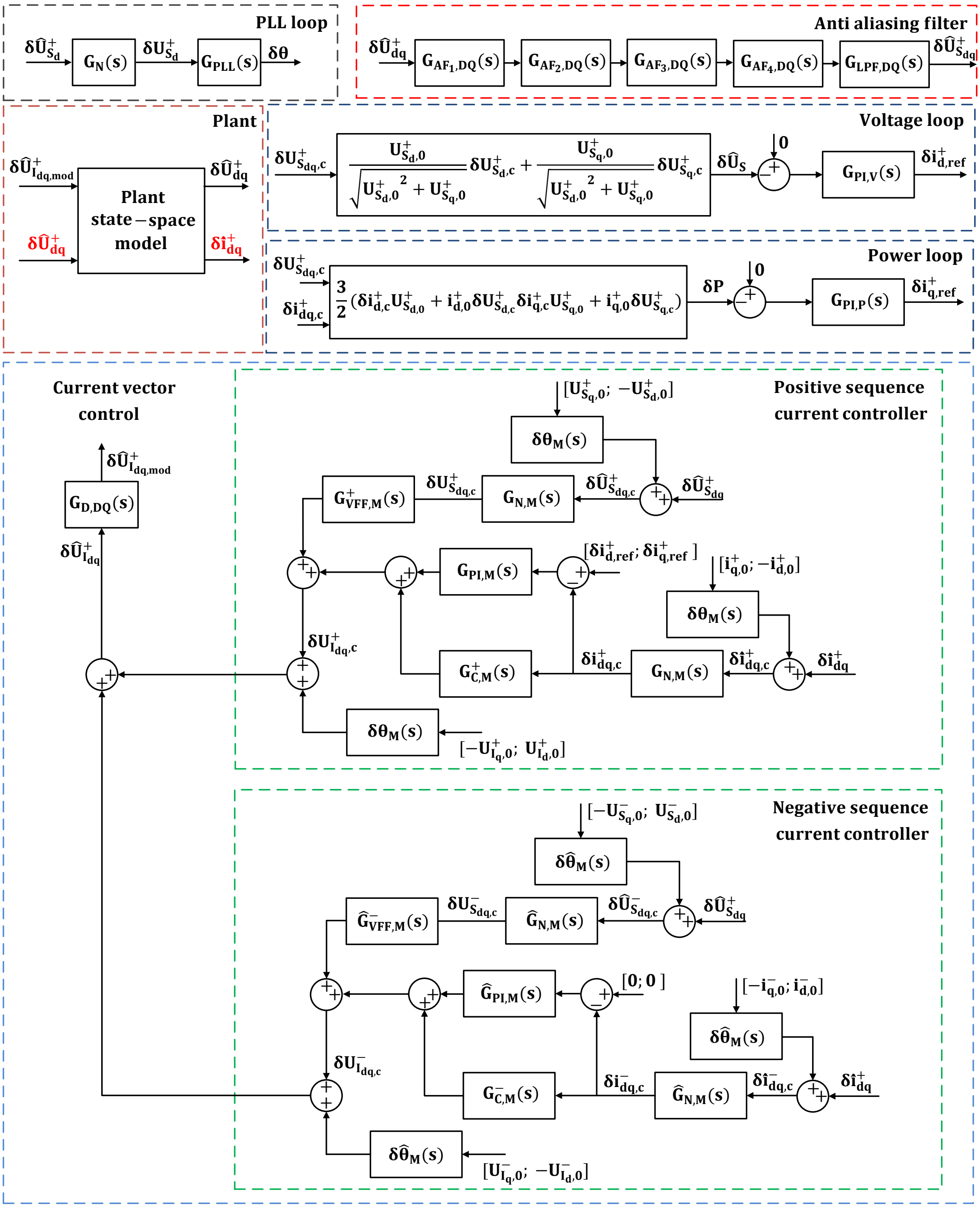

Figure C.5: Block diagram of the small-signal model used to calculated the small-signal converter admittance in the dq-frame.

The matrices A_f, B_f, C_f and D_f are:

$$A_f = \begin{bmatrix} -\frac{R_f}{L_f} & \omega_0 \\ -\omega_0 & -\frac{R_f}{L_f} \end{bmatrix}; B_f = \begin{bmatrix} \frac{1}{L_f} & 0 & -\frac{1}{L_f} & 0 \\ 0 & \frac{1}{L_f} & 0 & -\frac{1}{L_f} \end{bmatrix}; C_f = \begin{bmatrix} 1 & 0 \\ 0 & 1 \\ 0 & 0 \\ 0 & 0 \end{bmatrix}; D_f = \begin{bmatrix} 0 & 0 & 0 & 0 \\ 0 & 0 & 0 & 0 \\ 0 & 0 & 1 & 0 \\ 0 & 0 & 0 & 1 \end{bmatrix} \tag{C.23}$$

It is worth noticing that the $\delta U_{dq}(t)$ is both an input and an output. How such state-space model is included in the small-signal model of the system in Figure 4.2 is shown in Figure C.5. Such complete small-signal model is used to calculate the small-signal converter admittace in the dq-frame (see Section 4.1.1).

C.2 Translation of a transfer function from one frame to another

C.2.1 From the negative to the positive dq-frame

In this Section, the relation between the transfer function matrix $G_M(s)$ defined in the negative sequence dq-frame and its equivalent expression in the positive dq-frame is derived. The particular case where $G_M(s)$ has the structure defined in (C.24) is considering, where $G(s)$ is a generic transfer function.

$$\begin{bmatrix} y_d^-(s) \\ y_q^-(s) \end{bmatrix} = G_M(s) \begin{bmatrix} x_d^-(s) \\ x_q^-(s) \end{bmatrix} = \begin{bmatrix} G(s) & 0 \\ 0 & G(s) \end{bmatrix} \begin{bmatrix} x_d^-(s) \\ x_q^-(s) \end{bmatrix} \tag{C.24}$$

In (C.24), $y_{dq}^-(s)$ and $x_{dq}^-(s)$ are two generic signals defined in the negative dq-frame. Their corresponding expressions in the time domain are $y_{dq}^-(t)$ and $x_{dq}^-(t)$, i.e. $y_{dq}^-(t) = \mathcal{L}^{-1}\{y_{dq}^-(s)\}$ and $x_{dq}^-(t) = \mathcal{L}^{-1}\{x_{dq}^-(s)\}$.
The signal $y_{dq}^+(t)$, corresponding to the image of $y_{dq}^-(t)$ on the positive sequence dq-frame, can be obtained making use of the following $R_2(\theta(t))$ transformation [58], with

$\theta(t) = \omega_0 t$:

$$\begin{bmatrix} y_d^+(t) \\ y_q^+(t) \end{bmatrix} = R_2(\omega_0 t) \begin{bmatrix} y_d^-(t) \\ y_q^-(t) \end{bmatrix} = \begin{bmatrix} cos(2\omega_0 t) & sin(2\omega_0 t) \\ -sin(2\omega_0 t) & cos(2\omega_0 t) \end{bmatrix} \begin{bmatrix} y_d^-(t) \\ y_q^-(t) \end{bmatrix} \tag{C.25}$$

Equivalently, the signal $x_{dq}^-(t)$ can be related to its positive sequence dq-frame image $x_{dq}^+(t)$ applying the $R_{-2}(\omega_0 t)$ transform [58]:

$$\begin{bmatrix} x_d^-(t) \\ x_q^-(t) \end{bmatrix} = R_{-2}(\omega_0 t) \begin{bmatrix} x_d^+(t) \\ x_q^+(t) \end{bmatrix} = \begin{bmatrix} cos(2\omega_0 t) & -sin(2\omega_0 t) \\ sin(2\omega_0 t) & cos(2\omega_0 t) \end{bmatrix} \begin{bmatrix} x_d^+(t) \\ x_q^+(t) \end{bmatrix} \tag{C.26}$$

where in (C.25), (C.26), $\theta(t) = \omega_0 t$.
Hence, from (C.25), (C.26), a transfer function $\hat{G}(s)$ is defined such that:

$$\begin{bmatrix} y_d^+(s) \\ y_q^+(s) \end{bmatrix} = \begin{bmatrix} \hat{G}_{dd}(s) & \hat{G}_{dq}(s) \\ \hat{G}_{qd}(s) & \hat{G}_{qq}(s) \end{bmatrix} \begin{bmatrix} x_d^+(s) \\ x_q^+(s) \end{bmatrix} \tag{C.27}$$

By using Euler's formula [115], (C.26) can be reformulated as:

$$\begin{aligned} x_d^-(t) &= \frac{1}{2}(e^{2j\omega_0 t} + e^{-2j\omega_0 t})x_d^+(t) - \frac{1}{2j}(e^{2j\omega_0 t} - e^{-2j\omega_0 t})x_q^+(t) \\ x_q^-(t) &= \frac{1}{2j}(e^{2j\omega_0 t} - e^{-2j\omega_0 t})x_d^+(t) + \frac{1}{2}(e^{2j\omega_0 t} + e^{-2j\omega_0 t})x_q^+(t) \end{aligned} \tag{C.28}$$

whose corresponding Laplace transform $x_d^-(s)$ and $x_q^-(s)$ are:

$$\begin{aligned} x_d^-(s) &= \frac{1}{2}x_d^+(s-2j\omega) + \frac{1}{2}x_d^+(s+2j\omega) + \frac{1}{2}jx_q^+(s-2j\omega) - \frac{1}{2}jx_q^+(s+2j\omega) \\ x_q^-(s) &= -\frac{1}{2}jx_d^+(s-2j\omega) + \frac{1}{2}jx_d^+(s+2j\omega) + \frac{1}{2}x_q^+(s-2j\omega) + \frac{1}{2}x_q^+(s+2j\omega) \end{aligned} \tag{C.29}$$

Equivalently, by using Euler's formula, (C.25) can be rewritten as:

$$\begin{aligned} y_d^+(t) &= \frac{1}{2}(e^{2j\omega_0 t} + e^{-2j\omega_0 t})y_d^-(t) + \frac{1}{2j}(e^{2j\omega_0 t} - e^{-2j\omega_0 t})y_q^-(t) \\ y_q^+(t) &= -\frac{1}{2j}(e^{2j\omega_0 t} - e^{-2j\omega_0 t})y_d^-(t) + \frac{1}{2}(e^{2j\omega_0 t} + e^{-2j\omega_0 t})y_q^-(t) \end{aligned} \tag{C.30}$$

whose Laplace transform $y_d^-(s)$ and $y_q^-(s)$ are:

$$
\begin{aligned}
y_d^+(s) &= \frac{1}{2}y_d^-(s-2j\omega) + \frac{1}{2}y_d^-(s+2j\omega) - \frac{1}{2}jy_q^-(s-2j\omega) + \frac{1}{2}jy_q^-(s+2j\omega) \\
y_q^+(s) &= \frac{1}{2}jy_d^-(s-2j\omega) - \frac{1}{2}jy_d^-(s+2j\omega) + \frac{1}{2}y_q^-(s-2j\omega) + \frac{1}{2}y_q^-(s+2j\omega)
\end{aligned}
\tag{C.31}
$$

Thereby, from (C.29), (C.31), and (C.24), the following expressions can be obtained for $y_d^+(s)$ and $y_q^+(s)$:

$$
\begin{aligned}
y_d^+(s) &= \frac{1}{2}[G(s-2j\omega_0) + G(s+2j\omega_0)]x_d^+(s) + \frac{1}{2}j[G(s+2j\omega_0) - G(s-2j\omega_0)]x_q^+(s) \\
y_q^+(s) &= +\frac{1}{2}j[G(s-2j\omega_0) - G(s+2j\omega_0)]x_d^+(s) + \frac{1}{2}[G(s-2j\omega_0) + G(s+2j\omega_0)]x_q^+(s)
\end{aligned}
\tag{C.32}
$$

Equations (C.32) can be rewritten in a matrix format as:

$$
\begin{bmatrix} y_d^+(s) \\ y_q^+(s) \end{bmatrix} = \begin{bmatrix} \frac{1}{2}[G(s-2j\omega_0) + G(s+2j\omega_0)] & \frac{1}{2}j[G(s+2j\omega_0) - G(s-2j\omega_0)] \\ \frac{1}{2}j[G(s-2j\omega_0) - G(s+2j\omega_0)] & \frac{1}{2}[G(s-2j\omega_0) + G(s+2j\omega_0)] \end{bmatrix} \begin{bmatrix} x_d^+(s) \\ x_q^+(s) \end{bmatrix}
\tag{C.33}
$$

Hence, from(C.27), (C.33):

$$
\hat{G}_M(s) = \begin{bmatrix} \frac{1}{2}[G(s-2j\omega_0) + G(s+2j\omega_0)] & \frac{1}{2}j[G(s+2j\omega_0) - G(s-2j\omega_0)] \\ \frac{1}{2}j[G(s-2j\omega_0) - G(s+2j\omega_0)] & \frac{1}{2}[G(s-2j\omega_0) + G(s+2j\omega_0)] \end{bmatrix}
\tag{C.34}
$$

$\hat{G}_M(s)$ therefore represents the expression of $G_M(s)$ in the positive dq-frame.

C.2.2 From the *abc*- to the positive *dq*-frame

In this Section, the relation between the transfer function matrix $G_M(s)$ defined in the *abc*-frame and its equivalent expression in the *dq*-frame is derived. The particular case where $G_M(s)$ has the structure defined in (C.35) is considered, where $G(s)$ is a generic transfer function.

$$\begin{bmatrix} y_a(s) \\ y_b(s) \\ y_c(s) \end{bmatrix} = G_M(s) \begin{bmatrix} x_a(s) \\ x_b(s) \\ x_c(s) \end{bmatrix} = \begin{bmatrix} G(s) & 0 & 0 \\ 0 & G(s) & 0 \\ 0 & 0 & G(s) \end{bmatrix} \begin{bmatrix} x_a(s) \\ x_b(s) \\ x_c(s) \end{bmatrix} \tag{C.35}$$

The signals $y_{abc}(s)$ and $x_{abc}(s)$ are the Laplace transform [85] of the corresponding time domain signals $y_{abc}(t)$ and $x_{abc}(t)$, respectively. In other words $x_{abc}(s) = \mathcal{L}\{x_{abc}(t)\}$ and $y_{abc}(s) = \mathcal{L}\{y_{abc}(t)\}$. By applying the Park transform $T(\omega_0 t)$ (B.16) and its transpose $T^T(\omega_0 t)$ (B.17), such time domain signals can be related to their dq-frame counterparts, $y_{dq}(t)$ and $x_{dq}(t)$ respectively, as:

$$\begin{aligned}
\begin{bmatrix} x_d(t) \\ x_q(t) \end{bmatrix} &= \frac{2}{3} \cdot \begin{bmatrix} sin(\omega_0 t) & sin(\omega_0 t - \frac{2}{3}\pi) & sin(\omega_0 t - \frac{4}{3}\pi) \\ cos(\omega_0 t) & cos(\omega_0 t - \frac{2}{3}\pi) & cos(\omega_0 t - \frac{4}{3}\pi) \end{bmatrix} \begin{bmatrix} x_a(t) \\ x_b(t) \\ x_c(t) \end{bmatrix} \\
\begin{bmatrix} y_d(t) \\ y_q(t) \end{bmatrix} &= \frac{2}{3} \cdot \begin{bmatrix} sin(\omega_0 t) & sin(\omega_0 t - \frac{2}{3}\pi) & sin(\omega_0 t - \frac{4}{3}\pi) \\ cos(\omega_0 t) & cos(\omega_0 t - \frac{2}{3}\pi) & cos(\omega_0 t - \frac{4}{3}\pi) \end{bmatrix} \begin{bmatrix} y_a(t) \\ y_b(t) \\ y_c(t) \end{bmatrix} \\
\begin{bmatrix} x_a(t) \\ x_b(t) \\ x_c(t) \end{bmatrix} &= \begin{bmatrix} sin(\omega_0 t) & cos(\omega_0 t) \\ sin(\omega_0 t - \frac{2}{3}\pi) & cos(\omega_0 t - \frac{2}{3}\pi) \\ sin(\omega_0 t - \frac{4}{3}\pi) & cos(\omega_0 t - \frac{4}{3}\pi) \end{bmatrix} \begin{bmatrix} x_d(t) \\ x_q(t) \end{bmatrix} \\
\begin{bmatrix} y_a(t) \\ y_b(t) \\ y_c(t) \end{bmatrix} &= \begin{bmatrix} sin(\omega_0 t) & cos(\omega_0 t) \\ sin(\omega_0 t - \frac{2}{3}\pi) & cos(\omega_0 t - \frac{2}{3}\pi) \\ sin(\omega_0 t - \frac{4}{3}\pi) & cos(\omega_0 t - \frac{4}{3}\pi) \end{bmatrix} \begin{bmatrix} y_d(t) \\ y_q(t) \end{bmatrix}
\end{aligned} \tag{C.36}$$

From (C.36), by making use of Euler's formula [115], the following equations (C.37) and (C.38) can be derived for $y_{dq}(t)$ and $x_{abc}(t)$, respectively:

$$\begin{aligned}
y_d(t) &= \frac{2}{3}[sin(\omega_0 t)y_a(t) + sin(\omega_0 t - \frac{2}{3}\pi)y_b(t) + sin(\omega_0 t - \frac{4}{3}\pi)y_c(t)] \\
&= \frac{1}{3j}[(e^{j\omega_0 t} - e^{-j\omega_0 t})y_a(t) + (e^{j(\omega_0 t - \frac{2}{3}\pi)} - e^{-j(\omega_0 t - \frac{2}{3}\pi)})y_b(t) \\
&+ (e^{j(\omega_0 t - \frac{4}{3}\pi)} - e^{-j(\omega_0 t - \frac{4}{3}\pi)})y_c(t)] \\
y_q(t) &= \frac{2}{3}[cos(\omega_0 t)y_a(t) + cos(\omega_0 t - \frac{2}{3}\pi)y_b(t) + cos(\omega_0 t - \frac{4}{3}\pi)y_c(t)] \\
&= \frac{1}{3}[(e^{j\omega_0 t} + e^{-j\omega_0 t})y_a(t) + (e^{j(\omega_0 t - \frac{2}{3}\pi)} + e^{-j(\omega_0 t - \frac{2}{3}\pi)})y_b(t) \\
&+ (e^{j(\omega_0 t - \frac{4}{3}\pi)} + e^{-j(\omega_0 t - \frac{4}{3}\pi)})y_c(t)]
\end{aligned} \tag{C.37}$$

$$\begin{aligned}
x_a(t) &= sin(\omega_0 t)x_d(t) + cos(\omega_0 t)x_q(t) \\
&= \frac{1}{2j}(e^{j\omega_0 t} - e^{-j\omega_0 t})x_d(t) + \frac{1}{2}(e^{j\omega_0 t} + e^{-j\omega_0 t})x_q(t) \\
x_b(t) &= sin(\omega_0 t - \frac{2}{3}\pi)x_d(t) + cos(\omega_0 t - \frac{2}{3}\pi)x_q(t) \\
&= \frac{1}{2j}(e^{j(\omega_0 t - \frac{2}{3}\pi)} - e^{-j(\omega_0 t - \frac{2}{3}\pi)})x_d(t) + \frac{1}{2}(e^{j(\omega_0 t - \frac{2}{3}\pi)} + e^{-j(\omega_0 t - \frac{2}{3}\pi)})x_q(t) \\
x_c(t) &= sin(\omega_0 t - \frac{4}{3}\pi)x_d(t) + cos(\omega_0 t - \frac{4}{3}\pi)x_q(t) \\
&= \frac{1}{2j}(e^{j(\omega_0 t - \frac{4}{3}\pi)} - e^{-j(\omega_0 t - \frac{4}{3}\pi)})x_d(t) + \frac{1}{2}(e^{j(\omega_0 t - \frac{4}{3}\pi)} + e^{-j(\omega_0 t - \frac{4}{3}\pi)})x_q(t)
\end{aligned} \tag{C.38}$$

The corresponding Laplace transform signals of (C.37), (C.38) are:

$$\begin{aligned}
y_d(s) &= \frac{1}{3j}[y_a(s - j\omega_0) - y_a(s + j\omega_0) + y_b(s - j\omega_0)e^{-j\frac{2}{3}\pi} - y_b(s + j\omega_0)e^{j\frac{2}{3}\pi} \\
&+ y_c(s - j\omega_0)e^{-j\frac{4}{3}\pi} - y_c(s + j\omega_0)e^{j\frac{4}{3}\pi}] \\
y_q(s) &= \frac{1}{3}[y_a(s - j\omega_0) + y_a(s + j\omega_0) + y_b(s - j\omega_0)e^{-j\frac{2}{3}\pi} + y_b(s + j\omega_0)e^{j\frac{2}{3}\pi} \\
&+ y_c(s - j\omega_0)e^{-j\frac{4}{3}\pi} + y_c(s + j\omega_0)e^{j\frac{4}{3}\pi}]
\end{aligned} \tag{C.39}$$

$$\begin{aligned}
x_a(s) &= \frac{1}{2}[-jx_d(s - j\omega_0) + x_d(s + j\omega_0) + x_q(s - j\omega_0) + x_q(s + j\omega_0)] \\
x_b(s) &= \frac{1}{2}[-jx_d(s - j\omega_0)e^{-j\frac{2}{3}\pi} + x_d(s + j\omega_0)e^{j\frac{2}{3}\pi} + x_q(s - j\omega_0)e^{-j\frac{2}{3}\pi} + x_q(s + j\omega_0)e^{j\frac{2}{3}\pi}] \\
x_c(s) &= \frac{1}{2}[-jx_d(s - j\omega_0)e^{-j\frac{4}{3}\pi} + x_d(s + j\omega_0)e^{j\frac{4}{3}\pi} + x_q(s - j\omega_0)e^{-j\frac{4}{3}\pi} + x_q(s + j\omega_0)e^{j\frac{4}{3}\pi}]
\end{aligned} \tag{C.40}$$

Thereby, as from (C.35), $y_a(s) = G(s)x_a(s)$, $y_b(s) = G(s)x_b(s)$ and $y_c(s) = G(s)x_c(s)$, replacing the expression of $x_{abc}(s)$ given by (C.40) in the expression of $y_{dq}(s)$ provided by (C.39), the following equations can be derived:

$$\begin{aligned} y_d(s) &= \frac{1}{2}[G(s-j\omega_0)+G(s+j\omega_0)]x_d(s)+\frac{1}{2}j[G(s+j\omega_0)-G(s-j\omega_0)]x_q(s) \\ y_q(s) &= \frac{1}{2}j[G(s-j\omega_0)-G(s+j\omega_0)]x_d(s)+\frac{1}{2}[G(s-j\omega_0)+G(s+j\omega_0)]x_q(s) \end{aligned} \tag{C.41}$$

These can be reformulated in a matrix format as:

$$\begin{bmatrix} y_d(s) \\ y_q(s) \end{bmatrix} = \begin{bmatrix} \frac{1}{2}[G(s-j\omega_0)+G(s+j\omega_0)] & \frac{1}{2}j[G(s+j\omega_0)-G(s-j\omega_0)] \\ \frac{1}{2}j[G(s-j\omega_0)-G(s+j\omega_0)] & \frac{1}{2}[G(s-j\omega_0)+G(s+j\omega_0)] \end{bmatrix} \begin{bmatrix} x_d(s) \\ x_q(s) \end{bmatrix} \tag{C.42}$$

The matrix $G_{DQ}(s)$, defined as:

$$G_{DQ}(s) = \begin{bmatrix} \frac{1}{2}[G(s-j\omega_0)+G(s+j\omega_0)] & \frac{1}{2}j[G(s+j\omega_0)-G(s-j\omega_0)] \\ \frac{1}{2}j[G(s-j\omega_0)-G(s+j\omega_0)] & \frac{1}{2}[G(s-j\omega_0)+G(s+j\omega_0)] \end{bmatrix} \tag{C.43}$$

therefore represents the *dq*-frame expression of the *abc*-frame matrix $G_M(s)$ defined in (C.35).

For the purpose of illustration, Figure C.6 shows the elements of the *dq*-frame transfer function matrix of the anti-aliasing filter, derived as discussed in Section 3.1.1.4. In the shown case, the filter parameters are those of the asymmetrical regular sampling case (see Table 2.4). As it can be seen, the magnitude of the cross diagonal elements is much lower than that of the main diagonal components. Moreover, these latter elements have a trend similar to that of the *abc*-frame components of the filter (see Figure 2.18).

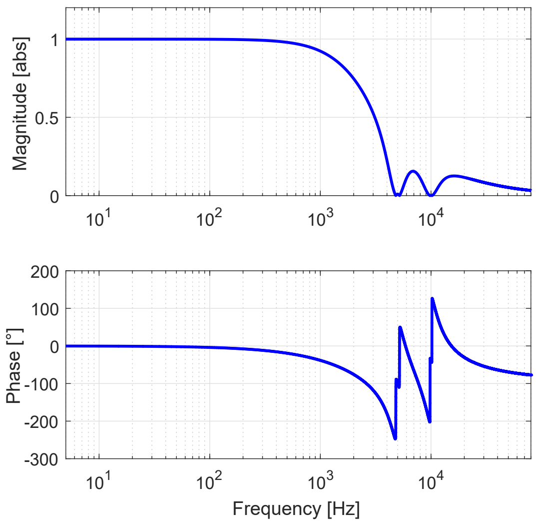

(a) dd-element

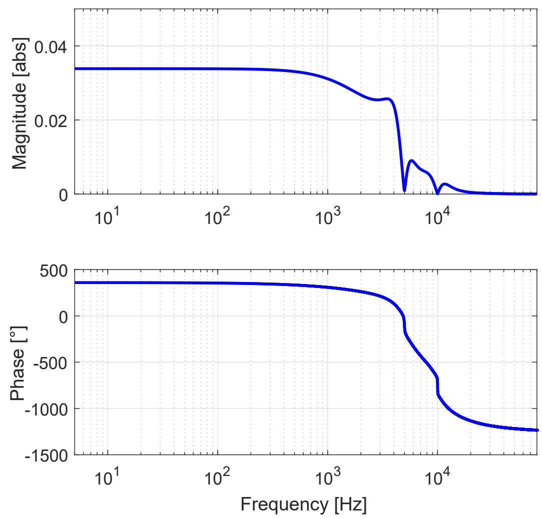

(b) dq-element

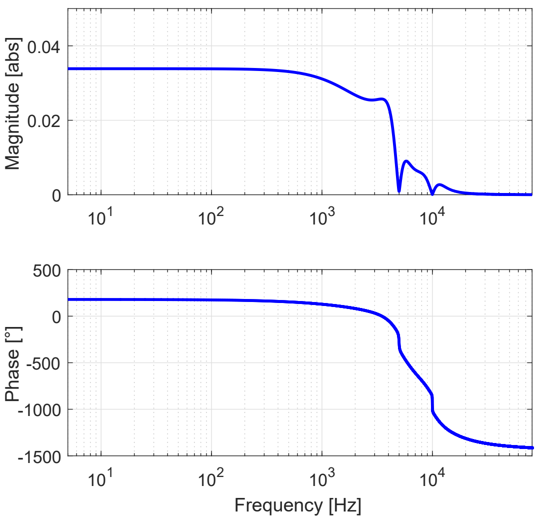

(c) qd-element

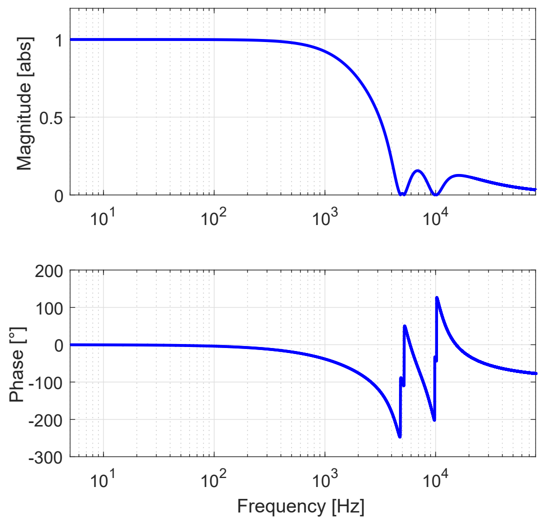

(d) qq-element

Figure C.6: Bode plots of the elements of the anti-aliasing filter transfer function matrix in the dq-frame.

C.3 Relation between dq- and pn-frame admittance

Two derivations of equations (4.3)-(4.4) are presented as follows. In Appendix C.3.1, a derivation which makes use of the matrices transformations D and $B(t)$ in the diagram in Figure 4.4, is provided. In Appendix C.3.2, an alternative derivation which makes use of the transformations C, $R(t)$ and F in the diagram in Figure 4.4, is presented.

C.3.1 Derivation of equations (4.3)-(4.4)

The presented derivation makes used of the matrices transformations D and $B(t)$ in the diagram in Figure 4.4. These are respectively defined as:

$$D = \frac{1}{\sqrt{2}} \begin{bmatrix} -j & 1 \\ j & 1 \end{bmatrix} \tag{C.44}$$

$$B(t) = \sqrt{2} \begin{bmatrix} e^{-j\omega_0 t} & 0 \\ 0 & e^{j\omega_0 t} \end{bmatrix} \tag{C.45}$$

In the following description, $U_{dq}(t)$ and $i_{dq}(t)$ are the expressions of, respectively, a generic voltage signal $U(t)$ and a generic current signal $i(t)$, in the dq-frame. Similarly, $U_{pn}(t)$ and $i_{pn}(t)$ are their expression in the pn-frame, respectively. It is assumed that the following relation can be defined between $U_{dq}(s)$ and $i_{dq}(s)$, with $U_{dq}(s) = \mathcal{L}\{U_{dq}(t)\}$, $i_{dq}(s) = \mathcal{L}\{i_{dq}(t)\}$:

$$\begin{bmatrix} i_d(s) \\ i_q(s) \end{bmatrix} = Y_{DQ}(s) \begin{bmatrix} U_d(s) \\ U_q(s) \end{bmatrix} = \begin{bmatrix} Y_{dd}(s) & Y_{dq}(s) \\ Y_{qd}(s) & Y_{qq}(s) \end{bmatrix} \begin{bmatrix} U_d(s) \\ U_q(s) \end{bmatrix} \tag{C.46}$$

Based on the diagram in Figure 4.4, the following equations can be formulated between $U_{dq}(t)$, $i_{dq}(t)$ and, respectively, $U_{pn}(t)$, $i_{pn}(t)$:

$$\begin{gathered} \begin{bmatrix} U_d(t) \\ U_q(t) \end{bmatrix} = D^{-1} \cdot B(t) \cdot \begin{bmatrix} U_p(t) \\ U_n(t) \end{bmatrix}, \\ \begin{bmatrix} i_d(t) \\ i_q(t) \end{bmatrix} = D^{-1} \cdot B(t) \cdot \begin{bmatrix} i_p(t) \\ i_n(t) \end{bmatrix} \end{gathered} \tag{C.47}$$

By indicating with $Y_{DQ}(t)$ the impulse response matrix associated to $Y_{DQ}(s)$, calculated as $Y_{DQ}(t) = \mathcal{L}^{-1}\{Y_{DQ}(s)\}$ [120], (C.46) can be rewritten in the time-domain as:

$$\begin{bmatrix} i_d(t) \\ i_q(t) \end{bmatrix} = \begin{bmatrix} Y_{dd}(t) & Y_{dq}(t) \\ Y_{qd}(t) & Y_{qq}(t) \end{bmatrix} * \begin{bmatrix} U_d(t) \\ U_q(t) \end{bmatrix} \tag{C.48}$$

where the symbol $*$ indicates the convolution operator [120]. By replacing the expressions of $i_{dq}(t)$ and $U_{dq}(t)$, given by (C.47), into (C.48), the following relation can be derived:

$$\begin{aligned} \begin{bmatrix} i_p(t) \\ i_n(t) \end{bmatrix} &= B^{-1}(t)D[\begin{bmatrix} Y_{dd}(t) & Y_{dq}(t) \\ Y_{qd}(t) & Y_{qq}(t) \end{bmatrix} * (D^{-1}B(t) \begin{bmatrix} U_p(t) \\ U_n(t) \end{bmatrix})] \\ &= \frac{1}{2} \begin{bmatrix} -je^{j\omega_0 t} & e^{j\omega_0 t} \\ je^{-j\omega_0 t} & e^{-j\omega_0 t} \end{bmatrix} [\begin{bmatrix} Y_{dd}(t) & Y_{dq}(t) \\ Y_{qd}(t) & Y_{qq}(t) \end{bmatrix} * (\begin{bmatrix} je^{-j\omega_0 t} & -je^{j\omega_0 t} \\ e^{-j\omega_0 t} & e^{j\omega_0 t} \end{bmatrix} \begin{bmatrix} U_p(t) \\ U_n(t) \end{bmatrix})] \\ &= \frac{1}{2} \begin{bmatrix} -je^{j\omega_0 t} & e^{j\omega_0 t} \\ je^{-j\omega_0 t} & e^{-j\omega_0 t} \end{bmatrix} (\begin{bmatrix} Y_{dd}(t) & Y_{dq}(t) \\ Y_{qd}(t) & Y_{qq}(t) \end{bmatrix} * \begin{bmatrix} je^{-j\omega_0 t}U_p(t) - je^{j\omega_0 t}U_n(t) \\ e^{-j\omega_0 t}U_p(t) + e^{j\omega_0 t}U_n(t) \end{bmatrix}) \end{aligned} \tag{C.49}$$

From which:

$$\begin{aligned} i_p(t) &= -\frac{1}{2}je^{j\omega_0 t}\{Y_{dd}(t) * [je^{-j\omega_0 t}U_p(t) - je^{j\omega_0 t}U_n(t)] \\ &+ Y_{dq}(t) * [e^{-j\omega_0 t}U_p(t) + e^{j\omega_0 t}U_n(t)]\} \\ &+ \frac{1}{2}e^{j\omega_0 t}\{Y_{qd}(t) * [je^{-j\omega_0 t}U_p(t) - je^{j\omega_0 t}U_n(t)] \\ &+ Y_{qq}(t) * [e^{-j\omega_0 t}U_p(t) + e^{j\omega_0 t}U_n(t)]\} \\ i_n(t) &= \frac{1}{2}je^{-j\omega_0 t}\{Y_{dd}(t) * [je^{-j\omega_0 t}U_p(t) - je^{j\omega_0 t}U_n(t)] \\ &+ Y_{dq}(t) * [e^{-j\omega_0 t}U_p(t) + e^{j\omega_0 t}U_n(t)]\} \\ &+ \frac{1}{2}e^{-j\omega_0 t}\{Y_{qd}(t) * [je^{-j\omega_0 t}U_p(t) - je^{j\omega_0 t}U_n(t)] \\ &+ Y_{qq}(t) * [e^{-j\omega_0 t}U_p(t) + e^{j\omega_0 t}U_n(t)]\} \end{aligned} \tag{C.50}$$

The Laplace transform of (C.50) is:

$$
\begin{aligned}
U_p(s) = &-\frac{1}{2}j\{Y_{dd}(s-j\omega_0)[ji_p(s)-ji_n(s-2j\omega_0)]\\
&+Y_{dq}(s-j\omega_0)[i_p(s)+i_n(s-2j\omega_0)]\}\\
&+\frac{1}{2}\{Y_{qd}(s-j\omega_0)[ji_p(s)-ji_n(s-2j\omega_0)]\\
&+Y_{qq}(s-j\omega_0)[i_p(s)+i_n(s-2j\omega_0)]\}\\
U_n(t) = &\frac{1}{2}j\{Y_{dd}(s+j\omega_0)[ji_p(s+2j\omega_0)-ji_n(s)]\\
&+Y_{dq}(s+j\omega_0)[i_p(s+2j\omega_0)+i_n(s)]\}\\
&+\frac{1}{2}\{Y_{qd}(s+j\omega_0)[ji_p(s+2j\omega_0)-ji_n(s)]\\
&+Y_{qq}(s+j\omega_0)[i_p(s+2j\omega_0)+i_n(s)]\}
\end{aligned}
\tag{C.51}
$$

By setting:

$$
\begin{aligned}
Y_{pp}(s) &= \frac{1}{2}[Y_{qq}(s-j\omega_0)-jY_{dq}(s-j\omega_0)+jY_{qd}(s-j\omega_0)+Y_{dd}(s-j\omega_0)],\\
Y_{pn}(s) &= \frac{1}{2}[Y_{qq}(s-j\omega_0)-jY_{dq}(s-j\omega_0)-jY_{qd}(s-j\omega_0)-Y_{dd}(s-j\omega_0)],\\
Y_{np}(s) &= \frac{1}{2}[Y_{qq}(s+j\omega_0)+jY_{dq}(s+j\omega_0)+jY_{qd}(s+j\omega_0)-Y_{dd}(s+j\omega_0)],\\
Y_{nn}(s) &= \frac{1}{2}[Y_{qq}(s+j\omega_0)+jY_{dq}(s+j\omega_0)-jY_{qd}(s+j\omega_0)+Y_{dd}(s+j\omega_0)]
\end{aligned}
\tag{C.52}
$$

equation (C.51) can be rewritten as:

$$
\begin{aligned}
i_p(s) &= Y_{pp}(s)U_p(s)+Y_{pn}(s)U_n(s-2j\omega_0)\\
i_n(s) &= Y_{np}(s)U_p(s+2j\omega_0)+Y_{nn}(s)U_n(s)
\end{aligned}
\tag{C.53}
$$

Based on (4.2), (C.52) and (C.53) correspond to (4.3) and (4.4), respectively.

C.3.2 Alternative derivation of equations (4.3)-(4.4)

An alternative derivation of equations (4.3)-(4.4) is presented as follows, which makes use of the transformations C, D and F in Figure 4.4. Two generic current and voltage signals, $i_{dq}(t)$ and $U_{dq}(t)$ respectively, are considered, which are defined in a nominal

dq-frame rotating anti-clockwise at ω_0. Their Laplace transforms are $i_{dq}(s) = \mathcal{L}\{i_{dq}(t)\}$ and $U_{dq}(s) = \mathcal{L}\{U_{dq}(t)\}$. It is assumed that a $Y_{DQ}(s)$ admittance matrix can be defined such that:

$$\begin{bmatrix} i_d(s) \\ i_q(s) \end{bmatrix} = Y_{DQ}(s) \begin{bmatrix} U_d(s) \\ U_q(s) \end{bmatrix} = \begin{bmatrix} Y_{dd}(s) & Y_{dq}(s) \\ Y_{qd}(s) & Y_{qq}(s) \end{bmatrix} \begin{bmatrix} U_d(s) \\ U_q(s) \end{bmatrix} \tag{C.54}$$

An equivalent relation can be defined in the time domain making use of the impulse response matrix $Y_{DQ}(t) = \mathcal{L}^{-1}\{Y_{DQ}(s)\}$ [120]:

$$\begin{bmatrix} i_d(t) \\ i_q(t) \end{bmatrix} = Y_{DQ}(t) * \begin{bmatrix} U_d(t) \\ U_q(t) \end{bmatrix} = \begin{bmatrix} Y_{dd}(t) & Y_{dq}(t) \\ Y_{qd}(t) & Y_{qq}(t) \end{bmatrix} * \begin{bmatrix} U_d(t) \\ U_q(t) \end{bmatrix} \tag{C.55}$$

where the symbol $*$ indicates the convolution operator. By indicating with $i_{abc}(t)$ the abc-frame signal corresponding to $i_{dq}(t)$, based on (B.17), this is calculated as:

$$\begin{bmatrix} i_a(t) \\ i_b(t) \\ i_c(t) \end{bmatrix} = T^T(\omega_0 t) \begin{bmatrix} i_d(t) \\ i_q(t) \end{bmatrix} = \begin{bmatrix} sin(\omega_0 t) & cos(\omega_0 t) \\ sin(\omega_0 t - \frac{2}{3}\pi) & cos(\omega_0 t - \frac{2}{3}\pi) \\ sin(\omega_0 t - \frac{4}{3}\pi) & cos(\omega_0 t - \frac{4}{3}\pi) \end{bmatrix} \begin{bmatrix} i_d(t) \\ i_q(t) \end{bmatrix} \tag{C.56}$$

Combining (C.55) and (C.56), and by using Euler's formula [115], the phase current $i_a(t)$, $i_b(t)$ and $i_c(t)$ can be expressed as:

$$\begin{aligned} i_a(t) &= cos(\omega_0 t)[Y_{qq}(t) * U_q(t) + Y_{qd}(t) * U_d(t)] \\ &+ sin(\omega_0 t)[Y_{dq}(t) * U_q(t) + Y_{dd}(t) * U_d(t)] \\ &= \frac{1}{2}(e^{j\omega_0 t} + e^{-j\omega_0 t})[Y_{qq}(t) * U_q(t) + Y_{qd}(t) * U_d(t)] \\ &+ \frac{1}{2j}(e^{j\omega_0 t} - e^{-j\omega_0 t})[Y_{dq}(t) * U_q(t) + Y_{dd}(t) * U_d(t)] \end{aligned} \tag{C.57}$$

$$\begin{aligned} i_b(t) &= cos(\omega_0 t - \frac{2}{3}\pi)[Y_{qq}(t) * U_q(t) + Y_{qd}(t) * U_d(t)] \\ &+ sin(\omega_0 t - \frac{2}{3}\pi)[Y_{dq}(t) * U_q(t) + Y_{dd}(t) * U_d(t)] \\ &= \frac{1}{2}(e^{j(\omega_0 t - \frac{2}{3}\pi)} + e^{-j(\omega_0 t - \frac{2}{3}\pi)})[Y_{qq}(t) * U_q(t) + Y_{qd}(t) * U_d(t)] \\ &+ \frac{1}{2j}(e^{j(\omega_0 t - \frac{2}{3}\pi)} - e^{-j(\omega_0 t - \frac{2}{3}\pi)})[Y_{dq}(t) * U_q(t) + Y_{dd}(t) * U_d(t)] \end{aligned} \tag{C.58}$$

$$\begin{aligned} i_c(t) &= cos(\omega_0 t - \frac{4}{3}\pi)[Y_{qq}(t) * U_q(t) + Y_{qd}(t) * U_d(t)] \\ &+ sin(\omega_0 t - \frac{4}{3}\pi)[Y_{dq}(t) * U_q(t) + Y_{dd}(t) * U_d(t)] \\ &= \frac{1}{2}(e^{j(\omega_0 t - \frac{4}{3}\pi)} + e^{-j(\omega_0 t - \frac{4}{3}\pi)})[Y_{qq}(t) * U_q(t) + Y_{qd}(t) * U_d(t)] \\ &+ \frac{1}{2j}(e^{j(\omega_0 t - \frac{4}{3}\pi)} - e^{-j(\omega_0 t - \frac{4}{3}\pi)})[Y_{dq}(t) * U_q(t) + Y_{dd}(t) * U_d(t)] \end{aligned} \tag{C.59}$$

By calculating the Laplace transform of (C.57), (C.58) and (C.59), and by setting $s = j\omega$, the following expressions can be obtained for $i_a(j\omega)$, $i_b(j\omega)$ and $i_c(j\omega)$:

$$\begin{aligned} i_a(j\omega) &= \frac{1}{2}[Y_{qq}(j(\omega - \omega_0))U_q(j(\omega - \omega_0)) + Y_{qd}(j(\omega - \omega_0))U_d(j(\omega - \omega_0))] \\ &+ \frac{1}{2}[Y_{qq}(j(\omega + \omega_0))U_q(j(\omega + \omega_0)) + Y_{qd}(j(\omega + \omega_0))U_d(j(\omega + \omega_0))] \\ &+ \frac{1}{2j}[Y_{dq}(j(\omega - \omega_0))U_q(j(\omega - \omega_0)) + Y_{dd}(j(\omega - \omega_0))U_d(j(\omega - \omega_0))] \\ &- \frac{1}{2j}[Y_{dq}(j(\omega + \omega_0))U_q(j(\omega + \omega_0)) + Y_{dd}(j(\omega + \omega_0))U_d(j(\omega + \omega_0))] \end{aligned} \tag{C.60}$$

$$\begin{aligned} i_b(j\omega) &= \frac{1}{2}e^{-j\frac{2}{3}\pi}[Y_{qq}(j(\omega - \omega_0))U_q(j(\omega - \omega_0)) + Y_{qd}(j(\omega - \omega_0))U_d(j(\omega - \omega_0))] \\ &+ \frac{1}{2}e^{j\frac{2}{3}\pi}[Y_{qq}(j(\omega + \omega_0))U_q(j(\omega + \omega_0)) + Y_{qd}(j(\omega + \omega_0))U_d(j(\omega + \omega_0))] \\ &+ \frac{1}{2j}e^{-j\frac{2}{3}\pi}[Y_{dq}(j(\omega - \omega_0))U_q(j(\omega - \omega_0)) + Y_{dd}(j(\omega - \omega_0))U_d(j(\omega - \omega_0))] \\ &- \frac{1}{2j}e^{j\frac{2}{3}\pi}[Y_{dq}(j(\omega + \omega_0))U_q(j(\omega + \omega_0)) + Y_{dd}(j(\omega + \omega_0))U_d(j(\omega + \omega_0))] \end{aligned} \tag{C.61}$$

$$
\begin{aligned}
i_c(j\omega) = &\frac{1}{2}e^{-j\frac{4}{3}\pi}[Y_{qq}(j(\omega-\omega_0))U_q(j(\omega-\omega_0)) + Y_{qd}(j(\omega-\omega_0))U_d(j(\omega-\omega_0))] \\
&+ \frac{1}{2}e^{j\frac{4}{3}\pi}[Y_{qq}(j(\omega+\omega_0))U_q(j(\omega+\omega_0)) + Y_{qd}(j(\omega+\omega_0))U_d(j(\omega+\omega_0))] \\
&+ \frac{1}{2j}e^{-j\frac{4}{3}\pi}[Y_{dq}(j(\omega-\omega_0))U_q(j(\omega-\omega_0)) + Y_{dd}(j(\omega-\omega_0))U_d(j(\omega-\omega_0))] \\
&- \frac{1}{2j}e^{j\frac{4}{3}\pi}[Y_{dq}(j(\omega+\omega_0))U_q(j(\omega+\omega_0)) + Y_{dd}(j(\omega+\omega_0))U_d(j(\omega+\omega_0))]
\end{aligned}
\tag{C.62}
$$

It is worth noticing that $i_a(j\omega)$, $i_b(j\omega)$ and $i_c(j\omega)$ are the Fourier transforms of $i_a(t)$, $i_bt)$ and $i_c(t)$, respectively [25]. By definition, these transforms are related to the corresponding $\hat{i}_a(j\omega)$, $\hat{i}_b(j\omega)$, $\hat{i}_c(j\omega)$ signal phasors [115], $\hat{i}_a(j\omega) = |i_a(j\omega)|e^{j\angle i_a(j\omega)}$, $\hat{i}_a(j\omega) = |i_a(j\omega)|e^{j\angle i_b(j\omega)}$, $\hat{i}_b(j\omega) = |i_c(j\omega)|e^{j\angle i_c(j\omega)}$. These $\hat{i}_{abc}(j\omega)$ phasors can be related to the signal symmetrical components, i.e. the positive and negative sequence phasors $\hat{i}_p(j\omega)$ and $\hat{i}_n(j\omega)$ as [99]:

$$
\begin{bmatrix} \hat{i}_p(j\omega) \\ \hat{i}_n(j\omega) \end{bmatrix} = F \begin{bmatrix} \hat{i}_a(j\omega) \\ \hat{i}_b(j\omega) \\ \hat{i}_c(j\omega) \end{bmatrix} = \frac{1}{3} \begin{bmatrix} 1 & a & a^2 \\ 1 & a^2 & a \end{bmatrix} \begin{bmatrix} \hat{i}_a(j\omega) \\ \hat{i}_b(j\omega) \\ \hat{i}_c(j\omega) \end{bmatrix}
\tag{C.63}
$$

where F is the Fortescue transform [101] while $a = e^{j\frac{2}{3}\pi}$. Its inverse F^{-1} is calculated as:

$$
\begin{bmatrix} \hat{i}_a(j\omega) \\ \hat{i}_b(j\omega) \\ \hat{i}_c(j\omega) \end{bmatrix} = F^{-1} \begin{bmatrix} \hat{i}_p(j\omega) \\ \hat{i}_n(j\omega) \end{bmatrix} = \begin{bmatrix} 1 & 1 \\ a^2 & a \\ a & a^2 \end{bmatrix} \begin{bmatrix} \hat{i}_p(j\omega) \\ \hat{i}_n(j\omega) \end{bmatrix}
\tag{C.64}
$$

By applying the Fortesque transform F to (C.60), (C.61) and (C.62), it is possible to calculate the corresponding Fourier transforms $i_p(j\omega)$ and $i_n(j\omega)$ as:

$$\begin{aligned} i_p(j\omega) &= \frac{1}{3}(i_a(j\omega) + ai_b(j\omega) + a^2 i_c(j\omega)) \\ &= ... \\ &= \frac{1}{2}U_q(j(\omega - \omega_0))[Y_{qq}(j(\omega - \omega_0)) - jY_{dq}(j(\omega - \omega_0))] \\ &+ \frac{1}{2}U_d(j(\omega - \omega_0))[Y_{qd}(j(\omega - \omega_0)) - jY_{dd}(j(\omega - \omega_0))] \end{aligned} \tag{C.65}$$

$$\begin{aligned} i_n(j(\omega)) &= \frac{1}{3}(i_a(j\omega) + a^2 i_b(j\omega) + ai_c(j\omega)) \\ &= ... \\ &= \frac{1}{2}U_q(j(\omega + \omega_0))[Y_{qq}(j(\omega + \omega_0)) + jY_{dq}(j(\omega + \omega_0))] \\ &+ \frac{1}{2}U_d(j(\omega + \omega_0))[Y_{qd}(j(\omega + \omega_0)) + jY_{dd}(j(\omega + \omega_0))] \end{aligned} \tag{C.66}$$

The next step of the derivation is to determine the relation between the Fourier transforms $U_{dq}(j\omega)$ and $U_{pn}(j\omega)$. A generic asymmetrical sinusoidal component $U_{abc}(t, \hat{\omega})$ of $U_{abc}(t)$ is considered, defined as:

$$\begin{bmatrix} U_a(t, \hat{\omega}) \\ U_b(t, \hat{\omega}) \\ U_c(t, \hat{\omega}) \end{bmatrix} = \begin{bmatrix} \overline{U}_a(\hat{\omega})cos(\hat{\omega}t + \theta_a(\hat{\omega})) \\ \overline{U}_b(\hat{\omega})cos(\hat{\omega}t + \theta_b(\hat{\omega})) \\ \overline{U}_c(\hat{\omega})cos(\hat{\omega}t + \theta_c(\hat{\omega})) \end{bmatrix} \tag{C.67}$$

$\hat{U}_p(j\hat{\omega})$ and $\hat{U}_n(j\hat{\omega})$ indicated the positive and negative sequence phasors associated to $U_{abc}(t, \hat{\omega})$. Based on (C.64), the relation between the signals $U_{abc}(t, \hat{\omega})$ and $\hat{U}_{pn}(j\hat{\omega})$ can be written as [99]:

$$\begin{aligned} \begin{bmatrix} U_a(t, \hat{\omega}) \\ U_b(t, \hat{\omega}) \\ U_c(t, \hat{\omega}) \end{bmatrix} &= \begin{bmatrix} \Re[\hat{U}_p(j\hat{\omega})e^{j\hat{\omega}t} + \hat{U}_n(j\hat{\omega})e^{j\hat{\omega}t}] \\ \Re[a^2\hat{U}_p(j\hat{\omega})e^{j\hat{\omega}t} + a\hat{U}_n(j\hat{\omega})e^{j\hat{\omega}t}] \\ \Re[a\hat{U}_p(j\hat{\omega})e^{j\hat{\omega}t} + a^2\hat{U}_n(j\hat{\omega})e^{j\hat{\omega}t}] \end{bmatrix} \\ &= \begin{bmatrix} \Re[\hat{U}_p(j\hat{\omega})e^{j\hat{\omega}t} + \hat{U}_n(j\hat{\omega})e^{j\hat{\omega}t}] \\ \Re[\hat{U}_p(j\hat{\omega})e^{j(\hat{\omega}t + \frac{4}{3}\pi)} + \hat{U}_n(j\hat{\omega})e^{j(\hat{\omega}t + \frac{2}{3}\pi)}] \\ \Re[\hat{U}_p(j\hat{\omega})e^{j(\hat{\omega}t + \frac{2}{3}\pi)} + \hat{U}_n(j\hat{\omega})e^{j(\hat{\omega}t + \frac{4}{3}\pi)}] \end{bmatrix} \end{aligned} \tag{C.68}$$

As $\Re[z] = \frac{1}{2}[z + z^*]$, equation (C.68) can be rewritten as:

$$\begin{bmatrix} U_a(t,\hat{\omega}) \\ U_b(t,\hat{\omega}) \\ U_c(t,\hat{\omega}) \end{bmatrix} = \frac{1}{2} \begin{bmatrix} [\hat{U}_p(j\hat{\omega}) + \hat{U}_n(j\hat{\omega})]e^{j\hat{\omega}t} + [\hat{U}_p^*(j\hat{\omega}) + \hat{U}_n^*(j\hat{\omega})]e^{-j\hat{\omega}t} \\ [\hat{U}_p(j\hat{\omega})e^{j\frac{4}{3}\pi} + \hat{U}_n(j\hat{\omega})e^{j\frac{2}{3}\pi}]e^{j\hat{\omega}t} + [\hat{U}_p^*(j\hat{\omega})e^{-j\frac{4}{3}\pi} + \hat{U}_n^*(j\hat{\omega})e^{-j\frac{2}{3}\pi}]e^{-j\hat{\omega}t} \\ [\hat{U}_p(j\hat{\omega})e^{j\frac{2}{3}\pi} + \hat{U}_n(j\hat{\omega})e^{+j\frac{4}{3}\pi}]e^{j\hat{\omega}t} + [\hat{U}_p^*(j\hat{\omega})e^{-j\frac{2}{3}\pi} + \hat{U}_n^*(j\hat{\omega})e^{-j\frac{4}{3}\pi}]e^{-j\hat{\omega}t} \end{bmatrix} \tag{C.69}$$

Applying the transformation $T^T(\omega_0 t)$, defined in (C.56), to (C.69) the resulting $U_d(t,\hat{\omega})$ and $U_q(t,\hat{\omega})$ signals are:

$$\begin{aligned} U_d(t,\hat{\omega}) &= \frac{2}{3}[U_a(t,\hat{\omega})sin(\omega_0 t) + U_b(t,\hat{\omega})sin(\omega_0 t - \frac{2}{3}\pi) + U_c(t,\hat{\omega})sin(\omega_0 t - \frac{4}{3}\pi)] \\ &= ... \\ &= |\hat{U}_p(j\hat{\omega})|cos((\hat{\omega} - \omega_0)t + \angle\hat{U}_p(j\hat{\omega}) + \frac{\pi}{2}) \\ &+ |\hat{U}_n(j\hat{\omega})|cos((\hat{\omega} + \omega_0)t + \angle\hat{U}_n(j\hat{\omega}) - \frac{\pi}{2}) \end{aligned} \tag{C.70}$$

$$\begin{aligned} U_q(t,\hat{\omega}) &= \frac{2}{3}[U_a(t,\hat{\omega})cos(\omega_0 t) + U_b(t,\hat{\omega})cos(\omega_0 t - \frac{2}{3}\pi) + U_c(t,\hat{\omega})cos(\omega_0 t - \frac{4}{3}\pi)] \\ &= ... \\ &= |\hat{U}_p(j\hat{\omega})|cos((\hat{\omega} - \omega_0)t + \angle\hat{U}_p(j\hat{\omega})) \\ &+ |\hat{U}_n(j\hat{\omega})|cos((\hat{\omega} + \omega_0)t + \angle\hat{U}_n(j\hat{\omega})) \end{aligned} \tag{C.71}$$

The results (C.70) and (C.71) show that the $U_{abc}(t,\hat{\omega})$ signal is associated to a sinusoidal signal in the *dq*-frame. In particular, its positive sequence component gives rise to a *dq*-frame sinusoidal signal at frequency $\hat{\omega} - \omega_0$, while its negative sequence component generates a *dq*-frame sinusoidal signal at frequency $\hat{\omega} + \omega_0$.

The Fourier transforms of (C.70) and (C.71), $U_d(j\omega,\hat{\omega})$ and $U_q(j\omega,\hat{\omega})$ respectively, are:

$$\begin{aligned} U_d(j\omega,\hat{\omega}) &= \mathcal{F}[\hat{U}_d(t,\hat{\omega})] \\ &= j\pi|\hat{U}_p(j\hat{\omega})|[e^{j\angle\hat{U}_p(j\hat{\omega})}\delta(\omega-\hat{\omega}+\omega_0)+e^{-j\angle\hat{U}_p(j\hat{\omega})}\delta(\omega+\hat{\omega}-\omega_0)] \\ &- j\pi|\hat{U}_n(j\hat{\omega})|[e^{j\angle\hat{U}_n(j\hat{\omega})}\delta(\omega-\hat{\omega}-\omega_0)+e^{-j\angle\hat{U}_n(j\hat{\omega})}\delta(\omega+\hat{\omega}+\omega_0)] \end{aligned} \quad (C.72)$$

$$\begin{aligned} U_q(j\omega,\hat{\omega}) &= \mathcal{F}[\hat{U}_q(t,\hat{\omega})] \\ &= \pi|\hat{U}_p(j\hat{\omega})|[e^{j\angle\hat{U}_p(j\hat{\omega})}\delta(\omega-\hat{\omega}+\omega_0)+e^{-j\angle\hat{U}_p(j\hat{\omega})}\delta(\omega+\hat{\omega}-\omega_0)] \\ &+ \pi|\hat{U}_n(j\hat{\omega})|[e^{j\angle\hat{U}_n(j\hat{\omega})}\delta(\omega-\hat{\omega}-\omega_0)+e^{-j\angle\hat{U}_n(j\hat{\omega})}\delta(\omega+\hat{\omega}+\omega_0)] \end{aligned} \quad (C.73)$$

where $\delta(x)$ is the Dirac delta function [115]. It is worth noticing that, by definition, $\hat{U}_p(j\hat{\omega})$ and $\hat{U}_n(j\hat{\omega})$ are related to the Fourier transforms $U_p(j\omega)$ and $U_n(j\omega)$ of the positive and negative sequence components $U_p(t,\hat{\omega})$ and $U_n(t,\hat{\omega})$ of $U_{abc}(t,\hat{\omega})$. In particular:

$$\begin{aligned} U_p(j\omega) &= \mathcal{F}[U_p(t,\hat{\omega})] \\ &= \int_0^\infty [\pi|\hat{U}_p(j\hat{\omega})|(e^{j\angle\hat{U}_p(j\hat{\omega})}\delta(\omega-\hat{\omega})+e^{-j\angle\hat{U}_p(j\hat{\omega})}\delta(\omega+\hat{\omega}))]d\hat{\omega} \end{aligned} \quad (C.74)$$

$$\begin{aligned} U_n(j\omega) &= \mathcal{F}[U_n(t,\hat{\omega})] \\ &= \int_0^\infty [\pi|\hat{U}_n(j\hat{\omega})|(e^{j\angle\hat{U}_n(j\hat{\omega})}\delta(\omega-\hat{\omega})+e^{-j\angle\hat{U}_n(j\hat{\omega})}\delta(\omega+\hat{\omega}))]d\hat{\omega} \end{aligned} \quad (C.75)$$

Applying Fourier theory, the generic voltage signal $U_{abc}(t)$ can be described as a sum of an infinite number of components $U_{abc}(t,\hat{\omega})$, with $\hat{\omega}\in[0,+\infty)$. By indicating with $U_d(t)$ and $U_q(t)$ the dq-components of $U_{abc}(t)$, their Fourier transforms are:

$$\begin{aligned} U_d(j\omega) &= \int_0^\infty U_d(j\omega,\hat{\omega})d\hat{\omega} \\ &= j\int_0^\infty [\pi|\hat{U}_p(j\hat{\omega})|(e^{j\angle\hat{U}_p(j\hat{\omega})}\delta(\omega-\hat{\omega}+\omega_0)+e^{-j\angle\hat{U}_p(j\hat{\omega})}\delta(\omega+\hat{\omega}-\omega_0))]d\hat{\omega} \\ &- j\int_0^\infty [\pi|\hat{U}_n(j\hat{\omega})|(e^{j\angle\hat{U}_n(j\hat{\omega})}\delta(\omega-\hat{\omega}-\omega_0)+e^{-j\angle\hat{U}_n(j\hat{\omega})}\delta(\omega+\hat{\omega}+\omega_0))]d\hat{\omega} \end{aligned} \quad (C.76)$$

$$
\begin{aligned}
U_q(j\omega) &= \int_0^{\infty} U_q(j\omega,\hat{\omega})d\hat{\omega} \\
&= \int_0^{\infty} [\pi|\hat{U}_p(j\hat{\omega})|(e^{j\angle\hat{U}_p(j\hat{\omega})}\delta(\omega-\hat{\omega}+\omega_0)+e^{-j\angle\hat{U}_p(j\hat{\omega})}\delta(\omega+\hat{\omega}-\omega_0))]d\hat{\omega} \\
&+ \int_0^{\infty} [\pi|\hat{U}_n(j\hat{\omega})|(e^{j\angle\hat{U}_n(j\hat{\omega})}\delta(\omega-\hat{\omega}-\omega_0)+e^{-j\angle\hat{U}_n(j\hat{\omega})}\delta(\omega+\hat{\omega}+\omega_0))]d\hat{\omega}
\end{aligned}
\tag{C.77}
$$

Based on (C.74), (C.75), (C.77) and (C.76), the following expressions can be written for $U_d(j\omega)$ and $U_q(j\omega)$:

$$
\begin{aligned}
U_d(j\omega) &= jU_p(j(\omega+\omega_0)) - jU_n(j(\omega-\omega_0)) \\
U_q(j\omega) &= U_p(j(\omega+\omega_0)) + U_n(j(\omega-\omega_0))
\end{aligned}
\tag{C.78}
$$

The result (C.78) shows that any spectral component which appears at frequency ω in the dq-frame signal can be associated to a positive sequence signal at frequency $\omega+\omega_0$ and to a negative sequence signal at frequency $\omega-\omega_0$.

Based on (C.65), (C.66) and (C.78), the following expressions are derived:

$$
\begin{aligned}
i_p(j\omega) &= \frac{1}{2}[U_p(j\omega)+U_n(j(\omega-2\omega_0))][Y_{qq}(j(\omega-\omega_0))-jY_{dq}(j(\omega-\omega_0))] \\
&+ \frac{1}{2}[jU_p(j\omega)-jU_n(j(\omega-2\omega_0))][Y_{qd}(j(\omega-\omega_0))-jY_{dd}(j(\omega-\omega_0))]
\end{aligned}
\tag{C.79}
$$

$$
\begin{aligned}
i_n(j\omega) &= \frac{1}{2}[U_p(j(\omega+2\omega_0))+U_n(j\omega)][Y_{qq}(j(\omega-\omega_0))+jY_{dq}(j(\omega-\omega_0))] \\
&+ \frac{1}{2}[jU_p(j(\omega+2\omega_0))-jU_n(j\omega))][Y_{qd}(j(\omega-\omega_0))+jY_{dd}(j(\omega-\omega_0))]
\end{aligned}
\tag{C.80}
$$

By setting:

$$
\begin{aligned}
Y_{pp}(s) &= \frac{1}{2}[Y_{qq}(s-j\omega_0)-jY_{dq}(s-j\omega_0)+jY_{qd}(s-j\omega_0)+Y_{dd}(s-j\omega_0)], \\
Y_{pn}(s) &= \frac{1}{2}[Y_{qq}(s-j\omega_0)-jY_{dq}(s-j\omega_0)-jY_{qd}(s-j\omega_0)-Y_{dd}(s-j\omega_0)], \\
Y_{np}(s) &= \frac{1}{2}[Y_{qq}(s+j\omega_0)+jY_{dq}(s+j\omega_0)+jY_{qd}(s+j\omega_0)-Y_{dd}(s+j\omega_0)], \\
Y_{nn}(s) &= \frac{1}{2}[Y_{qq}(s+j\omega_0)+jY_{dq}(s+j\omega_0)-jY_{qd}(s+j\omega_0)+Y_{dd}(s+j\omega_0)]
\end{aligned}
\tag{C.81}
$$

equations (C.79), (C.80) can be written as:

$$
\begin{aligned}
i_p(s) &= Y_{pp}(s)U_p(s) + Y_{pn}(s)U_n(s - 2j\omega_0), \\
i_n(s) &= Y_{nn}(s)U_n(s) + Y_{np}(s)U_p(s + 2j\omega_0)
\end{aligned}
\tag{C.82}
$$

Based on (4.2), (C.81) and (C.82) correspond to (4.3) and (4.4).

Appendix D

Hardware implementation of the inverter laboratory prototype

In this Appendix an outline of the hardware used to build the laboratory inverter prototype is provided.

D.1 Control board

The control board is the core element of the set-up. Its function is the execution of the inverter controller algorithm. The Xilinx Zynq-7000 ZC706 evaluation board has been used for this purpose. A detailed description of the ZC706 board characteristics is out of the scope of this work and can be found in [112]. The board is composed of a Processing System (PS) section and of a Programmable Logic (PL) unit. While the former includes two ARM® Cortex™-A9 MPCore™ processors [121], the latter is based on FPGA technology. The PS and the PL units operate simultaneously exchanging data and control signals.

D.2 Interface boards

The ZC706 board is connected both to a laptop to allow debugging of the controller algorithm and delivery of the recorded data, and to the rest of the set-up, in particular the ADC/DAC board and the gate driver. The connection to the ADC/DAC board is needed to acquire the plant signals read from the sensors and to deliver debugging signals to the oscilloscopes. The connection to the gate driver is necessary to provide this with the computed PWM pattern as well as to receive a diagnostic error signal generated by the driver.

The connection to the ADC/DAC board has been carried out through the LPC FMC port of the control board and makes use of an additional interface board, named FMC-PCI. This consists both of an FMC LPC 160-pin [122] and of a PCI/104-Express [123] connector, as detailed in Section D.2.1, where the design of the FMC-PCI board is discussed in more detail.

On the other hand, the connection to the gate driver has been made through the PMOD GPIO port of the control board. A voltage level shifter has been used in this connection to rise the level of the PWM voltage signals from 3.3 V to 5 V, thus making these signals compliant with the gate driver PWM input specifications [124]. Similarly, such voltage level shifter has been used to lower the voltage of the diagnostic signal generated by the driver, from 5 V to 3.3 V. The shifter is made up of two separate units, the VLS-Rx and the VLS-Rx boards. Further details on their design are reported in Section D.2.2.

D.2.1 FMC-PCI interface board

This board has been designed to connect the ADC/DAC board to the control board. It mounts both a FMC LPC 160-pin [122] and a PCI/104-Express [123] connector, as illustrated in Figure D.1.

The board is composed of six layers, four of which employed to accommodate the control and data signals. The remaining two layers are ground layers, used to allow a better Electromagnetic Interference (EMI) immunity. The schematics of the boards are reported in Figures D.6, D.7 and D.8 in Section D.7.

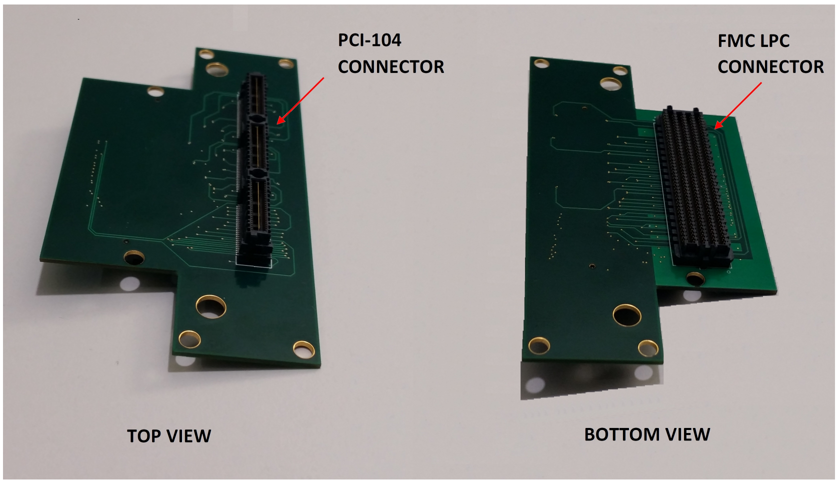

Figure D.1: Picture of the FMC-PCI interface board.

D.2.2 Level shifter interface board

In order to allow the exchange of signals between the control board and the gate driver, a voltage level shifter has been used. In fact, while the PMOD I/O signals of the control board have a higher voltage level of 3.3 V [112], the I/O inputs of the gate driver, whose model is SKHI 71 [124], have a minimum high voltage level equal to 4 V. A level shifter has been therefore used both to increase the voltage of the six PWM signals delivered to the gate driver (from 3.3 V to 5 V) and to reduce that of the error signal generated by the gate driver (from 5 V to 3.3 V). Such shifter is composed of two separate PCBs, the VLS-Tx board, which is connected to the control board, and the VLS-Rx board, which is connected to the gate driver. The change in the voltage amplitude of the signals is carried out by the VLS-Tx board, making use of two SN74LVCC3245A 8-bit voltage translators [125], one magnifies the PWM signal voltages, the other reduces the error signal voltage amplitude.

The digital information is delivered by a current signal. In particular, for each of the seven interface channels, the 0 data bit is encoded by no current flowing between the transmitting and the receiving ends of the communication channel. On the other hand, the 1 data bit is encoded by generating a non-zero current through the channel. The electrical diagrams corresponding to the PWM data and the error signal channels are respectively shown in Figures D.2 and D.3, while the PCB schematics of the two boards are reported in Figures D.9, D.10, D.11 and D.12 in Section D.7.

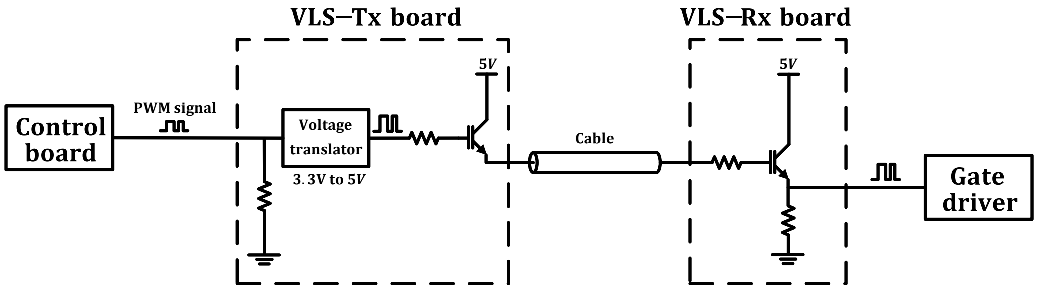

Figure D.2: Schematic diagram of the PWM signal transmission from the control board to the gate driver through the voltage level shifter.

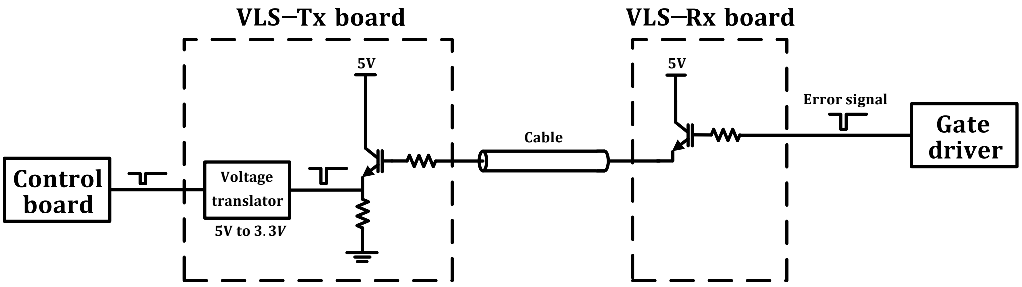

Figure D.3: Schematic diagram of the error signal transmission from the gate driver to the control board through the voltage level shifter.

D.3 ADC/DAC board

The ADC/DAC board is used, as above mentioned, to acquire the analogue signals generated by the sensors, converting them into a digital format to be sent to the control board. Furthermore, it converts the debug digital signals generated by the control board into an analogue format, suitable to be read by the connected oscilloscopes.

The board is equipped with 12 ADC inputs (only seven of them have been used), and 8 DAC outputs, all utilised. In more detail, the analogue signals generated by the sensors, which are in the range [−10 V, 10 V], are read by two ADC converter chips, each capable of reading up to six channels. The ADC conversion is carried out with a resolution of 12 bits and requires ≈ 2.3 μs. One single chip is used for the DAC conversion, carried out with a 12 bit resolution and generating analogue outputs in the

[−10 V, 10 V] range .

The ADC/DAC module requires a 24 V DC power supply and, as mentioned before, is connected to the ZC706 control board through the FMC-PCI interface board.

D.4 Gate driver

The adopted gate driver is the SKHI 71 model by Semikron [124]. It allows the delivery of the PWM pattern received by the control board to the converter IGBT modules. By making use of opto-couplers, it assures electrical isolation between the control board and the inverter. The driver has been configured to add a 1 μs dead-time to the PWM pulses sent to the IGBTs of the same inverter leg (additional dead-time is introduced via software by the control board, as discussed in Section E.2.4). Besides the six PWM inputs, the driver is also equipped with an active low diagnostic output to indicate unsafe operating conditions within the driver. Under these circumstances, the driver is automatically turned off [124]. Simultaneously, as soon as the control board detects the activation of such error signal, it resets its output PWM signals.

D.5 Converter

The converter used is the SKM75GB124D model by Semikron [126]. It is designed to operate with a DC voltage < 600 V and a forward current < 50 A under normal operating conditions, while being able to stand up to a 1200 V collector-to-emitter burst voltage and up to a 100 A burst collector current. The module is specifically suitable for switching applications, with reduced power losses (2.25 % under maximum rating conditions). Further technical specifications can be found in [126].

D.6 Sensors

Seven sensors have been used to measure the plant signals, namely the DC Voltage U_{DC}, the three phase voltage U and the inverter current i (see Figure 2.22). Besides measuring the electrical signal, each sensor also provides galvanic isolation between the plant components and the control board. For this purpose, Hall effect sensors have been chosen, the LV25-P sensor and the LA55-P sensor (both manufactured by LEM). They respectively measure voltage or current. The design of the sensor boards are discussed in more detail is the following Sections D.6.1 and D.6.2

D.6.1 Voltage Sensor

Four voltage sensors have been used to measure the plant three phase voltage U and the converter DC voltage U_{DC} in Figure 2.22. All of these sensors share the same design and make use of the LV25-P transducer, which also provides galvanic isolation between the plant and the control system.
As shown in Figure D.4, where a schemetic diagram of the sensor circuit is shown, the input voltage U_{in} is converted into a (primary) current I_{in} by means of the input resistor R_{in}. Having assumed a maximum input voltage $U_{in,max} = 300$ V and a nominal input current $I_{in,nom}$ of 7.5 mA [127], the resulting value of R_{in} has been calculated as:

$$R_{in} = \frac{U_{in,max}}{I_{in,nom}} \tag{D.1}$$

The secondary (output) current of the transducer, I_m, is converted into the voltage signal U_m by the 300 Ω resistor $R_{m,v}$. Such voltage is then increased by means of an operation amplifier used in its inverting configuration [128].
A 10 kΩ trimmer, R_G, is used to tune the gain G_v of the amplification stage, calculated as [128]:

$$G_v = \frac{U_{out}}{U_m} = -\frac{R_2 + R_G}{R_1}. \tag{D.2}$$

By choosing $R_1 = 10$ kΩ and $R_2 = 5.6$ kΩ , the value of R_G has been tuned such that:

$$G_V = \frac{U_{out}}{U_{in}} = -0.03 \tag{D.3}$$

where G_V is the overall gain of the sensor.

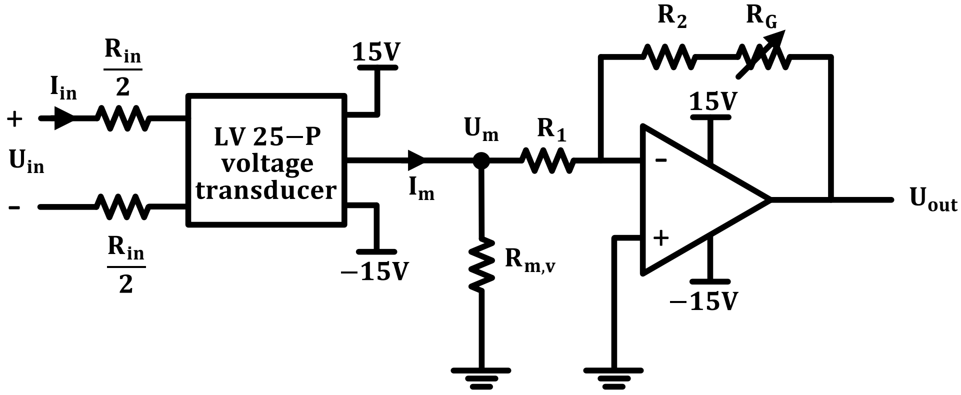

Figure D.4: Schematic diagram of the voltage sensor.

With such a sizing of the resistors, for an input voltage U_{in} in the [−300 V, 300 V] range, the corresponding output voltage of the sensor is in the [−9 V, 9 V] range (i.e. within the [−10 V, 10 V] range of the ADC inputs of the ADC/DAC board). It is worth noticing that the use of the variable resistor R_G has allowed a fine calibration of the sensor. An additional 10 kΩ trimmer (not shown in Figure D.4) has been used to compensate for the operational amplifier voltage offset. The PCB schematics of the sensor are reported in Figure D.13, in Section D.7.

D.6.2 Current Sensor

The structure of the current sensor is similar to that of the voltage one. In this case, only three sensors have been used, which measure the three phase inverter output current i in Figure 2.22. The LA55-P transducer has been employed which, like the LV25-P voltage transduser, also provides galvanic isolation between the plant and the controller. The transducer operates according to a closed-loop scheme where its output current is proportional both to the primary (input) current I_{in} and to the number N_t of turns of the input wire across the sensor aperture [129] (see Figure D.5).

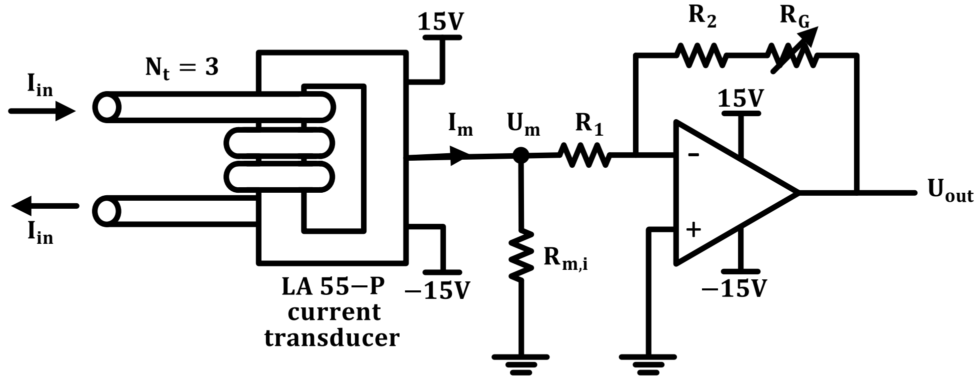

Figure D.5: Schematic diagram of the current sensor.

As shown in Figure D.5, the output current of the transducer, I_m, is converted into the voltage signal U_m by the 100 Ω resistor $R_{m,i}$. This voltage is then amplified using the same amplifier configuration adopted for the voltage sensor. The number N_t of turns of the primary current conductor has been set to three. $R_1 = 10$ kΩ, $R_2 = 5.6$ kΩ, while R_G is a 10 kΩ trimmer. Equation (D.2) also provides the gain of the current sensor amplification stage, with the trimmer tuned such that:

$$G_I = \frac{U_{out}}{I_{in}} = -0.4 \tag{D.4}$$

where G_I is the total gain of the sensor.

As the accepted voltage of the ADC/DAC board ADC inputs is, as aforementioned, in the [−10 V, 10 V] range, the corresponding input current that can be measured by the sensor is in the [−25 A, 25 A] range. A further 10 kΩ trimmer (not shown in Figure D.5) has been used to compensate for the operational amplifier voltage offset, as similarly done for the voltage sensor. The PCB schematics of the sensor are reported in Figure D.14, in Section D.7.

D.7 PCB schematics

In this Section, the schematics of the designed PCB boards are reported.

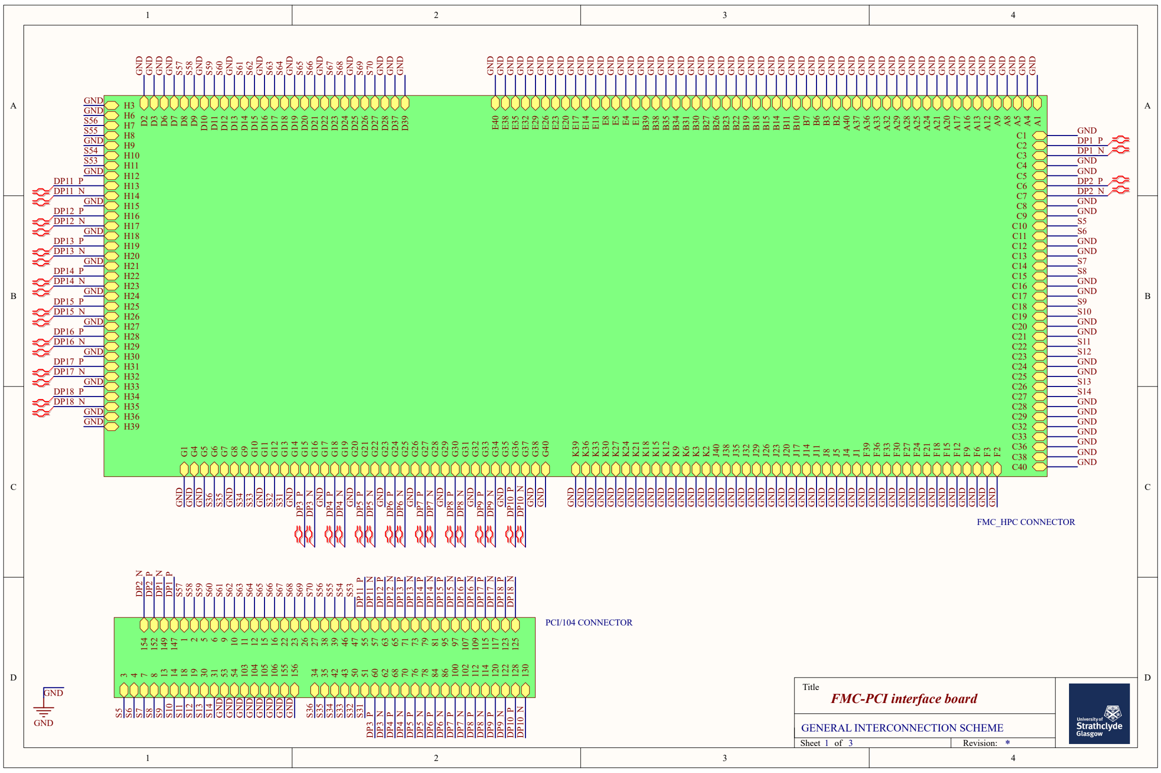

Figure D.6: Schematic diagram of the FMC-PCI interface board. General interconnection scheme.

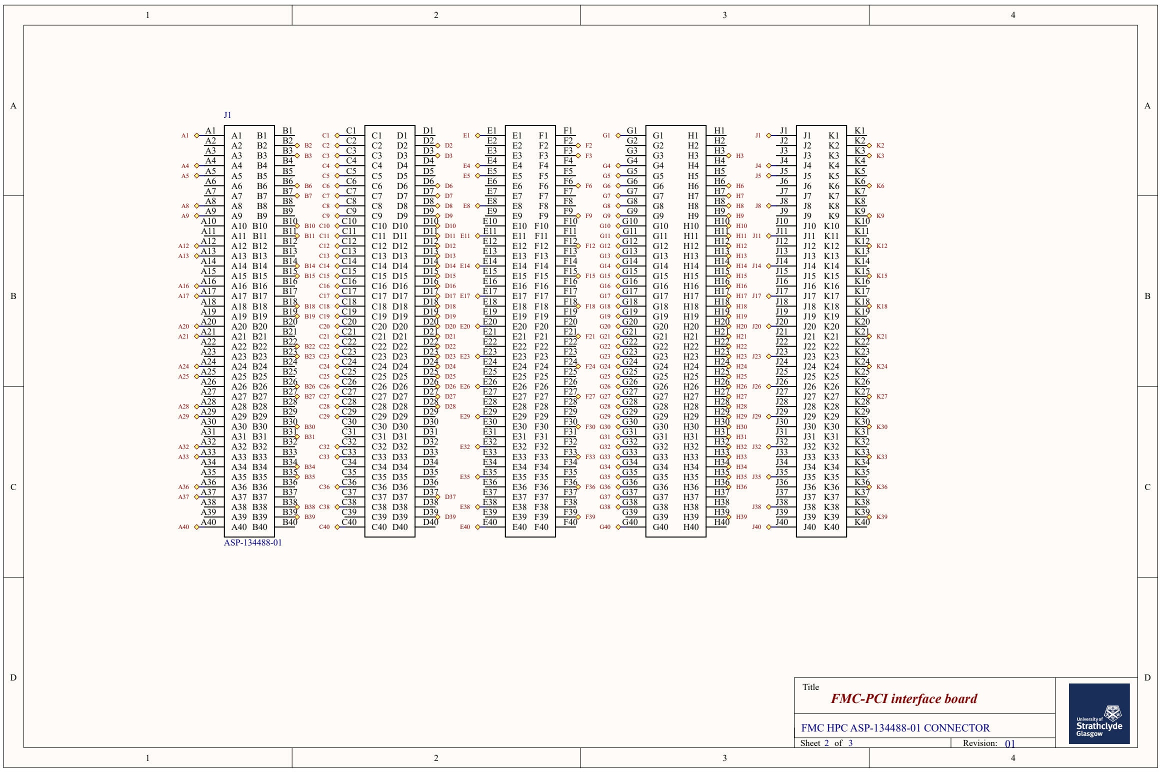

Figure D.7: Schematic diagram of the FMC-PCI interface board. FMC HPC ASP-134488-01 connector.

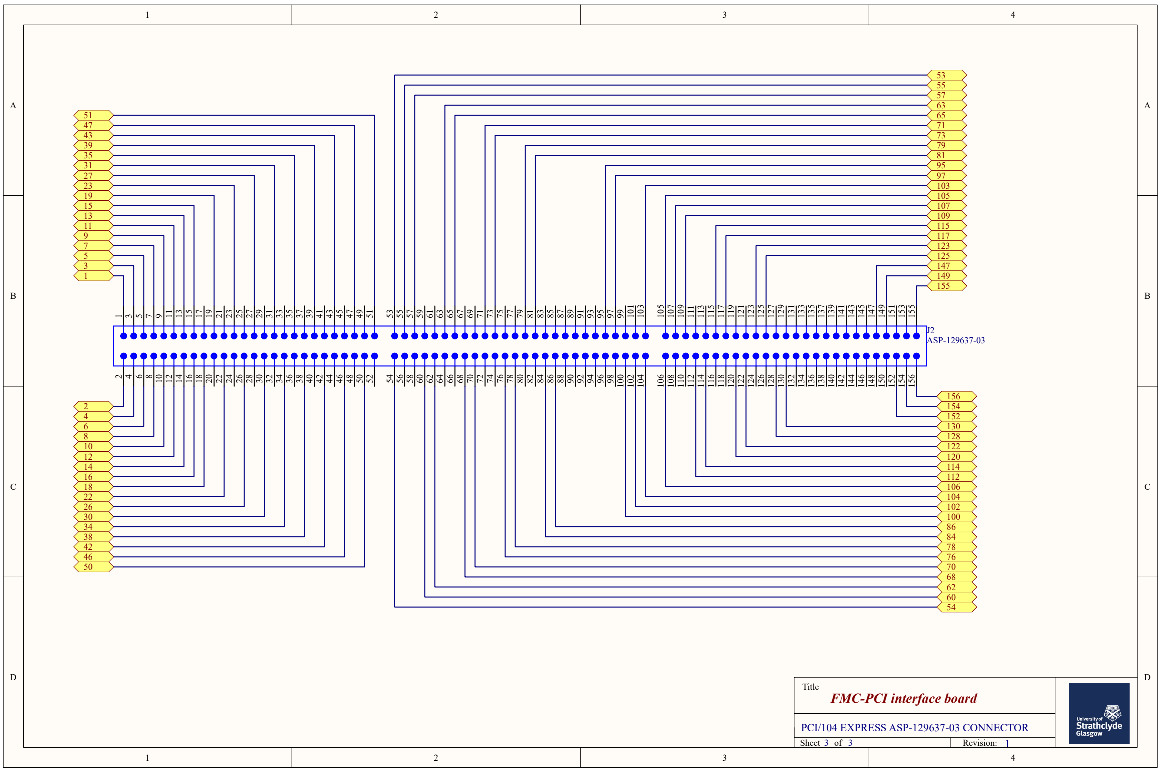

Figure D.8: Schematic diagram of the FMC-PCI interface board. PCI/104 Express ASP-129637-03 connector.

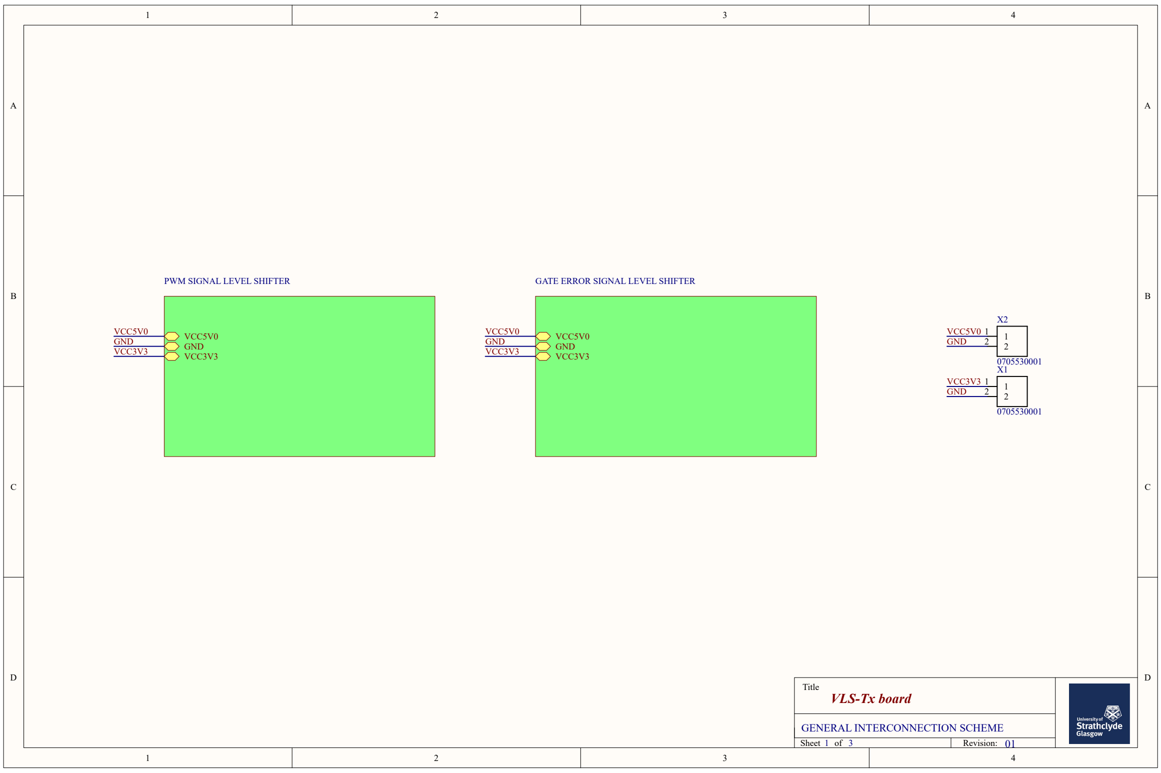

Figure D.9: Schematic diagram of the VLS-Tx level shifter board. General interconnection scheme.

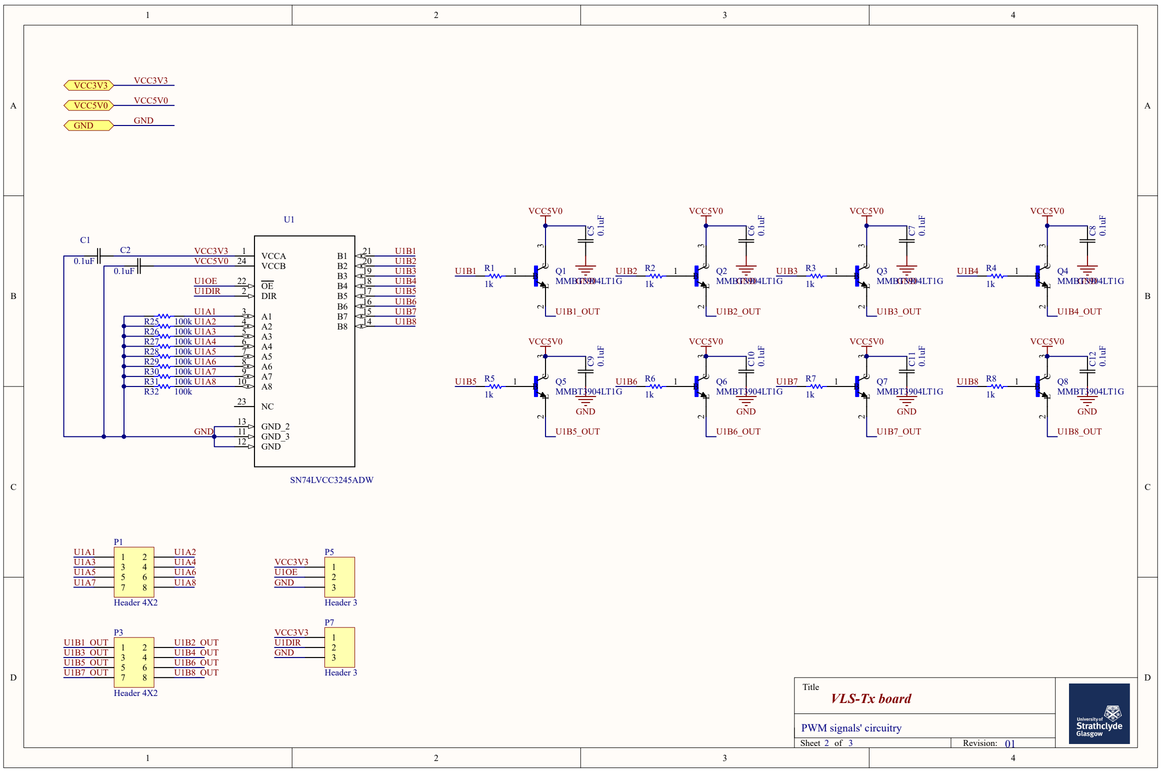

Figure D.10: Schematic diagram of the VLS-Tx level shifter board. PWM signals' circuitry.

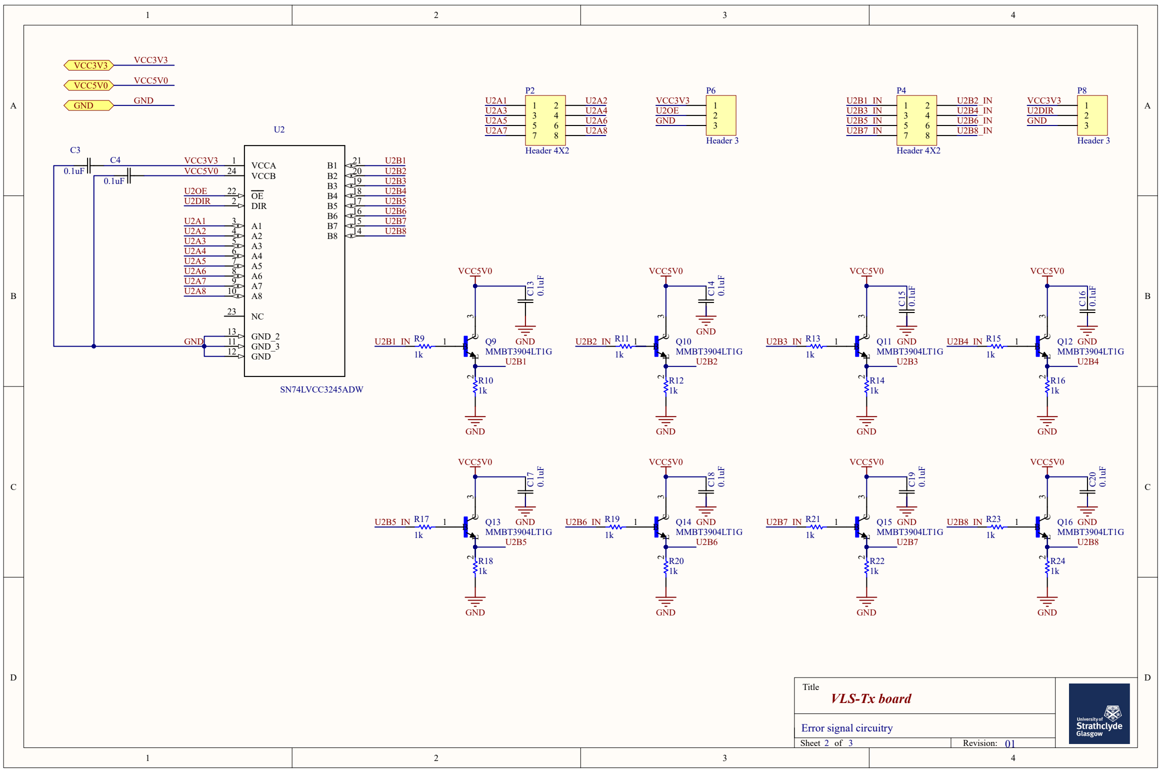

Figure D.11: Schematic diagram of the VLS-Tx level shifter board. Error signal circuitry.

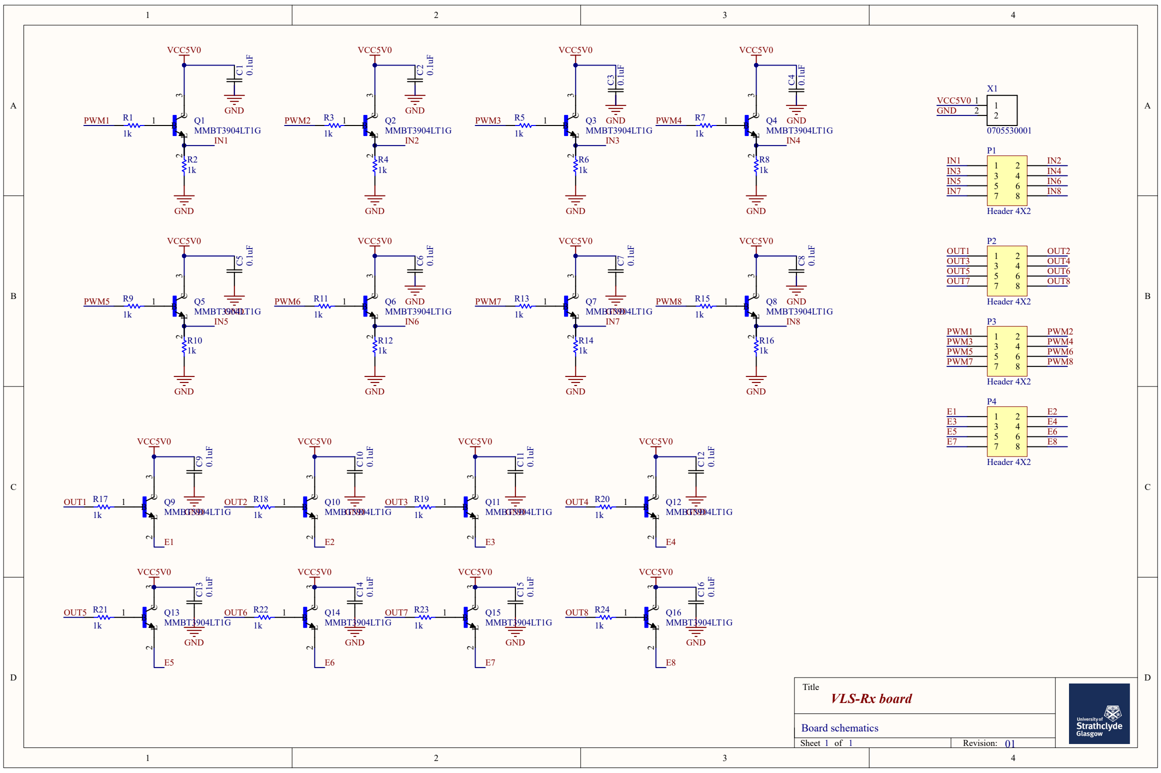

Figure D.12: Schematic diagram of the VLS-Rx level shifter board.

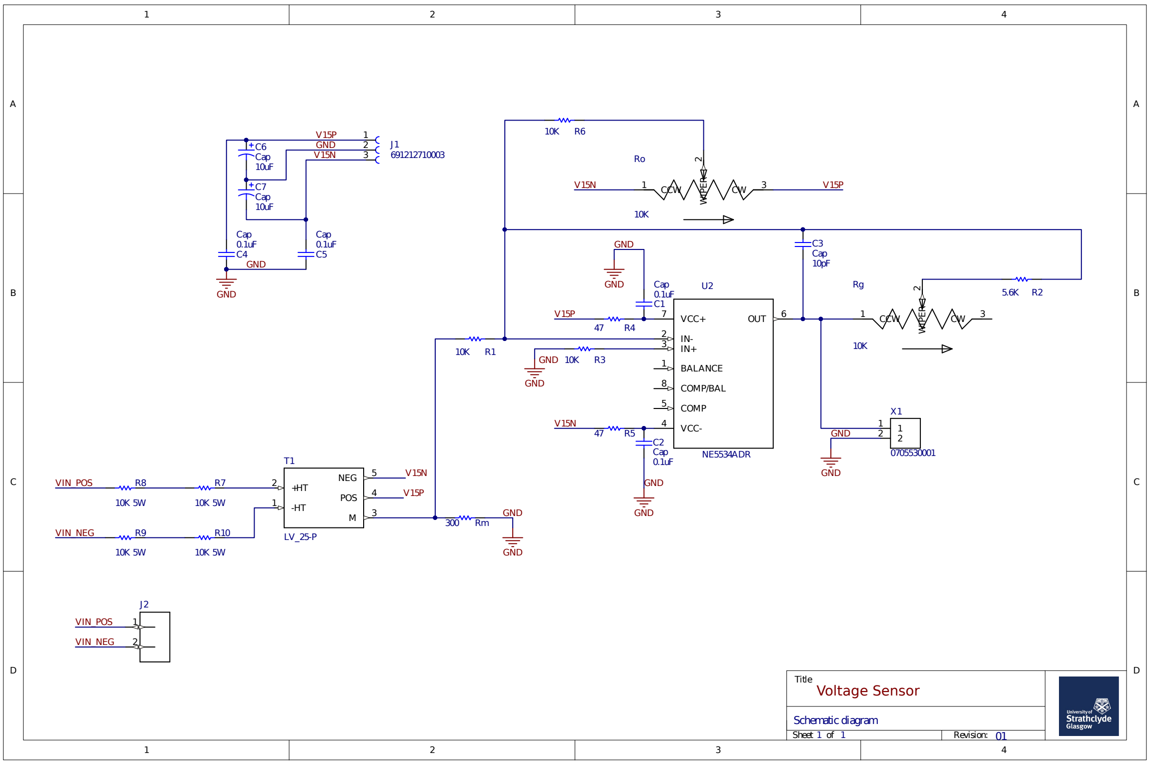

Figure D.13: Schematic diagram of the voltage sensor board.

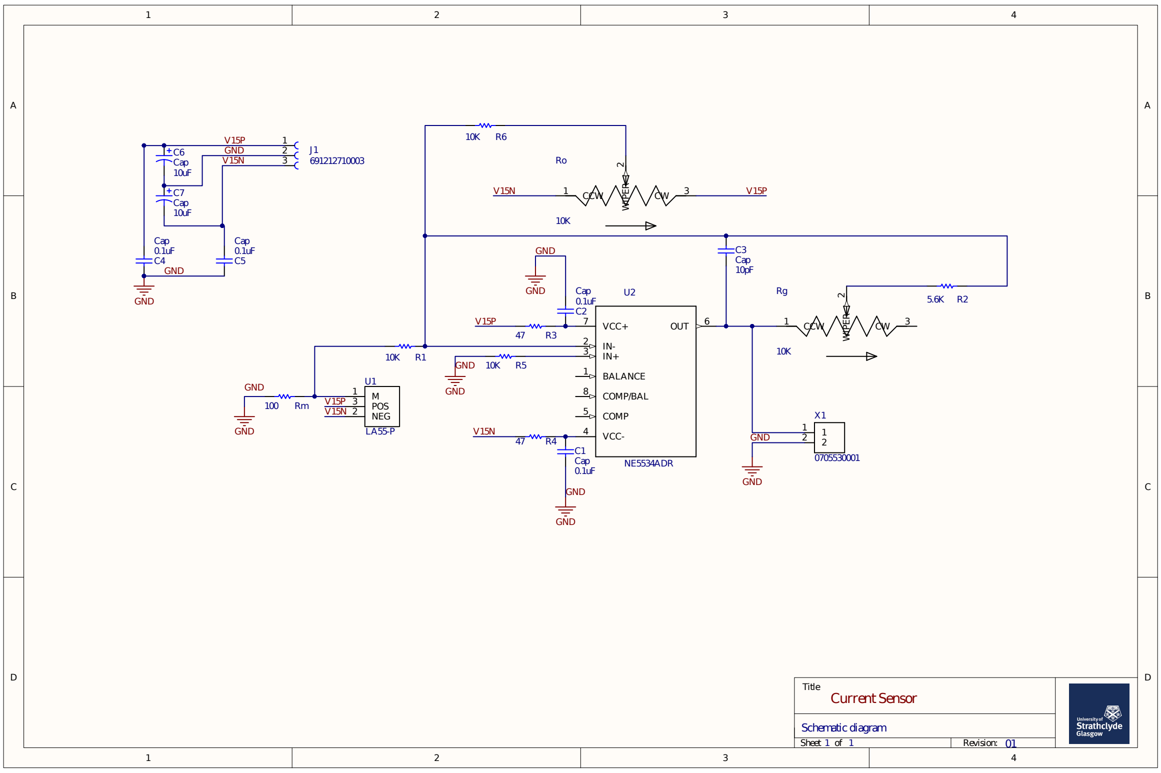

Figure D.14: Schematic diagram of the current sensor board.

Appendix E

Digital implementation of the controller algorithm

In this Appendix the implementation of the controller algorithm, executed by the two processor cores of the control board, is described. Such algorithm has been coded in C language. As described in Section 5.1, processor P1 samples the plant signals and filters the measured AC voltage. On the other hand, processor P2 executes the controller algorithm, calculating the PWM pattern used to modulate the inverter voltage. These data consist in six timers defining the turn on/off times of the inverter IGBT modules. These timers are loaded on the PL section of the control board and are used to determine the gate signals driving the inverter IGBT modules for the next T_{sample} period. The main sections of the algorithms executed by P1 and P2 are described as follows, in particular presenting the anti-aliasing filter, implemented in P1, and the vector control algorithm, executed by P2.
In Section E.3, a description of the methodology used to derive the *pn*-frame admittance frequency responses experimentally is provided.

E.1 Anti-aliasing filter

One of the main tasks of processor P1 is to pre-filter the meausured AC voltage U, before this is passed to P2. This is needed to avoid aliasing of the PWM harmonics present in the spectrum of U. Their existence at side-bands of the switching frequency (and of its integer multiples) [90] is confirmed in Figure E.1, where a detailed view of the magnitude spectrum of the experimentally measured phase a voltage, $U_a[n] = U_a(\bar{t}_n)$, sampled at f_{OS} by P1, is illustrated ($f_{OS} = 100$ kHz).

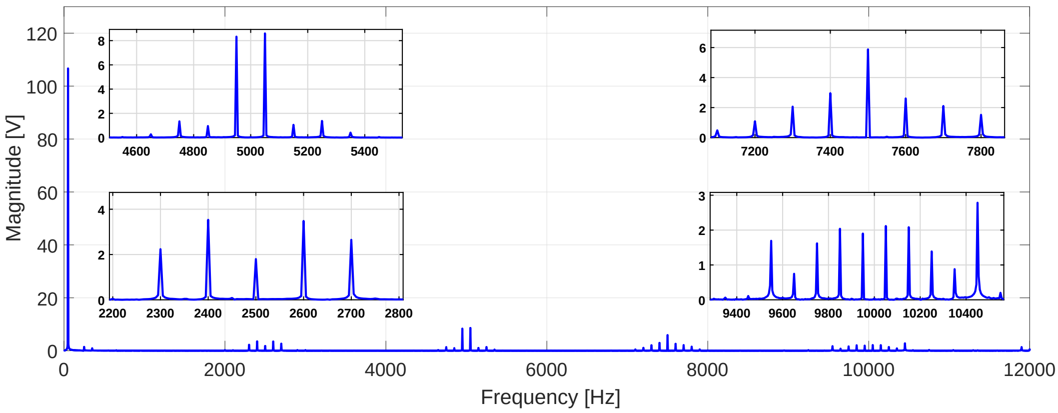

Figure E.1: Detailed view of the magnitude spectrum of the $U_a[n]$ (phase a). A sampling frequency of 100 kHz has been considered. Such signal has been obtained testing the grid-connected converter prototype corresponding to the scheme in Figure 2.27.

In the following description, asymmetrical sampling with a switching frequency of 2.5 kHz is assumed. By providing P2 with the samples $U_S[k] = U_S(t_k)$, which are sampled at a $f_{sample} = 5$ kHz rate, based on the Shannon sampling theorem [83], the voltage signal seen by P2 contains scaled replica of the $U(\bar{t}_n)$ spectrum, shifted by $\pm k f_{sample}$, with $k = 1, 2, 3, ... + \infty$. In more detail, by indicating with $X_U(f)$ the spectrum of U and with $X_{U_S}(f)$ the spectrum of U_S:

$$X_{U_S}(f) = \sum_{k=-\infty}^{+\infty} X_U(f - k f_{sample}) \tag{E.1}$$

Therefore, the result of P2 sampling the U signal measured by P1 at a f_{sample} rate is that the PWM harmonics of U will appear in the lower frequency range of $X_{U_S}(f)$. Such effect is called aliasing and is confirmed in Figure E.2, where the spectra of $U_a(\bar{t}_n)$ and $U_{S,a}(t_k)$ are compared. As it can be seen, such aliasing effect not only generates new components in the spectrum of $U_{S,a}(t_k)$, particularly evident at 150 Hz, 450 Hz and 2200 Hz, but also distorts the 50 Hz, 250 Hz and 350 Hz components of $U_a(\bar{t}_n)$. The presence of spectral components at 250 Hz and 350 Hz in the spectrum of $U_a(\bar{t}_n)$ is attributed to the harmonics in the grid voltage. It is pointed out that by sampling the inverter current at $t = t_k$, no aliasing occurs on the sampled current [82], [90]. Therefore, while no anti-aliasing filter is needed for the measured current [92], it is instead required for the measured AC voltage.

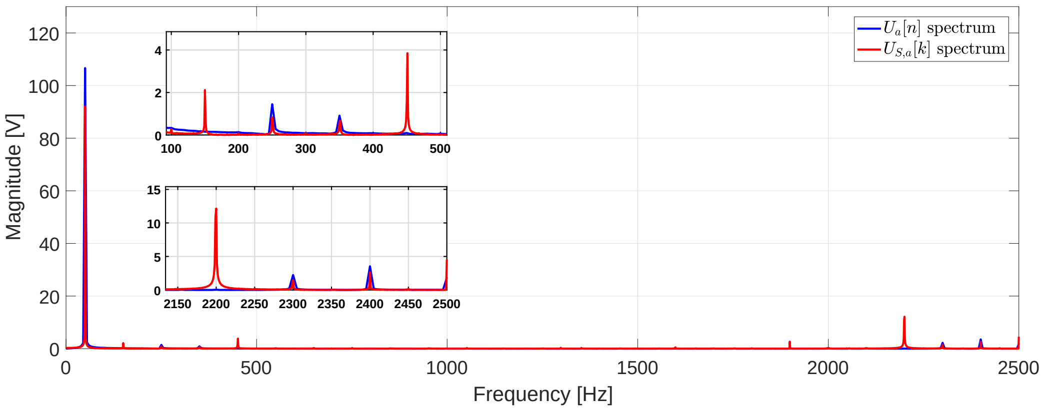

Figure E.2: Detailed view of the magnitude spectrum of the sampled AC voltage (phase a). Aliasing effect introduced by P2 sampling the AC voltage signal at 5 kHz. The signal has been obtained testing the grid-connected converter prototype corresponding to the scheme in Figure 2.27.

As discussed in Section 2.2.1.4, the anti-aliasing filter used in this work consists of a cascaded connection of four notch filters and of a first order low pass filter (see Figure E.3).

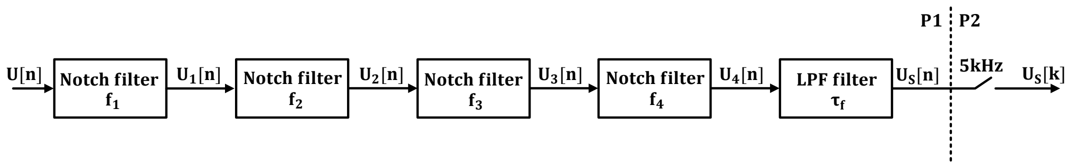

Figure E.3: Block diagram of the anti-aliasing filter used to filter the measured plant AC voltage.

The digital implementation of such filter is discussed as follows. The used discrete-time domain transfer funcion of the notch filter is [130]:

$$G_{AFn}(z) = G_{An} \cdot \frac{1 + a_n z^{-1} + z^{-2}}{1 + a_n \alpha_n z^{-1} + \alpha_n^2 z^{-2}} \tag{E.2}$$

where:

$$a_n = -2cos(\omega_n T_{OS}), \alpha_n \quad = e^{-\frac{1}{2Q}\omega_n T_{OS}}, G_{An} = \frac{1 + a_n \alpha_n + \alpha_n^2}{2 + a_n} \tag{E.3}$$

with $T_{OS} = \frac{1}{f_{OS}} = 10\ \mu$s. The expression of a_n and α_n have been derived by imposing same pole/zero locations for both $G_{AFn}(z)$ and $G_{AFn}(s)$, with $G_{AFn}(s)$ defined as [86], [131]:

$$G_{AFn}(s) = \frac{s^2 + \omega_n^2}{s^2 + \frac{\omega_n}{Q}s + \omega_n^2} \tag{E.4}$$

On the other hand, the discrete-time domain transfer function of the low pass filter is:

$$G_{LPF}(z) = \frac{T_{OS}}{(T_{OS} + \tau_f) - \tau_f z^{-1}} \tag{E.5}$$

This has been obtained from $G_{LPF}(s)$, defined in (E.6), by using the Backward Euler's integration method [131]. τ_f is the time constant of the filter.

$$G_{LPF}(s) = \frac{1}{1 + s\tau_f} \tag{E.6}$$

From (E.2) and (E.5), the signals $U_1[n]$, $U_2[n]$, $U_3[n]$, $U_4[n]$ and $U_S[n]$ in Figure E.3

are calculated as:

$$
\begin{aligned}
U_1[n] &= G_{A1} \cdot U[n] + G_{A1} \cdot a_1 \cdot U[n-1] + G_{A1} \cdot U[n-2] \\
&\quad - a_1 \cdot \alpha_1 \cdot U_1[n-1] - \alpha_1^2 \cdot U_1[n-2]; \\
U_2[n] &= G_{A2} \cdot U_1[n] + G_{A2} \cdot a_2 \cdot U_1[n-1] + G_{A2} \cdot U_1[n-2] \\
&\quad - a_2 \cdot \alpha_2 \cdot U_2[n-1] - \alpha_2^2 \cdot U_2[n-2]; \\
U_3[n] &= G_{A3} \cdot U_2[n] + G_{A3} \cdot a_3 \cdot U_2[n-1] + G_{A3} \cdot U_2[n-2] \\
&\quad - a_3 \cdot \alpha_3 \cdot U_3[n-1] - \alpha_3^2 \cdot U_3[n-2]; \\
U_4[n] &= G_{A4} \cdot U_3[n] + G_{A4} \cdot a_4 \cdot U_3[n-1] + G_{A4} \cdot U_3[n-2] \\
&\quad - a_4 \cdot \alpha_4 \cdot U_4[n-1] - \alpha_4^2 \cdot U_4[n-2]; \\
U_S[n] &= \frac{T_{OS}}{T_{OS} + \tau_f} U_4[n] + \frac{\tau_s}{T_{OS} + \tau_f} U_S[n-1];
\end{aligned}
\tag{E.7}
$$

Finally, $U_S[k]$ is the version of $U_S[n]$ sampled at f_{sample} (i.e. 5 kHz), as illustrated in Figure E.3.

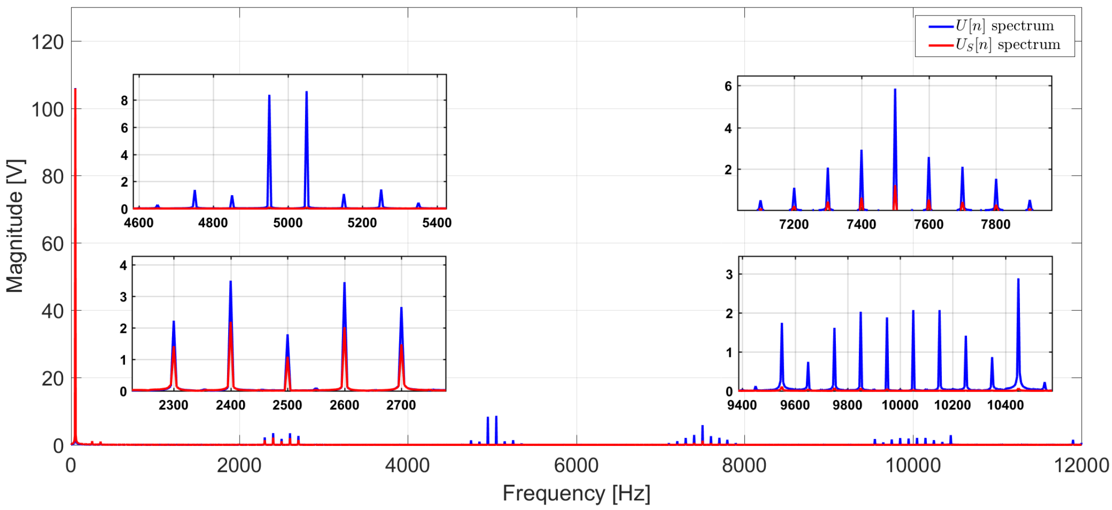

Figure E.4: Comparison between the spectrum of $U_a[n]$ and $U_{S,a}[n]$.

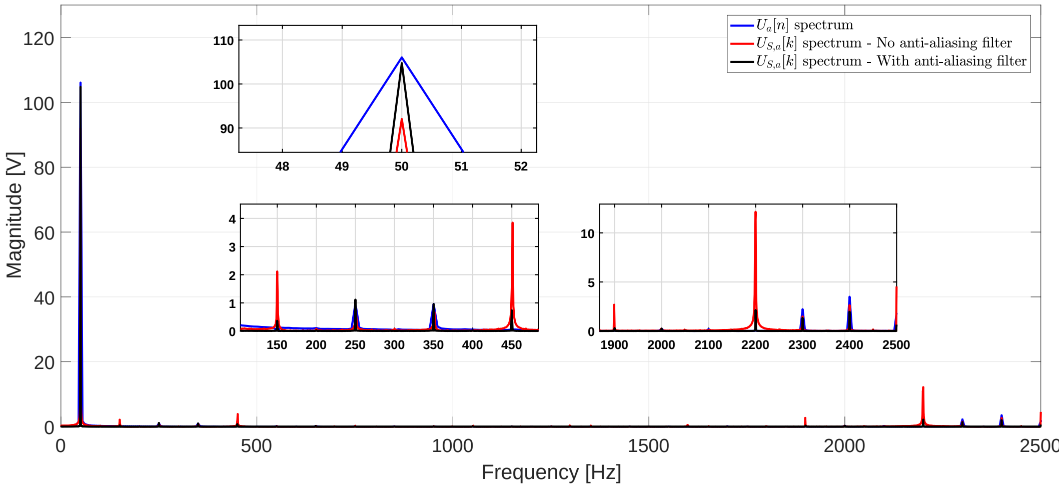

Figure E.5: Comparison between the spectrum of $U_a[n]$ and those of $U_{S,a}[k]$ (with and without the use of the anti-aliasing filter).

Figure E.4 compares the magnitude spectrum of $U_a[n]$ to that of $U_{S,a}[n]$ (phase a). The results confirm the effectiveness of the filter to attenuate the PWM harmonics at side-bands of both 5 kHz and 10 kHz. On the other hand, the PWM harmonics at side-bands of 2.5 kHz and 7.5 kHz are less attenuated, as only the low pass filter significantly exerts a filtering action on them. However, based on the Shannon sampling theorem [83], such harmonics do not generate significant alias in the low frequency range of $U_S[k]$, namely at frequencies less than 1.5 kHz, where the stability problems investigated in this work occur. Hence, despite of the fact that these harmonics reduce the quality of the voltage signal, they are seen as irrelevant to the stability study of the system, which is the main focus of this work.
Figure E.5 compares the spectra of $U_{S,a}[k]$, with the anti-aliasing filter either used or not, to the spectrum of $U_a[n]$. The results confirm the effectiveness of the filter to counteract the aliasing effects observed in Figure E.2, in particular avoiding the alteration of the 50 Hz component, and the generation of the aliased components at 150 Hz, 450 Hz and 2200 Hz.

E.2 Vector control algorithm

This algorithm is executed, as aforementioned, by P2 and aims to calculate the PWM timers necessary to modulate the inverter AC voltage. The main sections of the algorithm consist in the PLL calculations (described in Section E.2.1), the transformation of the acquired plant signals from the *abc*- to the *dq*-frame (described in Section E.2.2), the current loop calculations (described in Section E.2.3) and the SVM algorithm calculating the final PWM timers (described in Section E.2.4). The implementation of the baseline controller algorithm, based on the scheme in Figure 2.20, is described.

E.2.1 PLL

The aim of the PLL loop is to estimate the grid angle and the grid frequency, $\theta[k]$ and $f_{PLL}[k]$ respectively. A digital implementation of the operations defined by the block diagram in Figure 2.14 has been carried out. For this purpose, a discrete-time implementation of the PI controller employed by the PLL has been used. This has been obtained from the continuous-time domain equation describing the PI regulator operation [25]:

$$u_{PLL}(t) = u_{PLL}(t_0) + k_{p,PLL} \cdot e_{PLL}(t) + k_{i,PLL} \cdot \int_{t_0}^{t} e_{PLL}(t)dt \tag{E.8}$$

where $e_{PLL}(t)$ is the PI controller input, while $k_{p,PLL}$ and $k_{i,PLL}$ respectively are its proportional and integral gains. Applying the Backward Euler's approximation of the integral [131], the discrete-time equation corresponding to (E.8) is:

$$u_{PLL}[k] = k_{p,PLL} \cdot e_{PLL}[k] - k_{p,PLL} \cdot e_{PLL}[k-1] + k_{i,PLL} \cdot T_{sample} \cdot e_{PLL}[k] + u_{PLL}[k-1] \tag{E.9}$$

where, in particular, $e_{PLL}[k] = -U^{+}_{S,d}[k]$, i.e. the opposite of the *d*-component of the measured AC plant voltage in the positive *dq*-frame (see Figure 2.14). The output of the PI controller has been allowed to vary within the $[u_{PLL,min}, u_{PLL,max}]$ range, where $u_{PLL,max}$ and $u_{PLL,min}$ are the lower and the upper saturation limits of the regulator.

When these limits are reached an anti wind-up algorithm intervenes which operates as detailed in Table (E.1) [25]. The used values of $u_{PLL,min}$ and $u_{PLL,max}$ respectively are -20π rads^{-1} and 20π rads^{-1}. Based on the PLL block diagram shown in Figure 2.14, the PLL frequency $f_{PLL}[k]$ is then obtained as:

$$f_{PLL}[k] = \frac{u_{PLL}[k]}{2\pi} + f_0 \tag{E.10}$$

where $f_0 = 50$ Hz. The PLL angle $\theta[k]$ is finally derived by integrating $f_{PLL}[k]$ over time (see Figure 2.14), resulting in the following expression in the discrete-time domain

$$\theta[k] = 2\pi f_{PLL}[k] \cdot T_{sample} + \theta[k-1] \tag{E.11}$$

This has been obtaining applying the same Backward Euler's approximation of the integral operator, used to derive (E.9). In more detail, $\theta[k]$ has been confined to vary within the $[0, 2\pi]$ range.

It is worth mentioning that, despite of the fact that in this description the PLL loop calculations have been presented first, these are executed as last by the P2 algorithm. As a result of this, $\theta[k]$ and $f_{PLL}[k]$ are only used in the next iteration of the P2 algorithm, i.e. during the $[t_{k+1}, t_{k+2}]$ period. That being said, in the following Sections, P2 algorithm will be presented taking into consideration the $[t_k, t_{k+1}]$ period (see Figure 5.5). As such, the values $\theta[k-1]$ and $f_{PLL}[k-1]$ will be used in the formula that will be presented, which are the values calculated by the PLL loop in the $[t_{k-1}, t_k]$ period.

Table E.1: Operation of the PLL PI controller anti windup algorithm.

	$e_{PLL}[k] \geq 0$	$e_{PLL}[k] < 0$
$u_{PLL}[k-1] = u_{PLL,max}$	$u_{PLL}[k] = u_{PLL}[k-1]$	eq. (E.9)
$u_{PLL}[k-1] = u_{PLL,min}$	eq. (E.9)	$u_{PLL}[k] = u_{PLL}[k-1]$

E.2.2 Frame transformation

The algorithm executed by P2 bases its calculations on the plant data acquired at $t = t_k$. Firstly, as the controller operates in the dq-frame, the measured three phase signals, namely $U_S[k]$ and $i_S[k]$, are mapped onto the positive and negative dq-frames as detailed in equation (E.12). The Park transformations $T(\theta[k-1])$ and $T(-\theta[k-1])$ are employed to, respectively, derive the positive and negative sequence dq-components of $U_S[k]$ and $i_S[k]$, as discussed in Section 2.2.1.1.2. $\theta[k-1]$ is the PLL angle calculated during the $[t_{k-1},\, t_k]$ period (see the comments at the end of Section E.2.1).

$$\begin{aligned}
\begin{bmatrix} \hat{U}^+_{S,d}[k] \\ \hat{U}^+_{S,q}[k] \end{bmatrix} &= \frac{2}{3} \begin{bmatrix} sin(\theta[k-1]) & sin(\theta[k-1]-\frac{2}{3}\pi) & sin(\theta[k-1]-\frac{4}{3}\pi) \\ cos(\theta[k-1]) & cos(\theta[k-1]-\frac{2}{3}\pi) & cos(\theta[k-1]-\frac{4}{3}\pi) \end{bmatrix} \begin{bmatrix} U_{S,a}[k] \\ U_{S,b}[k] \\ U_{S,c}[k] \end{bmatrix} \\
\begin{bmatrix} \hat{i}^+_{d}[k] \\ \hat{i}^+_{q}[k] \end{bmatrix} &= \frac{2}{3} \begin{bmatrix} sin(\theta[k-1]) & sin(\theta[k-1]-\frac{2}{3}\pi) & sin(\theta[k-1]-\frac{4}{3}\pi) \\ cos(\theta[k-1]) & cos(\theta[k-1]-\frac{2}{3}\pi) & cos(\theta[k-1]-\frac{4}{3}\pi) \end{bmatrix} \begin{bmatrix} i_{a}[k] \\ i_{b}[k] \\ i_{c}[k] \end{bmatrix} \\
\begin{bmatrix} \hat{U}^-_{S,d}[k] \\ \hat{U}^-_{S,q}[k] \end{bmatrix} &= \frac{2}{3} \begin{bmatrix} sin(-\theta[k-1]) & sin(-\theta[k-1]-\frac{2}{3}\pi) & sin(-\theta[k-1]-\frac{4}{3}\pi) \\ cos(-\theta[k-1]) & cos(-\theta[k-1]-\frac{2}{3}\pi) & cos(-\theta[k-1]-\frac{4}{3}\pi) \end{bmatrix} \begin{bmatrix} U_{S,a}[k] \\ U_{S,b}[k] \\ U_{S,c}[k] \end{bmatrix} \\
\begin{bmatrix} \hat{i}^-_{d}[k] \\ \hat{i}^-_{q}[k] \end{bmatrix} &= \frac{2}{3} \begin{bmatrix} sin(-\theta[k-1]) & sin(-\theta[k-1]-\frac{2}{3}\pi) & sin(-\theta[k-1]-\frac{4}{3}\pi) \\ cos(-\theta[k-1]) & cos(-\theta[k-1]-\frac{2}{3}\pi) & cos(-\theta[k-1]-\frac{4}{3}\pi) \end{bmatrix} \begin{bmatrix} i_{a}[k] \\ i_{b}[k] \\ i_{c}[k] \end{bmatrix}
\end{aligned} \tag{E.12}$$

An adaptive notch filter is applied to extract the positive and negative sequence components from the results provided by (E.12) (see Figure 2.12). For its implementation, the same z-domain transfer function form (E.2) has been used, with the only difference that the filter tuned frequency now is equal to twice the PLL frequency (i.e. $2f_{PLL}[k-1]$) [130]:

$$G_N(z)[k] = G_{NF}[k] \cdot \frac{1 + a_N[k]z^{-1} + z^{-2}}{1 + a_N[k]\alpha_N[k]z^{-1} + \alpha_N^2[k]z^{-2}} \tag{E.13}$$

where

$$\begin{aligned} a_N[k] &= -2cos(4\pi f_{PLL}[k-1] \cdot T_{sample}), \\ \alpha_N[k] &= e^{-\frac{1}{2Q} \cdot 4\pi f_{PLL}[k-1] \cdot T_{sample}}, \\ G_{NF}[k] &= \frac{1 + a_N[k]\alpha_N[k] + \alpha_N^2[k]}{2 + a_N[k]} \end{aligned} \tag{E.14}$$

with $Q = 2$. This filter is applied to the 8 signals obtained with (E.12), hence extracting the desired positive and negative sequence dq-components of the voltage and current signals, as detailed in (E.15) and (E.16) respectively.

$$\begin{aligned} U_{S,d}^+[k] &= G_{NF}[k] \cdot \hat{U}_{S,d}^+[k] + G_{NF}[k] \cdot a_N[k] \cdot \hat{U}_{S,d}^+[k-1] + G_{NF}[k] \cdot \hat{U}_{S,d}^+[k-2] \\ &\quad - a_N[k] \cdot \alpha_N[k] \cdot U_{S,d}^+[k-1] - \alpha_N^2[k] \cdot U_{S,d}^+[k-2]; \\ U_{S,q}^+[k] &= G_{NF}[k] \cdot \hat{U}_{S,q}^+[k] + G_{NF}[k] \cdot a_N[k] \cdot \hat{U}_{S,q}^+[k-1] + G_{NF}[k] \cdot \hat{U}_{S,q}^+[k-2] \\ &\quad - a_N[k] \cdot \alpha_N[k] \cdot U_{S,q}^+[k-1] - \alpha_N^2[k] \cdot U_{S,q}^+[k-2]; \\ U_{S,d}^-[k] &= G_{NF}[k] \cdot \hat{U}_{S,d}^-[k] + G_{NF}[k] \cdot a_N[k] \cdot \hat{U}_{S,d}^-[k-1] + G_{NF}[k] \cdot \hat{U}_{S,d}^-[k-2] \\ &\quad - a_N[k] \cdot \alpha_N[k] \cdot U_{S,d}^-[k-1] - \alpha_N^2[k] \cdot U_{S,d}^-[k-2]; \\ U_{S,q}^-[k] &= G_{NF}[k] \cdot \hat{U}_{S,q}^-[k] + G_{NF}[k] \cdot a_N[k] \cdot \hat{U}_{S,q}^-[k-1] + G_{NF}[k] \cdot \hat{U}_{S,q}^-[k-2] \\ &\quad - a_N[k] \cdot \alpha_N[k] \cdot U_{S,q}^-[k-1] - \alpha_N^2[k] \cdot U_{S,q}^-[k-2]; \end{aligned} \tag{E.15}$$

$$\begin{aligned} i_d^+[k] &= G_{NF}[k] \cdot \hat{i}_d^+[k] + G_{NF}[k] \cdot a_N[k] \cdot \hat{i}_d^+[k-1] + G_{NF}[k] \cdot \hat{i}_d^+[k-2] \\ &\quad - a_N[k] \cdot \alpha_N[k] \cdot i_d^+[k-1] - \alpha_N^2[k] \cdot i_d^+[k-2]; \\ i_q^+[k] &= G_{NF}[k] \cdot \hat{i}_q^+[k] + G_{NF}[k] \cdot a_N[k] \cdot \hat{i}_q^+[k-1] + G_{NF}[k] \cdot \hat{i}_q^+[k-2] \\ &\quad - a_N[k] \cdot \alpha_N[k] \cdot i_q^+[k-1] - \alpha_N^2[k] \cdot i_q^+[k-2]; \\ i_d^-[k] &= G_{NF}[k] \cdot \hat{i}_d^-[k] + G_{NF}[k] \cdot a_N[k] \cdot \hat{i}_d^-[k-1] + G_{NF}[k] \cdot \hat{i}_d^-[k-2] \\ &\quad - a_N[k] \cdot \alpha_N[k] \cdot i_d^-[k-1] - \alpha_N^2[k] \cdot i_d^-[k-2]; \\ i_q^-[k] &= G_{NF}[k] \cdot \hat{i}_q^-[k] + G_{NF}[k] \cdot a_N[k] \cdot \hat{i}_q^-[k-1] + G_{NF}[k] \cdot \hat{i}_q^-[k-2] \\ &\quad - a_N[k] \cdot \alpha_N[k] \cdot i_q^-[k-1] - \alpha_N^2[k] \cdot i_q^-[k-2]; \end{aligned} \tag{E.16}$$

Once such components have been calculated, it is then possible to execute the current controller algorithm, according to the scheme in Figure 2.20. The result of this algorithm will be the dq-components of the PWM modulation functions, $m_{dq}[k]$. These will be used to calculate the PWM pattern applied in the following $[t_{k+1}, t_{k+2}]$ period. While the current controller algorithm is described in Section E.2.3, the calculation of the PWM timers is illustrated in Section E.2.4.

E.2.3 Current controller

As shown in Figure 2.20, the current controller is composed by four feedback loops, all having the same architecture with the PI regulator being the core control element. Equivalently to (E.9), the outputs of the four PI current regulators in Figure 2.20 are calculated as:

$$\begin{aligned}
u^+_{I,d}[k] &= k_{p,I} \cdot e^+_{I,d}[k] - k_{p,I} \cdot e^+_{I,d}[k-1] + k_{i,PLL} \cdot T_{sample} \cdot e^+_{I,d}[k] + u^+_{I,d}[k-1],\\
u^+_{I,q}[k] &= k_{p,I} \cdot e^+_{I,q}[k] - k_{p,I} \cdot e^+_{I,q}[k-1] + k_{i,PLL} \cdot T_{sample} \cdot e^+_{I,q}[k] + u^+_{I,q}[k-1],\\
u^-_{I,d}[k] &= k_{p,I} \cdot e^-_{I,d}[k] - k_{p,I} \cdot e^-_{I,d}[k-1] + k_{i,PLL} \cdot T_{sample} \cdot e^-_{I,d}[k] + u^-_{I,d}[k-1],\\
u^-_{I,q}[k] &= k_{p,I} \cdot e^-_{I,q}[k] - k_{p,I} \cdot e^-_{I,q}[k-1] + k_{i,PLL} \cdot T_{sample} \cdot e^+_{I,q}[k] + u^-_{I,q}[k-1],
\end{aligned} \tag{E.17}$$

where $k_{p,I}$ and $k_{p,I}$ respectively are the proportional and the integral gains of the regulator. The PI input errors in (E.17) are calculated as:

$$\begin{aligned}
e^+_{I,d}[k] &= i^+_{d,ref} - i^+_d[k],\\
e^+_{I,q}[k] &= i^+_{q,ref} - i^+_q[k],\\
e^-_{I,d}[k] &= i^-_{d,ref} - i^-_d[k],\\
e^-_{I,q}[k] &= i^-_{q,ref} - i^-_q[k],
\end{aligned} \tag{E.18}$$

Such as the PLL PI controller, the current PI regulators outputs are limited in a $[u_{I,min}, u_{I,max}]$ range, where $u_{I,max}$ and $u_{I,min}$ respectively are the lower and upper saturation limits of the these regulators. When these limits are reached, the same anti-windup strategy used for the PLL loop is applied [25], as detailed in the Table E.2.

The values of $u_{I,min}$ and $u_{I,max}$ respectively are $-0.4U_{DC}[k]$ and $0.4U_{DC}[k]$. Considering the controller scheme in Figure 2.20, a Voltage Feed Foward (VFF) term

Table E.2: Operation of the current PI controller anti windup algorithm.

	$e_I[k] \geq 0$	$e_I[k] < 0$
$u_I[k-1] = u_{I,max}$	$u_I[k] = u_I[k-1]$	eq. (E.17)
$u_I[k-1] = u_{I,min}$	eq. (E.17)	$u_I[k] = u_I[k-1]$

is used, which results from the application of a first order low pass filter on the positive and negative dq-components of the measured $U_S[k]$ signal (i.e. $U^+_{S,d}[k]$, $U^+_{S,q}[k]$, $U^-_{S,d}[k]$ and $U^-_{S,q}[k]$). Applying the same discrete-time trasnfer function formulation of the LPF filter (E.5), these VFF terms have been calculated as [131]:

$$\begin{aligned}
U^+_{VFF,d}[k] &= \frac{T_{sample}}{T_{sample}+\tau_p} U^+_{S,d}[k] + \frac{\tau_p}{T_{sample}+\tau_p} U^+_{VFF,d}[k-1], \\
U^+_{VFF,q}[k] &= \frac{T_{sample}}{T_{sample}+\tau_p} U^+_{S,q}[k] + \frac{\tau_p}{T_{sample}+\tau_p} U^+_{VFF,q}[k-1], \\
U^-_{VFF,d}[k] &= \frac{T_{sample}}{T_{sample}+\tau_n} U^-_{S,d}[k] + \frac{\tau_n}{T_{sample}+\tau_n} U^-_{VFF,d}[k-1], \\
U^-_{VFF,q}[k] &= \frac{T_{sample}}{T_{sample}+\tau_n} U^-_{S,q}[k] + \frac{\tau_n}{T_{sample}+\tau_n} U^-_{VFF,q}[k-1],
\end{aligned} \tag{E.19}$$

where τ_p and τ_n respectively are the positive sequence and the negative sequence time constants of the filter.

Based on the control scheme in Figure (2.20), the outputs of the four current feedback loops are calculated as:

$$\begin{aligned}
m^+_d[k] &= \frac{2}{U_{DC}[k]}(u^+_{I,d}[k] + U^+_{VFF,d}[k] - 2\pi f_{PLL}[k-1] \cdot i^+_q[k] \cdot L_f), \\
m^+_q[k] &= \frac{2}{U_{DC}[k]}(u^+_{I,q}[k] + U^+_{VFF,q}[k] + 2\pi f_{PLL}[k-1] \cdot i^+_d[k] \cdot L_f), \\
m^-_d[k] &= \frac{2}{U_{DC}[k]}(u^-_{I,d}[k] + U^-_{VFF,d}[k] + 2\pi f_{PLL}[k-1] \cdot i^-_q[k] \cdot L_f), \\
m^-_q[k] &= \frac{2}{U_{DC}[k]}(u^-_{I,q}[k] + U^-_{VFF,q}[k] - 2\pi f_{PLL}[k-1] \cdot i^-_d[k] \cdot L_f),
\end{aligned} \tag{E.20}$$

The negative sequence dq-components are then mapped on the positive dq-frame, based on (2.14), as:

$$
\begin{aligned}
m_d[k] &= m_d^+[k] + m_d^-[k]cos(2\phi_{PLL}[k-1]) + m_q^-[k]sin(2\phi_{PLL,k-1}), \\
m_{q,k} &= m_q^+[k] - m_d^-[k]sin(2\phi_{PLL}[k-1]) + m_d^+[k]cos(2\phi_{PLL,k-1}),
\end{aligned}
\tag{E.21}
$$

The results in (E.21) are used by the SVM algorithm to calculate the final PWM timers that will drive the IGBT modules in the next $[t_{k+1},\ t_{k+2}]$ sampling window. Their calculation is discussed in the following Section.

E.2.4 Calculation of PWM timers

A set of calculations is used to implement the SVM algorithm and, thereby, to determine the six PWM timers driving the converter IGBT modules in the next $[t_{k+1},\ t_{k+2}]$ (see Figure 5.5). For this purpose, the modulation indexes (E.21) are expressed in the $\alpha\beta$-frame applying the transformation (B.15). The resulting $m_\alpha[k]$ and $m_\beta[k]$ indexes are:

$$
\begin{aligned}
m_\alpha[k] &= m_d[k]sin(\phi_{PLL}[k-1]) + m_q[k]cos(\phi_{PLL}[k-1]), \\
m_\beta[k] &= -m_d[k]cos(\phi_{PLL}[k-1]) + m_q[k]sin(\phi_{PLL}[k-1]),
\end{aligned}
\tag{E.22}
$$

As discussed in Section A.2, from the result in (E.22) it is possible to derive the corresponding *abc*-frame modulation functions, according to the equations detailed in Tables A.1 and A.2. These respectively allow the identification of the $\vec{m}[k]$ sector and, thereby, of the $m_a[k]$, $m_b[k]$ and $m_c[k]$ indexes. Based on (A.1), such three phase modulation functions can be related to the turn-on times of Q_1, Q_3 and Q_5, which are the switches on the top of the inverter legs (see Figure 2.2). In particular, by respectively indicating these times as $T_{ON,a}[k]$, $T_{ON,b}[k]$ $T_{ON,c}[k]$, these can be calculated as:

$$
\begin{aligned}
T_{ON,a}[k] &= T_{sample}\frac{1+m_a[k]}{2} \\
T_{ON,b}[k] &= T_{sample}\frac{1+m_b[k]}{2} \\
T_{ON,c}[k] &= T_{sample}\frac{1+m_c[k]}{2}
\end{aligned}
\tag{E.23}
$$

whose corresponding off times are:

$$
\begin{aligned}
T_{OFF,a}[k] &= T_{sample} - T_{ON,a}[k] \\
T_{OFF,b}[k] &= T_{sample} - T_{ON,b}[k] \\
T_{OFF,c}[k] &= T_{sample} - T_{ON,c}[k]
\end{aligned}
\tag{E.24}
$$

As discussed in Appendix A, in the asymmetrical sampling technique [72] the modulation functions are sampled when the triangular carrier function is either equal to 1 or -1. While in the former case the Q_1, Q_3 and Q_5 switches are turned-off during the first portion of the T_{sample} period, in the latter case, Q_1, Q_3 and Q_5 are instead turned-on during such period (see Figure A.3). Hence, by indicating with $T_1[k]$, $T_3[k]$, $T_5[k]$ the PWM timers calculated by the controller algorithm for the Q_1, Q_3 and Q_5 switches, these are either the turn-off times (E.24) when the carrier is equal to 1 or the turn-on times (E.23) when the carrier is -1. By indicating with $T_2[k]$, $T_4[k]$, $T_6[k]$ the PWM timers of Q_2, Q_4 and Q_6, $T_1[k] = T_2[k]$, $T_3[k] = T_4[k]$, $T_5[k] = T_6[k]$, even though the states of Q_2, Q_4 and Q_6 are complementary to those of Q_1, Q_3 and Q_5, respectively.
The technique used by the implemented algorithm to define the PWM timers is summarised in Table E.3.

Table E.3: PWM timers without added dead-time.

Carrier value	$m_{abc}[k]$	top IGBT	bottom IGBT
1	$T_1[k] = T_2[k] = T_{OFF,a}[k]$	OFF	ON
	$T_3[k] = T_4[k] = T_{OFF,b}[k]$	OFF	ON
	$T_5[k] = T_6[k] = T_{OFF,c}[k]$	OFF	ON
-1	$T_1[k] = T_2[k] = T_{ON,a}[k]$	ON	OFF
	$T_3[k] = T_4[k] = T_{ON,b}[k]$	ON	OFF
	$T_5[k] = T_6[k] = T_{ON,b}[k]$	ON	OFF

For the proper operation of the converter, a dead-time must be introduced to avoid the IGBTs of the same converter leg from conducting simultaneously. Given that, as mentioned in Appendix D.4, a 1 μs dead-time is introduced by the gate driver, an extra $2T_{DT}$ dead-time has been introduced via software, with $T_{DT} = 0.5$ μs. By doing so, a total dead-time of 2 μs has been obtained. Taking into account such added T_{DT} dead-time, the final PWM timers calculated by the controller, namely $\hat{T}_1[k]$, $\hat{T}_2[k]$, $\hat{T}_3[k]$, $\hat{T}_4[k]$, $\hat{T}_5[k]$ and $\hat{T}_6[k]$, are as detailed in Table (E.4).

These timers are loaded on the PL section of the board and are used by six corresponding FPGA counters as threshold values to commutate the state of the associated PWM outputs.

Table E.4: PWM timers with added dead-time.

Carrier value	$m_{abc}[k]$	IGBT state
1	$\hat{T}_1[k] = T_1[k] + T_{DT}$	OFF
	$\hat{T}_2[k] = T_2[k] - T_{DT}$	ON
	$\hat{T}_3[k] = T_3[k] + T_{DT}$	OFF
	$\hat{T}_4[k] = T_4[k] - T_{DT}$	ON
	$\hat{T}_5[k] = T_5[k] + T_{DT}$	OFF
	$\hat{T}_6[k] = T_6[k] - T_{DT}$	ON
-1	$\hat{T}_1[k] = T_1[k] - T_{DT}$	ON
	$\hat{T}_2[k] = T_2[k] + T_{DT}$	OFF
	$\hat{T}_3[k] = T_3[k] - T_{DT}$	ON
	$\hat{T}_4[k] = T_4[k] + T_{DT}$	OFF
	$\hat{T}_5[k] = T_5[k] - T_{DT}$	ON
	$\hat{T}_6[k] = T_6[k] + T_{DT}$	OFF

E.3 Experimental calculation of the pn-frame small-signal admittance

The methodology used in the tests described in Section 4.1.3.2 to derive the pn-frame admittance frequency responses experimentally is described as follows. In particular, this technique allows the derivation of the pn-frame admittance resulting from the series combination of the converter admittance and of the admittance which is connected to the inverter AC terminals through its coupling reactor. Based on (4.5), the frequency response matrix of such admittance is formulated as:

$$Y_{m,PN}(j2\pi f) = \begin{bmatrix} Y_{m,pp}(j2\pi f) & Y_{m,pn}(j2\pi f) \\ Y_{m,np}(j2\pi(f-2f_0)) & Y_{m,nn}(j2\pi(f-2f_0)) \end{bmatrix} \tag{E.25}$$

In order to calculate the frequency responses $Y_{m,pp}(j2\pi f)$ and $Y_{m,np}(j2\pi(f-2f_0))$ in (E.25), a small-signal positive sequence perturbation $\delta m^+_{abc}[k]$ has been added to the steady-state abc-frame modulation indexes $m_{abc,0}[k]$:

$$\begin{aligned}
\delta m_a^+[k] &= \delta m_0 cos(\gamma[k]) \\
\delta m_b^+[k] &= \delta m_0 cos(\gamma[k] - \frac{2}{3}\pi) \\
\delta m_c^+[k] &= \delta m_0 cos(\gamma[k] - \frac{4}{3}\pi)
\end{aligned} \tag{E.26}$$

where δm_0 is the amplitude of the small-signal perturbation. The $\gamma[k]$ angle, confined in the [0 rad, 2π rad] range, is defined as:

$$\gamma[k] = 2\pi f_p \cdot T_{sample} + \gamma[k-1] \tag{E.27}$$

where f_p is the frequency of the applied small-signal perturbation. It is pointed out that $\gamma[k]$ is synchronized to the converter angle $\theta[k]$. As in the carried out tests, no PLL loop has been used, $\theta[k]$ has been calculated as:

$$\theta[k] = 2\pi f_0 \cdot T_{sample} + \theta[k-1] \tag{E.28}$$

and has been confined in the [0 rad, 2π rad] range. $f_0 = 50$ Hz. In these tests, asymmetrical regular sampling has been applied, with a converter switching frequency $f_s = 2.5$ kHz. Therefore, $T_{sample} = 200$ μs.

Based on (A.5), and taking into consideration the T_{sample} delay of the controller, the corresponding small-signal perturbation $\delta U_I[k]$ on the inverter output voltage is:

$$\begin{aligned}
\delta U_{I_a}[k+1] &= \frac{U_{DC}}{2}\delta m_0 cos(\gamma[k]) = \delta U_{I_0} cos(\gamma[k]) \\
\delta U_{I_b}[k+1] &= \frac{U_{DC}}{2}\delta m_0 cos(\gamma[k] - \frac{2}{3}\pi) = \delta U_{I_0} cos(\gamma[k] - \frac{2}{3}\pi) \\
\delta U_{I_c}[k+1] &= \frac{U_{DC}}{2}\delta m_0 cos(\gamma[k] - \frac{4}{3}\pi) = \delta U_{I_0} cos(\gamma[k] - \frac{4}{3}\pi)
\end{aligned} \tag{E.29}$$

with:

$$\delta U_{I_0} = \frac{U_{DC}}{2}\delta m_0 \tag{E.30}$$

In the test, the small-signal perturbation in (E.26) has been applied for a period of $1s$, recording the corresponding current feedback signal $i[k]$. This consists of 5000 samples, as $T_{sample} = 200\ \mu$s. A spectral analysis of this signal has been carried out, which indicated the presence of both a positive sequence component $\delta i^+_{pp}(j2\pi f_p)$ and of a negative sequence component $\delta i^-_{np}(j2\pi(f_p - 2f_0))$. Hence, $Y_{m,pp}(j2\pi f_p)$ and $Y_{m,np}(j2\pi(f_p - 2f_0))$ have been calculated as:

$$\begin{aligned} Y_{m,pp}(j2\pi f_p) &= \frac{|\delta i^+_{pp,a}(j2\pi f_p)|}{\delta U_{I_0}} \angle(\delta i^+_{pp,a}(j2\pi f_p) e^{-j2\pi f_p T_{sample}}) \\ Y_{C,np}(j2\pi(f_p - 2f_0)) &= \frac{|\delta i^-_{np,a}(j2\pi(f_p - 2f_0))|}{\delta U_{I_0}} \angle(\delta i^-_{np,a}(j2\pi(f_p - 2f_0)) e^{-j2\pi f_p T_{sample}}) \end{aligned} \tag{E.31}$$

Similarly, in order to calculate the $Y_{m,nn}(j2\pi f)$ and $Y_{m,pn}(j2\pi(f + 2f_0)$ terms in (E.25), a small-signal negative sequence deviation $\delta m^-_{abc}[k]$ has been added to $m_{abc,0}[k]$:

$$\begin{aligned} \delta m^-_a[k] &= \delta m_0 cos(\phi[k]) \\ \delta m^-_b[k] &= \delta m_0 cos(\phi[k] + \frac{2}{3}\pi) \\ \delta m^-_c[k] &= \delta m_0 cos(\phi[k] + \frac{4}{3}\pi) \end{aligned} \tag{E.32}$$

The recorded current feedback signal $i[k]$ now revealed the presence of a negative sequence spectral component $\delta i^-_{nn}(j2\pi f_p)$ and of a positive sequence component $\delta i^+_{pn}(j2\pi(f_p + 2f_0))$. Thereby, $Y_{m,nn}(j2\pi f_p)$ and $Y_{m,pn}(j2\pi(f_p + 2f_0))$ have been calculated as:

$$\begin{aligned} Y_{m,nn}(j2\pi f_p) &= \frac{|\delta i^-_{nn,a}(j2\pi f_p)|}{U_{I_0}} \angle(\delta i^-_{nn,a}(j2\pi f_p) e^{-j2\pi f_p T_{sample}}) \\ Y_{m,pn}(j2\pi(f_p + 2f_0)) &= \frac{|\delta i^+_{pn,a}(j2\pi(f_p + 2f_0))|}{U_{I_0}} \angle(\delta i^+_{pn,a}(j2\pi(f_p + 2f_0)) e^{-j2\pi f_p T_{sample}}) \end{aligned} \tag{E.33}$$

The test has been repeated for f_p varying in the [5 Hz, 990 Hz] range, which allowed the derivation of the experimental frequency responses $Y_{m,pp}(j2\pi f)$, $Y_{m,pn}(j2\pi(f +$

$2f_0)), Y_{m,np}(j2\pi(f-2f_0)), Y_{m,nn}(j2\pi f)$.

Appendix F

Publications and inventions

F.1 Publications

1. **Accepted**: G. Amico, A. Egea-Àlvarez, P. Brogan and S. Zhang, "Small-signal converter admittance in the *pn*-frame: systematic derivation and analysis of the cross-coupling terms", IEEE Transaction on Energy Conversion.

2. **Accepted**: G. Amico, A. Egea-Àlvarez, L. Xu, and P. Brogan, "Stability margin definition for a converter-grid system based on diagonal dominance property in the sequence-frame", IEEE EPE 2019 ECCE Europe Conference, Genova (Italy).

3. **Submission pending**: G. Amico, A. Egea-Àlvarez, P. Brogan and L. Xu, "Study of the diagonal dominance property of the converter-grid system in the sequence-frame and its implication of the stability analysis".

4. **Submission pending**: G. Amico, A. Egea-Àlvarez, P. Brogan and L. Xu, "Study of cable due wind farm resonances and mitigation technique".

F.2 Inventions

1. Paul Brogan, Paul Godridge, Gabriele Amico, Agusti Egea-Àlvarez, "PWM enhancement to minimize discrete delay ", Invention Disclosure no. 2019600740 GB, Siemens Gamesa Renewable Energy.